

LOW-LYING COLLECTIVE EXCITATIONS IN  
NEUTRON-RICH EVEN-EVEN SULFUR AND ARGON  
ISOTOPES STUDIED VIA INTERMEDIATE-ENERGY  
COULOMB EXCITATION AND PROTON SCATTERING

By

Heiko Scheit

A DISSERTATION

Submitted to  
Michigan State University  
in partial fulfillment of the requirements  
for the Degree of

DOCTOR OF PHILOSOPHY

Department of Physics and Astronomy

1998



# ABSTRACT

## LOW-LYING COLLECTIVE EXCITATIONS IN NEUTRON-RICH EVEN-EVEN SULFUR AND ARGON ISOTOPES STUDIED VIA INTERMEDIATE-ENERGY COULOMB EXCITATION AND PROTON SCATTERING

By

Heiko Scheit

The energies and  $B(E2; 0_{\text{g.s.}}^+ \rightarrow 2_1^+)$  values for the lowest  $J^\pi = 2^+$  states in the neutron-rich radioactive nuclei  $^{38,40,42}\text{S}$  and  $^{44,46}\text{Ar}$  were measured via intermediate-energy Coulomb excitation. Beams of these nuclei were produced by projectile fragmentation with energies per nucleon of  $E/A \approx 40$  MeV and directed onto a secondary Au target, where Coulomb excitation of the projectile took place. The subsequently emitted de-excitation photons were detected in an array of NaI(Tl) detectors, which allowed the identification of the first excited  $2^+$  states in these nuclei. The energies of the first excited  $J^\pi = 2^+$  states in  $^{40,42}\text{S}$  and  $^{44}\text{Ar}$  were established, while a previously observed state in  $^{46}\text{Ar}$  was assigned a definite spin. For all isotopes the  $B(E2; 0_{\text{g.s.}}^+ \rightarrow 2_1^+)$  was established. The results for  $^{40,42}\text{S}$  provide the first evidence of moderate collectivity ( $\beta_2 \approx 0.29$ ) near  $N = 28$ , while the effects of the  $N = 28$  shell closure persist in the  $Z = 18$  nucleus  $^{46}\text{Ar}$  ( $\beta_2 = 0.176(17)$ ). The deformation parameter of  $^{44}\text{Ar}$  was measured to be  $\beta_2 = 0.241(14)$ .

A proton scattering experiment was also performed on the unstable nuclei  $^{42,44}\text{Ar}$ . The measured cross sections have been compared to optical model calculations assuming rotational and vibrational excitation. The resulting deformation parameters indicate an isoscalar excitation.



Meiner Familie  
gewidmet



## ACKNOWLEDGMENTS

First and foremost I would like to thank Thomas Glasmacher. Thanks Thomas! You were a great boss. You gave me plenty of freedom (especially in my working hours) and you always knew when I needed a “kick in the butt” to get me going again. I want to especially thank you for sending me to the summer school in Erice, Sicily. (I won’t elaborate . . .)

I would like to thank Walt Benenson, Wolfgang Bauer, Wayne Repko, and Bernard Pope for serving on my Ph.D. committee.

Special thanks go to Maggie Hellström, since she got me started on the Coulomb excitation experiments. It all sounded so easy in the beginning...

Rich and Sharon, thanks for the nice times at your parties. I really enjoyed a lot; throwing darts, bottling beer, playing foosball, doing the BBQ, watching Wallace and Gromit . . . Your house was often the meeting point for the “international crew”, which I had the pleasure to know: Greg, Heather, Marielle, Roy, Razvan, Kurt, Justine, Peter, Marcus, Navin, Anu, Andreas, Thomas A., Yorick, Tiina, Theo, Bertram, Takashi, Valentina, Marilena, . . . (I am sure I forgot many more). I wonder who will keep things together after you leave.

I am thankful to the people that helped me during my graduate studies: Mike Thoennesen, Paul Cottle, Kirby Kemper, Rick Harkewicz, Rich Ibbotson, Dave Morrissey, Mathias Steiner, Peter Thirolf, Yorick Blumenfeld, Tiina Suomijärvi, Alex Brown, Gregers Hansen, Jim Brown, Keith Jewell.

Of course there are also my fellow students: Don – thanks for the good deal on my car, it wasn’t so bad after all, Jon, Mike F., Pat, Declan, Chris – sorry for going overboard in taking messages (from Sara or Jen? I forgot . . .), Joelle, Erik, Joann, Jing, Barry, Raman, Luke, Sally, Gerd . . . Maybe we will see each other at

some “boring” physics conference again. (Jac, was it 305 Schuss Village?) Thank you, Barry, for the times we spent (jointly) together and the many discussions. Daniel and Jac, thanks for introducing me to IGOR. Rich, Boris, Marcus, and Barry: thanks for proof reading my thesis. Unfortunately they didn’t check this section.

I thank the cyclotron staff members for their support. I really enjoyed doing the experiments here at the NSCL. I am also grateful for the generous financial support during my graduate studies.

The Sandhill Soaring Club also helped me to survive during the last 4 years and thanks, Jeff, for bringing me in contact with them. I would like to thank everybody that went to fly with me. It was a pleasure.

“Moi Droog” Boris, I know “In russia, we ...”

I hope I wasn’t too rude to you at times, but I am really glad to have you as a friend.

Well, now I need to say something about Marcus. Without you it would have been a lot more boring in East Lansing. I will never forget the many evenings and nights at the RIV and many other establishments in the area. Also, our discussions about physics and in general (“Did you have meat in the East Germany?”) have been very enlightening and useful. The analysis of my data without the “Driftellipsenmethode” would have been much more difficult. Your soccer expertise is very much appreciated.

I would like to thank my family, especially my mother. Their support made this work possible.

Finally, thanks to Simona, her cell phone, e-mail and the TeleGroup calling card.

# CONTENTS

<b>LIST OF TABLES</b>	<b>xiii</b>
<b>LIST OF FIGURES</b>	<b>xv</b>
<b>1 Introduction</b>	<b>1</b>
1.1 The Atomic Nucleus . . . . .	1
1.2 Nuclear Models . . . . .	2
1.2.1 Microscopic Models . . . . .	3
1.2.2 Collective Models . . . . .	5
1.3 Experimental Probes of Nuclear Structure . . . . .	9
1.3.1 Coulomb Excitation as an Electromagnetic Probe . . . . .	9
1.3.2 Proton Scattering as an Hadronic Probe . . . . .	10
1.4 Heavy sd-Shell Nuclei . . . . .	10
<b>2 Intermediate-Energy Coulomb Excitation</b>	<b>13</b>
2.1 General Description . . . . .	13
2.2 Excitation Cross Section . . . . .	15
2.2.1 Approximations . . . . .	16
2.2.2 The Excitation Cross Section . . . . .	17
2.2.3 Electric Versus Magnetic Excitations . . . . .	18
2.2.4 Equivalent Photon Method . . . . .	18
2.3 Basic Parameters . . . . .	19
2.3.1 Impact Parameter and Distance of Closest Approach . . . . .	19
2.3.2 Sommerfeld Parameter . . . . .	20
2.3.3 Adiabaticity Parameter . . . . .	20
2.3.4 Excitation Strength . . . . .	24
2.4 Experimental Considerations . . . . .	25
2.4.1 Projectile Excitation . . . . .	25
2.4.2 Radioactive Nuclear Beam Production . . . . .	26
2.4.3 Detection of De-Excitation Photons . . . . .	28
<b>3 Coulomb Excitation of <sup>38,40,42</sup>S and <sup>44,46</sup>Ar</b>	<b>35</b>
3.1 Introduction . . . . .	35
3.2 Experimental Procedure . . . . .	36
3.2.1 Secondary Beams . . . . .	36

3.2.2	Experimental Setup . . . . .	37
3.2.3	Particle Detection . . . . .	38
3.3	The NSCL NaI(Tl) Array . . . . .	41
3.3.1	Mechanical Setup and Principles of Operation . . . . .	41
3.4	Electronics . . . . .	43
3.4.1	Electronics for the NaI(Tl) Array . . . . .	45
3.4.2	Calibration and Gain Matching of the Detectors . . . . .	46
3.5	Analysis . . . . .	52
3.5.1	Stability of Calibration . . . . .	52
3.5.2	Angular Distributions . . . . .	52
3.5.3	Photon Yields . . . . .	58
3.5.4	Error Analysis . . . . .	58
3.6	Results and Discussion . . . . .	61
3.6.1	Observations . . . . .	61
3.6.2	Comparison to Theory . . . . .	64
<b>4</b>	<b>Direct Reactions</b>	<b>69</b>
4.1	Elastic Scattering . . . . .	71
4.1.1	Optical Model . . . . .	71
4.1.2	Effective Optical Potentials . . . . .	72
4.1.3	Microscopic Optical Potentials . . . . .	73
4.2	Inelastic Scattering . . . . .	76
4.2.1	Coupled Channels . . . . .	76
4.2.2	Nuclear Deformation . . . . .	77
4.2.3	$M_n/M_p$ . . . . .	78
<b>5</b>	<b>Proton Scattering of <sup>36,42,44</sup>Ar</b>	<b>81</b>
5.1	Experimental Setup . . . . .	82
5.1.1	Proton Detectors . . . . .	83
5.1.2	Beam Particle Tracking . . . . .	93
5.1.3	Electronics . . . . .	96
5.1.4	Kinematic Reconstruction . . . . .	98
5.2	Simulation . . . . .	102
5.2.1	Examples . . . . .	102
5.2.2	Efficiency . . . . .	103
5.3	Analysis . . . . .	103
5.3.1	Excitation Energy . . . . .	103
5.3.2	Problem with the Cross Section . . . . .	110
5.3.3	Deformation Parameters and $M_n/M_p$ . . . . .	117
<b>6</b>	<b>Summary</b>	<b>123</b>

<b>A</b>	<b>Coulomb Excitation</b>	<b>125</b>
A.1	Semi-Classical Approach and Perturbation Theory . . . . .	125
A.1.1	Cross Sections . . . . .	128
A.1.2	Relation Between Impact Parameter and Deflection Angle . .	129
A.2	Some Formulas . . . . .	130
A.2.1	Relations between $\beta_2$ , $Q_0$ , B(E2) . . . . .	130
A.2.2	Constants . . . . .	132
<b>B</b>	<b><math>\gamma</math>-Ray Angular Distribution Following Relativistic Coulomb Excitation</b>	<b>133</b>
B.1	General Structure . . . . .	134
B.2	Detailed Derivation . . . . .	135
B.2.1	What is $\langle I_{ff} M_{ff} \mathbf{k} \sigma   H_\gamma   I_f M_f \rangle$ ? . . . . .	135
B.2.2	The Angular Distribution . . . . .	138
B.3	Angular Distribution Using the Winther and Alder Excitation Amplitudes . . . . .	141
B.4	Summary of Formulas . . . . .	145
B.4.1	Angular Momentum Representation of the Rotation Matrix .	145
B.4.2	Some Properties of the Clebsch - Gordan - Coefficients and $3j$ -Symbols . . . . .	146
B.4.3	Some Properties of the $6j$ -symbols . . . . .	146
B.4.4	$Y_{lm}$ . . . . .	147
B.4.5	$\gamma - \gamma$ Correlation Function . . . . .	147
<b>C</b>	<b>Relativistic Kinematics</b>	<b>149</b>
C.1	Notation and Preliminaries . . . . .	149
C.2	Collision of Two Particles . . . . .	151
C.2.1	Relation Between $\theta_{cm}$ and $\theta_{lab}$ . . . . .	154
C.2.2	Solid Angle Relation . . . . .	155
C.3	Decay of $A$ into $B_i$ $\{i=1,2,\dots,N\}$ . . . . .	157
C.4	Summary of Formulas . . . . .	158
C.4.1	General . . . . .	158
C.4.2	Total Energy in the Center of Mass System $E_{cm}$ . . . . .	158
C.4.3	Individual Energies in the Center of Mass System . . . . .	158
C.4.4	Velocity of the Center of Mass in the Laboratory $\beta_{cm}$ . . . . .	159
C.4.5	Relation Between $\theta_{cm}$ and $\theta_{lab}$ . . . . .	159
C.4.6	Solid Angle Relation . . . . .	159
C.4.7	Invariant Mass . . . . .	160
<b>D</b>	<b>Simulation of the Proton Scattering Experiment</b>	<b>161</b>
D.1	Structure of Computer Code . . . . .	161
D.2	Description of Input File . . . . .	163
<b>E</b>	<b>Differential Cross Section</b>	<b>165</b>

<b>F</b>	<b>A New Method for Particle Tracking</b>	<b>169</b>
F.1	Traditional Tracking . . . . .	169
F.2	New Method . . . . .	170
F.2.1	Some Beam Physics . . . . .	170
F.2.2	Determination of Position and Slope . . . . .	173
F.2.3	Practical Method . . . . .	175
<b>G</b>	<b>Fitting of Spectra</b>	<b>177</b>
	<b>LIST OF REFERENCES</b>	<b>179</b>

# LIST OF TABLES

3.1	Parameters $a_0, a_2, a_4$ of the angular distribution. . . . .	53
3.2	Summary of uncertainties. . . . .	60
3.3	Experimental parameters and results. . . . .	68
4.1	Becchetti-Greenlees optical potential parameters. . . . .	73
5.1	Detector thicknesses in $\mu\text{m}$ . . . . .	87
5.2	Experimental Parameters. . . . .	110
5.3	Deformation parameters $\beta_2$ obtained with the various ECIS fits. . . . .	120
5.4	Summary of properties of argon isotopes. . . . .	122
C.1	Momenta of particles before and after scattering. . . . .	152
D.1	Explanation of input file for simulation. . . . .	164



# LIST OF FIGURES

1.1	Low-lying energy levels of $^{209}\text{Bi}$ . . . . .	4
1.2	Typical vibrational ( $^{114}\text{Cd}$ ) and rotational ( $^{238}\text{U}$ ) level schemes. . . . .	7
1.3	Energies of the first excited $2^+$ state $E(2_1^+)$ for even-even isotopes. . . . .	11
2.1	Classical picture of the projectile trajectory. . . . .	15
2.2	Adiabatic cutoff. . . . .	21
2.3	Cross sections for Coulomb excitation of $^{40}\text{S}$ as a function of beam energy for $^{40}\text{S}$ impinging on $^{197}\text{Au}$ . . . . .	23
2.4	Secondary Beam Production. . . . .	27
2.5	A typical experimental setup for intermediate energy Coulomb excitation. . . . .	29
2.6	Contributions to the photon energy resolution. . . . .	31
3.1	Setup around the secondary target. . . . .	37
3.2	Arrangement of the position sensitive NaI(Tl) detectors. . . . .	38
3.3	Illustration of pulse shape discrimination. . . . .	40
3.4	Energy-loss vs. total energy after the secondary Au target. . . . .	40
3.5	Arrangement of the position sensitive NaI(Tl) detectors. . . . .	42
3.6	Position calculated from the two PMT signals over the actual position of the collimated source. . . . .	43
3.7	Electronics Diagram. . . . .	44
3.8	Lead housing and photon collimator for the position calibration of the NaI(Tl) detectors. . . . .	46
3.9	Sample energy calibration curve. . . . .	48
3.10	Illustration of the position dependence. . . . .	48
3.11	Typical spectrum illustrating the correction for the Doppler shift. . . . .	50
3.12	Efficiency calibration. . . . .	51
3.13	Photon angular distributions for pure E2 transitions. . . . .	54
3.14	Angular Distribution of de-excitation photons. . . . .	55
3.15	The angular distribution in the laboratory system and in the center of mass. . . . .	56
3.16	The observed photon spectrum for $^{40}\text{S}$ . . . . .	58
3.17	Observed energies of $\gamma$ -rays as a function of position without correction. . . . .	62
3.18	Background subtracted photon spectra. . . . .	63
3.19	Shell model space and interactions. . . . .	66
3.20	Results. . . . .	67

4.1	Fit by Becchetti and Greenlees for the proton scattering cross sections.	74
5.1	Particle identification.	82
5.2	Setup around the secondary target.	83
5.3	Schematic 3D view of the setup around the secondary target.	85
5.4	Position sensitive silicon detector telescopes.	86
5.5	$^{228}\text{Th}$ $\alpha$ -source spectrum.	88
5.6	Energy calibration of strip detector backside.	89
5.7	Position calibration of the strip detector.	90
5.8	Signals that are registered by the individual detectors in the telescope as a function of proton energy.	91
5.9	Particle ID spectra in the telescopes.	94
5.10	Calibrated PPAC position spectrum.	95
5.11	Effect of target orientation and beam spot size on the angular resolution.	97
5.12	Electronics Diagram.	99
5.13	Kinematics for the reaction $^{36}\text{Ar}(p, p')$ at $E/A = 33.6$ MeV.	101
5.14	Simulated spectra under ideal conditions.	104
5.15	Simulation including target effects.	105
5.16	Simulation including target and detector effects.	106
5.17	Actual data.	107
5.18	Efficiency.	108
5.19	Excitation energy of $^{36}\text{Ar}$ .	109
5.20	Excitation energy spectra for $^{42}\text{Ar}$ and $^{44}\text{Ar}$ .	111
5.21	Comparison of the measured cross section to previously published data.	113
5.22	Relation between the proton laboratory energy and the center of mass scattering angle.	114
5.23	Ratio of the present data to the ones by Kozub.	116
5.24	Different fits are obtained depending on the chosen shape of the nucleus.	117
5.25	Measured cross sections and ECIS fits.	118
5.26	Deformation parameters obtained with the various fits.	119
5.27	A comparison of the extracted $M_n/M_p$ values.	121
5.28	A comparison of the extracted $M_n/M_p$ values.	121
6.1	Summary of results.	124
C.1	Schematic drawing of a collision of two particles.	152
C.2	Relation between $x, y$ , and $\theta$ .	156
F.1	Setup for particle tracking.	170
F.2	Phase-space-ellipse.	171
F.3	Comparison of old and new method.	174
F.4	Measured excitation energy.	176

# Chapter 1

## Introduction

### 1.1 The Atomic Nucleus

The atomic nucleus is a many-body system and consists of neutrons and protons which interact mainly via the strong interaction. Protons and neutrons are spin- $\frac{1}{2}$  particles and therefore obey Fermi-Dirac statistics. Nuclear sizes are on the order of 10 fm ( $= 10^{-14}$  m).

The structure of the nucleus is extremely complicated, mainly because of the small size of the nucleus and the strong (but short range) interaction between nucleons, which renders perturbation theory not applicable in most cases. Typical velocities of the nucleons in a nucleus are on the order of  $0.2 - 0.3$  c, and the corresponding de-Broglie wave length is approximately

$$\lambda = \frac{2\pi\hbar}{mv} \approx 4.5 \text{ fm} . \quad (1.1)$$

This wavelength is on the order of the size of the nucleus and hence a quantum mechanical description of the nucleus is essential.

## 1.2 Nuclear Models

The previous section hints at the complications one encounters while attempting to describe the nucleus theoretically. In general one has to solve the Schrödinger equation

$$\mathcal{H}\Psi = E\Psi . \quad (1.2)$$

The subject of nuclear structure theory is the determination of  $\mathcal{H}$  is, and the resulting wave-functions look. Even with an exact knowledge of  $\mathcal{H}$ , it is impossible to solve equation 1.2 exactly, except for the lightest nuclei. Therefore one introduces a model that focuses on certain aspects of the structure and neglects others. A broad range of nuclear models exists; depending on the physical problem some models are more convenient than others and offer more insight into the structure of a particular nucleus. Nuclear models can be divided into two major groups according to the choice of coordinates used to describe the nucleus.

Seemingly the most natural coordinates are those of the individual nucleons (i.e. the position  $\mathbf{r}$ , the spin  $\mathbf{s}$ , and isospin  $\boldsymbol{\tau}$ ), hence the nuclear states are described by

$$\Psi = \Psi(\mathbf{r}_1, \mathbf{s}_1, \boldsymbol{\tau}_1, \mathbf{r}_2, \dots) , \quad (1.3)$$

and the Hamiltonian  $\mathcal{H}$  is

$$\mathcal{H} = \sum_{i=1}^A \frac{p_i^2}{2m} + \frac{1}{2} \sum_{i,j} v(i, j) + \frac{1}{6} \sum_{i,j,k} v(i, j, k) + \dots , \quad (1.4)$$

where the sums go over all nucleons. These models are called microscopic models.

The other major group of nuclear models uses shape coordinates. These models are based on the collective degrees of freedom such as the center of mass  $\mathbf{R}$  and the quadrupole moment  $Q_{20}$  of the nucleus

$$\mathbf{R} = \frac{1}{A} \sum_{i=1}^A \mathbf{r}_i \quad Q_{20} = \sum_{i=1}^A r_i^2 Y_{20}(\Omega_i) \quad (1.5)$$

These are collective models.

### 1.2.1 Microscopic Models

The best known microscopic nuclear model is the shell model. In the shell model the nucleons in the nucleus are considered to move independently of each other in the central potential produced by all other nucleons. Thus the multitude of interactions between the nucleons is replaced by an external mean field. Originally this model was motivated by the observation of magic numbers of protons and neutrons. The numbers are 2, 8, 20, 28, 50, 82, and 126. It was observed that nuclei in which the neutron or proton number (or both) corresponds to a magic number were particularly stable. Discontinuities (peaks or dips) in other quantities e.g., energies of first excited states, neutron absorption cross sections, and binding energies were also observed. The properties of many nuclei in the vicinity of closed shells could easily be explained by the shell model. Figure 1.1 (taken from [1]) shows the excited states of  $^{209}\text{Bi}$ . In the simplest shell model this nucleus consists of an inert  $^{208}\text{Pb}$  core (a doubly magic nucleus), which creates a mean field, plus one proton in the  $h_{9/2}$  shell. Hence the spin and parity of the ground state is  $J^\pi = \frac{9}{2}^-$ . A number of excited levels can simply be explained by putting the extra proton into higher and higher orbits. The spins, parities, and even the excitation energies of these states can easily be predicted.

However, one can also see in figure 1.1 that there is a group of levels around 2.6 MeV that can not be explained in this simple way. These states correspond to an excitation in the  $^{208}\text{Pb}$  core coupled to the extra  $h_{9/2}$  proton. The first excited state in  $^{208}\text{Pb}$  is a  $J^\pi = 3^-$  state with an excitation energy of 2.6 MeV. Hence these states (in  $^{209}\text{Bi}$ ) have an energy of about 2.6 MeV, positive parity, and spins ranging from  $\frac{3}{2}$  to  $\frac{15}{2}$ . In order to explain these states within the shell model, the whole lead nucleus would have to be included into the shell model calculation, and the resulting wavefunction would correspond to a superposition of many single particle states. However, this coherent motion of many nucleons can be described more easily

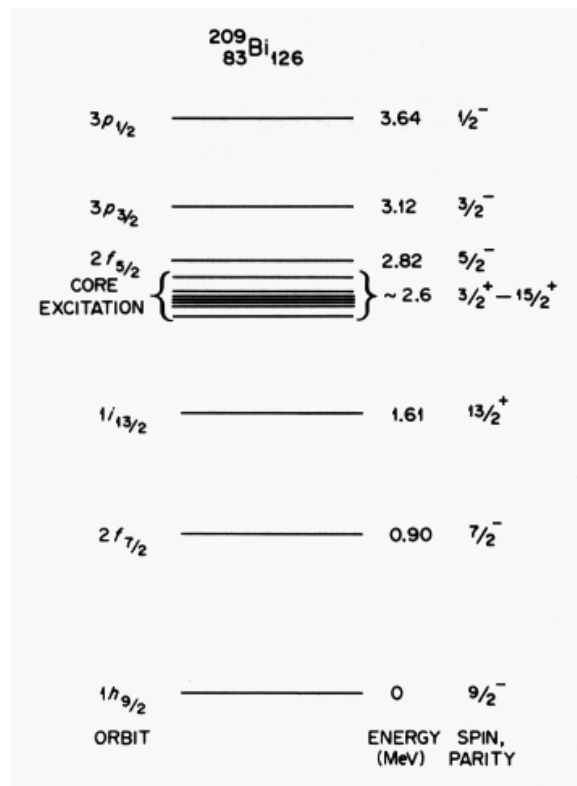


Figure 1.1: Low-lying energy levels of  $^{209}\text{Bi}$ . The group of states near 2.6 MeV are excitations of the  $^{208}\text{Pb}$  core.

in collective models, in which this  $3^-$  state is considered to be an octupole vibration of the nuclear surface.

The mean field is only the average smooth part of the interaction between the nucleons and does not include all interactions. The remaining part is called the residual interaction. This interaction gives rise to collective behavior within the shell model.

### 1.2.2 Collective Models

It was pointed out in the previous section that many features of nuclei in the vicinity of magic numbers can most easily be described by the shell model. Properties of nuclei in the mid-shell regions, however, can not be explained in this simple way. The behavior of these nuclei is best described in a collective model. The best examples of collective motion are the giant resonances, which occur in all nuclei. These excitations can be considered to be an oscillation of *all* neutrons and *all* protons. The emphasis is on *all*, since this is the most extreme contrast to the shell model, where, as in the  $^{209}\text{Bi}$  example, only *one* nucleon is responsible for the excitation.

Besides the giant resonances, nuclei in the mid-shell regions show low-lying states (much lower in energy than corresponding single particle states), with large matrix elements that couple these states. A nucleus that exhibits these features is said to be collective since the large matrix element can only arise if more than one nucleon participates in a coherent *collective* motion. The energy spacing between levels is by itself only an indication of collective motion: One can for instance guess that neighboring even-even nuclei with the same energy for the first excited state are similarly collective, but this might be misleading. The best measure of the collectivity in a transitions between two states is the reduced transition probability  $B(\pi\lambda)$ , where  $\pi$  and  $\lambda$  denote the parity and multipolarity of the transition operator. The  $B(\pi\lambda)$

is proportional to the square of the absolute value of the transition matrix element between states  $|i\rangle$  and  $|f\rangle$

$$B(\pi\lambda) \propto |\langle f | \mathcal{M}(\pi\lambda) | i \rangle|^2, \quad (1.6)$$

and can e.g. be deduced from the lifetimes of nuclear states or from measured excitation cross sections. Equation 1.6 shows why the reduced transition probability is such a good indicator of collective motion; it depends directly on the wave functions of the involved states.

Two major mechanisms are responsible for the low-lying collective states: One is the rotational motion of a statically deformed nucleus and the other is the vibration of the nuclear surface (without change in matter density within the nucleus). Two examples of collective nuclei are shown in figure 1.2, where the excited states of the even-even nuclei  $^{238}\text{U}$  and  $^{114}\text{Cd}$  are depicted. The level energies for  $^{238}\text{U}$  follow a very distinctive  $J(J+1)$  pattern (spacing increases linearly with  $J$ ) and the spins are spaced with  $\Delta J = 2$ . This spectrum is typical of a rigidly-deformed rotating body. The level scheme of  $^{114}\text{Cd}$  shows a completely different structure. One observes a  $2^+$  state at 0.56 MeV and at about twice this energy a set of states with quantum numbers  $0^+$ ,  $2^+$ , and  $4^+$  are seen. This is typical of a nuclear surface vibration. The first level corresponds to a one phonon state carrying angular momentum 2 and positive parity. Two phonons (corresponding to the first harmonic vibration) can then couple to  $0^+$ ,  $2^+$ , and  $4^+$ ; other values of  $J$  are not allowed because the phonons obey Bose-Einstein statistics.

In the rotational case mainly electric quadrupole transitions ( $E2$ ) occur between the states because of angular momentum and parity selection rules. One can show that the  $E2$  transition operator is identical to the quadrupole moment operator and therefore the  $B(E2)$  value is related to the *intrinsic* quadrupole moment  $Q_0$  of the

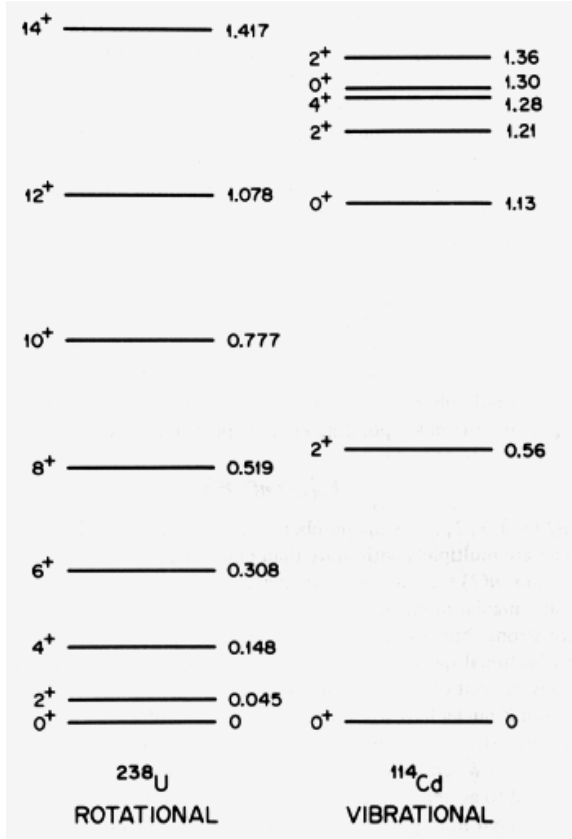


Figure 1.2: Typical vibrational ( $^{114}\text{Cd}$ ) and rotational ( $^{238}\text{U}$ ) level schemes. Level spacings that increase linearly with angular momentum indicate a statically deformed shape, whereas equal spacings indicate a vibrational nature of the excitation.

nucleus

$$B(E2) \propto Q_0^2 . \quad (1.7)$$

The factor of proportionality depends on the angular momentum  $J$  of the initial state and also on the quantum number  $K$  that characterizes the orientation of the deformed shape with respect to the quantization axis [2]. Assuming a symmetrically deformed shape

$$R(\theta) = R_0 (1 + \beta_2 Y_{20}(\theta, \phi)) , \quad (1.8)$$

where  $\beta_2$  is called the quadrupole deformation parameter. Using the definition of the quadrupole moment yields the following relation between the  $B(E2)$  value and the deformation parameter (to first order):

$$\beta_2 = \frac{4\pi}{3} \sqrt{B(E2; 0^+ \rightarrow 2^+)} \frac{1}{ZeR_0^2} , \quad (1.9)$$

where  $R_0$  is given by  $1.2 \text{ fm } A^{1/3}$ .

The deformation parameter given in equation 1.9 is a convenient measure of the collectivity in a nucleus, which allows the comparison of different nuclei throughout the periodic table, even if the nucleus is *not* statically deformed. For instance the ground state and the first excited state in the proton magic (non-collective) nucleus  $^{122}\text{Sn}$  is connected by a  $B(E2; 0^+ \rightarrow 2^+)$  of  $1930 e^2\text{fm}^4$ , which is much larger than collective values for nuclei in the  $A \approx 40$  region, which are typically  $400 e^2\text{fm}^4$ . The deformation parameter, on the other hand, for  $^{122}\text{Sn}$  is 0.1, which is comparable to deformation parameters of non-collective nuclei throughout the periodic table (e.g. the doubly magic  $^{40}\text{Ca}$  has a  $\beta_2$  of 0.122).

Typical deformation parameters range from 0.1 for non-collective nuclei to 0.5–0.6 for collective nuclei.

## 1.3 Experimental Probes of Nuclear Structure

The nucleus can be studied passively, e.g. by observing the radiation from radioactive decay, or by studying the nucleus's electronic environment through the observation of the hyperfine structure in atomic spectra.

The most fruitful approach, however, is to apply an external field and to study the reaction of the nucleus to this field. This is done by directing a beam of particles onto a target and observing the reaction products (other particles,  $\gamma$  rays, electrons, etc.).

Depending on the target-projectile combination and the relative velocity, different fields can be applied and the nucleus can be probed in various ways. The best probes are the ones that interact the least with the nucleus to be studied, so that it remains almost undisturbed. In addition, if the probe is weak, perturbative methods can be applied to extract the structure information. A possible drawback of a weakly interacting probe is a low reaction cross section.

### 1.3.1 Coulomb Excitation as an Electromagnetic Probe

The best understood probe available is the electromagnetic interaction. For instance, electron scattering is used to map the charge distribution deep inside the nucleus, where no hadronic probe can give reliable results. Another method, which has long been applied to stable nuclei, is Coulomb excitation, where a nucleus is excited in the Coulomb field of another nucleus. The energies of the subsequently emitted photons (conversion electrons or other particles) reveal the spacings between the levels in the nucleus and the cross sections can be related to nuclear matrix elements connecting these levels.

### 1.3.2 Proton Scattering as an Hadronic Probe

Coulomb excitation only probes the charge distribution of the nucleus since only the protons in the nucleus interact electromagnetically (neglecting the magnetic moments of the neutrons). Because of the Pauli principle, the like-nucleon interaction is about 3 times weaker than the unlike-nucleon interaction in a nucleus. Therefore, proton scattering ( $p, p'$ ) in the energy range of  $E/A \approx 10 - 50$  MeV, which corresponds to typical kinetic energies of nucleons in a nucleus, is mostly sensitive to the neutrons [3]. Information on both the neutron and the proton motion can be obtained by a comparison of the hadronic and the electromagnetic probe. The drawback of the hadronic probe is that the interaction is strong, and the structure information obtained is somewhat model dependent in contrast to the Coulomb excitation results, which are largely model independent.

## 1.4 Heavy sd-Shell Nuclei

One of the frontiers in nuclear structure research is the investigation of shell evolution far away from stability. The nuclei in the region of  $N=20-28$  and  $Z=14-20$  (heavy sd-shell nuclei) have attracted particular interest for several reasons. These nuclei are located in between two major neutron shells ( $N=20$  and  $N=28$ ), which are very pronounced for the stable isotopes. This is shown in figure 1.3, which includes the results of the present work and shows the energies of the first excited  $2^+$  states of the even-even nuclei for  $N$  up to 38 and for  $Z$  up to 28 are shown. The possibility of obtaining high-intensity secondary beams of these nuclei makes them particularly attractive experimentally. In addition, the nuclei in this region are large enough to show collective properties but are also sufficiently light that the neutron drip line can be approached. From the theoretical perspective full (no truncation) or almost full

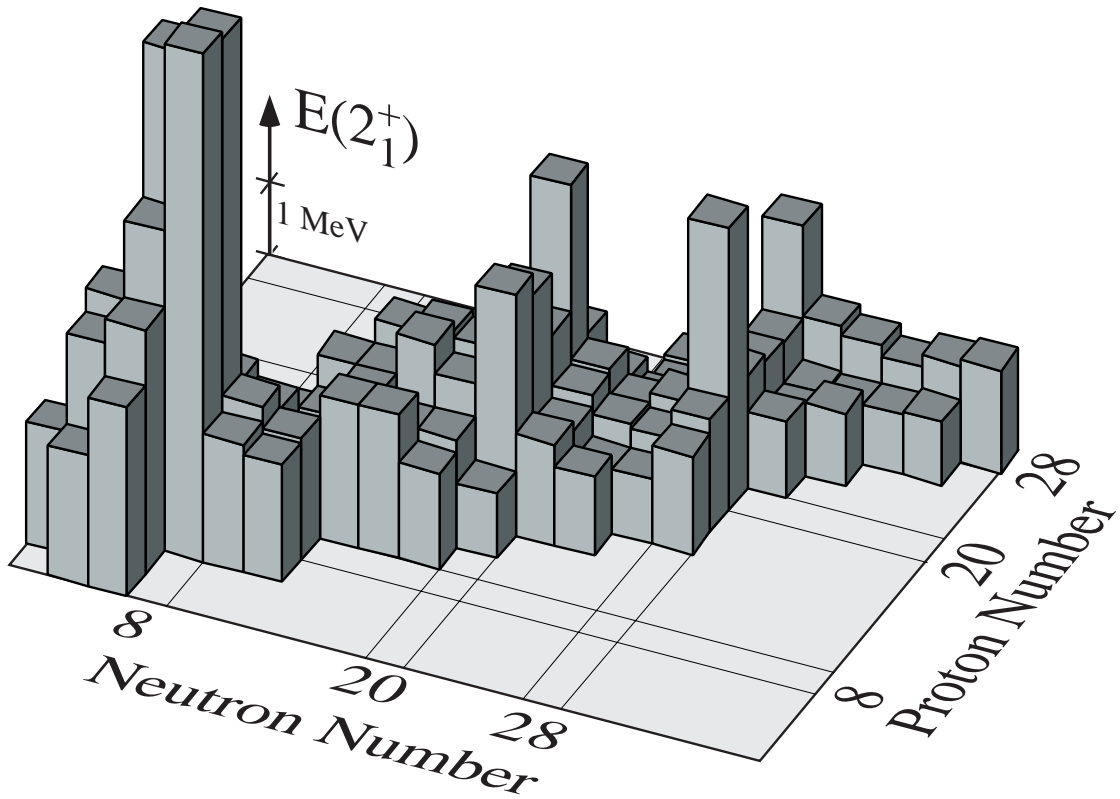


Figure 1.3: Energies of the first excited  $2^+$  state  $E(2_1^+)$  for even-even isotopes. Results of this thesis work are included. The magic numbers are indicated and one observes that the energies of magic nuclei are much larger than neighboring nuclei. Changes in the nuclear structure are expected, however, as the driplines are approached.

shell model calculations can be performed.

The unstable nuclei  $^{38,40,42}\text{S}$  and  $^{44,46}\text{Ar}$  have been studied via Coulomb excitation. An introduction to Coulomb excitation at intermediate energies is given in chapter 2, and the experimental details and results are presented in chapter 3. Chapter 4 gives an introduction to proton scattering, while the results of elastic and inelastic proton scattering on  $^{36,42,44}\text{Ar}$  are presented in chapter 5. Chapter 6 summarizes and compares the results obtained.

# Chapter 2

## Intermediate-Energy Coulomb Excitation

Following is a general description of intermediate-energy Coulomb excitation. The validity of the assumptions made is discussed, and an overview over the parameters pertaining to Coulomb excitation at intermediate energies is given.

### 2.1 General Description

Coulomb excitation is the excitation of the target nucleus in the electromagnetic field of the projectile, or vice versa.<sup>1</sup> For pure Coulomb excitation, where the nuclei stay outside the range of the strong force, the excitation cross section can be expressed in terms of the same multipole matrix elements that characterize the  $\gamma$  decay of excited nuclear states. Therefore, a determination of the Coulomb excitation cross section leads directly to the determination of basic nuclear structure information. The Coulomb excitation process, as outlined below, is well understood, and results are largely model independent.

---

<sup>1</sup>In the following target excitations will be considered. Projectile excitations can be considered by exchanging target and projectile quantities (i.e.  $Z_t \leftrightarrow Z_p, \dots$ ).

Keeping the bombarding energy below the Coulomb barrier ensures that no nuclear excitation can take place. This beam energy is typically of the order of a few MeV/nucleon. For example for  $^{40}\text{S}$  impinging on a  $^{197}\text{Au}$  target, a beam energy of  $E/A \leq 4$  MeV is sufficiently small to exclude nuclear excitations. Unfortunately, such beam energies are impracticable for radioactive beams produced by projectile fragmentation, the mechanism employed at the NSCL to produce and study nuclei far from stability. The beams have energies of several tens or even hundreds of MeV/nucleon, and if the beams were slowed down, they would lose quality and flux at the same time. Furthermore, the long range of the ions at high energies allows the use of thick secondary targets, which helps to compensate for the potentially low beam intensity.

In the intermediate energy range, defined here as  $E/A = 10\text{--}100\text{ MeV}$ , the easiest way to ensure the dominance of Coulomb excitation, as compared to nuclear excitation, is to limit the scattering angle of the projectile to small angles. This means that only events are considered in which the impact parameter is larger than a certain minimum distance defined by the maximum scattering angle. Also, events where violent reactions occur (corresponding to more central collisions) are rejected by requiring that the incoming beam particle be observed after the target.

The next sections outline how the measured cross sections are related to nuclear matrix elements. Basic parameters that are involved in Coulomb excitation are also discussed. The main references are [4, 5]. A description of the experimental setup follows in chapter 3.

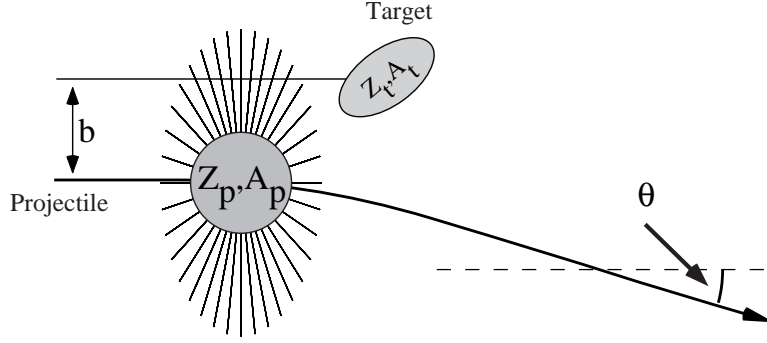


Figure 2.1: Classical picture of the projectile trajectory. The (in this picture statically deformed) target nucleus can be excited due to the tidal forces exerted by the electromagnetic field of the projectile.

## 2.2 Excitation Cross Section

Assuming that the projectile follows a Rutherford trajectory, the Coulomb excitation (CE) cross section is given by (more details are given in appendix A)

$$\left(\frac{d\sigma}{d\Omega}\right)_{\text{CE}} = \left(\frac{d\sigma}{d\Omega}\right)_{\text{Ruth}} P_{i\rightarrow f}, \quad (2.1)$$

where  $P_{i\rightarrow f}$  is the probability of excitation from the initial state  $|i\rangle$  to the final state  $|f\rangle$ . Treating the electromagnetic interaction potential  $V(\mathbf{r}(t))$  as a time-dependent perturbation,  $P_{i\rightarrow f}$  is obtained as

$$P_{i\rightarrow f} = |a_{i\rightarrow f}|^2 \quad \text{with} \quad a_{i\rightarrow f} = \frac{1}{i\hbar} \int_{-\infty}^{\infty} e^{i\omega_f t} \langle f|V(\mathbf{r}(t))|i\rangle dt. \quad (2.2)$$

The amplitudes  $a_{i\rightarrow f}$  can be expressed as a product of two factors

$$a_{i\rightarrow f} = i \sum_{\lambda} \chi_{i\rightarrow f}^{(\lambda)} f_{\lambda}(\xi), \quad (2.3)$$

where the excitation strength  $\chi$  is a measure of the strength of the interaction and the function  $f(\xi)$  measures the degree of adiabaticity of the process in terms of the adiabaticity parameter  $\xi$ . Section 2.3 gives a detailed discussion of these and other parameters involved.

### 2.2.1 Approximations

Winther and Alder [5] obtained a closed formula for the Coulomb excitation cross section by assuming straight line trajectories and a static target.

As shown in appendix A.1.2, the momentum transfer to the target perpendicular to the direction of motion is given by

$$\gamma m_t v_t = \Delta p_{\perp}^{(t)} = \frac{2Z_t Z_p e^2}{b v_p}, \quad (2.4)$$

where  $Z_{p(t)}$  is the proton number of the projectile(target),  $b$  is the impact parameter,  $v_p$  is the (incident) projectile velocity, and  $v_t$  is the target recoil velocity after the collision.  $\gamma$  is the relativistic factor and  $m_t$  is the mass of the target nucleus. For collisions considered in this work ( $Z_t \approx 80$ ,  $Z_p \approx 20$ ,  $m_t \approx 200 u$   $v_p \approx 0.3 c$ , and  $b = 15$  fm) recoil velocities of  $v_t < 0.2\% c$  are obtained. This by itself might seem quite high, but typical collision times are on the order of  $50\text{fm}/c \approx 1.5 \cdot 10^{-22}\text{s}$  and the corresponding flight path of the recoiling target nucleus of  $0.1$  fm is much less than the nuclear radius of about  $7$  fm.<sup>2</sup> Therefore, the assumption that the target nucleus remains at rest during the collision process is justified, which allows the use of a coordinate system with the target nucleus located (fixed) at the origin. A correction for the small target recoil can be introduced [5].

The deflection angle of the projectile in the laboratory is given by

$$\theta_{lab} = \frac{2Z_t Z_p e^2}{\gamma m_p v_p^2} b^{-1}. \quad (2.5)$$

Inserting the values given above, deflection angles of only a few degrees are obtained. Hence the assumption of a straight-line trajectory is justified.

---

<sup>2</sup>Nuclear radii can be estimated as  $R = 1.25 \text{ fm } A^{\frac{1}{3}}$  with  $A$  being the mass number of the nucleus.

## 2.2.2 The Excitation Cross Section

The excitation cross section can be obtained by integrating the excitation probability from a minimum impact parameter  $b_{min}$ , determined by the experimental conditions (e.g. a maximum scattering angle), to infinity. An approximate result is obtained by introducing the adiabatic cutoff and integrating the absolute square of the excitation strength (equation 2.3)  $|\chi|^2$  from  $b_{min}$  to  $b_{max}$ , instead of integrating  $P_{if} = |\chi f(\xi)|^2$  from  $b_{min}$  to infinity:<sup>3</sup>

$$\sigma = 2\pi \int_{b_{min}}^{\infty} P_{if} b db \approx 2\pi \int_{b_{min}}^{b_{max}} |\chi|^2 b db . \quad (2.6)$$

$b_{max}$  can be estimated as

$$b_{max} = \frac{\gamma v}{\omega_{fi}} = \frac{\gamma \hbar v}{\Delta E} \approx \frac{\gamma 197}{\Delta E} \text{MeV fm} , \quad (2.7)$$

where  $\Delta E$  is the energy of the transition and  $\omega_{fi} = \frac{\Delta E}{\hbar}$ . This leads to an approximate expression for the excitation cross section of parity  $\pi$  and multipolarity  $\lambda$

$$\sigma_{\pi\lambda} \approx \left( \frac{Z_t e^2}{\hbar c} \right)^2 \frac{B(\pi\lambda, 0 \rightarrow \lambda)}{e^2} \pi b_{min}^{2(1-\lambda)} \cdot \begin{cases} (\lambda - 1)^{-1} & \text{for } \lambda \geq 2 \\ 2 \ln \left( \frac{b_{max}}{b_{min}} \right) & \text{for } \lambda = 1 , \end{cases} \quad (2.8)$$

where  $b_{max} \gg b_{min}$  was assumed.  $B(\pi\lambda, 0 \rightarrow \lambda)$  is the reduced transition probability, defined as

$$\begin{aligned} B(\pi\lambda, I_i \rightarrow I_f) &= \sum_{\mu M_f} |\langle J_f M_f | \mathcal{M}(\pi\lambda\mu) | J_i M_i \rangle|^2 \\ &= \frac{1}{2J_i + 1} |\langle J_f || \mathcal{M}(\pi\lambda) || J_i \rangle|^2 , \end{aligned}$$

where  $\mathcal{M}(\pi\lambda\mu)$  is the multipole operator for electromagnetic transitions. The exact expression for the excitation cross section, summed over parities and multiplicities, derived in [5], is

$$\sigma_{i \rightarrow f} = \left( \frac{Z_p e^2}{\hbar c} \right)^2 \sum_{\pi\lambda\mu} k^{2(\lambda-1)} \frac{B_t(\pi\lambda, I_i \rightarrow I_f)}{e^2} \left| G_{\pi\lambda\mu} \left( \frac{c}{v} \right) \right|^2 g_{\mu}(\xi(b_{min})) . \quad (2.9)$$

---

<sup>3</sup>i.e. the function  $f$  is approximated by a step function.

Here  $k = \frac{E_\gamma}{\hbar c}$ ,  $Z_p$  is the proton number of the projectile,  $E_\gamma = \Delta E$  is the excitation energy, and  $B_t(\pi\lambda, I_i \rightarrow I_f)$  is the reduced transition probability of the target nucleus. The Winther and Alder functions  $G$  and  $g$  are explained in appendix A.

It follows that the excitation cross section is directly proportional to the reduced transition probability

$$\sigma_{i \rightarrow f} \propto B_t(\pi\lambda, I_i \rightarrow I_f). \quad (2.10)$$

Thus, the  $B(\pi\lambda)$  value can be extracted from a cross section measurement.

### 2.2.3 Electric Versus Magnetic Excitations

Electric and magnetic fields of a moving charge are related through

$$|\mathbf{B}| = \frac{v}{c} |\mathbf{E}| \quad (2.11)$$

Therefore for intermediate- or high-energy Coulomb excitation, of interest here, ( $\frac{v}{c} \approx 0.3$ – $0.5$ ) magnetic excitations are possible and must be considered if not forbidden otherwise, e.g. by selection rules. In contrast, in low-energy Coulomb excitation ( $\frac{v}{c} \approx 0.1$ ) only electric excitations are of importance.

### 2.2.4 Equivalent Photon Method

In principle, Coulomb excitation can be viewed as the absorption of virtual photons by the target nucleus. These virtual photons are produced by the moving projectile and the equivalent photon number (the number of *real* photons that would have an equivalent net effect for one particular transition) is related to the Fourier transform of the time-dependent electromagnetic field produced by the projectile.

One can express the Coulomb excitation cross section as

$$\sigma_{i \rightarrow f} = \sum_{\pi\lambda} \int N_{\pi\lambda}(\omega) \sigma_\gamma^{(\pi\lambda)}(\omega) \frac{d\omega}{\omega}, \quad (2.12)$$

where the spectrum of photons of multipolarity  $\lambda$  is determined by the equivalent photon number  $N_{\pi\lambda}(\omega)$  and the photoabsorption cross section is given by  $\sigma_{\gamma}^{(\pi\lambda)}(\omega)$ . The photoabsorption cross section for *real* photons is given by [6]

$$\sigma_{\gamma}^{(\pi\lambda)}(\omega) = \frac{(2\pi)^3(\lambda+1)}{\lambda((2\lambda-1)!!)^2} \rho(\epsilon) k^{2\lambda+1} B(\pi\lambda), \quad (2.13)$$

where  $\rho(\epsilon)$  is the density of final states and is usually given as a  $\delta$ -function for discrete nuclear states

$$\rho(\epsilon) = \delta(E_i + \epsilon - E_f) = \delta(\epsilon - E_{\gamma}). \quad (2.14)$$

Inserting equation 2.13 into 2.12 and comparing the result to equation 2.9 gives the number of equivalent photons of multipolarity  $\pi\lambda$  [6]

$$N_{\pi\lambda}(\omega) = Z_p^2 \frac{e^2}{\hbar c} \frac{l((2l+1)!!)^2}{(2\pi)^3(\lambda+1)} \sum_{\mu} \left| G_{\pi\lambda\mu} \left( \frac{c}{v} \right) \right|^2 g_{\mu}(\xi). \quad (2.15)$$

Since the number of equivalent photons can be determined the photoabsorption cross section can be related to the Coulomb excitation cross section and vice versa. This is used e.g. to derive astrophysically important photodissociation cross sections from Coulomb excitation results [7].

## 2.3 Basic Parameters

### 2.3.1 Impact Parameter and Distance of Closest Approach

As shown in appendix A the equation

$$\theta_{lab} = \frac{2Z_t Z_p e^2}{\gamma m_p v_p^2} b^{-1} \quad (2.16)$$

relates the impact parameter  $b$  to the deflection angle  $\theta_{lab}$  in the laboratory system.  $Z_{t,p}$  are the proton numbers of the target and projectile,  $m_p$  is the mass of the projectile and  $v_p$  is its incident velocity. It was shown in the previous section that straight-line trajectories are a good approximation, and therefore the distance

of closest approach is nearly equal to the impact parameter. The latter has to be larger than the sum of the two nuclear radii plus 2–4 fm [8] to ensure the dominance of Coulomb excitation:

$$D \approx b \leq R_t + R_p + \Delta_s \quad \text{with} \quad \Delta_s \sim 2\text{--}4 \text{ fm} . \quad (2.17)$$

The nuclear radii can be estimated as  $R = 1.25 \text{ fm } A^{\frac{1}{3}}$ , where  $A$  is the mass number of the nucleus [9]. A minimum distance can be ensured experimentally by limiting the scattering angle of the projectile to be below a certain maximum scattering angle

$$\theta \leq \theta_{max} \implies b \geq b_{min}(\theta_{max}) . \quad (2.18)$$

### 2.3.2 Sommerfeld Parameter

The Sommerfeld parameter  $\eta$  compares the physical dimensions of the classical orbit, in this case the impact parameter  $b$ , with the de Broglie wavelength  $\lambda$  of the relative motion of the two particles

$$\eta = \frac{b}{\lambda} = \frac{b \gamma m_p v_p}{\hbar} \quad \text{with} \quad \gamma = \frac{1}{\sqrt{1 - \beta^2}} \quad \text{and} \quad \beta = \frac{v_p}{c} . \quad (2.19)$$

$m_p$  is the projectile mass,  $v_p$  the projectile velocity in the laboratory system. Typical values are  $\eta \approx 1000$ , meaning that a wave packet containing several waves is still small compared to the dimensions of the trajectory. Such a wave packet will move along the classical trajectory, justifying the use of the semi-classical approach in the calculation of the Coulomb excitation cross section.

### 2.3.3 Adiabaticity Parameter

If the time-dependent perturbation potential changes slowly the nucleus follows the perturbation adiabatically and no excitation is possible. This is the adiabatic cutoff, which is schematically illustrated in figure 2.2. This cutoff is parameterized in terms

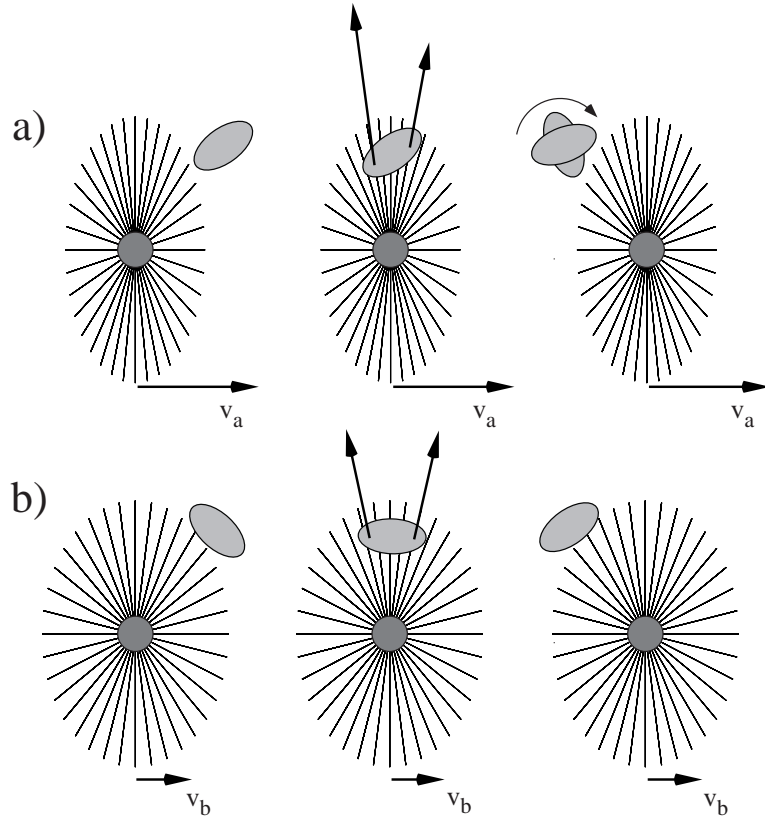


Figure 2.2: Adiabatic limit: In panel a) the collision time is short enough for the adiabaticity parameter  $\xi$  to be small and excitations are possible. Indicated by the arrows are the force vectors acting on the nucleus. Because of the orientation of the nucleus a torque is generated which gives rise to excitations. However, in panel b) the nucleus *is able* to follow the motion of the projectile, no torque is generated and no excitations can occur, even though the field strengths ( $\sim \chi$ ) are similar in both cases.

of the adiabaticity parameter  $\xi$ , which is defined as the ratio of the collision time  $\tau_{\text{coll}}$  to the time of internal motion in the nucleus  $\tau_{\text{nucl}}$

$$\xi = \frac{\tau_{\text{coll}}}{\tau_{\text{nucl}}} . \quad (2.20)$$

If  $\xi$  is large, because the projectile velocity is low or the impact parameter is large, then no excitation is possible.

In appendix A it is shown that the electric field component in the x-direction  $E_x$  (perpendicular to the direction of motion) produced by the projectile at the target position is given by

$$E_x = \frac{\gamma E_0}{(1 + (t/\tau)^2)^{\frac{3}{2}}} \quad \text{with} \quad \tau = \frac{b}{\gamma v_p} \quad \text{and} \quad E_0 = \frac{e Z_p}{b^2} . \quad (2.21)$$

Therefore  $\tau$  defines the collision time

$$\tau_{\text{coll}} = \frac{b}{\gamma v_p} \quad (2.22)$$

and the time scale for the nuclear motion is given as  $\tau_{\text{nucl}} = \omega_{\text{fi}}^{-1} = \frac{\hbar}{\Delta E}$ . Hence

$$\xi = \omega_{\text{fi}} \frac{b}{\gamma v_p} = \frac{\Delta E b}{\hbar \gamma v_p} . \quad (2.23)$$

For  $v \sim 0.3c$  and  $b \sim 15$  fm it follows that

$$\xi \sim \frac{\Delta E}{5 \text{ MeV}} . \quad (2.24)$$

$\xi$  should be smaller than unity for excitations to occur, and thus low-lying collective states with energies of several MeV can be excited. Going to even higher beam energies, e.g.  $v \sim 0.5c$ , states in the giant resonance region with excitation energies of 10 – 20 MeV can readily be excited. Figure 2.3 shows the Coulomb excitation cross section as a function of beam energy for low-lying collective states and giant resonance states for dipole and quadrupole excitations for  $^{40}\text{S}$  impinging on  $^{197}\text{Au}$ . In both cases the giant resonance states are assumed to exhaust the electromagnetic

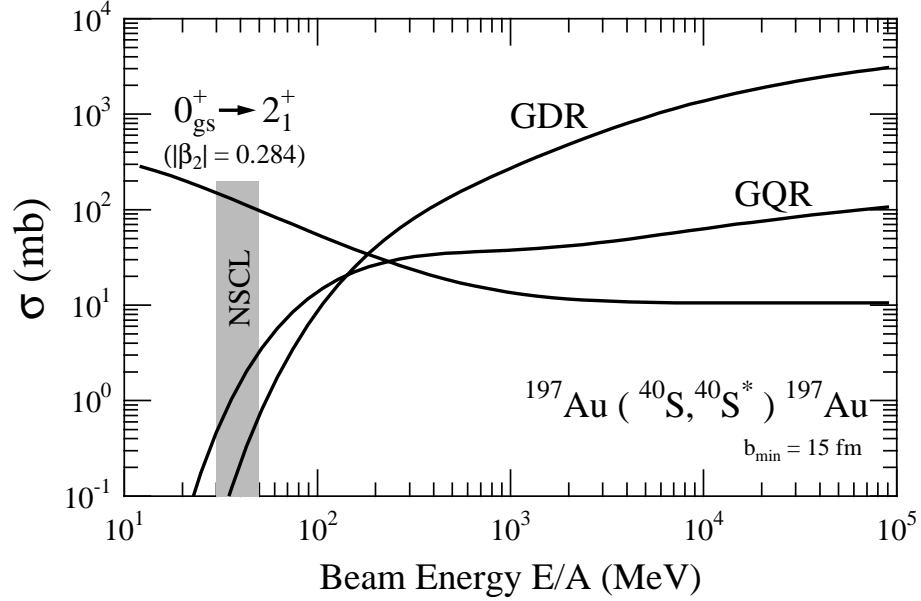


Figure 2.3: Cross sections for Coulomb excitation of  $^{40}\text{S}$  as a function of beam energy for  $^{40}\text{S}$  impinging on  $^{197}\text{Au}$ , with constant minimum impact parameter cutoff  $b_{min} = 15$  fm. The energy region accessible with radioactive beams at the NSCL is indicated. The rising giant resonance cross section can be traced to the reduction of the adiabaticity parameter. The drop of the cross section for the low-lying collective state is caused by a diminishing excitation strength parameter, due to a shorter collision time.

sum rules [5]. It follows that in the region between 30 and 50 MeV, which is the energy region where the highest secondary beam yield can currently be achieved at MSU, only low-lying collective states can be excited. At higher energies, however, giant resonance states will also be populated [10].

For Coulomb excitation below the Coulomb barrier, where  $E/A \sim$  few MeV, the adiabatic cutoff essentially limits the possible excitation energies to be below 1–2 MeV. The excitation to higher lying collective states is nevertheless possible, since the strength parameter (see next section) can become large. In this case first-order perturbation theory is no longer valid and multiple excitations can occur.

### 2.3.4 Excitation Strength

As mentioned in section 2.2 the excitation amplitude can be expressed as a product of two factors:

$$a_{i \rightarrow f} = i \sum_{\lambda} \chi_{i \rightarrow f}^{(\lambda)} f_{\lambda}(\xi). \quad (2.25)$$

$f(\xi)$  is a measure of the adiabaticity as a function of the adiabaticity parameter, as stated in the previous section, and  $\chi$  measures the strength of the excitation from state  $|i\rangle$  to state  $|f\rangle$ . Classically,  $\chi_{i \rightarrow f}^{(\lambda)}$  is a measure of the strength of the interaction of the monopole field of the projectile with the  $\lambda$ -pole component of the field created by the target nucleus. The monopole-monopole interaction gives rise to the Rutherford trajectory (and is treated classically). The next higher order is monopole-dipole interaction, which is not important for low energy excitations, because nuclei can not have a static electric dipole moment.<sup>4</sup> Dynamic dipole-moments are nevertheless possible and they give rise to the giant dipole resonance, which can be found in all nuclei. Most nuclei, though, have a static (intrinsic) quadrupole moment, making the monopole-quadrupole interaction the most important for low-lying (collective) states. Classically the field of the projectile exerts a tidal force (for  $\lambda = 2$ ) on the two lobes of the target nucleus and the resulting torque can excite the nucleus (see figure 2.2).  $\chi$  depends on the internal structure of the target nucleus, e.g. its quadrupole moment for  $\lambda = 2$ , the strength of the monopole field of the projectile nucleus,<sup>5</sup> and the duration of the interaction, the collision time  $\tau_{\text{coll}}$ . Hence  $\chi$  can be estimated as

$$\chi^{(\pi\lambda)}(b) \approx \frac{V_{\lambda}(b)\tau_{\text{coll}}}{\hbar} \approx \frac{Z_t e \langle f | \mathcal{M}(\pi\lambda\mu) | i \rangle}{\hbar\gamma v b^{\lambda}}, \quad (2.26)$$

where  $V_{\lambda}(b)$  is the monopole- $\lambda$ -pole interaction potential, which has a  $b^{-(\lambda+1)}$  dependence.

---

<sup>4</sup>Parity and time-reversal invariance forbid the existence of static electric dipole moments.

<sup>5</sup>The quadrupole moment of the target nucleus interacts with the derivative of the external electric field. The interaction energy is given by  $-\frac{1}{6}Q_{ij}\frac{\partial E_i}{\partial x_j}$  [11].

The matrix element  $\langle f | \mathcal{M}(\pi\lambda\mu) | i \rangle$  can be estimated as the square root of the  $B(E2\uparrow)$ . A collective transition in the  $A=40$  region, which is of interest in this work, might have a  $B(E2) = 300 e^2 \text{fm}^4$  [12]; assuming furthermore  $v = 0.3 c$  and  $b = 15 \text{ fm}$  it follows that, even for collective states and heavy projectiles, values of only about  $\chi \approx 0.15$  are obtained and perturbation theory is justified.  $\chi$  can also be thought of as the number of  $(\pi\lambda)$  quanta that are exchanged in one collision. Using equation A.10 one can also calculate the excitation probability at the minimum impact parameter, which has the highest probability. Typical values are on the order of 1%.

Hence, Coulomb excitation at intermediate or relativistic energies is mostly a one step process.

## 2.4 Experimental Considerations

In the following sections some experimental matters that need to be considered for a successful experiment will be discussed. Attention will be focused on projectile excitation of radioactive nuclear beams and the detection of  $\gamma$  rays as a method of measuring Coulomb excitation cross sections.

### 2.4.1 Projectile Excitation

In traditional Coulomb excitation the target nucleus is studied by bombarding it with heavy ion beams with energies below the Coulomb barrier. Since targets can only be produced from stable isotopes — with few exceptions where long-lived isotopes have been formed into targets — the powerful method of Coulomb excitation has been limited to stable isotopes and the vast majority of nuclei (only about 10% of all known nuclei are stable) have been inaccessible by it.

This changed with the construction of radioactive nuclear ion beam facilities, as described in the next section. Using projectile excitation (i.e. the interest lies

in exciting the projectile nucleus instead of the target nucleus; see figure 2.5) one can study all nuclei that can be made into a beam with sufficient intensity. This has opened up the possibility to study many previously inaccessible nuclei far from stability. It is also possible to use a cocktail beam consisting of many different isotopes if an event-by-event particle identification is possible.

## 2.4.2 Radioactive Nuclear Beam Production

There are two main methods for the production of radioactive nuclear beams. One method is known as Isotope Separation On-Line (ISOL). Facilities that are working or are coming on line in the near future are HRIBF at Oak Ridge, SPIRAL in France, ISOLDE at CERN, and the REX-ISOLDE experiment, which will accelerate radioactive nuclei produced by ISOLDE. In the ISOL approach a high-energy, light-ion beam is stopped in a production target, where fragmentation of the target occurs. The resulting fragments diffuse out of the target, are transported to an ion source, and are then accelerated to the desired energy.

An alternative method employed at MSU, RIKEN in Japan, GANIL in France, and GSI in Germany is projectile fragmentation. More details on these and other methods of radioactive beam production are given in [13].

### Projectile Fragmentation

The principle of projectile fragmentation is illustrated in figure 2.4. The primary beam impinges on the target, and even though most of the beam particles pass through the target without reacting, a considerable number of primary beam particles collide with the target nuclei and fragmentation occurs. A variety of fragments are produced and a system of magnetic dipoles and quadrupoles together with an energy degrader (a piece of material in which the projectile loses energy) is used to reduce the number

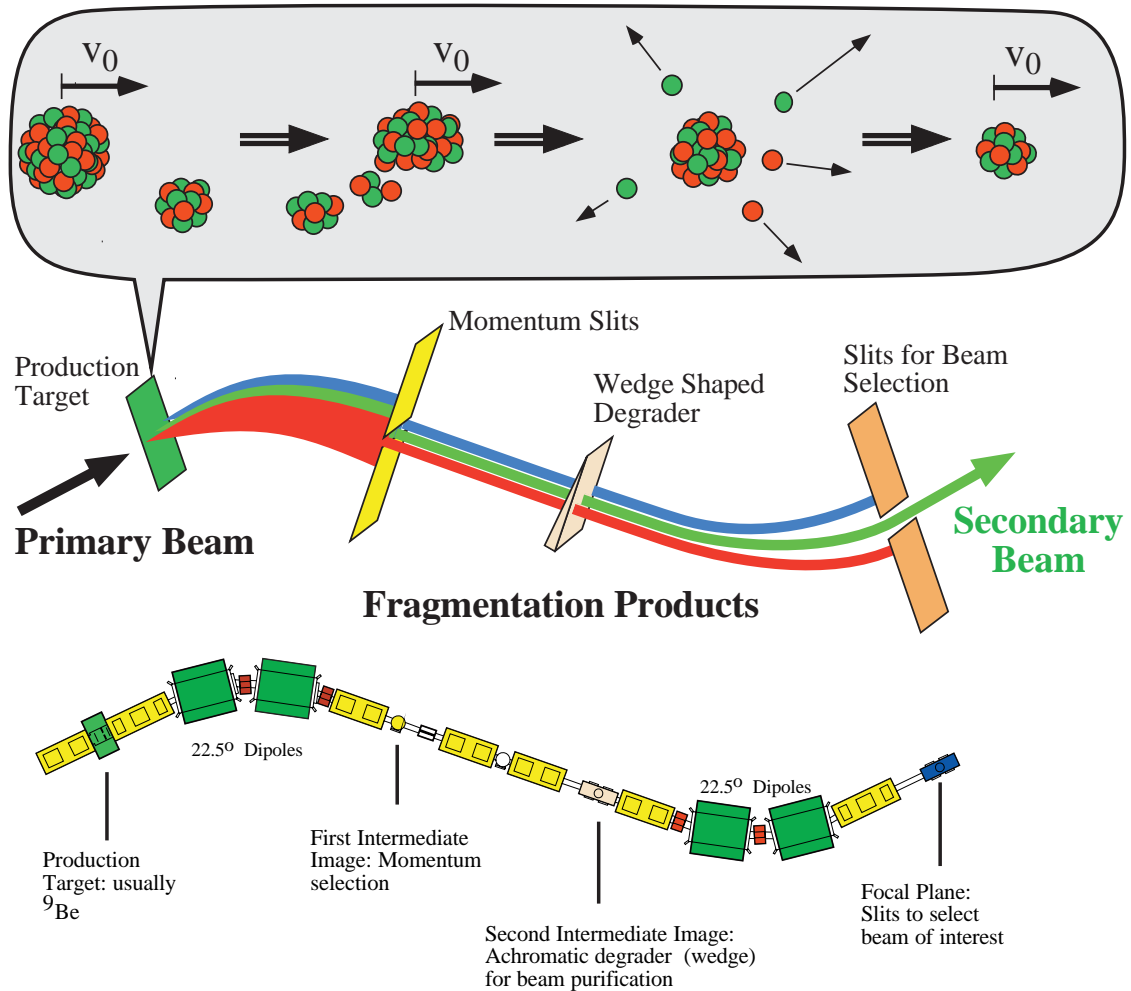


Figure 2.4: Secondary Beam Production: Illustrated here is projectile fragmentation on the example of the A1200 fragment separator at the NSCL. The primary beam strikes the target and several nucleons are removed from the projectile nucleus. Due to the different energy losses of the fragments and the primary beam in the target, the resulting fragments have a large (longitudinal) momentum spread. Slits are used to reduce this spread. The various ions have different energy losses in the degrader and therefore have different magnetic rigidities after the degrader. The second set of dipoles spatially separates different ion species.

of unwanted fragments and to produce a secondary beam. The desired ions are transported to the experimental area where a secondary target is located, which serves as the Coulomb excitation target. The production of secondary beams at the NSCL using the A1200 fragment separator is now very common and the initial identification and setup takes, depending on the nuclei wanted, from a few hours to at most one day. For more details on the A1200 fragment separator see [14].

Notable properties of beams produced by projectile fragmentation are: a) high beam velocities, typically between 30–50% the speed of light, b) potentially low secondary beam intensities, especially for the most exotic<sup>6</sup> nuclei, which are often the most interesting ones, and c) a poor beam quality, due to the production mechanism; the large transverse and longitudinal momentum spreads (up to  $\Delta p_{\parallel}/p_{\parallel} = \pm 1.5\%$  at MSU) result in a large beam spot size (around one cm) and a considerable beam emittance.

The time from the production of the secondary isotopes to the arrival at the experimental station is on the order of a few hundred ns to one  $\mu\text{s}$ . Therefore it is possible to study extremely short-lived isotopes.

### 2.4.3 Detection of De-Excitation Photons

After Coulomb excitation to a bound state the excited nucleus decays back to the ground state by emitting a  $\gamma$  ray. The measurement of the  $\gamma$ -ray energy readily reveals the spacing between the involved energy levels and the number of detected  $\gamma$  rays can be used to determine the Coulomb excitation cross section which is directly related to transition matrix elements of the nucleus (see section 2.2).

---

<sup>6</sup>i.e. very neutron or proton rich compared to stable nuclei with the same mass number.

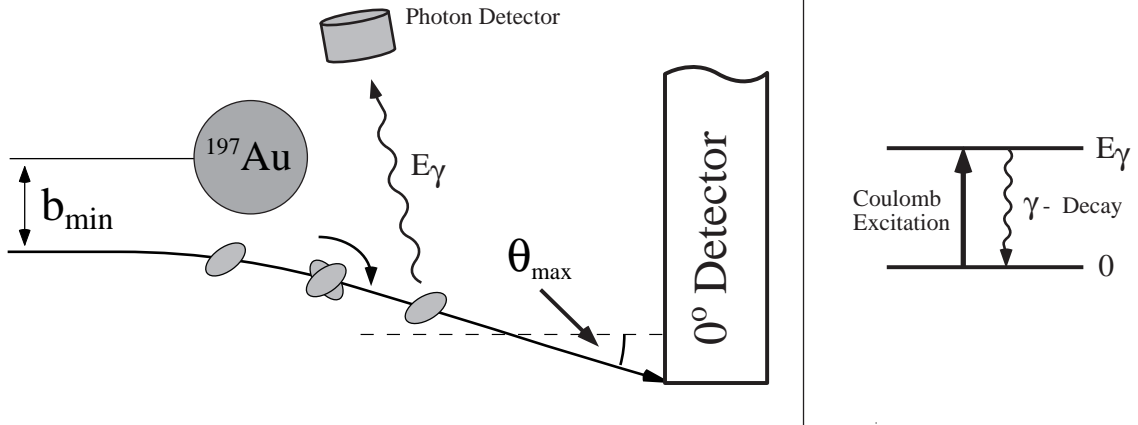


Figure 2.5: A typical experimental setup for intermediate energy Coulomb excitation: The beam particle is detected in a detector covering only forward angles. When particle- $\gamma$  coincidences are measured, this limited extend of the detector ensures the dominance of Coulomb excitation by limiting the impact parameter to be above a certain minimum  $b_{\min}$ . For each Coulomb excitation at least one  $\gamma$  ray is emitted, which can be detected in a suitable detector.

### Energy Resolution and Doppler Broadening

The beam velocities of particles produced by projectile fragmentation are very high, about 30–50% of the speed of light. Thus the  $\gamma$ -ray energy is Doppler shifted considerably, as can be seen from the relation between the photon energy in the projectile and the laboratory frame,  $E_{cm}$  and  $E_{lab}$  respectively<sup>7</sup>

$$E_{cm} = \gamma E_{lab}(1 - \beta \cos(\theta_{lab})). \quad (2.27)$$

$\theta_{lab}$  is the angle between the direction of motion of the particle and the direction of the  $\gamma$  ray,  $\beta$  is the beam velocity in units of the speed of light, and  $\gamma$  is the usual relativistic factor. Since, in an experiment, a single photon detector covers a range in solid angle, the width of the full-energy peak<sup>8</sup> is increased. In addition the spread in beam velocities  $\Delta\beta$ , due to energy loss in the target and the intrinsic beam energy

<sup>7</sup>Since only one photon-emitting particle, the projectile, is considered here the subscript  $_{cm}$  refers to the projectile rest frame and *not* to the center of mass of projectile and target.

<sup>8</sup>Events where the total photon energy was measured form the full-energy peak in the energy spectrum.

spread, will also contribute to the energy resolution. Using

$$\Delta E_{lab}^2 = \left( \frac{\partial E_{lab}}{\partial \beta} \right)^2 \Delta \beta^2 + \left( \frac{\partial E_{lab}}{\partial \theta} \right)^2 \Delta \theta^2 \quad (2.28)$$

it follows that the contribution to the energy resolution, due to the Doppler effect is

$$\left( \frac{\Delta E_{lab}^{(\gamma)}}{E_{lab}^{(\gamma)}} \right)_{\text{dopp}}^2 = \left( \frac{\cos(\theta_{lab})}{1 - \beta \cos(\theta_{lab})} - \beta \gamma^2 \right)^2 \Delta \beta^2 + \left( \frac{\beta \sin(\theta_{lab})}{1 - \beta \cos(\theta_{lab})} \right)^2 \Delta \theta^2. \quad (2.29)$$

Figure 2.6 shows that these contributions are quite significant and that an accurate determination of the photon direction is very important. To the resolutions shown one should add the intrinsic energy resolution of the detector, which is for high-purity germanium detectors on the order of 0.1% and for NaI(Tl) detectors on the order of 7%. Figure 2.6 illustrates that the use of a NaI(Tl) detector is almost sufficient, since the resolution is dominated by the Doppler effect for an angular resolution of  $\Delta \theta = 10^\circ$ . In practice, the assumption of  $\Delta \beta = 0.05$  is quite high. Even though this value corresponds to a typical energy loss in the secondary target (see table 3.3), most of the particles considered in the present work decay outside the target and therefore have the same speed when emitting the photon, as discussed in the next paragraph.

In order to correct for the Doppler Shift one needs to know not only where the photon interacts in the detector but also the position where the excited nucleus  $\gamma$ -decays. The transition rate for E2 transitions is given by (see [9])<sup>9</sup>

$$W(\text{E2}) = 1.23 \cdot 10^9 \cdot \left( \frac{E_\gamma}{\text{MeV}} \right)^5 \cdot \left( \frac{B(\text{E2})}{e^2 \text{ fm}^4} \right) \cdot s^{-1}, \quad (2.30)$$

and the mean lifetime can be obtained as the inverse:  $\tau = W^{-1}$ . For  $^{40}\text{Ar}$  a lifetime of the first excited state of 1.2 ps is obtained, and for  $^{40}\text{S}$ , which was measured as part of this thesis work, the lifetime is 22 ps. The path traveled by the particle in the laboratory is given by  $s = \gamma v \tau$ . Hence, assuming  $v = 0.3c$ , distances on the order of 0.1 mm to 1 mm are traversed between excitation and  $\gamma$  decay. Therefore,

---

<sup>9</sup>E2 transitions are the only mode of  $\gamma$  decay relevant to this work.

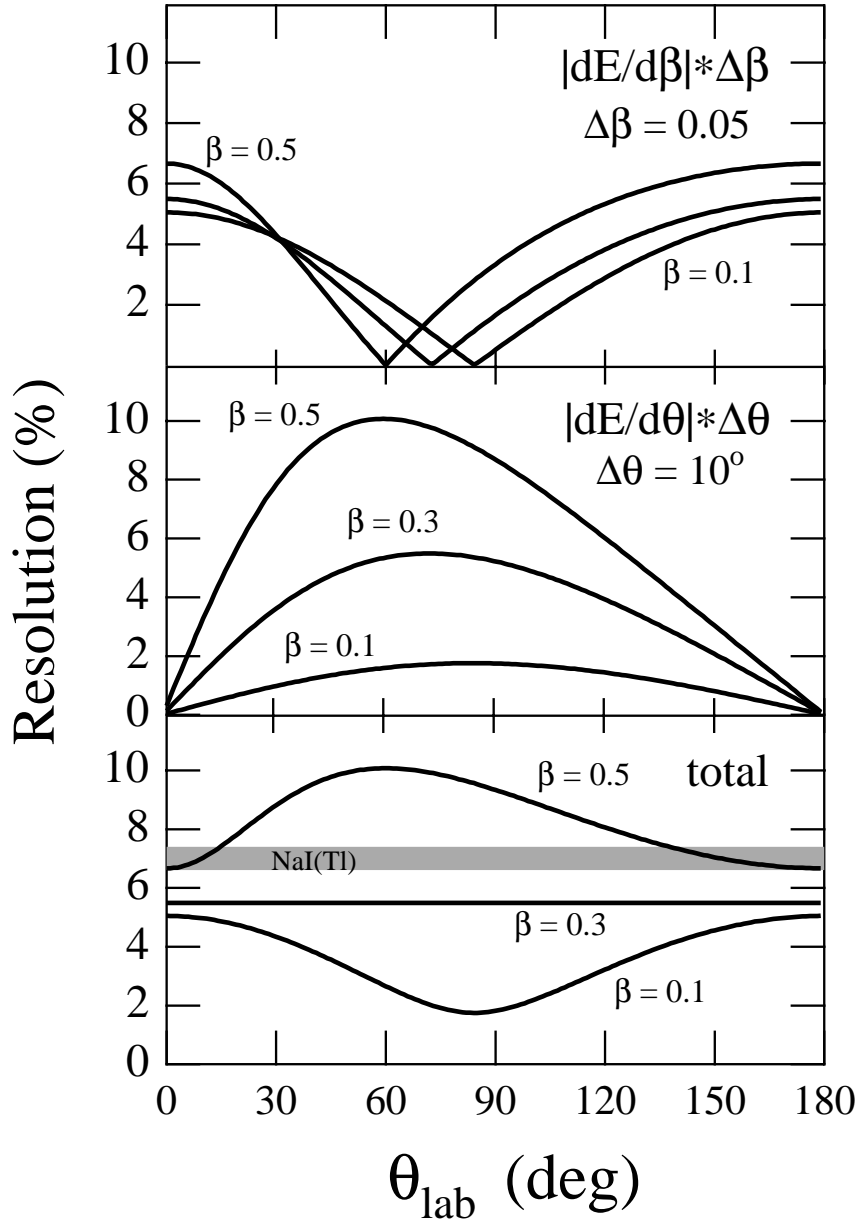


Figure 2.6: Contributions to the photon energy resolution resulting from the energy spread of the beam (top) and from the detector's angular resolution (middle). The quadratic sum of the two contributions is shown in the bottom. Also indicated is the intrinsic energy resolution of a NaI(Tl) detector. In practice, the assumption of  $\Delta\beta = 0.05$  is quite high. Even though this value corresponds to a typical energy loss in the secondary target, most of the particles, considered in the present work, decay outside the target and therefore have the same speed when emitting the photon.

as a typical target thickness is on the order of 0.1 mm ( $200 \frac{\text{mg}}{\text{cm}^2}$   $^{197}\text{Au}$  target), most particles decay in the target or shortly after the target and the target position can be taken as the origin of the detected photons. But, since as outlined above, many nuclei decay outside the target (even if only shortly after it), as in the  $^{40}\text{S}$  case here of interest, one has to be careful about what to assume for the speed of the projectile, since the speed at the center of the target might not be the optimum value.

As shown above, the accurate determination of the photon direction is very important in order to obtain good energy resolution. A discussion on the choice of detector is given in section 3.3, where the NSCL NaI(Tl) array is discussed.

## Cross Section

In order to obtain the cross section one needs to know the number of beam particles that have been excited. This can be related to the number of photons emitted, since the nuclei de-excite, after Coulomb excitation, by emitting at least one photon. Other decay mechanisms, such as internal conversion or particle emission [15], are very unlikely for the nuclei studied here.

**Detection Efficiency.** Unfortunately not all  $\gamma$  rays that are emitted can be detected. A large number will escape, because they either do not hit the detector or they do not interact while passing through the detector. Therefore one has to know the  $\gamma$ -ray detection efficiency  $\epsilon_{\text{tot}}$  of the detector setup. In general  $\epsilon$  will be a function of the  $\gamma$  ray energy and the photon direction. The source of the photons is assumed to be the center of the target. The efficiency for a certain direction and energy is defined as

$$\epsilon = \epsilon(E_\gamma, \Omega) = \frac{\# \text{ of photons detected with direction } \Omega}{\# \text{ of photons emitted into direction } \Omega}, \quad (2.31)$$

where  $\Omega$  stands for the direction defined by  $\theta$  and  $\phi$  in spherical coordinates. The detection efficiency, if the photons are emitted isotropically, is given by

$$\epsilon_{\text{tot}} = \int \epsilon d\Omega . \quad (2.32)$$

This is not the case for photons emitted after Coulomb excitation. However, the angular distribution of the photons can be calculated, as shown in appendix B. The total efficiency is obtained by folding the detector efficiency with the calculated angular distribution  $W(\Omega)$

$$\epsilon_{\text{tot}}(E_\gamma) = \frac{\int_{\Omega} W(\Omega) \cdot \epsilon(E_\gamma(\Omega), \Omega) d\Omega}{\int_{\Omega} W(\Omega) d\Omega} . \quad (2.33)$$

As indicated  $\epsilon$  depends in two ways on the photon direction  $\Omega$ ; directly and from the dependence of the photon energy on  $\Omega$  due to the Doppler effect. The resulting total efficiency depends, of course, only on the photon energy.

The total number of Coulomb excitations  $N_{\text{CE}}$  is found by dividing the number of detected photons  $N_\gamma$  by the total detection efficiency  $\epsilon_{\text{tot}}$

$$N_{\text{CE}} = \frac{N_\gamma}{\epsilon_{\text{tot}}} \quad (2.34)$$

The Coulomb excitation cross section  $\sigma$  is defined as the ratio of the number of excitations  $N_{\text{CE}}$  to the product of the number of incoming beam particles  $N_b$  and the number of target nuclei per unit area  $N_t$

$$\sigma = N_{\text{CE}} \frac{1}{N_b N_t} = \frac{N_\gamma}{\epsilon_{\text{tot}}} \frac{1}{N_b N_t} . \quad (2.35)$$

Therefore the cross section can be determined by measuring the number of emitted photons.



# Chapter 3

## Coulomb Excitation of $^{38,40,42}\text{S}$ and $^{44,46}\text{Ar}$

### 3.1 Introduction

Two of the basic properties of nuclei are their level structure and the transition matrix elements by which these levels are coupled. This information can be related to the shape of the nucleus. Nuclei that are spherical or stiff against deformation show large excitation energies and small coupling strengths. Nuclei that are deformed or soft against deformation have small excitation energies and larger coupling strengths. As pointed out in chapter 1, a large coupling strength indicates collective motion, since a single particle can not give rise to large matrix elements.

A region in the chart of nuclei where little is known about the collectivity of nuclei is the region of the neutron-rich sulfur and argon isotopes. The structure of these nuclei is of particular interest as they are located between two major neutron shell gaps ( $N=20$  and  $N=28$ ), which are well known for the stable isotones. However, Sorlin *et al.* predicted in [16], based on  $\beta$ -lifetime measurements, a rapid weakening of the  $N=28$  shell gap below  $^{48}\text{Ca}$ . Shortly thereafter Werner *et al.* [17] published

similar conclusions based on relativistic mean field and Hartree-Fock calculations. In addition, the nuclei in this region play an important role in the nucleosynthesis of the heavy Ca, Ti, and Cr isotopes [16].

As discussed in chapters 1 and 2 a direct measurement of the excitation energy of the first excited  $J^\pi = 2^+$  state together with a transition strength measurement can give conclusive experimental evidence about the collectivity of these nuclei. The availability of a very high intensity  $^{48}\text{Ca}$  beam at the NSCL at MSU [18] makes the production of secondary beams of these nuclei possible through projectile fragmentation. The beam intensities (10–2000 particles/s) are sufficiently high to perform intermediate energy Coulomb excitation experiments. In a first experiment five isotopes ( $^{38,40,42}\text{S}$ ,  $^{44,46}\text{Ar}$ ) were studied; the excitation energies of the first excited states and the corresponding  $B(E2\uparrow)$  values were determined.

## 3.2 Experimental Procedure

### 3.2.1 Secondary Beams

Primary beams of  $^{48}\text{Ca}^{13+}$  and  $^{40}\text{Ar}^{12+}$  with energies up to  $E/A = 80$  MeV and intensities as high as  $5 \text{ pA}^1$  were produced with the NSCL room temperature electron cyclotron resonance (RTECR) ion source and the K1200 cyclotron. The  $^{48}\text{Ca}$  beam was produced using a new technique discussed in [18]. The secondary sulfur and argon beams were obtained via the fragmentation of the primary beams in a  $379 \text{ mg/cm}^2$   $^9\text{Be}$  primary target located at the mid-acceptance target position of the A1200 fragment separator [14]. The rates and purities of the secondary beams are listed in Table 3.3.

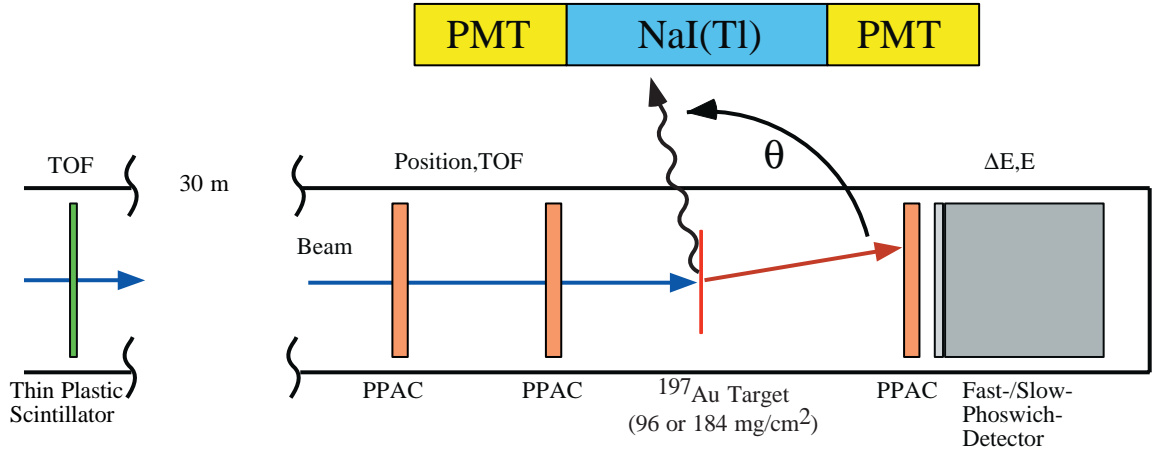


Figure 3.1: Setup around the secondary target.

### 3.2.2 Experimental Setup

Figure 3.1 shows the setup around the secondary target. The time of flight (TOF) between a thin plastic scintillator located after the A1200 focal plane and a parallel plate avalanche counter (PPAC) [19] located in front of the secondary target provided identification of the fragment before interacting in the secondary target as shown in figure 5.1. A fast–slow phoswich detector, which is described in section 3.2.3, was located at zero degrees with respect to the beam axis and allowed the identification of the beam particle after interacting in the target. The target thicknesses for the various beams are listed in table 3.3. Tracking detectors (PPACs) allowed particle tracking before and after the target (mainly used during beam tuning). Photons were detected in coincidence with beam particles by the NSCL NaI(Tl) array, which is described in section 3.3. Figure 3.2 shows the arrangement of the NaI(Tl) detectors in the experiment.

$${}^{11} \text{ p nA (particle nA)} = 10^{-9} \cdot \frac{1}{1.6 \cdot 10^{-19}} \frac{\text{particles}}{\text{s}} \approx 6.2 \cdot 10^9 \frac{\text{particles}}{\text{s}}$$

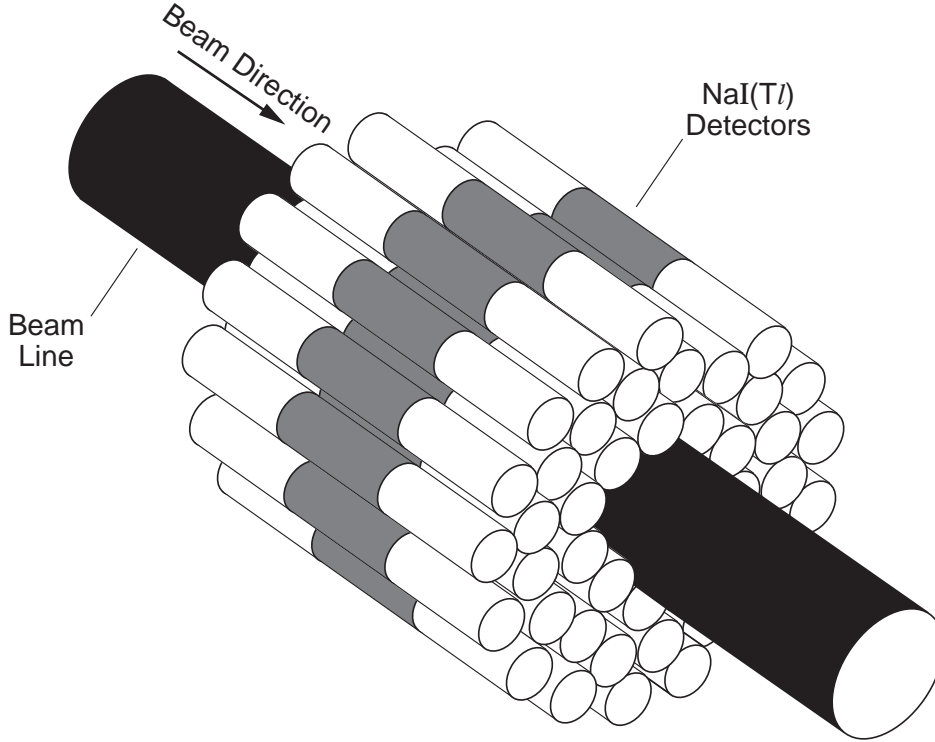


Figure 3.2: Arrangement of the position sensitive NaI(Tl) detectors.

### 3.2.3 Particle Detection

The forward particle detector serves several purposes: (a) It provides particle identification after the target on an event-by-event basis, (b) it ensures that only photons are analyzed that are emitted from beam particles scattered into laboratory angles of less than a certain maximum scattering angle. This angle is defined by the radius of the detector and the distance to the target (in this case  $\theta_{lab}^{max} = 4.1^\circ$ ), (c) it provides the trigger (start detector), (d) it counts the number of incoming beam particles (needed for the normalization of the cross section), and (e) it is used to measure photons in timed coincidence with beam particles, which strongly reduces the background, since it is possible to distinguish photons emitted from the target from photons emitted from the zero degree detector.

The beam-particle detector used in this experiment consisted of a 0.6 mm thick

fast plastic scintillator (Bicron, BC400) followed by 10 cm of slow plastic scintillator material (Bicron, BC444). The detector is cylindrical and has a diameter of 101.6 mm (4"). A light guide followed the slow plastic and light was collected by two 5 cm diameter photomultiplier tubes (PMT). The thickness of the fast plastic was chosen so that the particles in this experiment lose about 20–30% of their energy in the fast plastic. The remaining energy is deposited in the slow plastic. The PMT signal, which was proportional to the produced scintillation light, was split into two streams and in one the full charge is collected (giving the total energy). In the other stream only the first pulse of charge (due to the fast plastic scintillator) was integrated (giving the energy loss in the fast plastic). This is illustrated in figure 3.3. The total signal is a sum of two components. By integrating the total charge (slow gate) the total energy is determined. An integration of the first part of the signal (fast gate) yields a signal roughly proportional to the energy loss in the fast plastic scintillator. This pulse-shape discrimination allowed the identification of the beam particle after the target. The detector had excellent  $Z$  resolution, but the neutron number was not completely resolved. Nevertheless, events from the breakup of the projectile could be rejected. Figure 3.4 shows a typical  $\Delta E$ - $E$  spectrum.

The detector could tolerate rates as high as  $5 \cdot 10^4$  particles/s. The detector was arranged so that fragments scattered into laboratory angles less than  $\theta_{lab}^{max} = 4.1^\circ$  were detected. For all beams, in this work, this opening angle corresponded to an impact parameter which is about 3–4 fm larger than the sum of the two nuclear radii, thereby ensuring the dominance of Coulomb excitation.

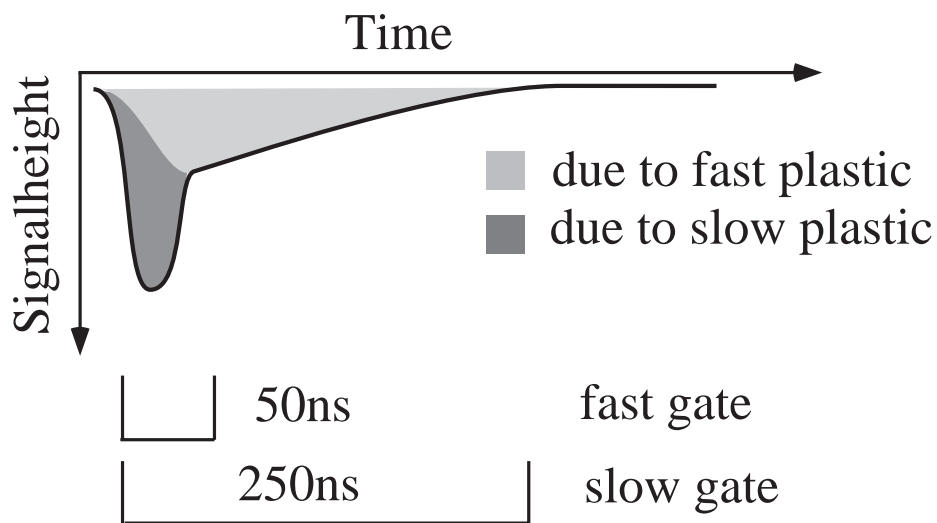


Figure 3.3: Illustration of pulse shape discrimination. The total signal is a superposition of two components, a slow (light grey) and a fast (dark grey) contribution.

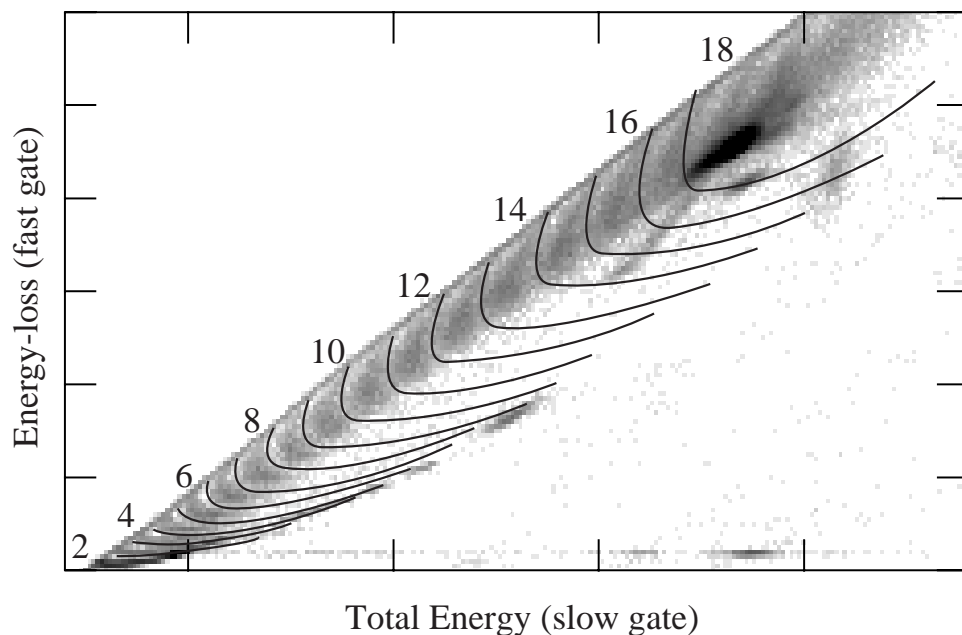


Figure 3.4: Energy-loss vs. total energy after the secondary Au target. The main contribution is the unreacted  $^{44}\text{Ar}$  beam ( $Z=18$ ). If the beam particle collides with a gold nucleus fragmentation can occur and the resulting fragments are observed. The different  $Z$ -bands are indicated and clearly resolved.

## 3.3 The NSCL NaI(Tl) Array

### 3.3.1 Mechanical Setup and Principles of Operation

Each NaI(Tl) crystal is cylindrical, 17.1 cm long and 5.0 cm in diameter and encapsulated in a 2 mm thick aluminum shield. Quartz windows, 0.5 cm thick, are attached at both ends. A 5 cm diameter photomultiplier tube (PMT) is optically coupled to each window. For mechanical stability the aluminum shield of the NaI(Tl) crystal is rigidly connected (epoxied) to a second aluminum pipe which holds the PMT and the connectors for high voltage (HV) input and signal output. In addition, each PMT is surrounded by a 0.5 mm thick magnetic shield. A total of 38 detectors are arranged in an aluminum frame in 3 concentric rings, of 11 (inner), 17 (middle) and 10 (outer) detectors, oriented co-axially to the particle beam axis around a 150 mm diameter beam pipe (figure 3.5). The radii of the three detector rings are 10.8 cm, 16.9 cm and 21.8 cm. As assembled the full array is 60 cm long, 51 cm wide and 55 cm high. When operated at its standard dedicated setup the array is surrounded by a 16 cm thick layer of lead to shield the scintillators from ambient background and  $\gamma$  rays originating from the beam particles stopping in the fast-slow phoswich detector located at zero degrees with respect to the beam axis. The room background  $\gamma$  rate is reduced, depending on the threshold settings, by about a factor of 100.

When a  $\gamma$  ray interacts with the crystal a certain number of scintillation photons, proportional to the deposited energy, are produced, and about half propagate to each end of the crystal. Assuming an exponential attenuation, the light output on each side is described by the following formulas:

$$E_1 \propto E e^{-\mu(\frac{L}{2}+x)} \quad \text{and} \quad E_2 \propto E e^{-\mu(\frac{L}{2}-x)}, \quad (3.1)$$

where  $x$  is the distance of the interaction point from the center of the crystal,  $L$  is its total length,  $\mu$  describes the attenuation of the light.  $E$  is the total energy

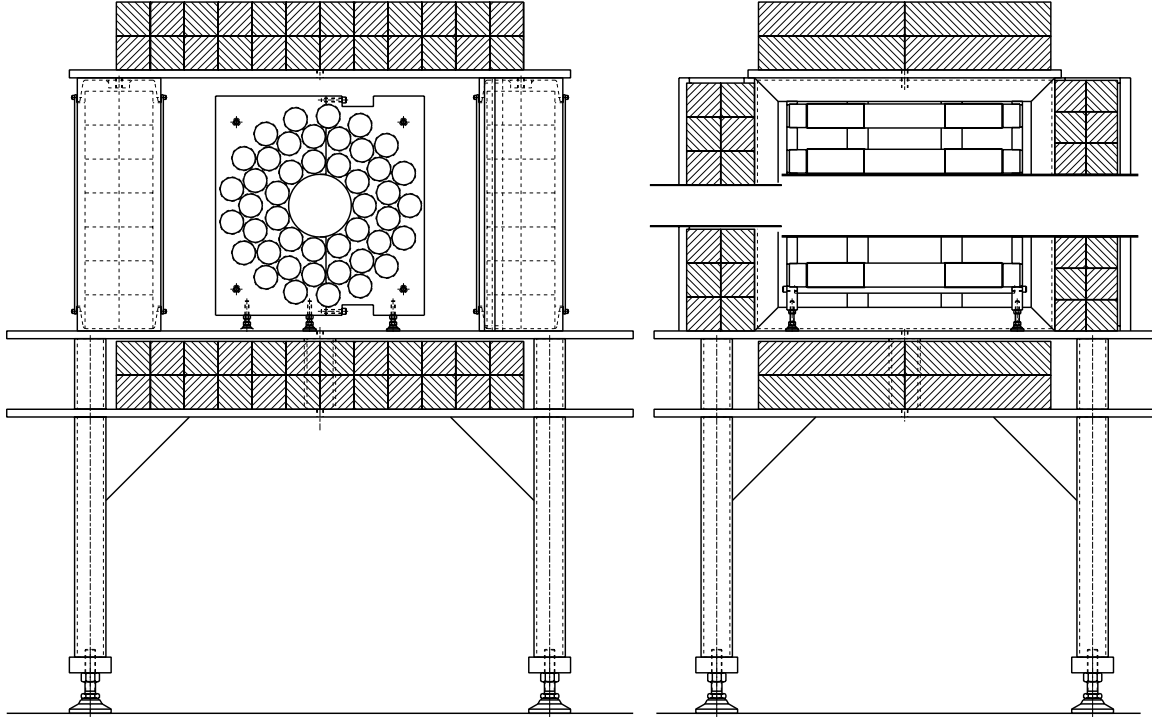


Figure 3.5: Arrangement of the position sensitive NaI(Tl) detectors. The array is surrounded by a 16 cm thick layer of lead to shield from background radiation.

deposited, and  $E_1$  and  $E_2$  are the measured signals. The omitted factor of proportionality includes the gain of the PMTs and amplifiers. Exponential attenuation of the scintillation light along each NaI(Tl) crystal can be achieved in various ways, e.g. by uniformly coating the crystal surface with a light absorbing substance or by diffusing the surface of the crystal [20, 21]. Similar detectors have successfully been used in the APEX experiment at Argonne National Laboratory [21]. It follows from equations 3.1 that one can recover the total energy and the interaction position through:

$$E \propto \sqrt{E_1 E_2} \quad \text{and} \quad x \propto \log(E_1/E_2) . \quad (3.2)$$

A more detailed derivation including the errors on these quantities is given in [20, 21].

There are several effects that change this idealized picture: The assumption of exponential attenuation of the scintillation light is only valid when the interaction point is close to the center of the detector, while at the edges solid angle effects (which lead to a reduction of the light absorption) are more important. This effect can be

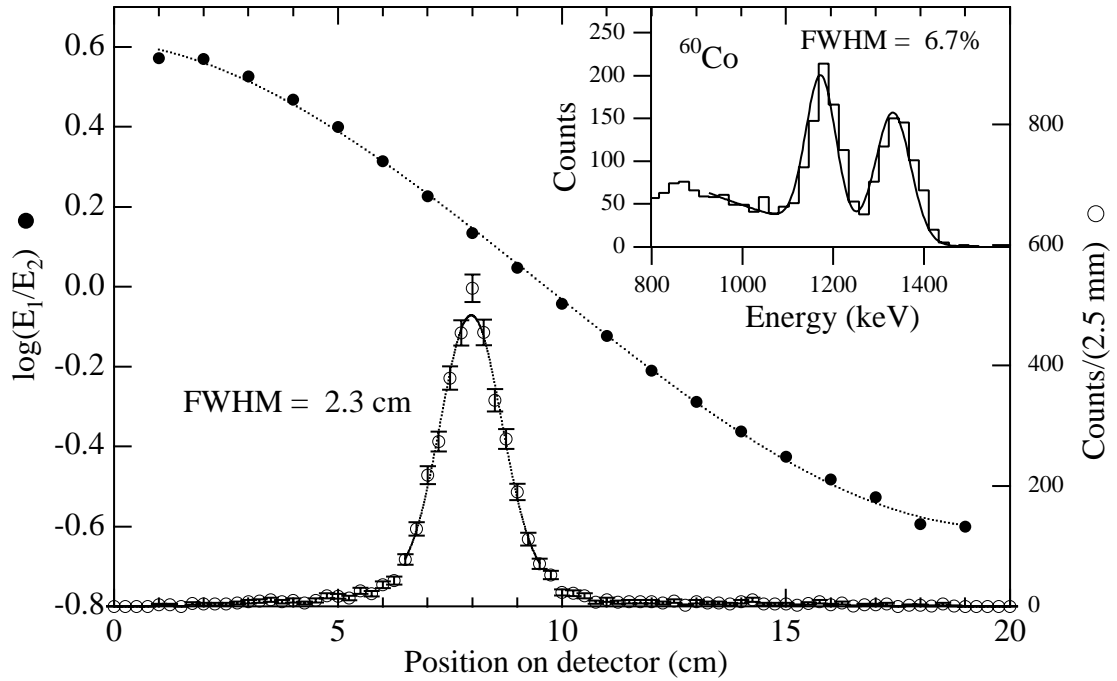


Figure 3.6: Position calculated from the two PMT signals over the actual position of the collimated source. In the central region the relation is linear, while close to the edges of the detector the curve flattens because the assumption of exponential light attenuation is no longer valid. The open circles show a sample position spectrum with the source located at 8 cm. The dotted lines are cubic and Gaussian fits to the calibration curve and the position spectrum, respectively. The inset shows an energy spectrum with the source at the same position. The line is a double Gaussian fit with a quadratic background.

corrected through a cubic position calibration which nicely describes the turnover of the position calibration curve close to the edges of the detector (figure 3.6).

### 3.4 Electronics

Figure 3.7 shows the electronics diagram for the Coulomb excitation experiment. The Master Trigger was defined as a coincidence between a beam particle and a single NaI(Tl) PMT. In addition to particle- $\gamma$  coincidences, particles without a coincidence  $\gamma$  ray (particle singles) were also measured at a rate of every 500th incoming beam

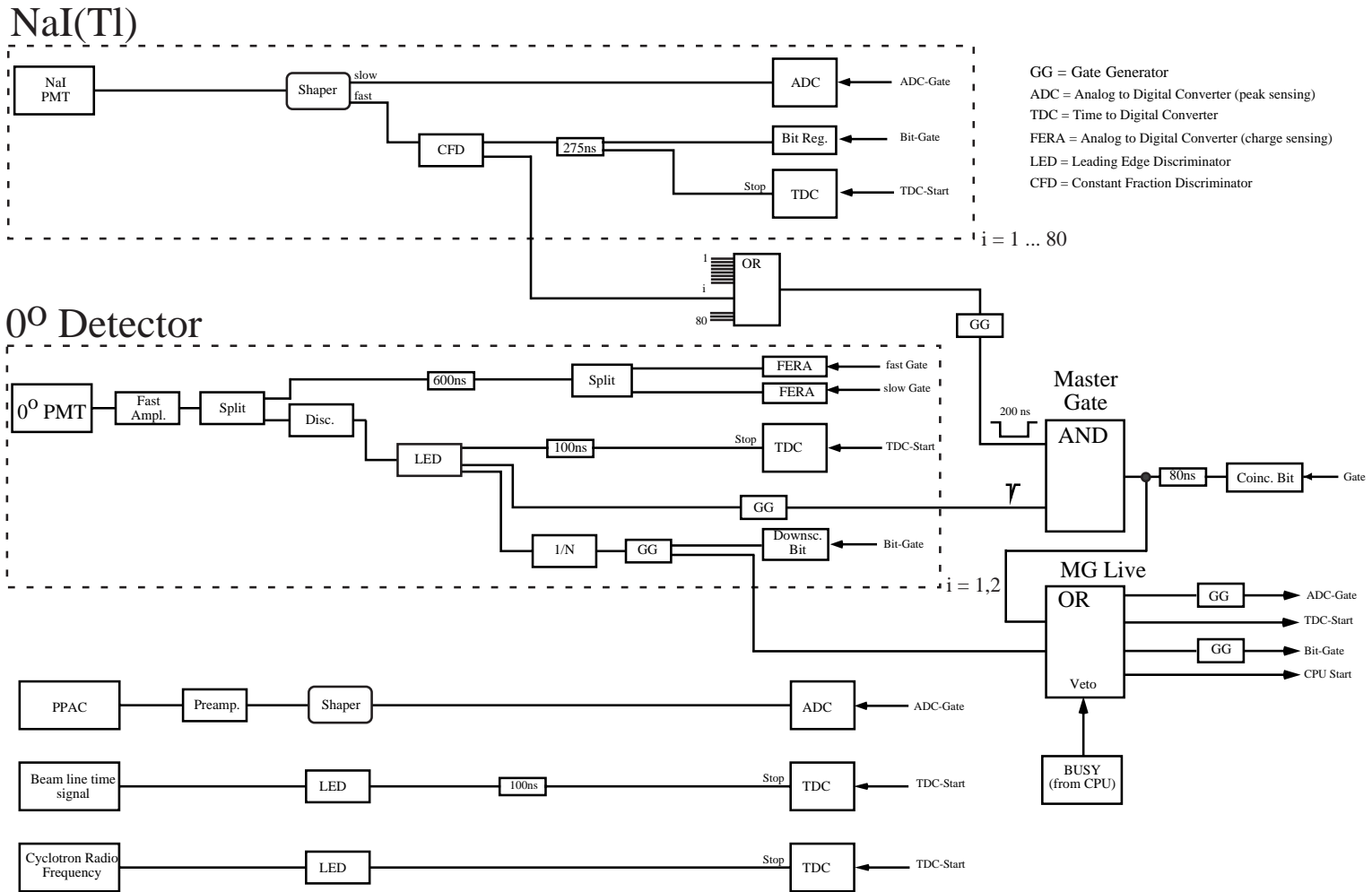


Figure 3.7: Electronics Diagram.

particle (down-scaled particles), which allowed the determination of the total number of incident beam particles.

### 3.4.1 Electronics for the NaI(Tl) Array

A multi-channel high voltage (HV) power supply (LeCroy System 1440) provided typically +1400 V to each PMT. Signals from the PMTs were fed into shaping amplifiers (custom built at NSCL/MSU) and the resulting signals were used for discrimination and energy measurement. The fast output (30 ns shaping time) of each shaper was fed into a constant fraction discriminator (LeCroy MSU 1806 CFD, LeCroy 3420) whose output signal was used for the generation of an event trigger, a scaler signal, and a timing signal. The event trigger required, in addition to a  $\gamma$  signal, a beam particle signal in timed coincidence. After a trigger signal had been generated, all PMTs that belonged to a NaI(Tl) in which at least one PMT fired (according to the bit register, LeCroy 4448) were read out. The energy was obtained from the slow output of the shaping amplifier ( $5\mu s$  shaping time) by digitizing the resulting signals by 8-channel Silena peak sensing ADCs (Silena 4418/V). The trigger, whose signal is correlated in time with the beam particle signal, initiated a start signal for all time to digital converters (TDCs) which were stopped by individual PMT signals and therefore measured the time between detection of the photon and the beam particle. (The TDCs consisted of a combination of time-to-FERA converters (LeCroy TFC 4303) followed by charge integrating ADCs (LeCroy FERA 4300B). Between the START and STOP signals the former applied a constant voltage (-50 mV) on the input terminal of the latter, which resulted in a signal proportional to the time between the START and the STOP signal.) The TDC range was set to 200 ns, which corresponded to the length of the coincidence window between photons and beam particles. The time spectra helped to distinguish between photons emitted from the target and photons

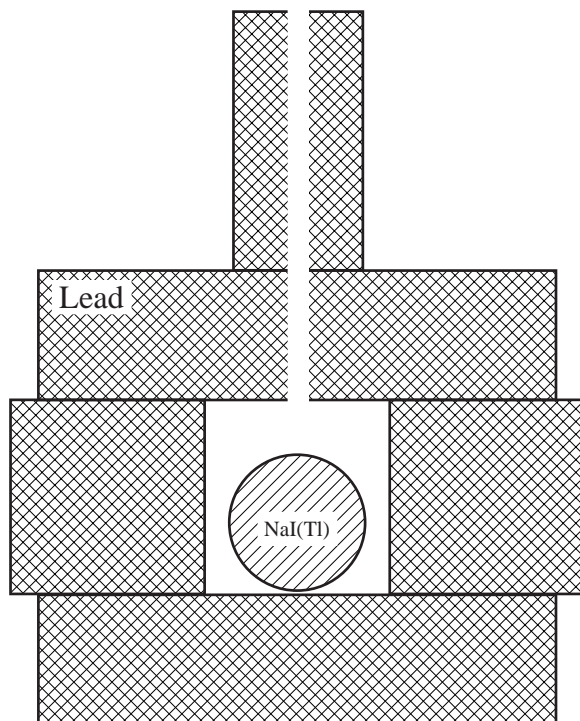


Figure 3.8: Lead housing and photon collimator for the position calibration of the NaI(Tl) detectors. A 0.5 MBq  $^{60}\text{Co}$  source was positioned at the top end of the opening.

emitted by particles stopping in the zero degree detector. The event read-out time was about 300  $\mu\text{s}$ .

### 3.4.2 Calibration and Gain Matching of the Detectors

Before and after the experiment a position, energy, and efficiency calibration of the NSCL NaI(Tl) array was performed.

For the position calibration a collimated  $\gamma$ -ray source was constructed, which consisted of a 8 mm wide and 15 cm long cylindrical opening in two lead bricks, and a 0.5 MBq  $^{60}\text{Co}$  source, which was positioned at one end of the opening. Each NaI(Tl) detector was inserted into a lead housing (shown in figure 3.8) to shield it from ambient background and the collimated source was initially positioned so that the photons are directed at the center of the crystal (in longitudinal and transverse direction). Then a

first coarse gain adjustment was performed by tuning the PMT HV through a visual inspection of the PMT signal amplitudes. Afterwards the shaper gains were adjusted to the desired dynamic range, depending on the expected maximum  $\gamma$ -ray energy (4 MeV in this case), while, at the same time, keeping the total gain of two signal processing chains, belonging to the same detector, matched by centering the peak of the reconstructed position (as defined by equation 3.2) around zero, from which it follows that  $E_1 = E_2$ . The dynamic range was chosen large enough to account for the asymmetry in signal height when the  $\gamma$  ray interacted close to the edges of the detector, i.e. since we wanted to detect photons in a range of up to 4 MeV we had to make sure that no component of the signal processing chain saturated if this photon deposited all its energy close to one PMT. Therefore the range of the shaper was set about a factor of 1.5 higher, which looks like a 6 MeV range for photons interacting in the center of the crystal.

After each detector was matched it was moved in steps of 1–2 cm, according to a measuring tape attached to each detector, to different positions; the data was digitized and recorded on magnetic tape for later analysis. Figure 3.6 shows the reconstructed position, as defined in equation 3.2, versus the true position. One can see that in the central region of the detector the correlation is linear, while at the edges the assumption of equations 3.1 are no longer valid and the curve flattens. The data points were fitted with a third order polynomial, which nicely describes the turnover of the curve close to the edges of the detector.

Photon sources of  $^{88}\text{Y}$ ,  $^{152}\text{Eu}$ , and  $^{228}\text{Th}$  were used for an energy calibration. They provided calibration points from a few 100 keV to 2.6 MeV. Since the raw energy was not completely independent of position, a position dependent energy calibration was performed by applying position cuts to the energy spectra (10 cuts per detector). In between these slices we interpolated to obtain a smoothly varying calibration as a

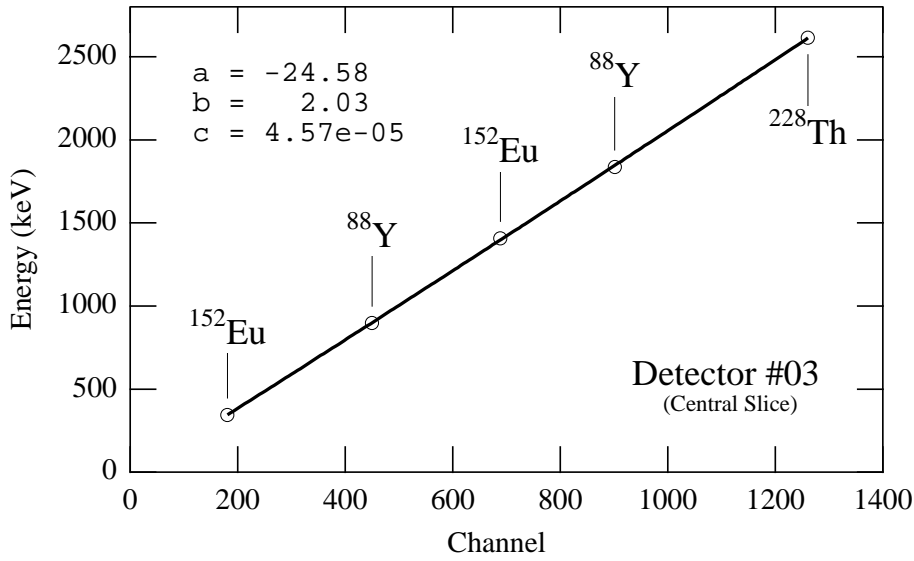


Figure 3.9: Sample energy calibration curve. A quadratic fit was used. The photon sources used for each point are indicated.

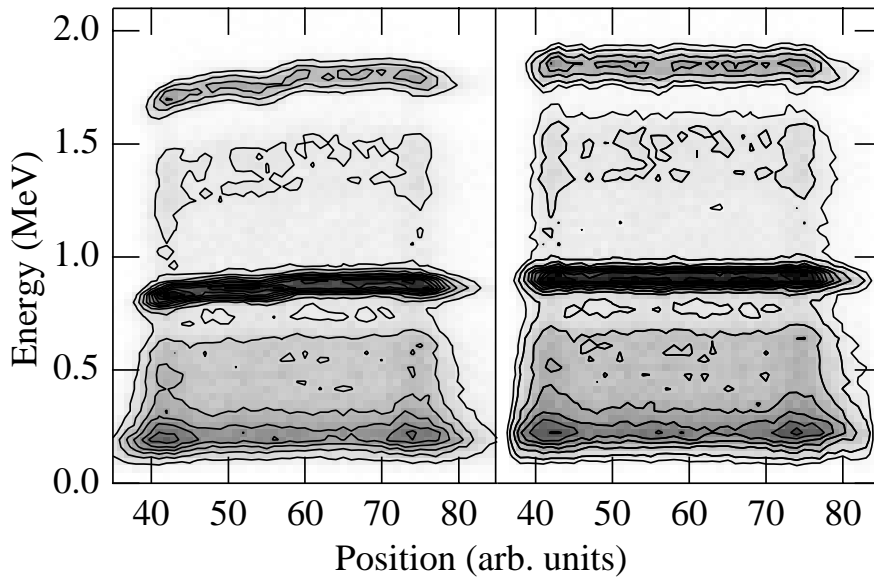


Figure 3.10: Illustration of the position dependence: The left panel shows the uncalibrated energy over the position for an  $^{88}\text{Y}$  source. The right panel shows the same spectrum after a position dependent energy calibration.

function of position. Figure 3.9 shows the energy calibration curve for the central position slice of detector number 3. The effect of the position dependent energy calibration is illustrated in figure 3.10. Shown is the measured (reconstructed) energy over position for an  $^{88}\text{Y}$  source spectrum. One can see that after the calibration the measured energy is independent of position whereas some distortion is present in the uncalibrated spectrum. The sources of these distortions might have been non-uniformities in the NaI(Tl) crystal, which changed the light attenuation along the NaI(Tl) crystal from the ideal exponential behavior (see section 3.3).

The detectors had an average position resolution of about 2 cm and an energy resolution of about 8% at 662 keV. The 2 cm position resolution translated into a contribution to the energy resolution, due to the Doppler effect, of 5% for the inner 11 detectors, whereas without the position information the energy resolution would have been much worse. This is illustrated in figure 3.11. The top panel shows an energy spectrum without Doppler corrections for the case of  $^{40}\text{S}$  on  $^{197}\text{Au}$ . A peak at 547.5 keV is visible, which corresponds to a transition in  $^{197}\text{Au}$ , which served as the (stationary) target nucleus. Also visible is a “bump” around 900 keV. The bottom panel shows the same spectrum, but each event has been Doppler corrected using the known photon interaction position in the NaI(Tl) detectors. Now one can clearly see a peak centered at 891 keV which corresponds to the  $\gamma$  decay of the first excited state in the radioactive isotope  $^{40}\text{S}$ . The measured resolution is 8.7% and only slightly larger than the resolution obtained from a stationary source.

From the given detector length and the radius of the inner ring of detectors it follows that for a source located at the center of the array the geometrical efficiency is close to  $2\pi$  (assuming an azimuthal coverage of 80%). The photopeak efficiency for gamma radiation can be determined in two different ways. One method is to use photon sources that emit two or more  $\gamma$  quanta in coincidence. Gating on one

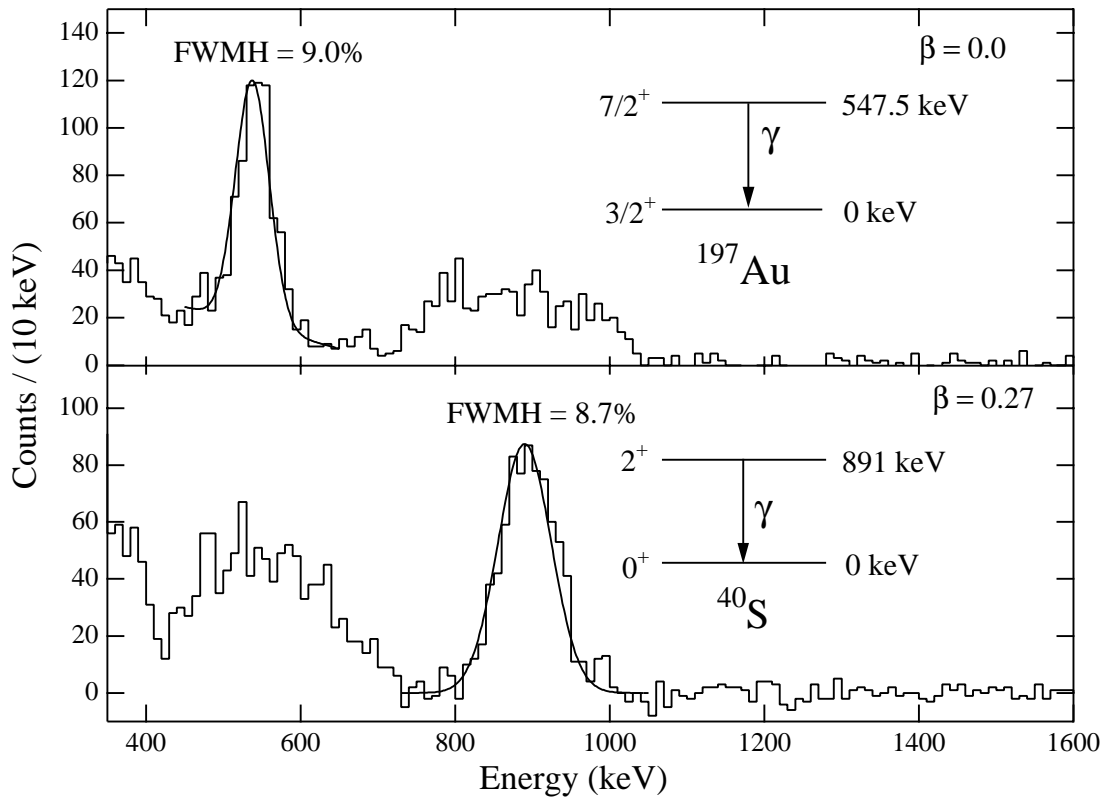


Figure 3.11: Typical spectrum illustrating the correction for the Doppler shift. The top panel shows the raw  $\gamma$ -ray spectrum, while the bottom panel shows the same spectrum corrected for the Doppler shift using the position information of the NaI(Tl) detectors.

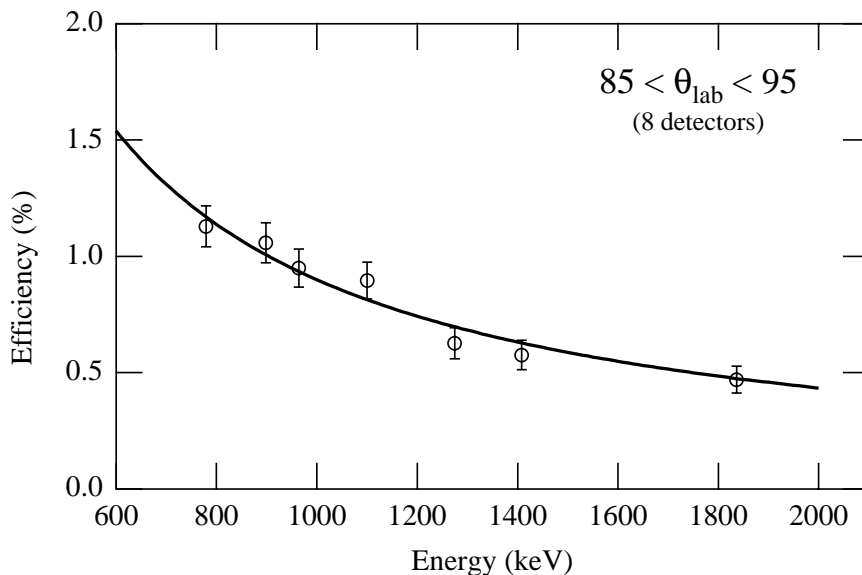


Figure 3.12: Efficiency calibration. The used points are from gamma transitions resulting from the decay of  $^{22}\text{Na}$ ,  $^{88}\text{Y}$ , and  $^{152}\text{Eu}$ . The coincidence method applied to the first two sources gave an absolute calibration, while  $^{152}\text{Eu}$  was used for a relative calibration.

photopeak energy of the cascade in a specific detector and integrating the number of counts registered by all other detectors in the photopeak of the corresponding second  $\gamma$  transition (and taking into account the coincidence ratio between the two transitions) leads to a value for the absolute photopeak efficiency of the detector array. The advantage of this method is that it is not necessary to have an absolute calibration of the photon source. The other method consists of using a calibrated photon source and applying corrections for the dead time of the data acquisition system. Both methods were compared and gave consistent results.

Figure 3.12 shows efficiency calibration points from several sources.  $^{22}\text{Na}$ ,  $^{88}\text{Y}$  provided absolute points through the coincidence method, whereas the points from  $^{152}\text{Eu}$  were used as a relative calibration. The functional form of the fit was  $\epsilon = A \cdot E_{\gamma}^B$ , where  $A$  and  $B$  are fit parameters with  $B$  yielding values around -1 (i.e.  $\epsilon \propto \frac{1}{E}$ ). The photopeak efficiency for the inner 11 detectors, was about 10% at 890 keV and scaled

roughly with inverse energy in the region between 0.7 and 2 MeV. The exact values for the nuclei studied here are listed in table 3.3.

## 3.5 Analysis

### 3.5.1 Stability of Calibration

During the course of the experiment unexpected energy shifts over time were observed; only two detectors had a stable energy and position calibration, determined by comparing source calibrations at the end and the beginning of the experiment. The most probable causes were gain shifts in the photomultiplier tubes, which have been used extensively. For subsequent experiments several PMTs were reglued and loose high voltage and signal leads were resoldered, which improved the gain stability.

Nevertheless, the statistics in the two stable detectors were sufficient to establish the energy of the first excited states in these nuclei. Since  $\gamma$ -ray peaks due to transitions in the projectile nucleus were observed in most detectors, an additional energy calibration was performed in order to move the peaks (corresponding to the first excited states) to the correct energies, as determined by the two stable detectors. In all, 8 detectors (all, except the most unstable) were used for the extraction of the Coulomb excitation cross section.

### 3.5.2 Angular Distributions

In appendix B it is shown that the angular distribution of the de-excitation photons is given by

$$W(\theta) = \sum_{k \text{ even}} a_k P_k(\cos(\theta)), \quad (3.3)$$

l	m	$a_0$	$a_2$	$a_4$	$b_{min}(\text{fm})$	E/A (MeV)
1	0	$\frac{1}{4\pi}$	-1	0		pure E1
1	1	$\frac{1}{4\pi}$	$\frac{1}{2}$	0		
2	0	$\frac{1}{4\pi}$	$\frac{5}{7}$	$-\frac{12}{7}$		pure E2 transitions
2	1	$\frac{1}{4\pi}$	$\frac{5}{14}$	$\frac{8}{7}$		
2	2	$\frac{1}{4\pi}$	$-\frac{5}{7}$	$-\frac{2}{7}$		
2		$\frac{1}{4\pi}$	-0.535	-0.152	15	40
2		$\frac{1}{4\pi}$	-0.663	-0.239	15	200
2		$\frac{1}{4\pi}$	-0.405	-0.082	25	40

Table 3.1: Parameters  $a_0$ ,  $a_2$ ,  $a_4$  of the angular distribution for pure transitions and distributions in intermediate energy Coulomb excitation. The value for  $a_0$  ensures the proper normalization.

with

$$a_k = \sum_{\mu, L, L'} \left| G_{\lambda\mu} \left( \frac{c}{v} \right) \right|^2 g_{\mu}(\xi) (-)^{\mu} \begin{pmatrix} \lambda & \lambda & k \\ \mu & -\mu & 0 \end{pmatrix} \cdot \left\{ \begin{matrix} I_f & I_f & k \\ \lambda & \lambda & I_i \end{matrix} \right\} F_k(L, L', I_{ff}, I_f) \sqrt{2k+1} \delta_L \delta_{L'}.$$

Using equation B.14 one can also obtain the  $a_k$  for pure  $E\lambda m$  transitions. Listed in table 3.1 are the  $a_k$ 's for pure E1 and E2 transitions together with the calculated coefficients for actual distributions. Figure 3.13 shows the angular distributions for pure E2 transitions and the calculated transitions from table 3.1. The similarity of the actual distributions with the  $l=2, m=2$  case shows that the main contribution to the excitation results from maximum angular momentum transfer along the beam direction, as shown analytically in [5].

The importance of considering the angular distribution is illustrated in figure 3.14. Shown are the ( $\phi$  integrated) angular distributions for isotropic  $\gamma$  decay and  $\gamma$  decay following Coulomb excitation of  $^{40}\text{S}$  on a  $^{197}\text{Au}$  target at  $E/A = 40$  MeV. Here, the detector efficiency was approximated as a step function. In this case the measured cross section would have been overpredicted by 14% if the angular distribution were

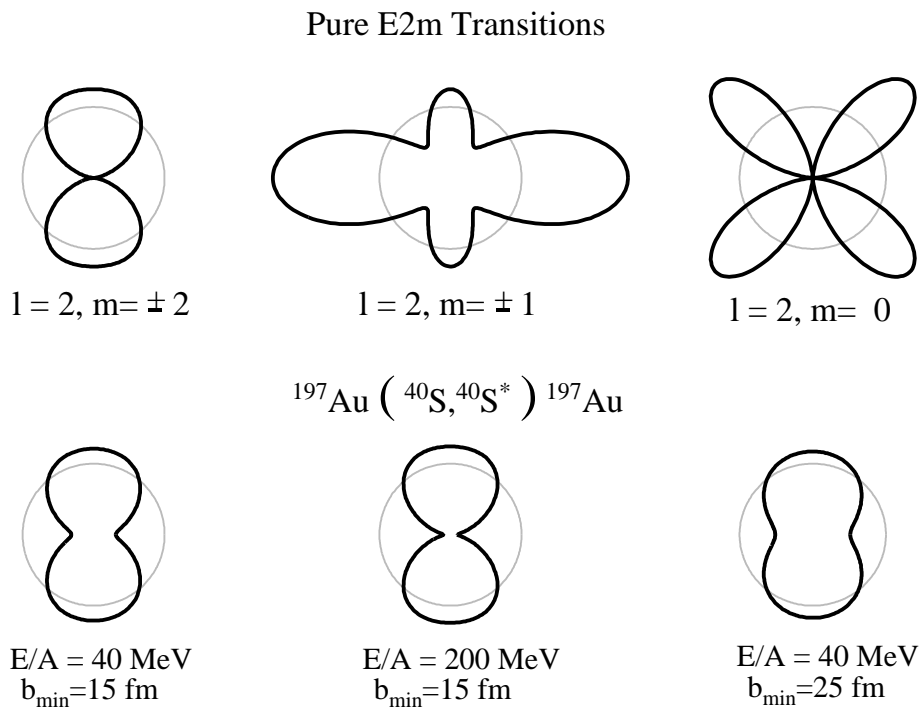


Figure 3.13: The top row shows the angular distributions for pure E2 transitions. The quantization axis, which is identical to the beam direction, is going from the left to the right. The bottom row shows angular distributions for different beam energies and impact parameters. One can see that the main contribution results from maximum angular momentum transfer along the beam direction (similarity to the pure  $l=2, m=2$  case).

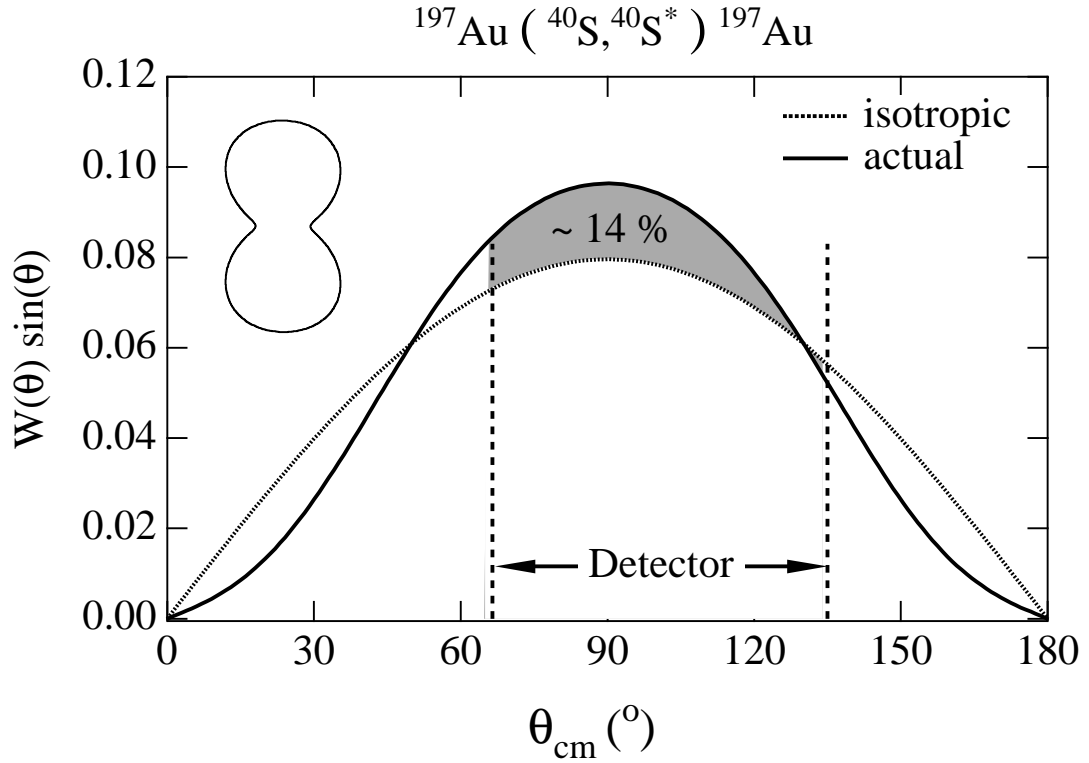


Figure 3.14: Angular Distribution of de-excitation photons. The area under the curve corresponds to the geometric efficiency. Neglecting the angular distribution of photons would result in a 14% larger cross section measurement.

not considered. Figure 3.15 shows the angular distribution in the laboratory system.

### Folding with the Efficiency

With the angular distribution normalized to unity

$$\int_{4\pi} W(\Omega) d\Omega = 1 \quad (3.4)$$

the total efficiency is obtained as

$$\begin{aligned} \epsilon_{\text{tot}} &= \int_{\Omega} W(\Omega) \epsilon(E_{\gamma}(\Omega), \Omega) d\Omega \\ &= \sum_i \int_{\Omega_i} W(\Omega) \epsilon(E_{\gamma}(\Omega), \Omega) d\Omega \end{aligned}$$

— Center of Mass  
..... Laboratory ( $\beta=0.284$ )

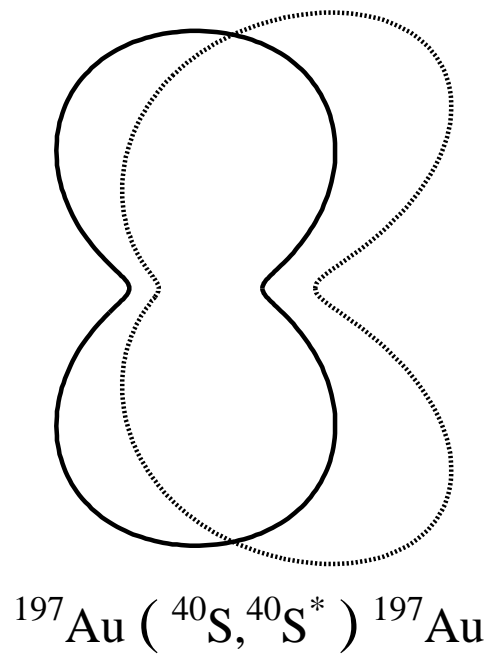


Figure 3.15: The angular distribution in the laboratory system and in the center of mass.

$$= \sum_i \epsilon(E_\gamma(\Omega_i), \Omega_i) \int_{\Omega_i} W(\Omega) d\Omega .$$

In the last step it was assumed that the efficiency is constant in the range  $\Omega_i$ .<sup>2</sup>

During the source calibration, using either the coincidence method or a calibrated photon source, the following quantity is measured:

$$\epsilon_\Omega^{(\text{iso})} = \frac{1}{4\pi} \int_{\Omega} \epsilon(\Omega) d\Omega . \quad (3.5)$$

This is the efficiency integrated over  $\Omega$  (as indicated by the subscript  $\Omega$ ), with the weight ( $= \frac{1}{4\pi}$ ) corresponding to an isotropic distribution. (If  $N$  photons are emitted isotropically then  $\epsilon_\Omega^{(\text{iso})} \cdot N$  photons are detected within the solid-angle range  $\Omega$ .)

Assuming that  $\epsilon(\Omega)$  is constant within  $\Omega$  it follows that

$$\epsilon(\Omega) = \frac{4\pi}{\Omega} \epsilon_\Omega^{(\text{iso})} . \quad (3.6)$$

Hence the total photo peak efficiency is given by

$$\epsilon_{\text{tot}} = \sum_i \frac{4\pi}{\Omega_i} \epsilon_{\Omega_i}^{(\text{iso})}(E_\gamma) \int_{\Omega_i} W(\Omega) d\Omega , \quad (3.7)$$

where  $\epsilon_{\Omega_i}^{(\text{iso})}(E_\gamma)$  is obtained from the efficiency calibration and  $W(\Omega)$  is obtained from formula B.17.

In this experiment the whole array was segmented (in software) into 7 regions ( $\Omega_{1,\dots,7}$ ) defined by cuts in  $\theta$  ( $45\text{--}55^\circ, \dots, 115\text{--}125^\circ$ ). For each of these regions the efficiency was experimentally determined and the photon angular distribution was calculated and integrated. Subsequently formula 3.7 was used to obtain the total efficiencies, which are listed in table 3.3 for all five isotopes.

---

<sup>2</sup>In the previous and following expressions  $\Omega$  is used to label both a range in solid angle, as the  $\Omega$  under the integral sign, and a direction in spherical coordinates  $\Omega = (\theta, \phi)$ , as the  $\Omega$  in the argument of  $\epsilon()$  or  $W()$ . It should be clear from the context what is meant.

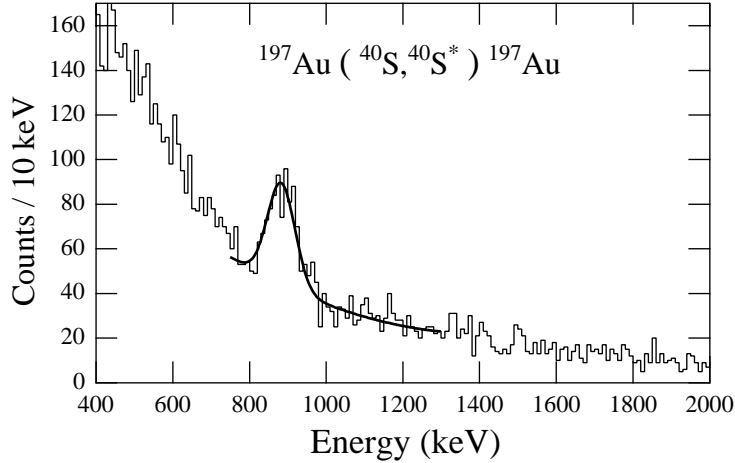


Figure 3.16: The observed photon spectrum for  $^{40}\text{S}$ . A Gaussian fit with quadratic background was used to determine the peak area.

### 3.5.3 Photon Yields

The number of emitted photons was obtained by integrating the observed  $\gamma$ -ray spectra. A sample spectrum is shown in figure 3.16. No cuts have been applied, besides the requirement of the correct isotopes before ( $\Delta E$ -TOF) and after ( $\Delta E$ - $E$ ) the target. In contrast, the spectra shown in figure 3.18 have been obtained by requiring a photon multiplicity (fold) of one and a cut was made in the time spectra corresponding to photons emitted from the target. This condition could not be applied in the cross section determination, since the peaks due to the target and zero degree detector were not completely resolved. The spectrum in figure 3.16 is fitted well by a Gaussian peak with quadratic background.

### 3.5.4 Error Analysis

The uncertainties on the extracted excitation energies and the measured  $B(E2)$  values are calculated by using standard error propagation [22]. The sources for systematic and statistical errors will be discussed for the example of  $^{40}\text{S}$ .

## Excitation Energy

**Statistical Errors.** The largest contribution to the statistical error was the intrinsic resolution of the NaI(Tl) detectors, as discussed in sections 2.4.3 and 3.3. Other contributions were the uncertainty in the angle of the photon and the uncertainty in the velocity of the  $\gamma$ -emitting particle, due to energy loss in the target and the initial beam energy spread. Both of these contribute to the energy resolution via the Doppler shift. All of these uncertainties manifest themselves in the width of the measured peak in the energy spectrum.

**Systematic Errors.** The only systematic error, besides the error in the energy calibration parameters, was the uncertainty in the target position with respect to the photon detectors, which was estimated to be 5 mm. This includes:

- the position of target with respect to beam-line
- the position of NaI(Tl) array with respect to beam-line
- the position of NaI(Tl) detectors in the array (there is a 1–2 mm play)
- the position of measuring tape on the detectors

The resulting systematic error for the measured energy was 1.25%. In subsequent experiments this contribution was reduced through the use of a position calibration device that calibrates the detector position relative to a certain point on the beam line [23]. Therefore the last three points of the previous list can be replaced by the uncertainty in positioning of the calibration device, which is very small.

## Cross Section

**Statistical Errors.** The only statistical error was due to the counting of photons in the photopeak. The numerical value was obtained by fitting the peak in the photon spectra (figure 3.16) and therefore includes the uncertainty in the background as well as the uncertainty in the peak.

Quantity	Contribution	Magnitude	Result on Quantity
Energy	statistical		0.4%
	calibration parameters		5 keV
	beam velocity	0.1%	<0.01%
	target position	5 mm	1.25%
	total		1.4%
Efficiency	calibration parameters		8 %
	$\theta_{max}$	0.1°	0.4 %
	beam velocity	0.1%	<0.1%
	total		8 %
Cross section	statistical		5 %
	efficiency		8 %
	total		10 %
B(E2↑)	$\theta_{max}$	0.1°	5 %
	excitation energy	1.4%	2.8 %
	beam velocity	0.1%	0.3%
	cross section	10 %	10 %
	total		12 %

Table 3.2: Summary of uncertainties in the excitation energy, the detection efficiency, the excitation cross section, and the B(E2↑) value for the  $^{40}\text{S}$  measurement.

**Systematic Errors.** The largest contribution to the uncertainty of the cross section came from uncertainties in the determination of the photon detection efficiency. The uncertainty in the efficiency includes contributions from the fit of the calibration curve, by far the largest contribution, and contributions due to the calculated angular distribution, which depends on  $\theta_{\max}$  (see figure 3.13). In subsequent experiments the error due to the efficiency calibration was reduced by the use of calibrated photon sources. Here, one does not have to apply gates, which raises the number of counts by an order of magnitude, and thus reduces the statistical uncertainty.

### **B(E2 $\uparrow$ ) value**

**Statistical Errors.** The statistical error is the same as that of the cross section because of the linear relationship between excitation cross section and B(E2) value (equation 2.9).

**Systematic Errors.** Besides the systematic errors from the cross section there were also uncertainties in the calculation of the factor of proportionality, the Winther and Alder functions  $G_{\pi\lambda\mu}$  and  $g_{\mu}$ . Contrary to the cross section the B(E2) value depends strongly on the maximum scattering angle and this uncertainty has to be considered.

Table 3.2 lists the error sources and the contributions for the  $^{40}\text{S}$  case as an example. For the other cases the systematic errors are very similar and are not explicitly listed. The final results with total errors are listed in table 3.3.

## **3.6 Results and Discussion**

### **3.6.1 Observations**

Photons emitted from the fast moving fragments ( $v \approx 0.3c$ ) could be clearly distinguished from photons emitted from the stationary target by their Doppler shifts.

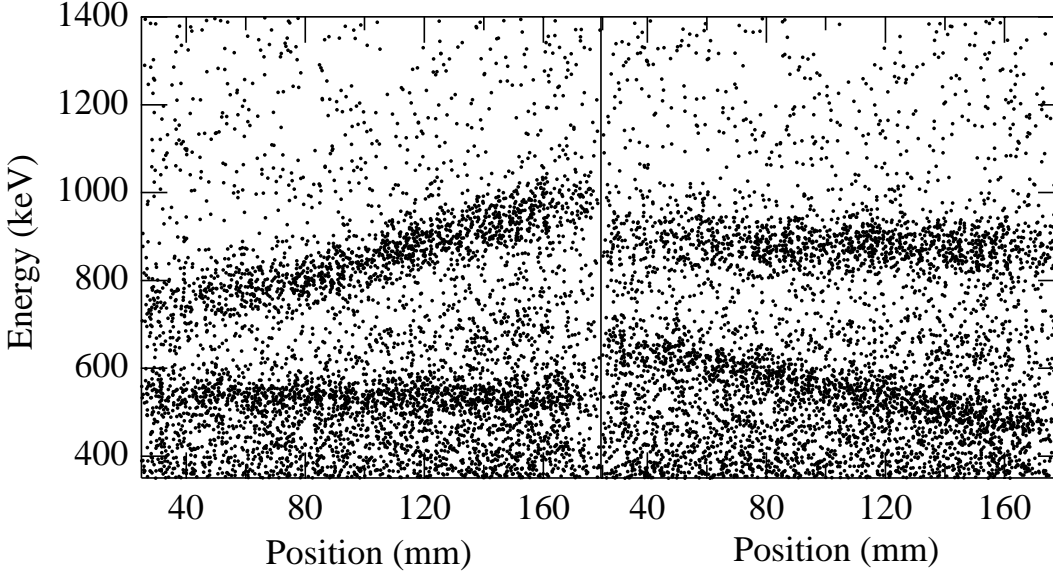


Figure 3.17: Observed energies of  $\gamma$ -rays as a function of position without correction for Doppler shifting (left panel) and with the Doppler correction (right panel) for the  $^{40}\text{S}+^{197}\text{Au}$  reaction. The target was located at 90 mm. The  $\gamma$ -rays near 547 keV are from the gold target, while those near 890 keV are from the  $(2_1^+ \rightarrow 0_{g.s.}^+)$  transition in the projectile.

Figure 3.17 shows the  $\gamma$ -ray energy spectrum as a function of position in the NaI(Tl) detectors for the  $^{40}\text{S}+^{197}\text{Au}$  reaction. The left panel shows the  $\gamma$ -ray energies in the laboratory rest frame; i.e. before any Doppler shift adjustment. In this panel, the energy of the 547 keV ( $\frac{7}{2}^+ \rightarrow g.s.$ ) transition from the  $^{197}\text{Au}$  target is independent of position, while the energy observed for the  $2_1^+ \rightarrow 0_{g.s.}^+$   $\gamma$ -ray from the projectile  $^{40}\text{S}$  depends on the position and, therefore, on the angle at which it was emitted. For forward angles a higher energy is observed, whereas for backward angles a lower energy is measured. The right panel shows the same energy spectrum, but each event has been corrected for the Doppler shift. Therefore this spectrum corresponds to the projectile rest frame ( $v = 0.27c$ ). In this panel, the energy of the  $\gamma$ -ray from the projectile is constant, while the energy of the target  $\gamma$ -ray now varies as a function of position.

The Doppler-corrected, background-subtracted  $\gamma$ -ray spectra for all five nuclei

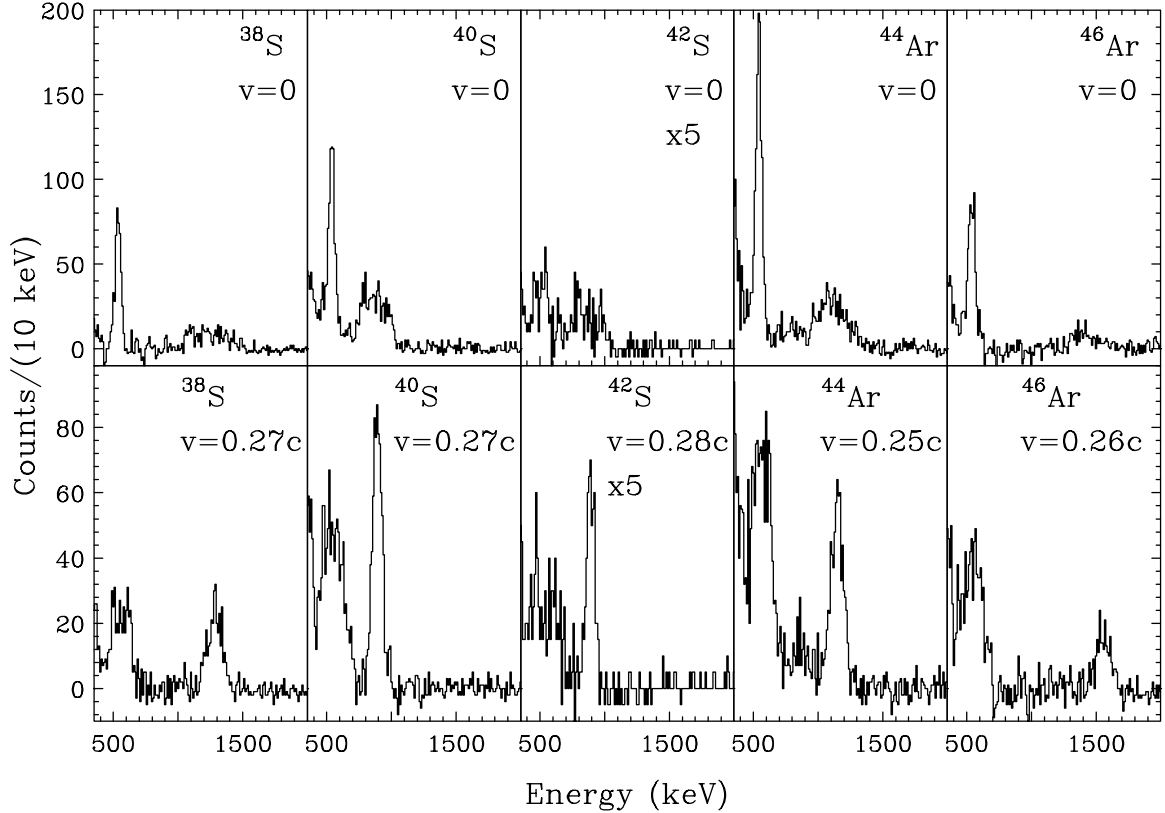


Figure 3.18: Upper panels contain background subtracted photon spectra in the laboratory frame. The 547 keV ( $7/2^+ \rightarrow g.s.$ ) transition in the gold target is visible as a peak, while the ( $2^+ \rightarrow g.s.$ ) transitions in each projectile are very broad. Lower panels contain Doppler-corrected, background-subtracted  $\gamma$ -ray spectra.

studied here are shown in figure 3.18. All five spectra clearly show one photo-peak associated with each projectile. The measured energies of the  $2_1^+$  states and  $B(E2; 0_{g.s.}^+ \rightarrow 2_1^+)$  values are listed in Table 3.3. It should be noted that the  $B(E2 \uparrow)$  result obtained here for  $^{38}\text{S}$  is consistent with the lower limit set on the lifetime of the  $2_1^+$  state by Olness *et al.* [24]. In addition, the well-known energy of the  $2_1^+$  state of  $^{38}\text{S}$  [25, 26] was used to check the energy calibration procedure.

No excited states have been observed previously in  $^{40,42}\text{S}$ , but excited states have been reported for  $^{44,46}\text{Ar}$ . Crawley *et al.* [27] observed states in  $^{44}\text{Ar}$  using the  $^{48}\text{Ca}(^3\text{He}, ^7\text{Be})$  reaction and judged the  $2_1^+$  state of  $^{44}\text{Ar}$  to lie at 1.61 MeV. The spectra in the study of Crawley *et al.* are quite difficult to interpret because the

background peaks are much larger than those from  $^{44}\text{Ar}$ . If the 1.144 MeV state, proposed here as the  $2_1^+$  state, was populated in the experiment of Crawley *et al.*, it would have been obscured by a peak corresponding to an excited state of  $^7\text{Be}$ . Mayer *et al.* [28] reported an energy of 1.55 MeV for the corresponding state in  $^{46}\text{Ar}$  from their work with the  $^{48}\text{Ca}(^{14}\text{C}, ^{16}\text{O})$  reaction in agreement with the present work.

### 3.6.2 Comparison to Theory

Self-consistent mean field techniques [17] predict permanent quadrupole deformations in  $^{40,42}\text{S}$  of  $\beta_2 \sim 0.25$ , only slightly smaller than those measured here (see Table 3.3). For  $^{44,46}\text{Ar}$ , Werner *et al.* [17] did not provide definitive predictions but instead showed that their two calculation techniques (Hartree-Fock+Skyrme and relativistic mean field) give very different answers for these two nuclei. The Hartree-Fock calculations yield a significant prolate deformation ( $\beta_2 = +0.17$ ) for  $^{44}\text{Ar}$  and an oblate deformation ( $\beta_2 = -0.13$ ) for  $^{46}\text{Ar}$ . On the other hand, the relativistic mean field calculations yield  $\beta_2 = -0.13$  for  $^{44}\text{Ar}$  and  $\beta_2 = 0.00$  for  $^{46}\text{Ar}$ . The experimental  $B(E2; 0_{g.s.}^+ \rightarrow 2_1^+)$  results agree better with the Hartree-Fock results, since a non-zero deformation is measured for  $^{46}\text{Ar}$  ( $\beta_2 = 0.18(2)$ ) and a relatively large deformation is measured for  $^{44}\text{Ar}$  ( $\beta_2 = 0.24(2)$ ). The effects of the  $N = 28$  major shell gap persist in  $^{46}\text{Ar}$  because it is less deformed than  $^{44}\text{Ar}$  and its deformation and the energy of its first excited state are similar to  $^{50}\text{Ti}$  ( $E(2_1^+) = 1554$  keV,  $\beta_2 = 0.17$ , [29]). It would be of considerable interest to measure the  $2_1^+$  state of  $^{44}\text{S}$  to see whether the  $N = 28$  shell gap is still present even further from the line of stability.

While the shapes of  $^{40,42}\text{S}$  can be understood with the mean field calculations of Werner *et al.* [17] which attempt to account for changes in single particle binding energies and residual interactions away from the line of stability, the data for all nuclei measured here except  $^{46}\text{Ar}$  can also be explained with shell model calculations

which use empirical interactions obtained from nuclei close to the stability line. These calculations were carried out in a model space in which the protons occupy the  $0d_{5/2}$ ,  $0d_{3/2}$  and  $1s_{1/2}$  ( $sd$ ) orbitals and the neutrons occupy the  $0f_{7/2}$ ,  $1p_{3/2}$ ,  $0f_{5/2}$  and  $1p_{1/2}$  ( $pf$ ) orbitals. For many of the nuclei under consideration the dimension of the full  $\pi(sd)-\nu(pf)$  model space is too large, and the calculations reported here have been truncated by leaving out the  $0f_{5/2}$  and  $1p_{1/2}$  neutron orbitals. With this truncation the dimension for the  $2^+$  state in  $^{42}\text{S}$  is 4335. For some nuclei such as  $^{48}\text{Ca}$  and  $^{46}\text{Ar}$ , this truncation can be compared to those performed in a model space which includes the  $0f_{5/2}$  and  $1p_{1/2}$  orbitals, and the results for the orbital occupations and excitation energies of the  $2^+$  states are found to be very similar. The Wildenthal  $sd$ -shell interaction [30], the recent FPD6  $pf$ -shell interaction [31] and the WBMB  $sd-pf$  cross-shell interaction [32] was used. This latter cross-shell interaction successfully accounts for the properties of the  $N = 20 - 22$  nuclei including the intruder state deformation in  $^{32}\text{Mg}$  [32]. The model space used and interactions are illustrated in figure 3.19. The  $B(E2)$  values were calculated using proton and neutron effective charges of  $e_p = 1.35e$  and  $e_n = 0.65e$ , respectively, which were chosen to reproduce the E2 transition strengths of the proton  $sd$ -shell transitions in  $^{36}\text{S}$  and  $^{38}\text{Ar}$  [25] and neutron  $pf$ -shell transitions in  $^{48}\text{Ca}$  [33].

In the top two panels of Fig. 3.20, the measured  $\beta_2$  values are compared to the results of the mean field calculations of Werner *et al.* and the present shell model calculations. The mean field calculations slightly underpredict the measured values for  $^{40,42}\text{S}$  and the shell model calculations slightly overpredict  $\beta_2$  for these nuclei. However, the shell model calculation predicts that the  $\beta_2$  value of  $^{46}\text{Ar}$  is *larger* than that of  $^{44}\text{Ar}$ , contrary to the downward trend in the data, which can be explained by the persistence of the  $N = 28$  shell closure. The increase in  $B(E2)$  for the shell-model calculation is related to the crossing of the  $0d_{3/2}$  and  $1s_{1/2}$  proton orbitals

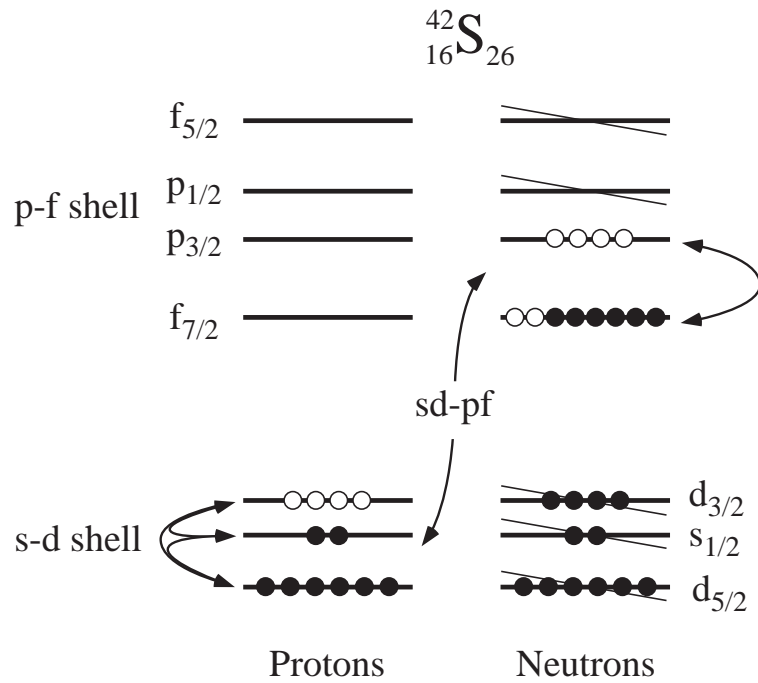


Figure 3.19: Shell model space and interactions. The protons occupy the  $\pi(\text{sd})$  shell and the neutrons the  $\nu(\text{pf})$  shell. The model space was truncated in the calculations and the  $\nu 0f_{5/2}$  and  $\nu 1p_{1/2}$  orbitals have been left out. The arrows indicate the interactions used. The s- and p-shells below the sd-shell are not shown and are filled with 8 particles.

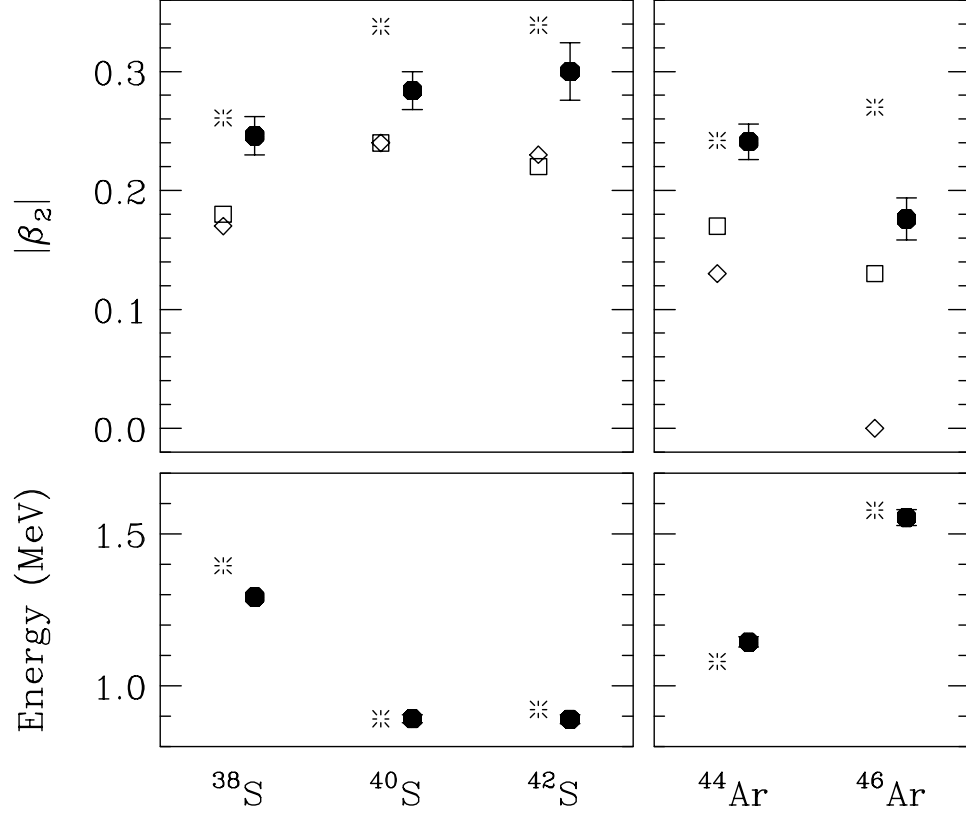


Figure 3.20: The top two panels compare the experimental quadrupole deformation parameters  $|\beta_2|$  (solid points) to shell model calculations (stars) described in the text, relativistic mean field calculations (open diamonds) and Hartree-Fock (open squares) calculations. The bottom two panels compare the experimental excitation energies  $E(2^+)$  (solid points) to the shell model calculations (stars).

observed between  $^{35}\text{K}$  (which has a  $3/2^+$  ground state [25]) and  $^{37}\text{K}$  (which has a  $1/2^+$  ground state [25]). The bottom two panels of figure 3.20 show that the shell model calculations successfully reproduce the energies  $E(2_1^+)$  in the nuclei reported here.

The results presented demonstrate that a direct measurement of  $B(E2; 0_{g.s.}^+ \rightarrow 2_1^+)$  is necessary to determine the nuclear collectivity, which is interpreted in terms of the deformation, and that the energies of the  $2_1^+$  states (without the  $B(E2)$  values) are not sufficient to deduce the deformation on the basis of systematics. For example, the global systematics of Raman *et al.* [34] give  $\beta_2 = 0.4$  from the energies of the  $2_1^+$  states in  $^{40,42}\text{S}$ . The experimental  $\beta_2$  deformations are significantly smaller.

secondary beam	<sup>38</sup> S	<sup>40</sup> S	<sup>42</sup> S	<sup>44</sup> Ar	<sup>46</sup> Ar
Energy (MeV/nucleon)	39.2	39.5	40.6	33.5	35.2
Beam purity	0.99	0.65	0.55	0.99	0.99
Typical intensity on target (s <sup>-1</sup> )	50,000	17,000	1,800	50,000	27,000
Target thickness/(mg/cm <sup>2</sup> )	184.1	184.1	184.1	93.5	93.5
Energy loss in target (MeV/nucleon)	9.1	8.4	7.9	5.1	4.9
Beam velocity (c)	0.269	0.271	0.276	0.254	0.262
$\theta_{cm}^{max}$	4.916	4.958	5.003	5.041	5.085
Efficiency (%)	4.66	7.24	7.28	5.36	3.75
Energy of first excited state (keV)	1286(19)	891(13)	890(15)	1144(17)	1554(26)
$\sigma(E2; 0_{g.s.}^+ \rightarrow 2_1^+, \theta_{lab} \leq 4.1^\circ)$ (mb)	59(7)	94(9)	128(19)	81(9)	53(10)
$B(E2; 0_{g.s.}^+ \rightarrow 2_1^+)$ (e <sup>2</sup> fm <sup>4</sup> )	235(30)	334(36)	397(63)	345(41)	196(39)
$ \beta_2 $	0.246(16)	0.284(16)	0.300(24)	0.241(14)	0.176(17)

Table 3.3: Experimental parameters and results. The purity of the secondary beam is for reference only; the secondary fragments were positively identified on an event by event basis and only desired fragments were analyzed. The energy spread of the secondary beam was  $\pm 3\%$ .

In summary, the energies and  $B(E2; 0_{g.s.}^+ \rightarrow 2_1^+)$  values of the  $2_1^+$  states of <sup>38,40,42</sup>S and <sup>44,46</sup>Ar have been measured using intermediate-energy Coulomb excitation. The isotopes <sup>40,42</sup>S are deformed, indicating the presence of a new region of deformed nuclei near  $N = 28$ . The data on the  $2_1^+$  state in <sup>46</sup>Ar demonstrate that the  $N = 28$  major shell gap persists at  $Z = 18$ . Both the mean field calculations and shell model calculations using empirical interactions can approximately reproduce the behavior of the  $2_1^+$  states of <sup>40,42</sup>S.

# Chapter 4

## Direct Reactions

In this chapter a short introduction to direct nuclear reactions is given. The main references are [35, 1, 36].

When a nucleon collides with a nucleus it can penetrate into the nucleus and form a compound system. These are compound nucleus reactions. On the other hand, nuclei have a relatively sharp surface, and it is likely that the incoming nucleon collides with a single nucleon, or a normal mode of nuclear motion, and the residual particle (which could be the same as the incoming particle as in elastic scattering or some other reaction product) escapes immediately. This kind of reaction is called a direct reaction because usually only a single (direct) interaction is involved in the scattering process.

Since in a direct reaction no intermediate system is formed, the wavefunctions of the initial and final states overlap, and useful information on the initial configuration can be obtained from the final state.

In order to extract nuclear structure information from direct reactions, the reaction dynamics has to be known. Cross sections depend on a nuclear matrix element, which contains both the wavefunctions of the nuclear states and the effective two-body interaction  $V_{\text{eff}}$  mediating the transition between these states. Consequently, a priori

knowledge of the effective interaction is necessary in order to use direct reactions as a spectroscopic tool [37, 38]. Two approaches have been devised to obtain  $V_{\text{eff}}$ . One approach is empirical and discussed briefly in section 4.1.2. The other is entirely theoretical and is outlined in section 4.1.3.

Direct reactions can further be classified as *inelastic scattering* (e.g.  $(p, p')$ ), as *stripping* (e.g.  $(d, p)$ ) or *pick-up* (the inverse of stripping, e.g.  $(p, d)$ ) reactions, and as *knock-out* (e.g.  $(p, p'p'')$ ) reactions. Each of these reactions has particular advantages for the study of certain aspects of nuclear structure. Stripping (or pick-up) as well as knock-out reactions are useful in studying the single particle nature of nuclei; in particular spectroscopic factors can be obtained.

Inelastic scattering, on the other hand, is particularly effective in exciting collective states. One can imagine that the incoming projectile touches the nuclear surface and brings the drop (using the liquid drop model) into a state of oscillation, or if the nucleus is deformed, makes it rotate. The excitation cross section is then dependent on the degree of collectivity of the nucleus. A deformed nucleus (or a nucleus soft against vibration) is easy to excite, in contrast to a spherical (closed shell) nucleus. The results are somewhat model dependent, mainly because the projectile and the target interact strongly and perturbative methods can hardly be applied. In contrast, Coulomb excitation (see chapter 2) is well understood and largely model independent, giving very reliable results.

Coulomb excitation is only sensitive to the protons in the nucleus, and a different experimental probe is needed to get information on the neutrons. Because of the Pauli principle, the like-nucleon interaction is about 3 times weaker than the unlike-nucleon interaction in a nucleus. Therefore proton scattering  $(p, p')$  in the energy range of  $E/A \approx 10 - 50$  MeV, which corresponds to typical kinetic energies of nucleons in a nucleus, is mostly sensitive to the neutrons [3]. Information on both the neutron

and the proton motion can be obtained by comparing the two experimental probes. Section 4.2.3 shows how the ratio of the neutron and proton matrix elements  $M_n/M_p$  can be extracted.

## 4.1 Elastic Scattering

The simplest interaction between an incident particle and a target nucleus is elastic scattering. The particle's direction of motion and/or state of polarization is changed, without loss of kinetic energy.

### 4.1.1 Optical Model

Direct or shape elastic scattering occurs when the incident particle interacts with the nucleus as a whole. This interaction can be described fairly well by an average nucleon-nucleus interaction as single absorbing potential well: the optical potential

$$V(r) = (U + iW)f(r) . \quad (4.1)$$

$U$  and  $W$  are the real and imaginary parts of the potential and  $f(r)$  is a Woods-Saxon form factor. This form is usually not sufficient to describe the elastic scattering data and surface  $W_D$  and spin-orbit  $V_{SO}$  terms are introduced.

$$V(r) = V_C(r) - V \cdot f(x_0) - i \left\{ W \cdot f(x_w) - 4W_D \frac{d}{dx_D} f(x_D) \right\} + \left( \frac{\hbar}{m_\pi c} \right)^2 V_{SO} (\mathbf{L} \cdot \boldsymbol{\sigma}) \frac{1}{r} \frac{d}{dr} f(x_{SO}) , \quad (4.2)$$

where

$$V_C(r) = \begin{cases} \frac{Z_t Z_p e^2}{r} & \text{for } r \geq R_C \\ \frac{Z_t Z_p e^2}{2R_C} \left( 3 - \frac{r^2}{R_C^2} \right) & \text{for } r \leq R_C . \end{cases} \quad (4.3)$$

$V_C(r)$  is the Coulomb electrostatic potential of a uniformly charged sphere of radius  $R_C = r_C A^{\frac{1}{3}}$ . The other terms in equation 4.2 are the real, imaginary, and spin-orbit

parts of the optical potential. The form factors  $f(x_i)$  are given in Woods-Saxon form

$$f(x_i) = \frac{1}{1 + e^{x_i}} \quad \text{with} \quad x_i = \frac{r - r_i A^{\frac{1}{3}}}{a_i}, \quad (4.4)$$

even though other functions can in principle be used.  $a_i$  is called the diffuseness parameter. Approximate values for the parameters are  $a \approx 0.6$  fm,  $r \approx 1.2$  fm,  $V \approx 50$  MeV,  $W \approx 10$  MeV, and  $V_{SO} \approx 8$  MeV (see [36]).

The real part of the optical potential describes the refraction of the incoming wave and the imaginary part takes into account all non-elastic processes through absorption.

This potential is inserted into the Schrödinger equation

$$\nabla^2 \Psi + \frac{2m}{\hbar^2}(E - V)\Psi = 0, \quad (4.5)$$

whose solution is expressed in the form of an incoming plane wave plus an outgoing spherical wave

$$\Psi \propto e^{ikz} + \frac{e^{ikr}}{r} f(\theta), \quad (4.6)$$

and hence the (elastic) differential cross section is given by

$$\frac{d\sigma}{d\Omega} = |f(\theta)|^2. \quad (4.7)$$

Practically one obtains the scattering amplitude  $f$  from the phase-shifts  $\delta_L$

$$f(\theta) = \frac{1}{2ik} \sum_L (2L + 1)(e^{2i\delta_L} - 1)P_L(\cos(\theta)). \quad (4.8)$$

Here,  $P_L(x)$  are the Legendre Polynomials. Calculations are done numerically. A very powerful computer code, which was used in this analysis, is ECIS [39].

### 4.1.2 Effective Optical Potentials

The usual procedure is to adjust the parameters of the optical potential (potential depths, radii, and diffusenesses), as given in equation 4.2, until the calculation agrees

	strength $V, W$ (MeV)	radius $r$ (fm)	diffuseness $a$ (fm)
$V$	$54.0 - 0.32E + 0.4Z/A^{1/3} + 24(N - Z)/A$	1.17	0.75
$W$	$0.22E - 2.7$	1.17	0.75
$W_D$	$11.8 - 0.25E + 12.0(N - Z)/A$	1.32	$0.51 + 0.7(N - Z)/A$
$V_{so}$	6.2	1.01	0.75

Table 4.1: Becchetti-Greenlees optical potential parameters [40] for elastic proton scattering.

with the measurement. Often several sets of parameters reproduce the measured elastic cross section equally well, and the nuclear structure information extracted is model dependent. However, if data are available for neighboring nuclei, one can demand that the optical parameters vary slowly as one changes neutron number, proton number, and beam energy. A comprehensive analysis of a wide range of proton-scattering data for energies  $E_p$  below 50 MeV and  $A \geq 40$  was performed by Becchetti and Greenlees [40]. The optical parameters in their work were parameterized in terms of the neutron number  $N$ , proton number  $Z$ , and the incident lab energy of the proton  $E$ . The optimum parameters found in [40] are given in table 4.1.

The optical parameters obtained in this way are empirical and based on systematics for stable isotopes. Thus it is not clear if these parameters are applicable when investigating nuclei with large neutron excess. Also, the lowest mass number  $A$  that was included in Becchetti and Greenlees' fit around a proton laboratory energy of  $E_p \approx 30$  MeV was 56 which deviates considerably from the nuclei studied here.

### 4.1.3 Microscopic Optical Potentials

A more fundamental approach is given by Jeukenne, Lejeune, and Mahaux (JLM) [41]. The authors derived a complex microscopic optical potential based solely on nuclear matter calculations. The derived potential can reproduce proton elastic scattering angular distributions, provided that the imaginary potential is adjusted by a

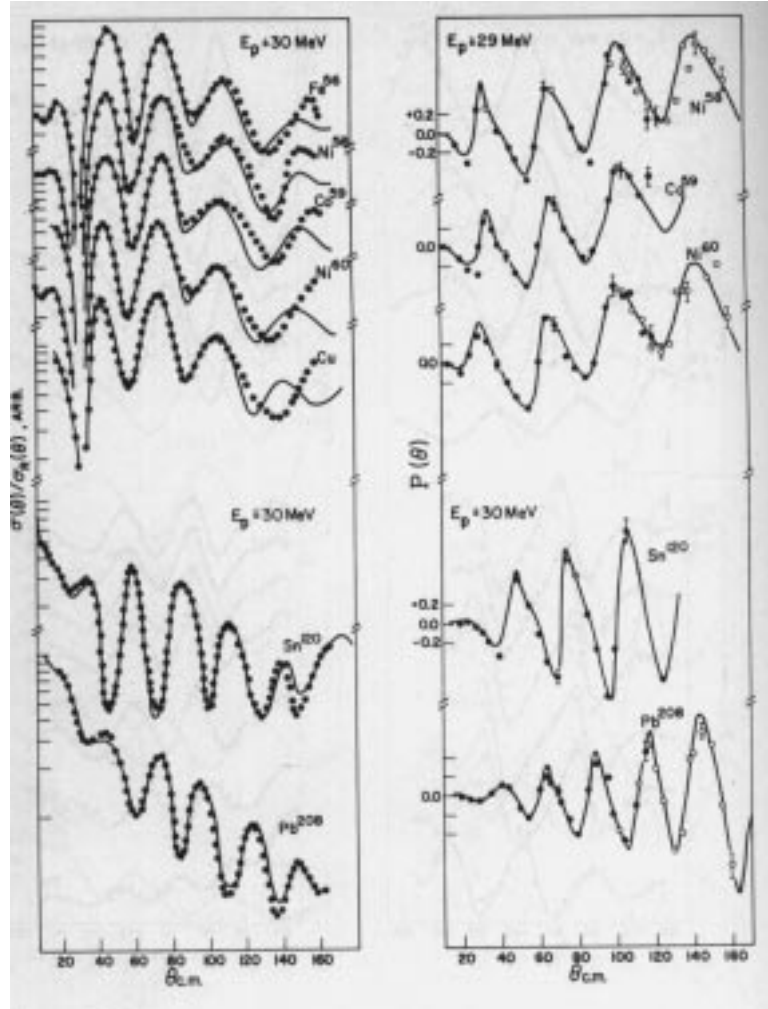


Figure 4.1: This figure shows the fit by Becchetti and Greenlees for the proton scattering cross sections on different targets around  $E_p = 30$  MeV. The lowest mass number included in this energy range was 56.

normalization  $\lambda_w$  of about 0.8 [42].

The main idea in the JLM approach is to fold a more or less well known nucleon nucleon interaction  $u$  with calculated nuclear densities  $\rho$  resulting in a potential

$$V(r) = \int \rho(r_1)u(|\mathbf{r} - \mathbf{r}_1|)dr_1^3. \quad (4.9)$$

The subtleties lie in the determination of the different parts of the optical potential, such as the real volume and surface terms, and imaginary terms. (see [41]).

With the cost of computing power becoming rapidly decreasing, realistic density calculations have become possible. Recent theoretical advances give promising results. For instance Kelley *et al.* [43] measured the elastic and inelastic proton scattering cross section on the radioactive isotope  $^{38}\text{S}$ . The cross sections were interpreted by fitting the data using the Becchetti-Greenlees optical parameters and applying the prescription by Bernstein [3] to obtain the ratio of neutron to proton matrix elements (see section 4.2.3). The resulting  $M_n/M_p$  is 2.06, which is unreasonably large (see section 4.2.3). A different analysis was performed on the same data by Alamanos *et al.* [44]. They used the JLM method with nuclear matter and transition densities obtained from shell model calculations. The resulting  $M_n/M_p$  is 1.58, which is much closer to the expected value of  $N/Z = 1.37$ . A possible source for the discrepancy of the two methods is that especially for the neutron rich isotopes the neutron and proton densities, and hence the corresponding potentials, have different root mean square radii. This difference is not included in standard Woods-Saxon form factors, which are the same for both neutrons and protons.

One might conclude that the use of an average phenomenological potential of Woods-Saxon form is inadequate for studies of neutron rich nuclei, since the microscopic approach seems to give more reliable results.

## 4.2 Inelastic Scattering

Inelastic scattering occurs when the projectile interacts with the target leaving either the target or the projectile in an excited state. Energy is removed from the relative motion of the two particles and transformed into energy of the intrinsic motion of either particle.

There are two simple pictures of this process. In terms of the single particle shell model one can think of a single nucleon lifted into a higher shell, whereas in the collective picture the scattered particle induces as surface vibration or a rotation if the nucleus is statically deformed.

In this work we are interested in the second picture and the theoretical interpretation is done using the coupled channel formalism.

### 4.2.1 Coupled Channels

The Schrödinger equation for the whole system of two colliding particles, represented by the wavefunction  $\Psi(r, \xi)$ , is [36]

$$(T - V(r, \xi) + H(\xi))\Psi(r, \xi) = E\Psi(r, \xi) . \quad (4.10)$$

The (intrinsic) nuclear states  $\chi$  are defined by

$$H(\xi)\chi_\alpha(\xi) = \epsilon_\alpha\chi_\alpha(\xi) , \quad (4.11)$$

where  $\alpha$  labels the intrinsic states. The total wavefunction (including the relative motion) can then be written as a superposition of the intrinsic states

$$\Psi(r, \xi) = \sum_{\alpha} \psi_{\alpha}(r)\chi_{\alpha}(\xi) , \quad (4.12)$$

where the sum  $\alpha$  goes over all states of the nucleus (discrete and continuum). The coefficients of the expansion depend on the relative position of the two nuclei. Inserting

4.11 and 4.12 into equation 4.10 yields

$$(T - E + \epsilon_\alpha)\psi_\alpha(r) = \sum_{\alpha'} V_{\alpha\alpha'}\psi_{\alpha'}(r) , \quad (4.13)$$

with

$$V_{\alpha\alpha'} = \int \chi_\alpha^*(\xi)V(r, \xi)\chi_{\alpha'}(\xi)d\xi . \quad (4.14)$$

Equation 4.13 constitutes as set of coupled equations for the wavefunction of the elastic and *all* inelastic channels.

In practice one can only include a few of the inelastic channels in the calculation and one compensates for the neglected channels by letting the interaction potential be complex.

In our case, only two states have been included: the ground state and the first excited  $2^+$  state.

## 4.2.2 Nuclear Deformation

The interaction potential  $V(r, \xi)$  depends on the character of the excited state. For example, a statically deformed nucleus can be described by a potential that depends on the orientation of the nucleus

$$V = V(r - R(\theta, \phi)) \quad \text{and} \quad R(\theta, \phi) = R_0(1 + \beta Y_2^0(\theta, \phi)) , \quad (4.15)$$

where  $\beta$  is the deformation parameter. Hence,

$$V = V(r - R_0) - \beta R_0 Y_2^0(\theta, \phi) \frac{dV}{dr} . \quad (4.16)$$

The first term is the usual spherical optical potential, and the second term describes coupling between the incident and outgoing (inelastic) channels.

### 4.2.3 $M_n/M_p$

In order to compare the neutron to the proton motion, one calculates  $M_n/M_p$ , which is the ratio of the neutron to proton matrix elements, which defined as

$$\begin{aligned} M_{n(p)} &= \langle J_f || \sum_{n(p)} r_i^\lambda Y_\lambda(\Omega_i) || J_i \rangle \\ &= \int_0^\infty \rho_{f_i}^{n(p)}(r) r^{\lambda+2} dr, \end{aligned}$$

where  $\rho_{f_i}^{n(p)}$  are the neutron (proton) transition densities. The  $B(E\lambda)$  value is related to the proton matrix element through

$$B(E\lambda, J_i \rightarrow J_f) = \frac{|M_p|^2}{2J_i + 1}. \quad (4.17)$$

$M_n/M_p$  can be obtained by a comparison of a hadronic probe (in this case proton scattering) with an electromagnetic probe (Coulomb excitation) via a description by Bernstein *et al.* [3]

$$\begin{aligned} \frac{M_n}{M_p} &= \frac{b_p}{b_n} \left( \frac{\delta_{(p,p')}}{\delta_{em}} \left( 1 + \frac{b_n N}{b_p Z} \right) - 1 \right) \\ &= \frac{b_p}{b_n} \left( \frac{\delta_{(p,p')}}{\delta_{em}} - 1 \right) + \frac{\delta_{(p,p')}}{\delta_{em}} \frac{N}{Z} \\ &= \frac{N}{Z} \left( \frac{\delta_{(p,p')}}{\delta_{em}} + \frac{Z b_p}{N b_n} \left( \frac{\delta_{(p,p')}}{\delta_{em}} - 1 \right) \right). \end{aligned} \quad (4.18)$$

Here,  $b_{n(p)}$  are the relative sensitivities of the (hadronic) probe to the neutrons (protons) in the nucleus and  $\delta_{em}$  and  $\delta_{(p,p')}$  are the deformation lengths ( $\delta = \beta R$ ) obtained via the electromagnetic probe and via  $(p, p')$ , respectively. The last equation can be interpreted in the following sense: The ratio of the matrix elements is equal to  $N/Z$  times a factor that is the ratio of the deformations measured via  $(p, p')$  and Coulomb excitation. Because of the different sensitivities of the probes a correction term has to be added, which is given as the relative difference of the deformations measured with the two probes. In other words, if  $(p, p')$  was a probe that is only sensitive to

the neutrons then  $b_p = 0$  and

$$\frac{M_n}{M_p} = \frac{N}{Z} \frac{\delta_{(p,p')}}{\delta_{\text{em}}} . \quad (4.19)$$

From the collective model one expects a ratio  $M_n/M_p = N/Z$ , since the neutron and proton liquids move in the same way. In contrast, one also expects deviations from this simple picture, especially in the vicinity of closed shells. A nucleus with a single closed shell should not yield a value of  $M_n/M_p = N/Z$ , since e.g. the neutrons form a spherical closed shell and hence  $M_n = 0$  [3]. However, core polarization restores the isoscalar character of the excitation to a large extent and brings  $M_n/M_p \sim N/Z$ , even for single closed shell nuclei [45]. Nevertheless a ratio  $M_n/M_p$  that deviates from  $N/Z$  is an indication of the importance of shell effects in the structure of these nuclei.



# Chapter 5

## Proton Scattering of $^{36,42,44}\text{Ar}$

The availability of high-intensity radioactive beams creates new possibilities in nuclear structure studies through the use of direct reactions in inverse kinematics. Specifically the neutron-rich sulfur and argon isotopes have become accessible through projectile fragmentation of  $^{48}\text{Ca}$ , as described in section 3.1.

Proton scattering in inverse kinematics was pioneered in an experiment by Kraus *et al.* [33], which measured the proton elastic and inelastic scattering on the  $\beta$ -unstable isotope  $^{56}\text{Ni}$ . The low energy of the recoiling protons limits the target thickness to about 2–4 mg/cm<sup>2</sup> and high beam intensities, of about  $10^4\text{s}^{-1}$ , are needed to perform the experiment in a reasonable amount of time (one or two days). Even with thin targets the energy resolution is only about 800 keV (FWHM). Since the nuclear states have to be resolved, an additional limit is put on the nuclei that can be studied. Usually in even-even nuclei the first excited  $2^+$  state is well separated from the ground state and other excited states. Here, we focused on the even-even isotopes  $^{42,44}\text{Ar}$ . As a check the  $N = Z$  nucleus  $^{36}\text{Ar}$  was also investigated [46, 47]. The  $^{36}\text{Ar}$  nucleus has equal numbers of protons and neutrons ( $N = Z$ ) and should yield a ratio  $M_n/M_p$  of unity by isospin symmetry [6].

The secondary beams of  $^{42,44}\text{Ar}$  were produced as described in section 3.2.1. The

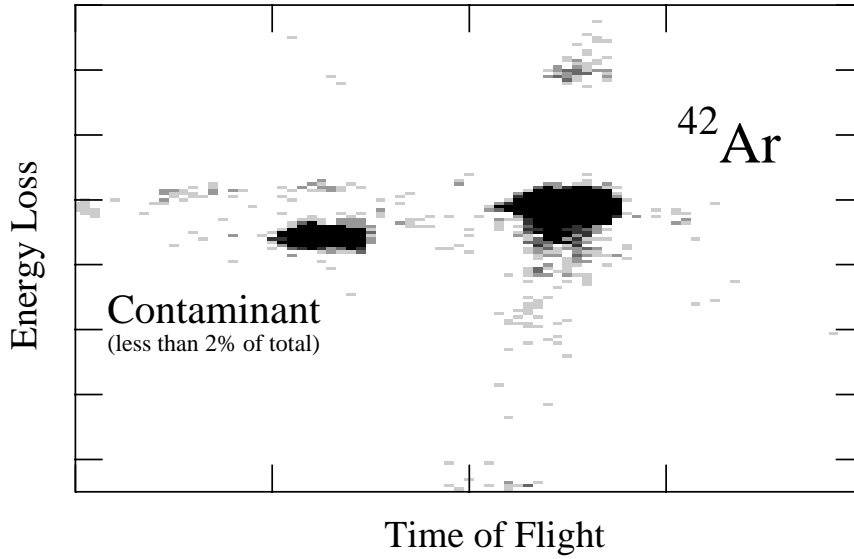


Figure 5.1: The incoming particles were identified according to their time of flight and energy loss in the fast scintillator of the zero degree detector. The desired beam, in this case  $^{42}\text{Ar}$ , and the contaminants are completely separated.

$^{36}\text{Ar}$  beam was produced directly in the K1200 cyclotron, where the beam was injected from the Superconducting Electron Cyclotron Resonance ion source. The beam energy was adjusted with the help of a variable degrader and the A1200. The beam energies for all three isotopes were about  $E/A = 33$  MeV. The exact values together with the target thicknesses and other experimental parameters are listed in table 5.2 on page 110.

## 5.1 Experimental Setup

The experimental setup in the S2 vault is schematically shown in figure 5.2. The incoming beam particles were tracked with two PPACs located 0.8 m and 1.8 m in front of the target. As in the Coulomb excitation experiment (chapter 3) the projectiles were identified according to their time of flight (TOF) as shown in figure 5.1.

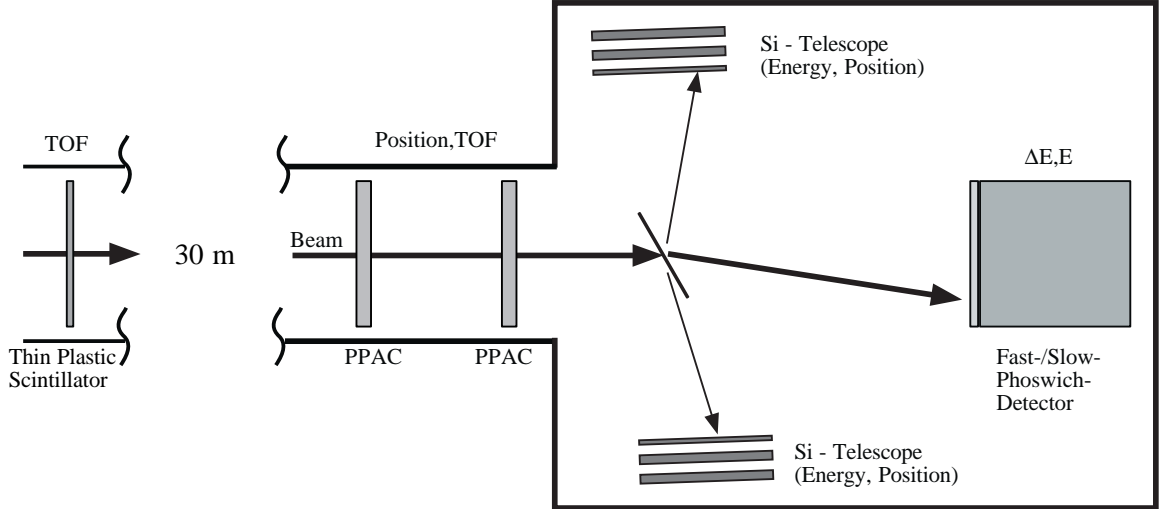


Figure 5.2: Setup around the secondary target for the  $(p, p')$  experiment.

The target, a  $2.7 \text{ mg/cm}^2$  polypropylene  $(\text{CH}_2)_n$  foil, was located close to the center of the NSCL 32" scattering chamber. It was oriented at an angle of  $60^\circ$  with respect to the beam axis, thus providing an effective target thickness of  $3.12 \text{ mg/cm}^2$ . The tilt of the target allows the protons, which are scattered toward angles of approximately  $80^\circ$  in the laboratory system, to easily escape from the target. The kinematics of the reaction is discussed in section 5.1.4.

The scattered beam particles were detected in a fast-slow phoswich detector and were identified as described in section 3.2.3, the only difference being that the detector had only one photo multiplier tube and had a smaller diameter of 3", which corresponds to scattering angles of about  $5^\circ$ . Typical projectile scattering angles are on the order of  $1^\circ$  (refer to the lower panel in figure 5.13) and therefore all scattered particles are detected.

### 5.1.1 Proton Detectors

The recoiling protons were observed in a set of four telescopes, each of which consisted of a silicon strip detector ( $300 \mu\text{m}$ ) followed by two silicon PIN detectors ( $500 \mu\text{m}$

each). The arrangement of the four telescopes is shown in figure 5.3. The telescopes were mounted at a distance from the target of about 23 cm. Telescopes 1 and 2 covered angles from  $\theta_{lab} = 67^\circ - 79^\circ$  and telescopes 3 and 4 covered angles from  $\theta_{lab} = 70^\circ - 82^\circ$ .

### **Position Sensitive Strip Detector**

The strip detectors were about  $300 \mu\text{m}$  thick (see table 5.1) and had, as all other detectors in the telescope, an active area of  $5 \times 5 \text{ cm}^2$ . One side of the strip detector was segmented into 16 resistive strips, whose resistance was about  $3 \text{ k}\Omega$  over the strip length of 5 cm. Each of these strips was read out on both ends, and the position of the incident proton was reconstructed from the two signals assuming charge division. Thus the detector provided position information in 2 dimensions, where the direction perpendicular to the strips was given by the strip number itself. Within a strip the measured position resolution was about 0.5 mm for a 5 MeV signal. This should be compared to the strip width of about 3.1 mm. The telescopes were mounted so that lines of constant  $\theta$  were roughly perpendicular to the strips. Therefore a much better angular ( $\theta$ ) resolution was achieved as compared to an orientation with the strips along the lines of constant  $\theta$  (better by a factor of  $3.1/0.5$  at 5 MeV). Angular resolution is crucial for the distinction of elastic from inelastic scattering. The unsegmented back side of the detector was used to obtain an energy signal. Figure 5.4 shows a schematic of the telescope and the working principle of the strip detector.

### **Silicon PINs**

Since protons with an energy of more than about 6 MeV were not stopped in the  $300 \mu\text{m}$  thick strip detector, it is followed by two  $500 \mu\text{m}$  thick silicon PINs. These three silicon detectors stopped protons up to an energy of about 14 MeV. The com-

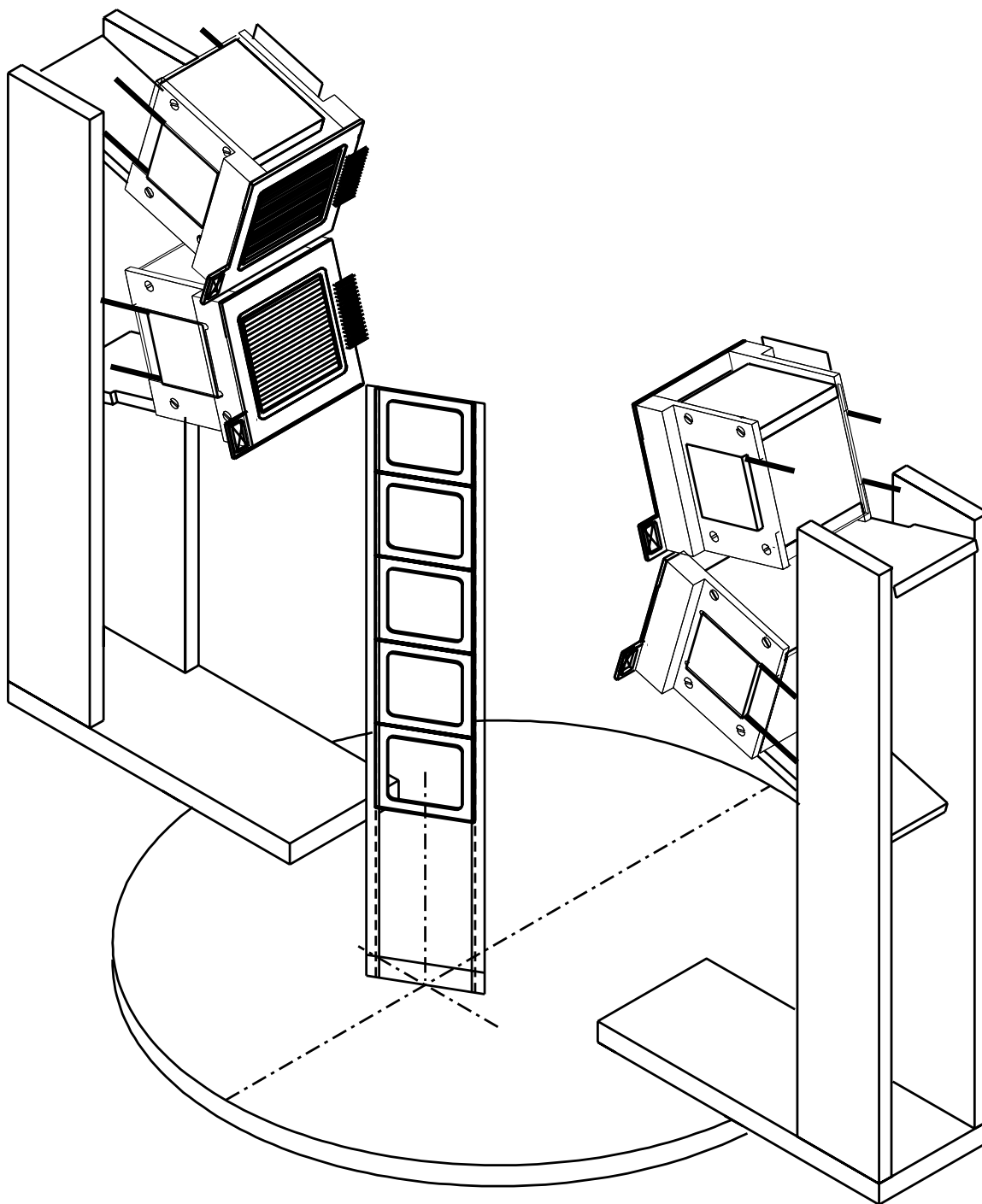


Figure 5.3: Schematic 3D view of the setup around the secondary target for the  $(p, p')$  experiment. The beam is going from left to right. The telescopes are labeled from one through four starting with the top right-hand telescope and counting clockwise. Telescopes one and two cover the same scattering angles, as do three and four.

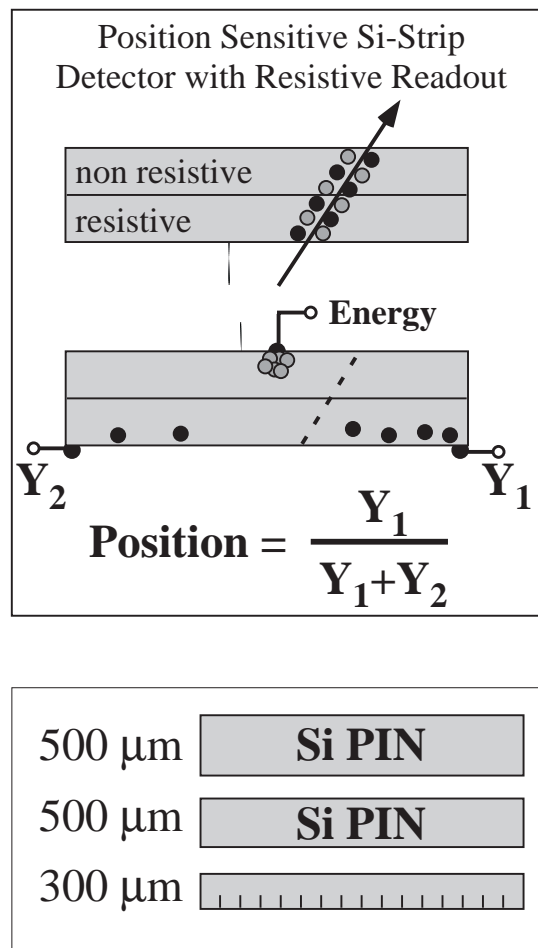


Figure 5.4: Position sensitive silicon detector telescopes. The telescope composition is shown in the bottom part and a schematic of the operating principle of the strip detector is shown in the top part.

Telescope	Strip	PIN 1	PIN 2
1	305	471	475
2	296	467	464
3	299	462	469
4	301	462	476

Table 5.1: Detector thicknesses in  $\mu\text{m}$ .

bination of the three signals allowed the identification of protons that had a higher energy and thus were not stopped. This was achieved by comparing the proton energy deduced from the measured energy loss in the first two detectors ( $E_{\text{from\_E2}}$ ), with the sum of all detectors ( $E3$ ). If  $E_{\text{from\_E2}}$  was equal to  $E3$  then the proton had been stopped in the third detector and the total proton energy was given by  $E3$ . If, on the other hand,  $E3$  was not equal to  $E_{\text{from\_E2}}$  then the proton had passed through all silicon detectors and the proton energy was reconstructed from the energy loss in all three detectors, using the known relation between the proton range in silicon as a function of energy [48]. In order to reconstruct the proton energy from the energy loss the detector thicknesses had to be known. They are listed in table 5.1.

### Energy and Position Calibration

All proton detectors were calibrated with a  $^{228}\text{Th}$   $\alpha$ -source. Figure 5.5 shows the  $\alpha$ -energy spectrum measured with one of the silicon PINs. Indicated in the plot are the  $\alpha$ -energies and the corresponding parent nuclei. The peak centroids and errors were obtained by fitting the sum of a Gaussian and a skew Gaussian to the spectra. The skew Gaussian (an exponential tail convoluted with a Gaussian resolution) fits the low-energy tail that can be observed in figure 5.5. A sample calibration curve is shown in figure 5.6.

The position along the strips of the strip detectors was calibrated using a mask containing a set of 1 mm wide slits separated by a center-to-center distance of 6 mm.

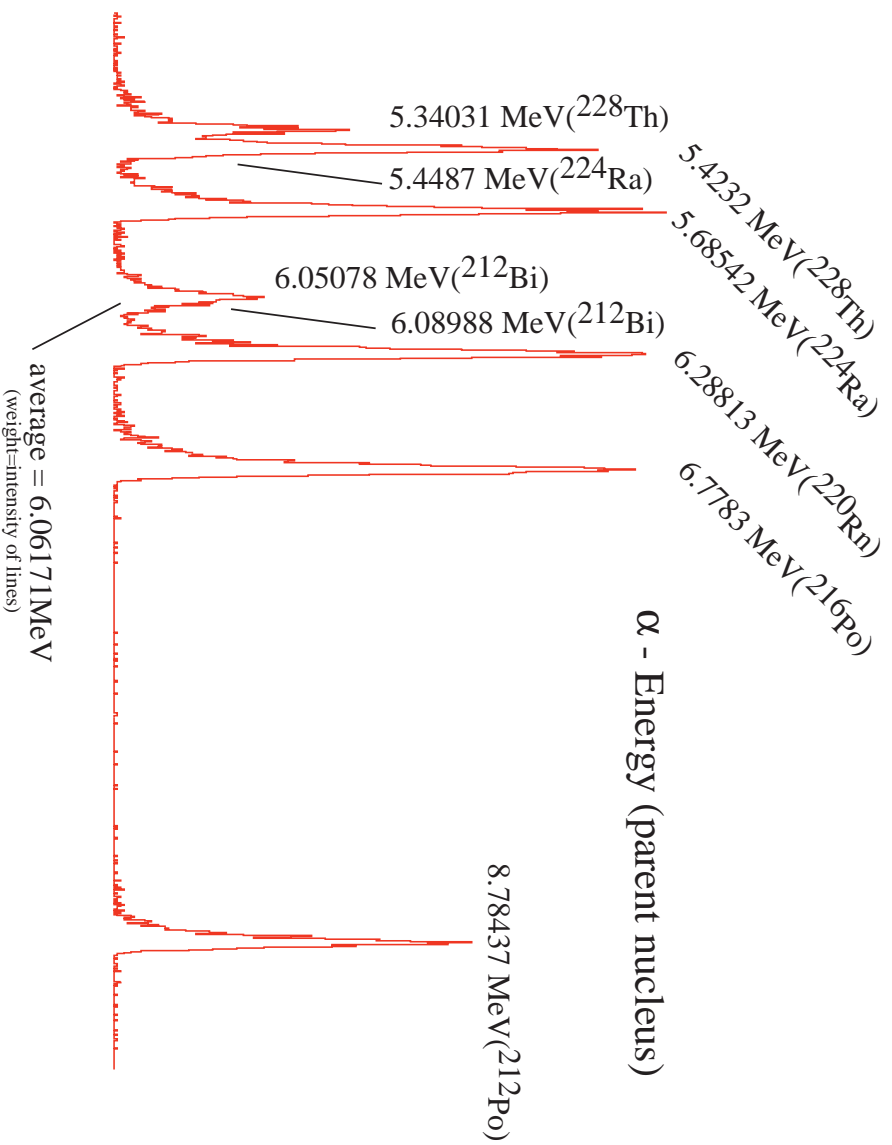


Figure 5.5: A  $^{228}\text{Th}$   $\alpha$ -source was used for the energy calibration of the silicon detectors. The  $\alpha$  energies and the corresponding parent isotopes are indicated.

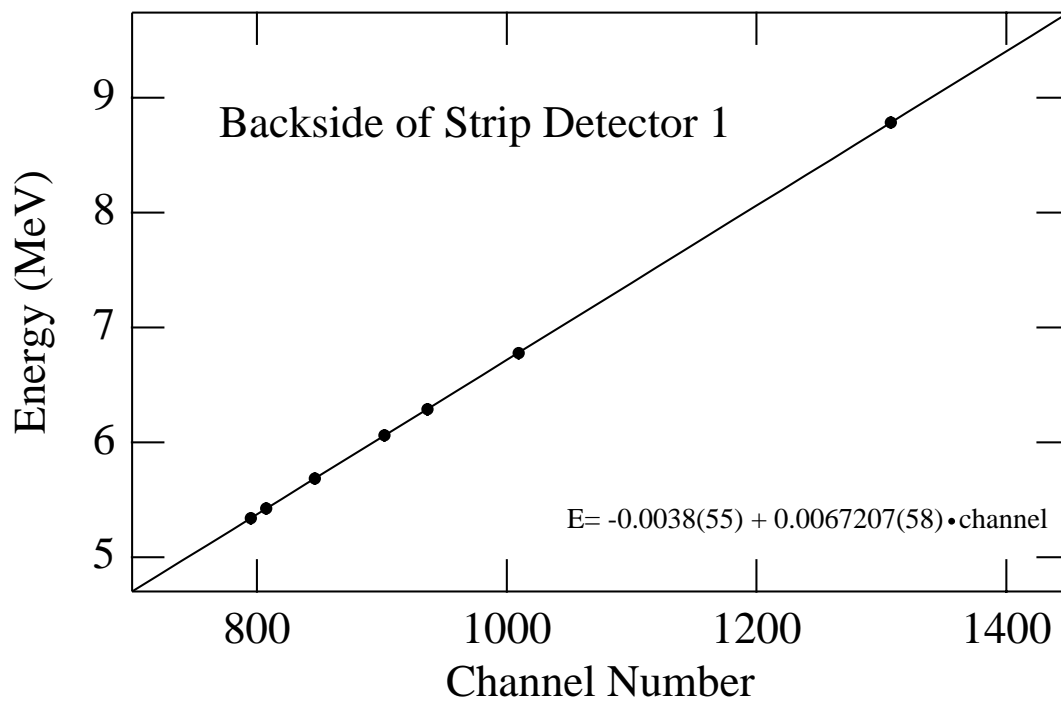


Figure 5.6: Energy calibration of strip detector backside for telescope 1. A linear fit is shown in addition to the data points. The error bars on the data points are smaller than the size plotted symbol.

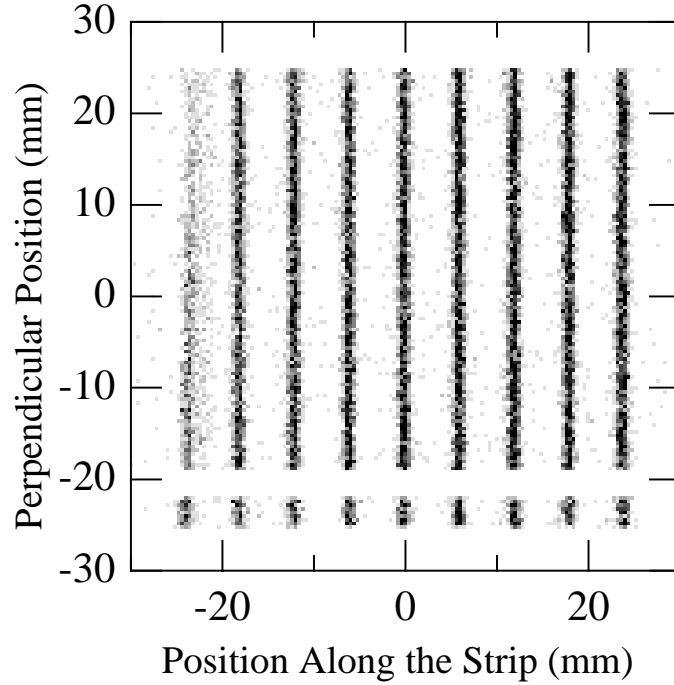


Figure 5.7: Position calibration of the strip detector. The position perpendicular to the strips was randomized. One strip was not working properly and was excluded from the analysis. The distance between the 1 mm wide slits in the mask is 6 mm (center-to-center).

A raw position was calculated from the two measurements on either end of a single strip as  $x = y_A/(y_A + y_B)$ , where  $y_{A,B}$  are the measured signals. The true position was obtained by fitting the raw positions, measured with the calibration mask, to the true position using a 3rd order polynomial. A calibrated 2D position spectrum, with the mask on the detector is shown in figure 5.7.

### Proton Identification

Protons with an energy of more than 6 MeV and less than 14 MeV passed through the strip detector and were stopped in either the first or the second PIN. Figure 5.8 shows the energy loss in the individual detectors as a function of proton energy. This allows the identification of protons through the  $\Delta E-E$  method illustrated in figure 5.9 (lower panels). Proton bands can be seen clearly. Protons with an energy of less than

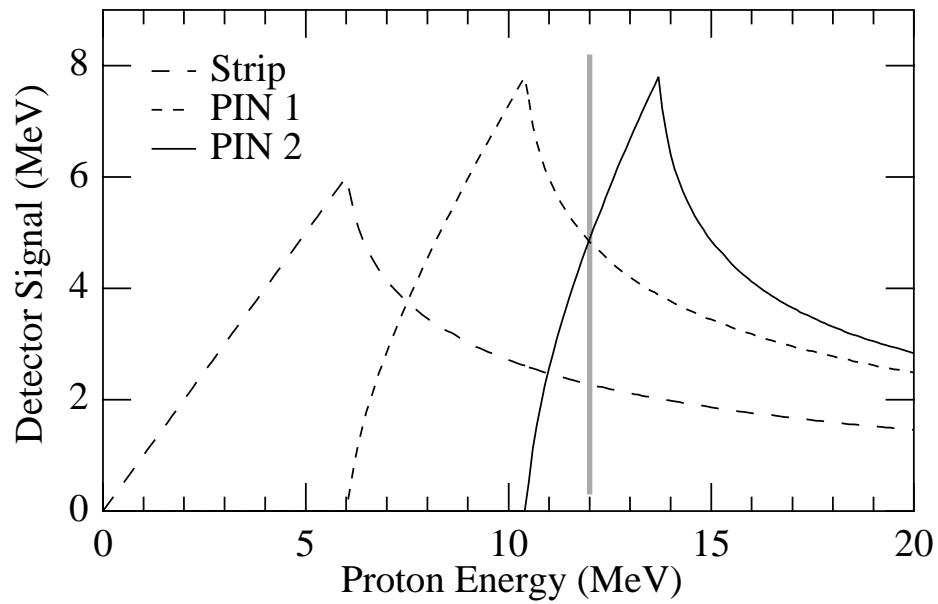
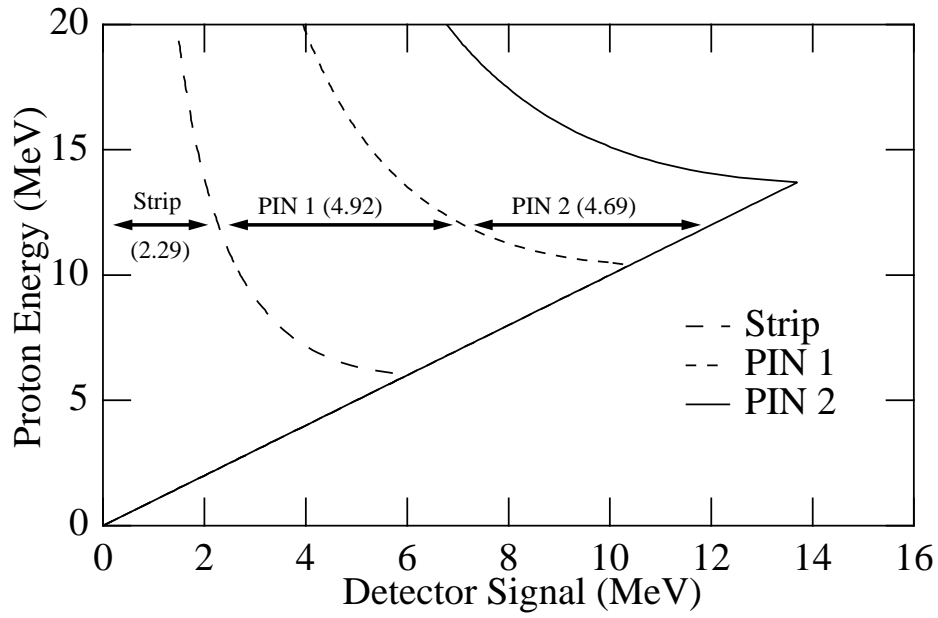


Figure 5.8: Signals that are registered by the individual detectors in the telescope as a function of proton energy. As an example, a 12 MeV proton will lose 2.3 MeV in the strip detector, 4.9 MeV in the first PIN, and 4.7 MeV in the second PIN.

6 MeV were stopped in the strip detector and they could therefore not be identified by the previous method. However, their time of flight (TOF) to the strip detector was measured and different isotopes can be identified using a E–TOF matrix. This is shown in the top right-hand panel of figure 5.9. The time resolution of 2 ns did not allow a complete separation of the different isotopes, but the band structure can be observed.

In order to remove all non-proton events from the analysis the identification of the scattered *beam* particle in the zero degree detector was required. As can be seen in the left-hand panel of figure 5.9, this condition alone removes almost all non-proton background.

This can be understood by considering the possible reactions that lead to particles other than protons being emitted into laboratory angles  $\theta_{lab}$  around  $80^\circ$ . One possibility is the occurrence of violent reactions on the carbon nuclei in the target. These reactions, however, lead to the breakup of the projectile and hence are rejected by the requirement of observing the beam particle after the target. Nucleon transfer reactions such as (p,d),(p,t), and (p, $^3,^4\text{He}$ ). can not produce the non-proton background since they are very forward focused because of the negative  $Q$ -value. (The total kinetic energy has decreased by  $|Q|$ , which is on the order of several MeV.) For instance, the  $Q$ -value for the reaction  $p(^{36}\text{Ar}, ^{35}\text{Ar})d$  is  $Q = -13$  MeV and from equation C.20 a maximum possible scattering angle for the deuteron in the laboratory of around  $\theta_{lab}^{\max} = 32^\circ$  is inferred. Hence these particles can not hit the detectors that are mounted around  $\theta_{lab} = 80^\circ$ .

The groups of events marked **A** and **B** in the left-hand panels in figure 5.9, which are disconnected from the proton bands, are protons that miss the last PIN (**B**) or the first PIN (**A**). These protons enter the telescope close to the edge of the detector and not perpendicular to the detector plane. Consequently, it is possible to traverse

the strip detector and miss the PIN, which is located about 5 mm behind the strip detector. The energy for these events has been reconstructed from the measured energy loss.

### 5.1.2 Beam Particle Tracking

Beam particle tracking before the target is essential for an accurate determination of the scattering angle, which in turn is needed to distinguish elastic from inelastic scattering. The tracking detectors were calibrated using a hole mask with a grid of 2 mm diameter holes separated by a center-to-center distance of 1 cm. At the center of the mask was an additional fine grid with 1 mm diameter holes separated by 2.5 mm. A sample calibration spectrum is shown in figure 5.10.

#### New Tracking Method

Unfortunately the in-beam position resolution of the PPACs was not as good as expected. The reason was an (unexplained) strong rate dependence of the position signal from one of the detectors. A test with an  $\alpha$ -source, prior to the experiment, gave a resolution of about 2 mm (FWHM). With the beam, at a rate of about 30,000 particles/s, the resolution deteriorated to about 8 mm for PPAC 1 and to about 3.5 mm for PPAC 2. With these resolutions it would have been impossible to separate the first excited state from the ground state in telescopes 3 and 4, which depend more on good tracking than telescopes 1 and 2 because of the orientation of the target. The target was rotated, so that the lowest energy protons could traverse the smallest target thickness. Thus the normal to the target surface should point as much as possible towards telescopes 3 and 4 which will see the lowest energy protons, since these telescopes are located at larger laboratory angles. This however means that a good position resolution of the tracking detectors is crucial, since a small change in the

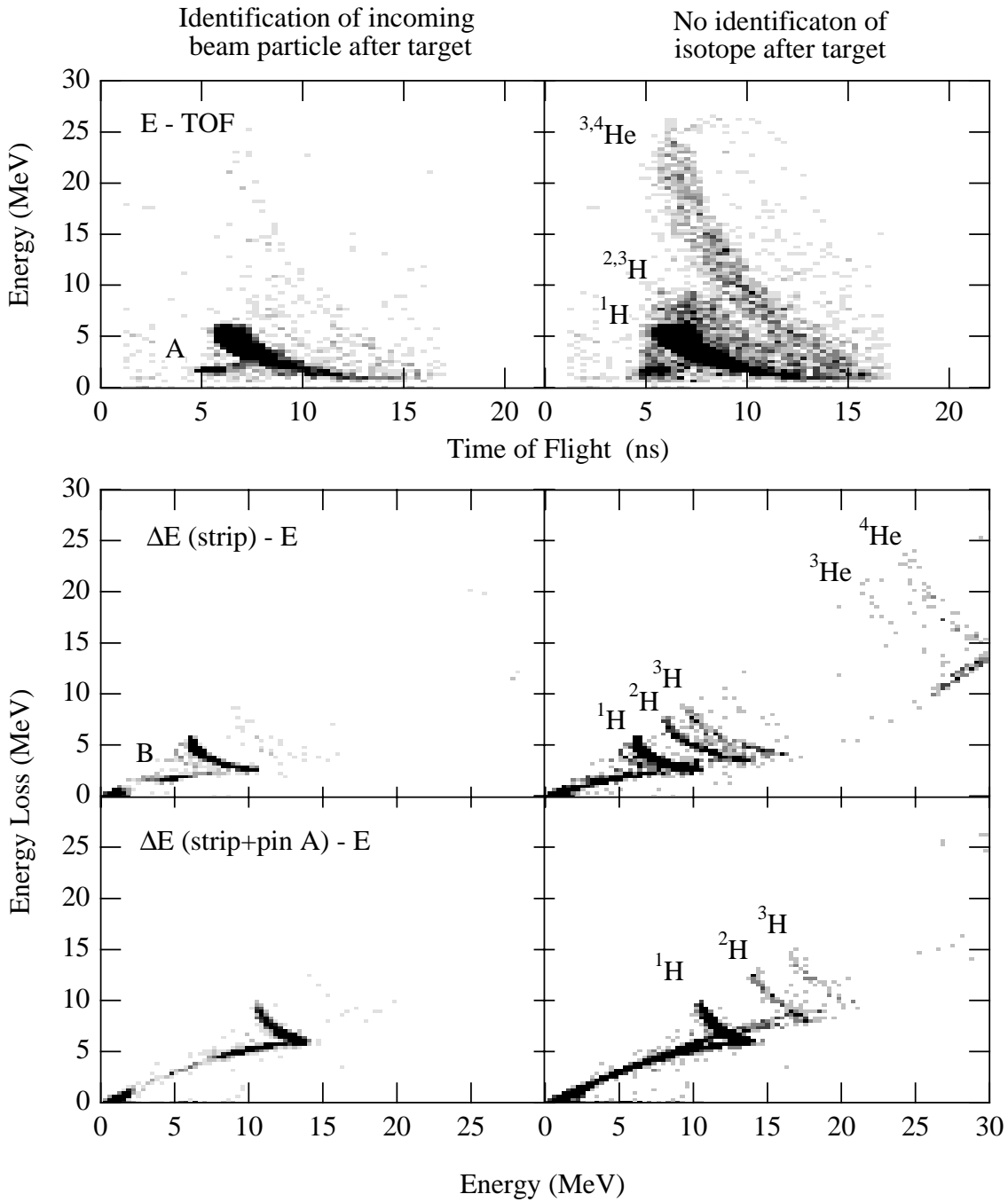


Figure 5.9: Particle ID spectra in the telescopes. The identification of the incoming beam particle after the target, in the zero-degree detector  $\Delta E$ - $E$  spectrum, is sufficient to remove the non-proton background from the analysis. Particle ID spectra without any cut are shown on the right-hand side and bands from protons, deuterons, tritons, and even  ${}^{3,4}\text{He}$  can be seen. With the requirement of observing the beam particle after the target (left-hand side) only the proton band remains, with very little background. See text for the groups of counts labeled A and B.

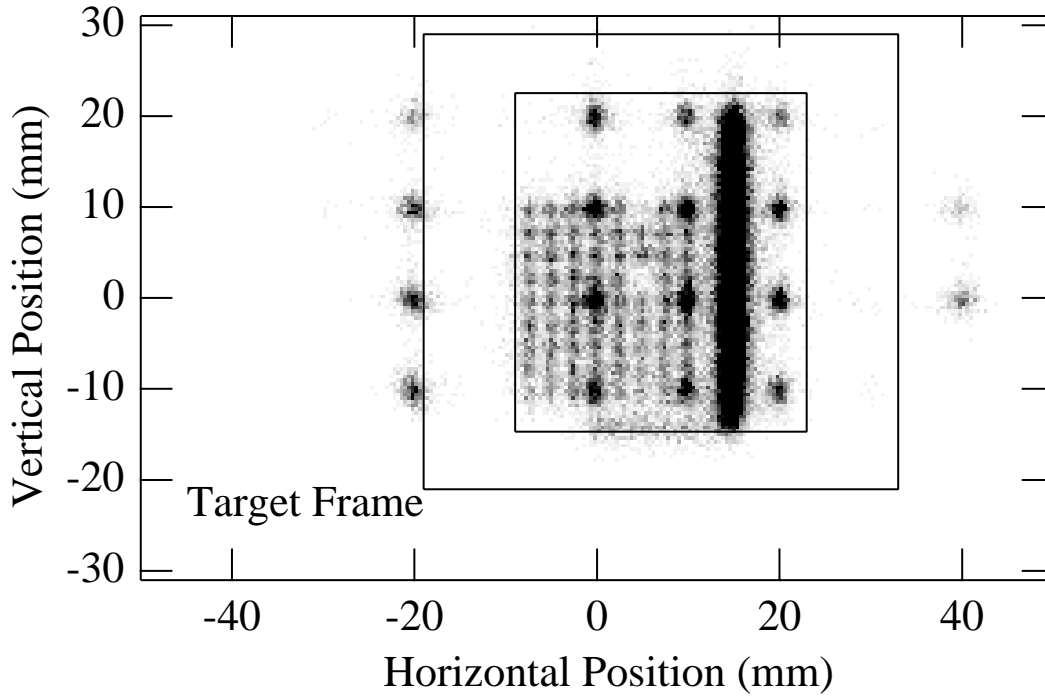


Figure 5.10: Calibrated PPAC position spectrum. The shadow of the target frame is visible. Broken off drill bits can be seen in two of the small 1 mm holes close to the center of the target frame. The separation of the large (2 mm) holes is 1 cm and the 1 mm holes in the center are separated by 2.5 mm. The L-shaped pattern (the lower part is barely visible behind the target frame) served to check the correct orientation of the reconstructed position. The incident rate was about 600  $^{36}\text{Ar}/\text{s}$  at  $E/A=33.6$  MeV. The applied voltage on the detector was 550 V and the gas pressure was 5 Torr (2,2,4 Trimethylpentane).

position on the target results in a large change in angle at which this point is viewed from the telescopes as illustrated in figure 5.11. On the other hand telescopes 1 and 2 “look” almost parallel onto the target surface and are therefore not so dependent on the particle tracking, even though they also benefit from good tracking results, since the beam direction itself enters into the determination of the scattering angle.

Since the usual method of calculating the beam particle trajectory (i.e. one calculates the trajectory assuming the beam particle crossed the two points that were measured by the tracking detectors) did not lead to resolved states in telescope 3 and 4 a novel technique was employed to obtain the trajectory, which gave satisfactory results. This technique, which uses information on the beam itself (i.e. the relation between the position of the particle and the slope of a particle trajectory), is described in appendix F.

### 5.1.3 Electronics

The electronics for the strip detector constituted the largest part of the setup, since for each strip detector 32 channels (2·16 strips) had to be read out. In the electronics diagram (figure 5.12) the strips are labeled 1A through 16A and 1B through 16B, where A and B correspond to either side of one of the 16 strips. The signals from the strips were first amplified by charge sensitive preamps developed at Washington University and built by PICO systems (Kirkwood, MO). The preamps had a feedback capacitance  $c_f$  of 1 pf ( $V_{\text{out}} \propto Q/c_f$ , where  $Q$  is the released charged in the strip detector), which resulted in a high signal gain. The preamp signals were fed into shaping amplifiers with a shaping time of 300 ns. This small shaping time was necessary because, contrary to capacitive noise, the noise spectrum of the resistive strip is high at low frequencies. The shaping time could not be lowered below that value, since below that integration time, high-frequency pickup in the shapers be-

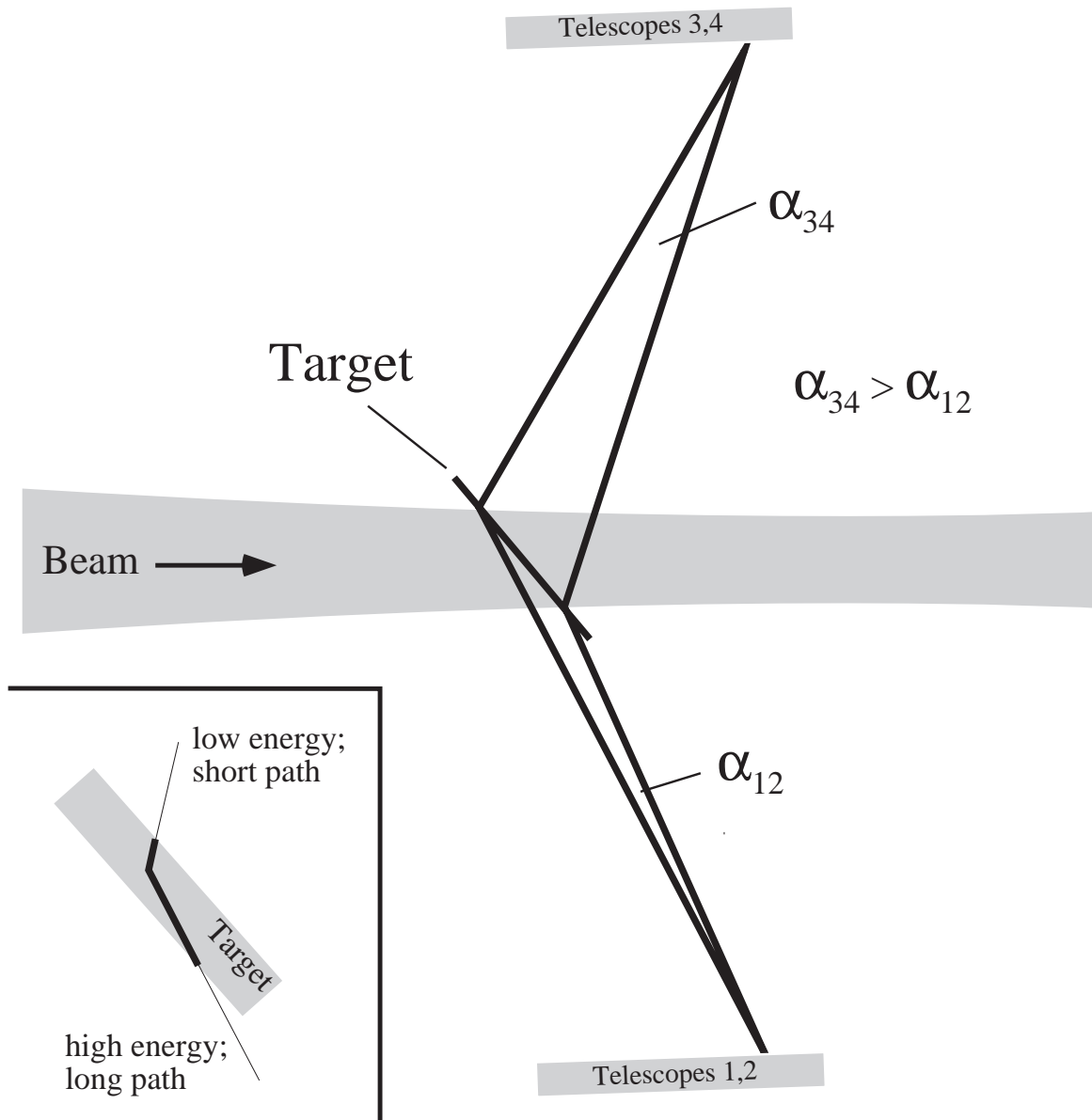


Figure 5.11: Effect of target orientation and beam spot size on the angular resolution  $\alpha$  for the different telescopes. Telescopes 1 and 2 have a better resolution, since they “look” almost parallel onto the target surface. The target angle was chosen so that the lowest energy protons have to traverse the smallest target thickness as indicated in the lower left-hand side. The protons scattered towards telescopes 1 and 2 have to traverse a large amount of target material (as shown in the inset), but the proton energy is sufficiently high. Protons scattered towards telescopes 3 and 4 have a lower energy, but the target material is small enough to still allow a good energy resolution. The drawing is not to scale.

came the dominant source of noise. (The shapers have a high channel density of 16 channels per single width CAMAC module and therefore the circuits are not built for high-frequency applications.) This shaping time gave sufficient position resolution of about 0.5 mm for a 5 MeV signal. The shaped signals were digitized by 16-channel CAMAC peak sensing ADCs (P/S 7164H).

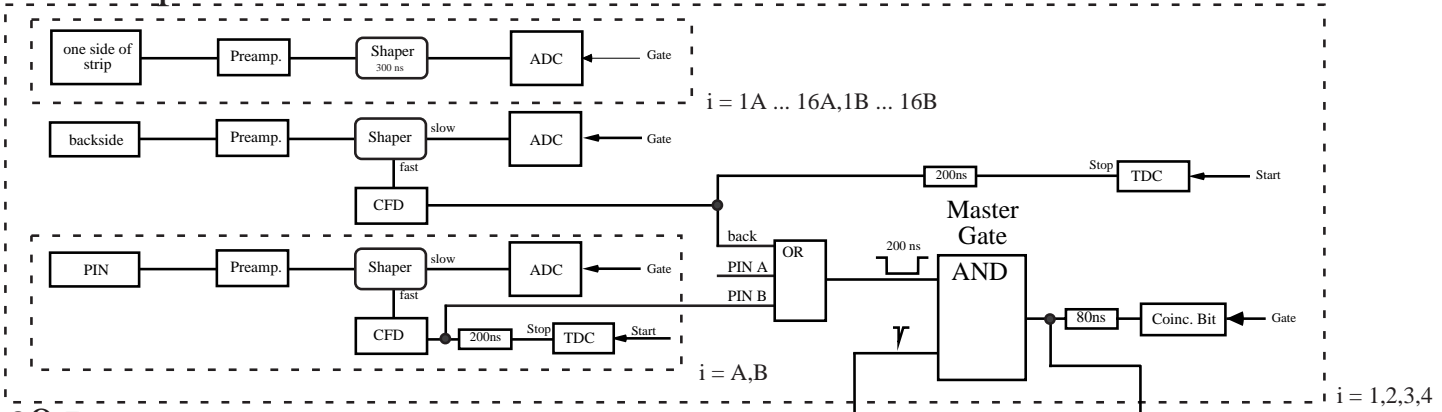
The chosen shaping time would have resulted in a poor energy resolution (about 200 keV), if the energy had been determined from the sum of the two signals belonging to one strip. However, the energy signal in the strip detector was obtained by feeding the signal of the *unsegmented* back side (hence no resistive noise) into a preamp followed by a shaper with a shaping time of about 5  $\mu$ s. The same setup was used for the PIN detectors. This resulted in a good energy resolution of about 50 keV (FWHM) for all silicon detectors.

The fast signals from the shapers for the strip backside and the PINs were input into constant fraction discriminators (Tennelec TC 455), whose output signals were ORed (for each telescope separately). This telescope-OR had a width of 200 ns and if within that time a beam particle signal was observed a master trigger was generated. For each telescope a coincidence bit was set and all detectors belonging to a telescope that triggered were read out. In addition to particle-proton coincidences 'downscaled' (1/500) beam particle singles (i.e. events where only a beam particle was registered) were also measured for the normalization of the scattering cross section. The readout of the zero degree detector is essentially identical to that described in section 3.2.3.

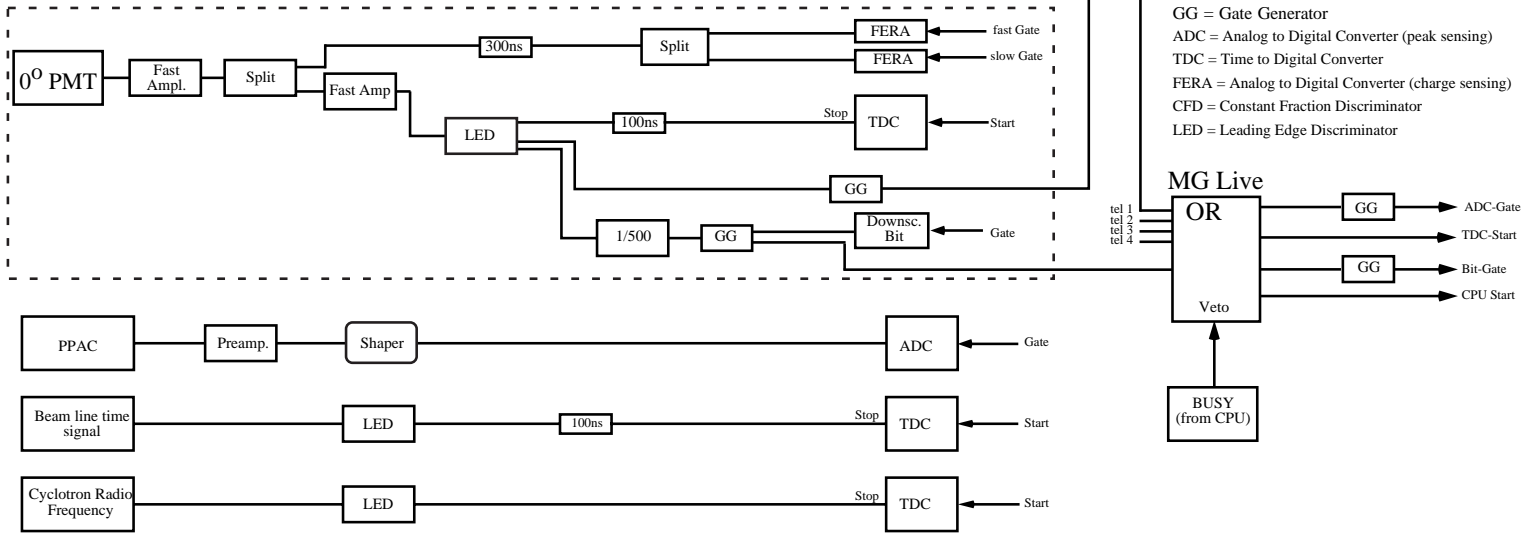
#### 5.1.4 Kinematic Reconstruction

The purpose of the present experiment was to obtain the  $(p, p')$  differential cross section  $d\sigma/d\Omega$  as a function of center of mass scattering angle  $\theta_{cm}$ . In order to separate the elastic from the inelastic events the excitation energy of the particle, or

# Telescope



# 0° Detector



GG = Gate Generator  
 ADC = Analog to Digital Converter (peak sensing)  
 TDC = Time to Digital Converter  
 FERA = Analog to Digital Converter (charge sensing)  
 CFD = Constant Fraction Discriminator  
 LED = Leading Edge Discriminator

MG Live  
 Veto  
 OR  
 tel 1  
 tel 2  
 tel 3  
 tel 4

ADC-Gate  
 TDC-Start  
 Bit-Gate  
 CPU Start

BUSY (from CPU)

Figure 5.12: Electronics Diagram.

equivalently its mass, after the scattering had to be determined. These two quantities can be obtained from the measured quantities  $\theta_{lab}({}^1\text{H})$  and  $E_{lab}({}^1\text{H})$  through a Lorentz transformation. See appendix C and section 5.3.1 for details.

## Inverse Kinematics

For a better understanding of the kinematics it is illustrative to look at the kinematic lines, which connect lines of constant  $Q$ -value in a plot that shows energy versus scattering angle in the laboratory system.

The kinematics in this experiment is different from normal kinematics where a heavy particle is bombarded with lighter one. Here, the light particle constitutes the target and one speaks of inverse kinematics. The kinematic lines for the  $p({}^{36}\text{Ar}, {}^{36}\text{Ar})$  reaction at  $E/A = 33.6$  MeV are shown in solid in figure 5.13. The top part shows the relation of lab energy to lab angle for the recoiling protons and the bottom part for the scattered beam particles. The lines of constant  $\theta_{cm}$  for the protons (top part of figure), shown dashed, are almost independent of  $\theta_{lab}$  in the range covered by the telescopes. Therefore a very good angular resolution was obtained in the center of mass, since the energy in the laboratory system was measured with high precision. Figure 5.13 also illustrates the importance of good angular resolution, since good energy resolution in the lab system is not sufficient to distinguish the excited state from the ground state.

The bottom part of figure 5.13 shows the kinematic lines of the scattered beam particles. The intrinsic beam energy spread of the secondary beam, typically on the order of 1%, together with a high beam emittance make the use of a magnetic spectrometer, such as the S800, to detect the scattered beam particles (without measuring protons) impossible, since even with particle tracking the nuclear states could not be resolved. Another drawback is the background on the carbon atoms in the plastic

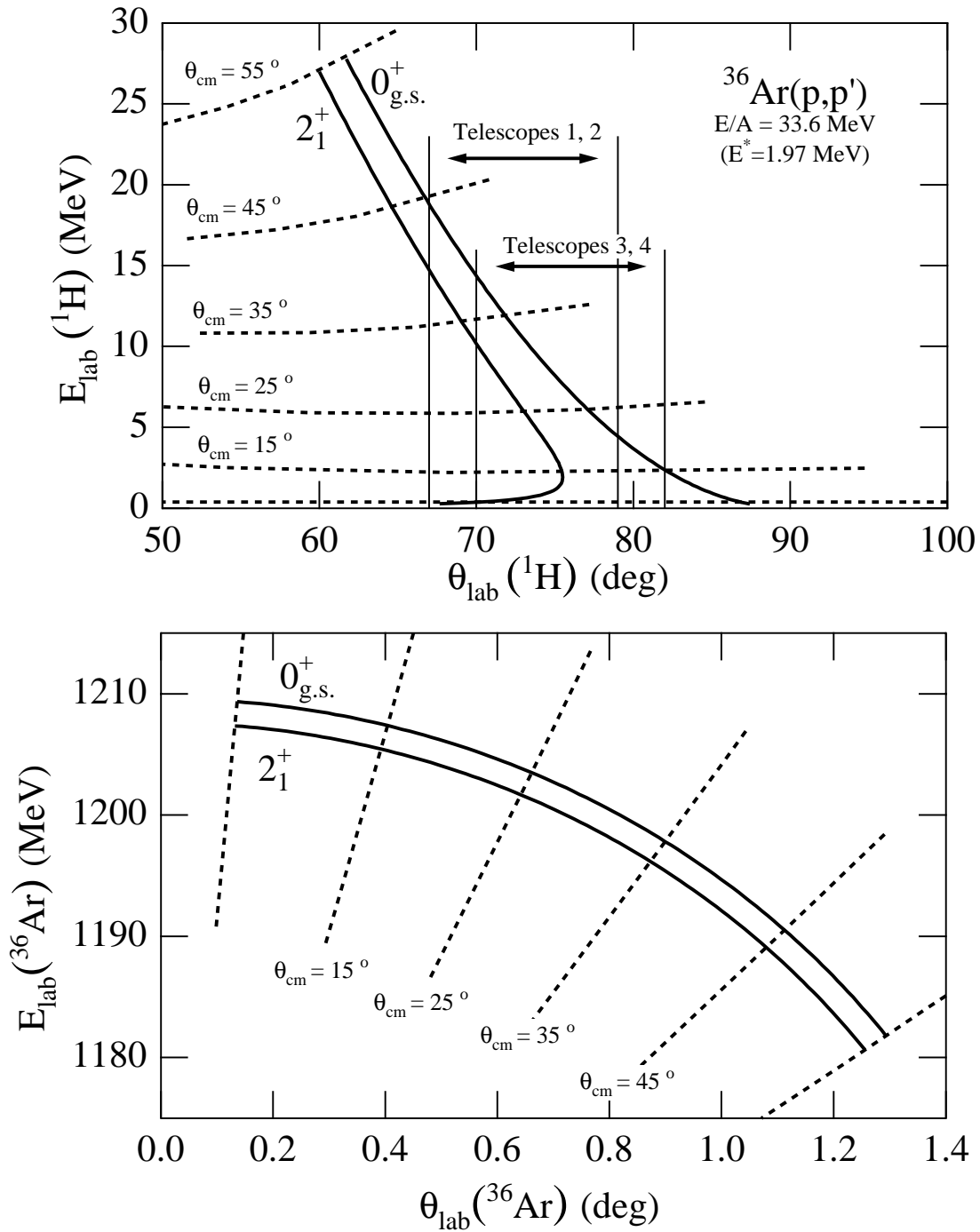


Figure 5.13: Kinematics for the reaction  $^{36}\text{Ar}(p,p')$  at  $E/A = 33.6$  MeV.

target, which would be indistinguishable from the scattering on protons for small angles. In addition the recoil energy from the photon that is emitted after excitation further reduces the resolution.

## 5.2 Simulation

A simulation program was written in DEC FORTRAN [49]. The program simulates the full detector response, the geometry of the setup, the beam emittance, as well as energy loss and angular straggling of the recoil protons in the target. A description of the program is given in appendix D.

### 5.2.1 Examples

The simulation can be used to investigate the influence of certain effects, such as energy loss in the target or detector resolutions, on the final energy and angular resolution. In the following a few examples are given: Figure 5.14 shows the resulting spectra for an ideal case, i.e. all detectors have perfect resolution and there is no straggling or energy loss in the target. The top two panels show the kinematic lines, which are identical to the ones shown in figure 5.13, except that here the detector acceptance restricts the scattering angle in the lab. The middle panels show the (reconstructed) excitation energy over the (reconstructed) center of mass scattering angle and the projection of these spectra on the energy axis is shown in the bottom two panels. In figure 5.15 all target effects have been included. The differences between the spectra for telescope 1 and telescope 3 are due to the target orientation. Figure 5.16 shows the result of the simulation when all target and detector effects are included.

One can see that the resolution after the inclusion of the detector effects is not much larger than that with only the target effects for telescopes 1 and 2. However,

the resolution in telescopes 3 and 4 shows a strong dependence on the resolution of the detectors, especially the position resolution of the tracking detectors. Figure 5.17 shows measured data and the agreement with figure 5.16 is quite good.

## 5.2.2 Efficiency

The simulation program can also be used to calculate the proton detection efficiency (acceptance of the telescopes). Figure 5.18 shows the calculated efficiency for telescope 3. In the central region around  $\theta_{cm} = 25^\circ$  the efficiency is nearly independent of the scattering angle  $\theta_{cm}$  and the value corresponds to the geometrical efficiency of the setup given by

$$\begin{aligned} \epsilon &= \frac{\text{width of detector}}{2\pi(\text{distance to target})} \\ &= \frac{(13/16) \cdot 5 \text{ cm}}{2\pi \cdot 23 \text{ cm}} \\ &\approx 0.028 . \end{aligned}$$

The factor of 13/16 was introduced, since for this telescope 3 out of 16 strips were not working and hence the active width of the detector was  $(13/16) \cdot 5 \text{ cm}$ . For scattering angles close to the edges of the detectors the efficiency goes from its maximum to zero in a manner that can not be obtained through geometrical considerations, since here the beam spot size and the angular spread of the beam are important. Most of the data points are not affected by the correction for the detector efficiency.

## 5.3 Analysis

### 5.3.1 Excitation Energy

From the measured laboratory angle  $\theta_{lab}$  and the measured proton energy  $E_{lab}$  the excitation energy was reconstructed using the equations given in appendix C. For each

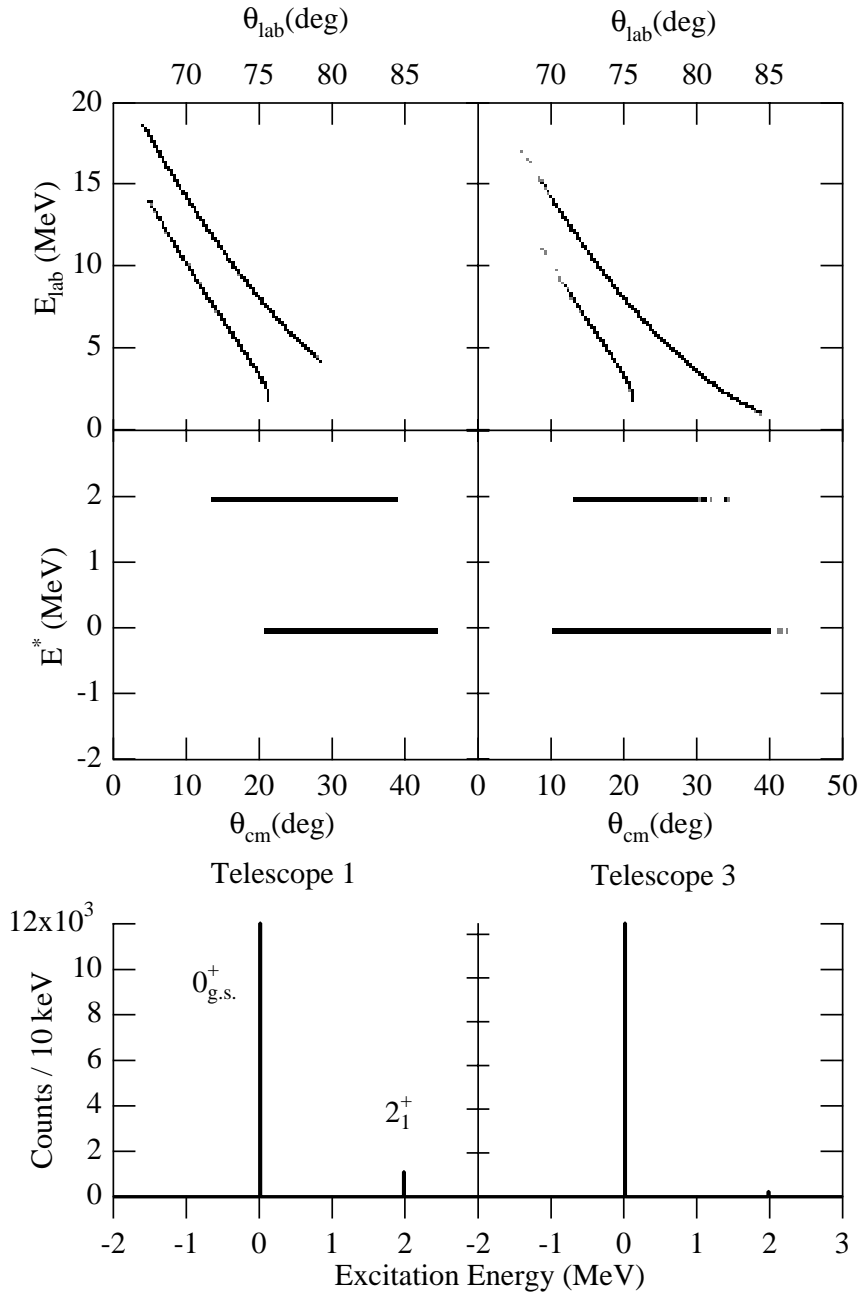


Figure 5.14: Simulated spectra under ideal conditions. The left-hand panels show the spectra for telescope 1 and the right-hand panels shows the spectra for telescope 3. The top row depicts the spectra measured in the laboratory system. The middle two spectra show excitation energy plotted over the center of mass angle and the bottom panels show excitation energy spectra (projection of the middle panels on the energy axis). The top row reproduces the kinematic lines shown in figure 5.13

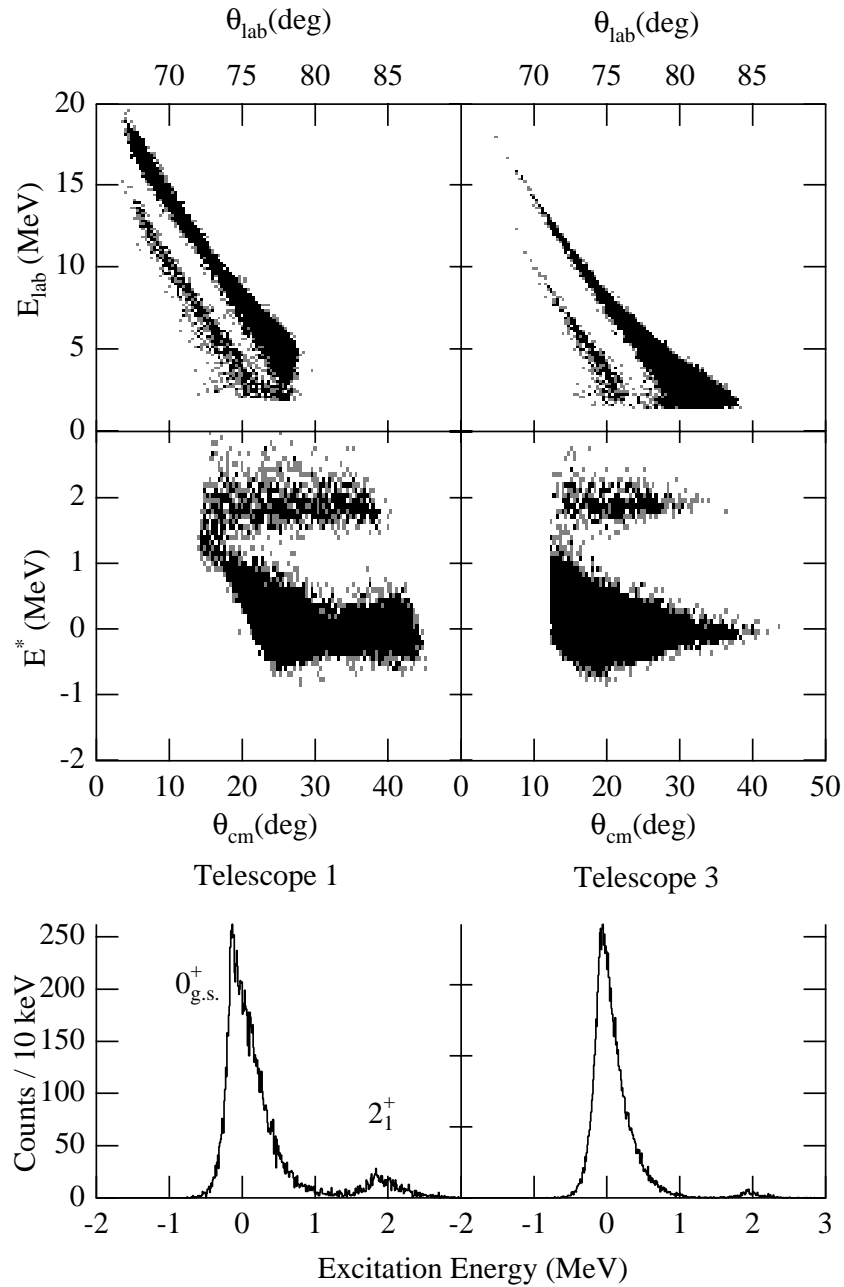


Figure 5.15: Same as figure 5.14, except a  $2.7 \text{ mg/cm}^2$  polypropylene target was included (energy loss and angular straggling).

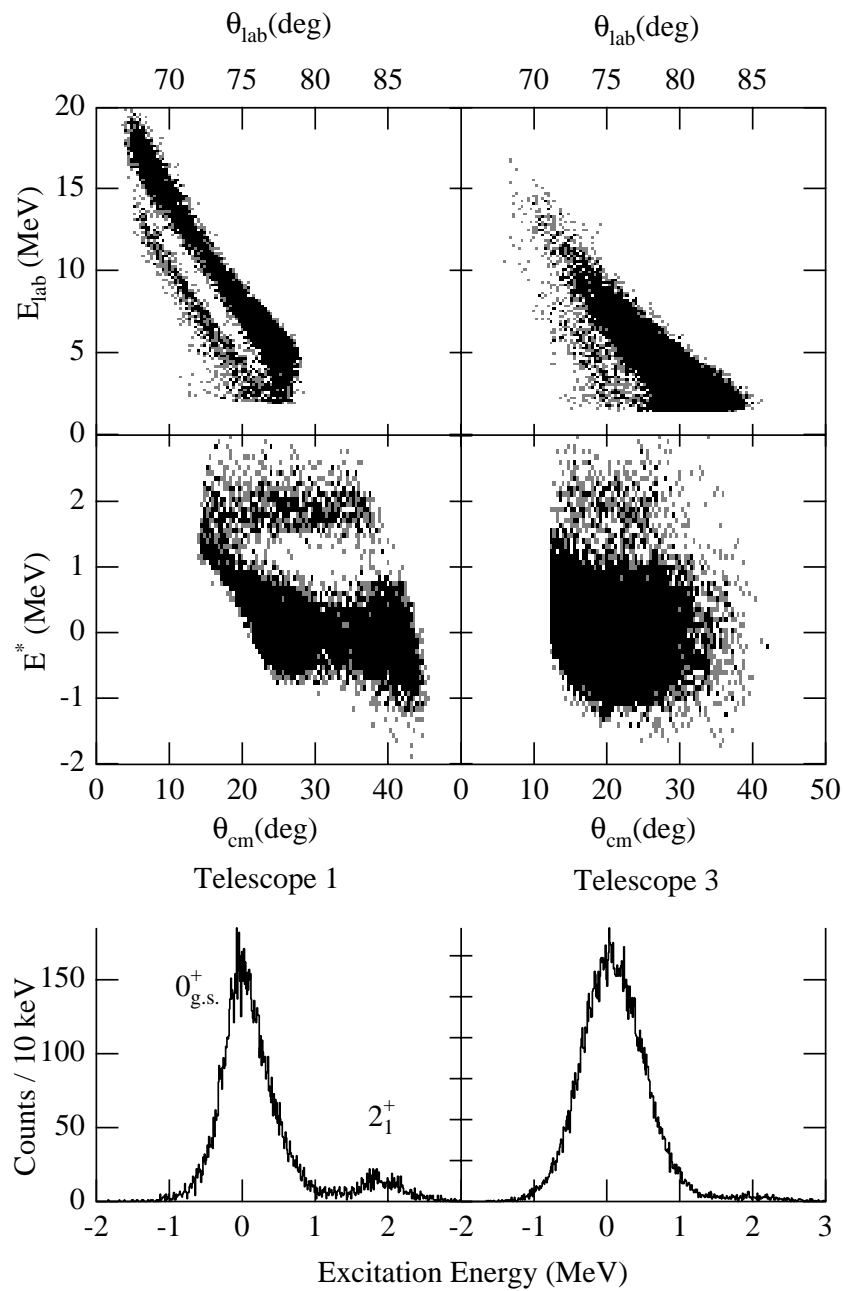


Figure 5.16: Same as figure 5.14, but this time the full detector response, in addition to the effects of the target, have been included. The used input file is given in section D.2

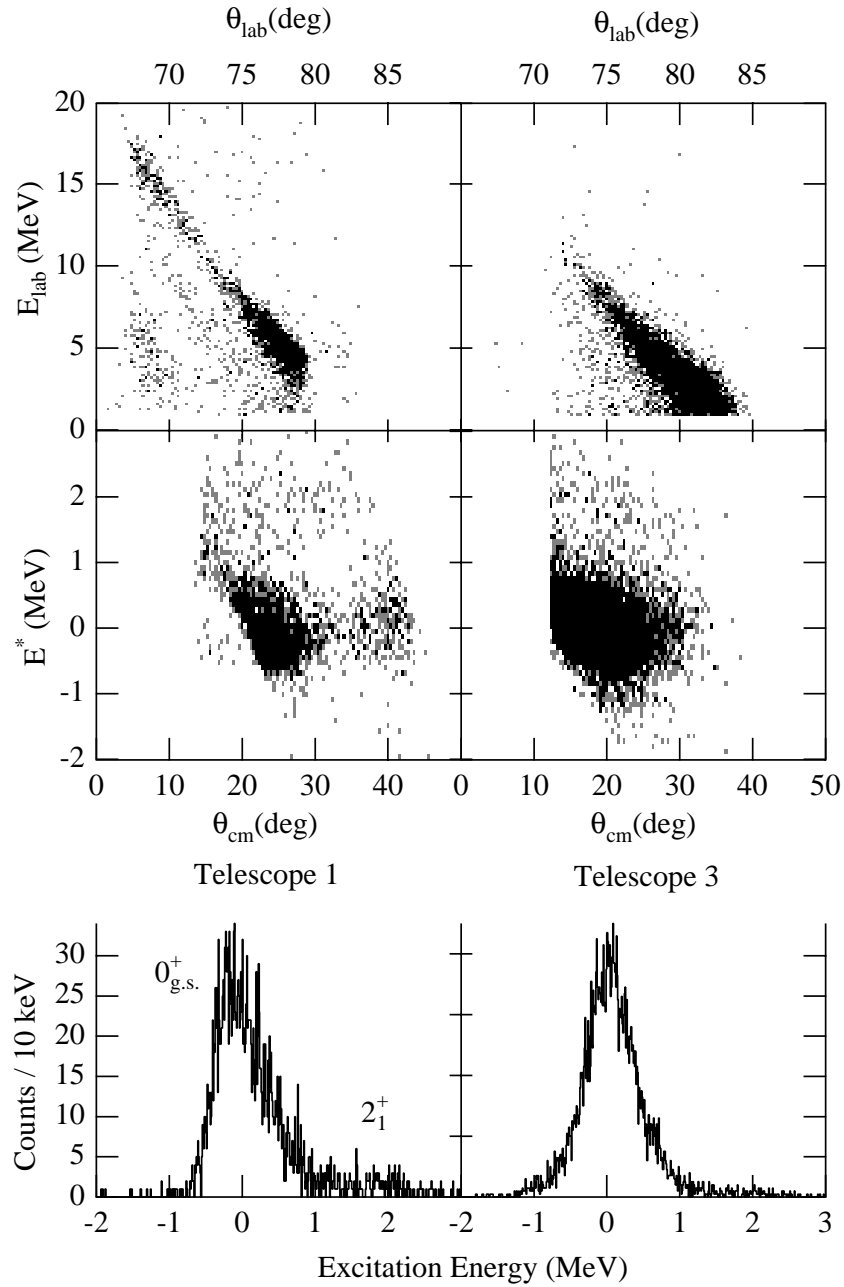


Figure 5.17: Actual data. The agreement to figure 5.16 is quite good.

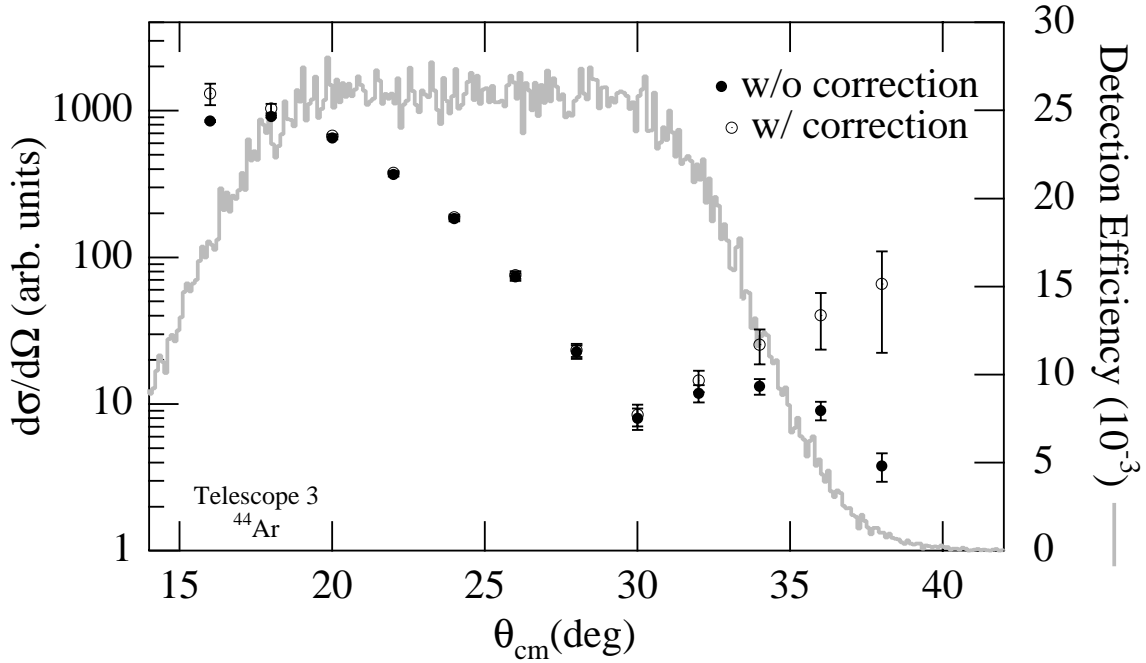


Figure 5.18: Efficiency. The open data points show the elastic cross section after a correction for the detection efficiency, whereas the solid points have not been corrected.

event a 4-vector was generated that has the direction  $\theta_{lab}$  and a fourth component  $E_{lab}({}^1\text{H}) = m_p + T_{lab}({}^1\text{H})$ , where  $m_p$  is the proton mass and  $T_{lab}({}^1\text{H})$  is the measured kinetic energy. A Lorentz boost was applied to this vector with velocity  $\beta$ , which corresponds to the velocity of the center of mass in the laboratory system. The result is the total center of mass energy of the proton  $E_{B'_{cm}}$  as the fourth component of the resulting 4-vector and the center of mass scattering angle, which is given in the first 3 components. By solving equation C.42 for the mass of particle  $A'$  (using the same notation as in appendix C)

$$m_{A'}^2 = E_{cm}^2 + m_{B'}^2 - 2 E_{B'_{cm}} E_{cm} \quad (5.1)$$

the excitation energy is obtained as

$$E^* = m_{A'} - m_A . \quad (5.2)$$

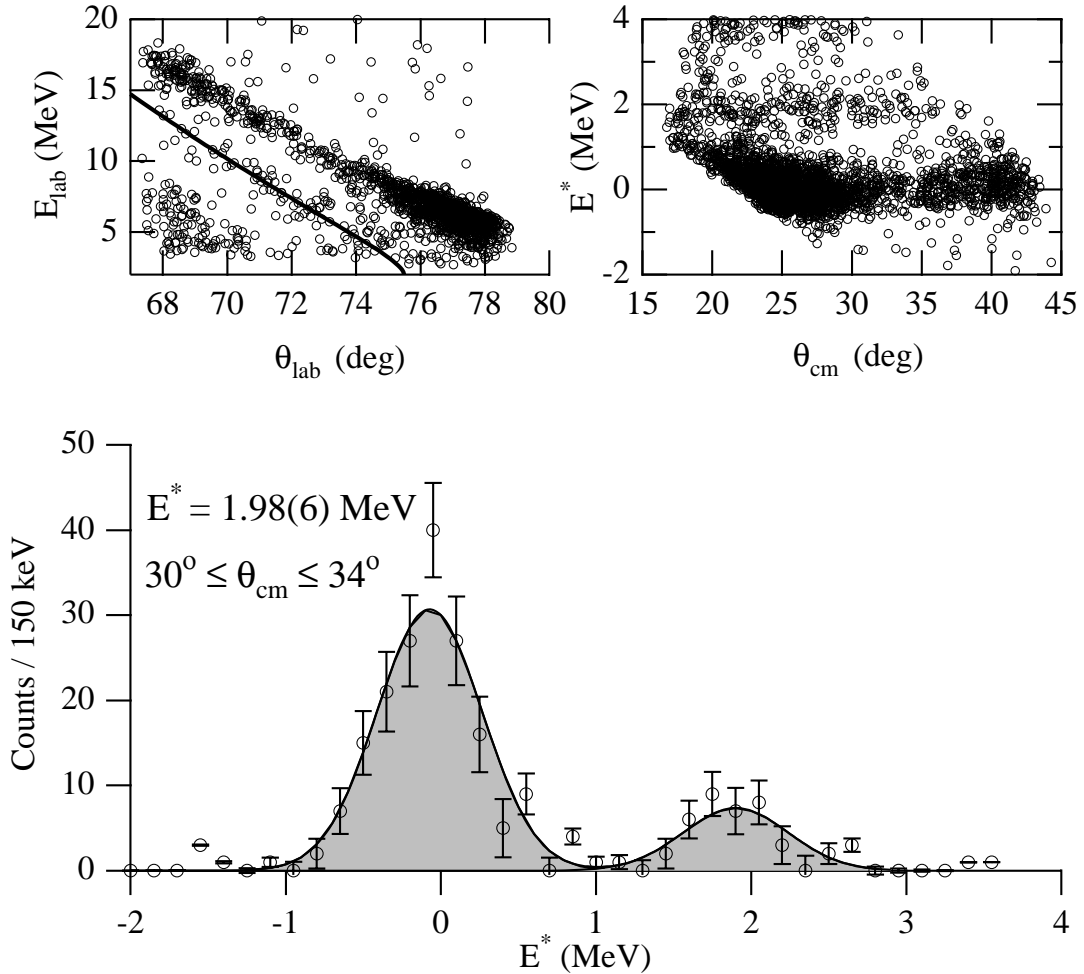


Figure 5.19: The measured proton energy plotted over the measured lab angle for  $^{36}\text{Ar}$  is shown in the top left-hand panel. Events belonging to the ground state and the first excited state can be seen. The top right-hand panel shows the same events, but the excitation energy and center-of-mass scattering angle have been reconstructed. The bottom panel shows an excitation energy spectrum with an angular cut of  $30^\circ \leq \theta_{\text{cm}} \leq 34^\circ$ . The excitation energy of the first excited state in  $^{36}\text{Ar}$  (adopted value 1.97039(5) MeV) is reproduced. The energy resolution is about 800 keV (FWHM).

Isotope	E (MeV)	E/A (MeV)	# of particles
<sup>36</sup> Ar	1209	33.6	1,832 · 10 <sup>6</sup>
<sup>42</sup> Ar	1386	33.0	2,275 · 10 <sup>6</sup>
<sup>44</sup> Ar	1461	33.2	2,417 · 10 <sup>6</sup>

Table 5.2: Experimental Parameters: The beam energies and number of incident particles are listed for each isotope. The (effective) target thickness was 3.118 mg/cm<sup>2</sup> in all cases.

Here  $m_{B'}$  is the proton mass, which is equal to  $m_B$  since it is the same before and after the scattering.  $E_{cm}$  is the total center of mass energy given by equation C.38. The results of this procedure are illustrated in figure 5.19. The top left-hand panel shows the proton energy as a function of laboratory scattering angle. Two groups of counts can be clearly distinguished: Most counts are located around a diagonal line that corresponds to the kinematic line for elastic scattering. The other counts are located along a line almost parallel to the elastic events and the corresponding kinematics line is shown explicitly in the figure. The top right-hand panel shows the same events, but for each event the center of mass scattering angle and the excitation energy was calculated according to the previously described method. A projection on the energy axis of this spectrum with the condition that the center of mass scattering angle be in the range of 30–34° results in the spectrum shown in the bottom. The nuclear states are clearly separated and the measured excitation energy corresponds to the adopted value for the first excited state in <sup>36</sup>Ar [25].

Figure 5.20 shows the excitation energy spectrum measured for <sup>42,44</sup>Ar and in each case the measured energy agrees with the adopted value.

### 5.3.2 Problem with the Cross Section

1° wide cuts in the center of mass scattering angle were applied to the excitation energy spectra; the resulting spectra were fitted with two gauss peaks. The resulting

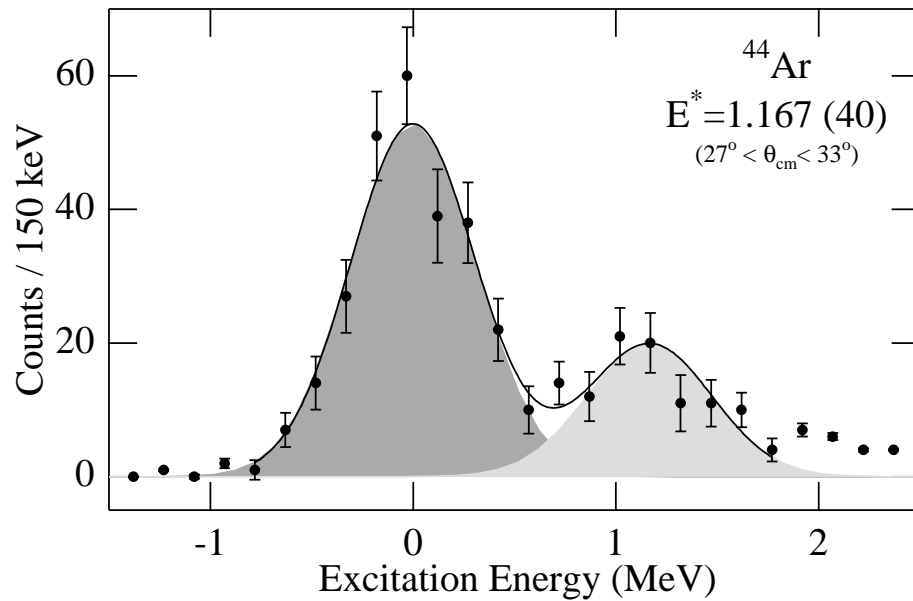
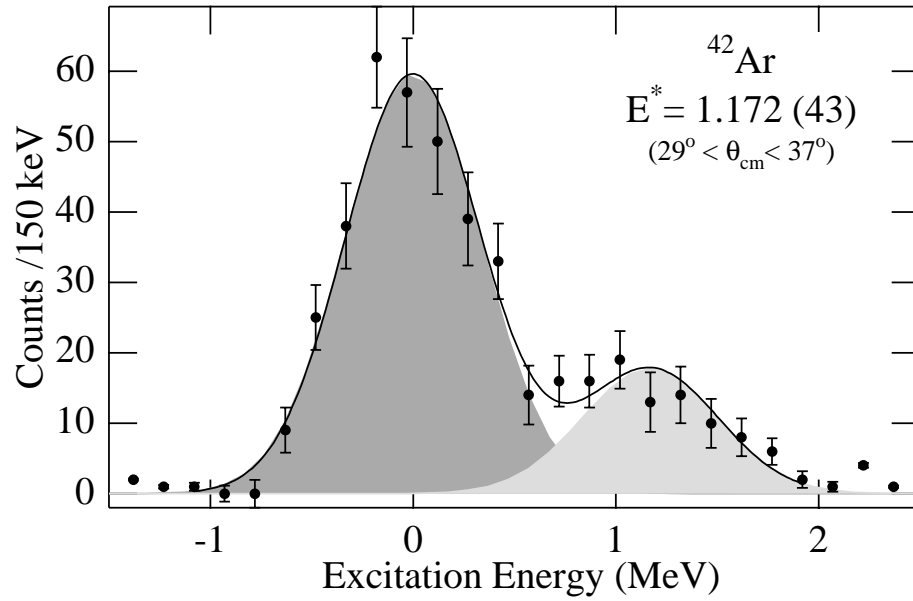


Figure 5.20: Shown are excitation energy spectra for  $^{42}\text{Ar}$  and  $^{44}\text{Ar}$ . The excitation energies are reproduced. The adopted values are 1.2082(3) MeV for  $^{42}\text{Ar}$  and 1.144(17) MeV for  $^{44}\text{Ar}$ , where the latter was measured in this work.

areas, the known target thickness, and total number of incoming beam particles were then used to calculate the differential cross section (see equation E.5) for elastic and inelastic scattering.

Figure 5.21 shows the resulting cross sections for the known case of  $^{36}\text{Ar}$ . One observes that the cross section for elastic scattering does not follow the previous measurement by Kozub [46]. Similarly the inelastic cross section, which is compared to a measurement by Johnson and Griffiths [47], seems to fall below the older data points. At about  $28\text{--}29^\circ$  the measured cross sections drop by about a factor of 2. A similar behavior can be seen by comparing the Becchetti-Greenlees optical model calculation to the  $^{44}\text{Ar}$  data which are shown in the lower part. The same is observed for  $^{42}\text{Ar}$ . Of course, one does not expect the Becchetti-Greenlees calculation to reproduce the data exactly, but especially the height of the maximum might be better reproduced. An additional reason to suspect a problem is the systematics of the other argon isotopes. Cross sections for  $^{40}\text{Ar}$  [50],  $^{43}\text{Ar}$  [51] do not show such a drop in cross section and the height of the maximum around  $\theta_{cm} \approx 40^\circ$  is almost independent of isotope and beam energy.

In the following different possible explanations for the drop in detection efficiency are presented: The same angle in the center of mass (for all isotopes) corresponds to the same proton energy in the laboratory, which gives some credence to an electronics problem that only occurs if the proton energy is above a certain value (which is around 8 MeV). This value can be obtained from figure 5.22 which shows the relation between the scattering angle in the center of mass and the laboratory proton energy. Figure 5.22 shows that the relation is almost independent of excitation energy, which can also be seen in figure 5.13. Hence the elastic and inelastic cross sections drop at the same angle. However it also follows from figure 5.22 that this energy (8 MeV) does not correspond to any of the detector thresholds and it is therefore unclear what

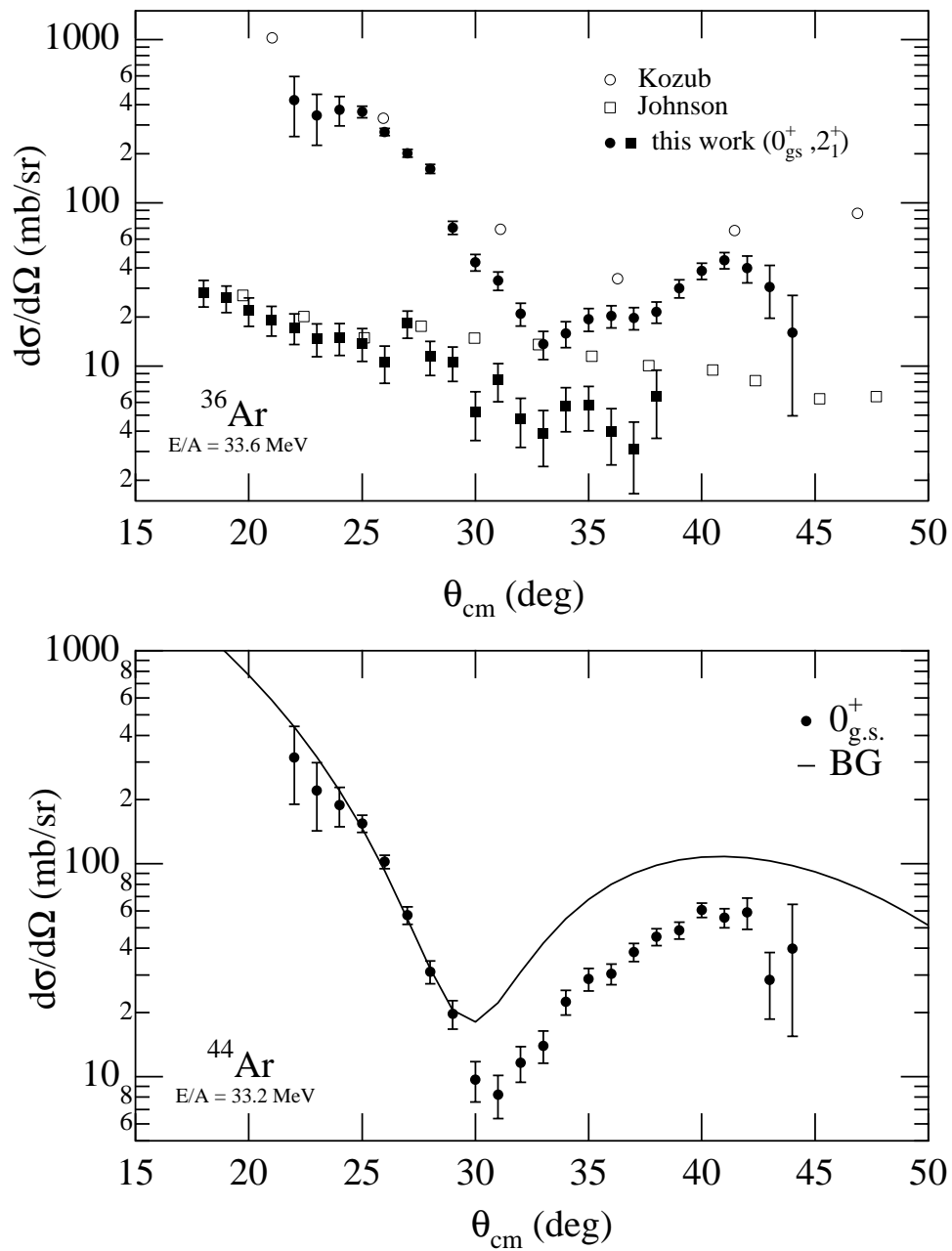


Figure 5.21: Comparison of the measured cross section to previously published data. One can see that neither the elastic not the inelastic cross section agrees with the old data for angles larger than  $28^\circ$ . The lower graph shows the large disagreement between the Bechetti-Greenlees calculation and the measured data for  $\theta_{cm} > 28^\circ$  for  $^{44}\text{Ar}$ .

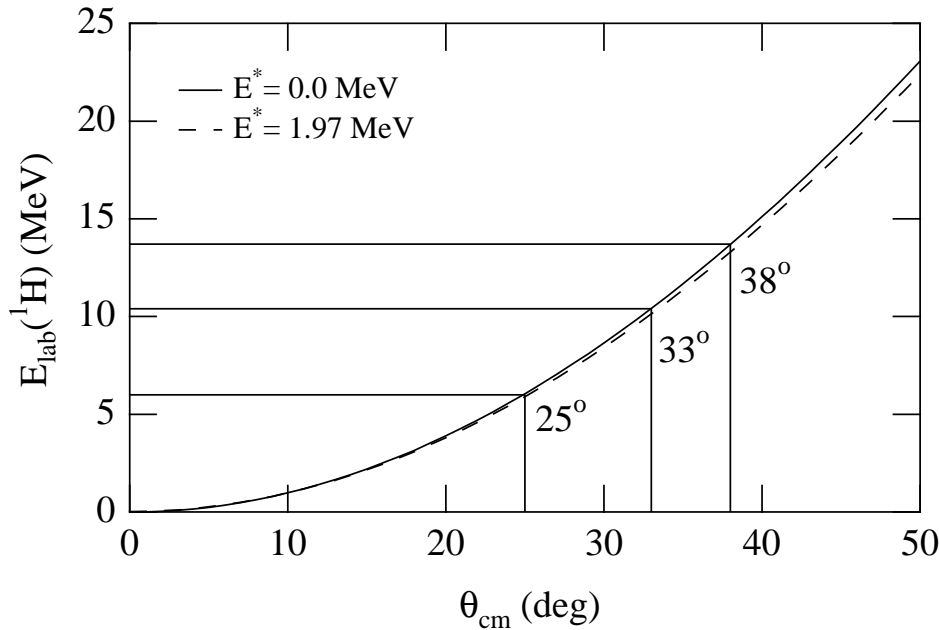


Figure 5.22: Relation between the proton laboratory energy and the center of mass scattering angle. The energies at which the proton is not stopped in the strip detector, the first PIN, and the second PIN are indicated. The corresponding angles are also shown. The insensitivity of the relation between  $E_{lab}$  and  $\theta_{cm}$  on the excitation energy  $E^*$  should be noted (the two curves are almost on top of each other). The same relationship is obtained for  $^{42,44}\text{Ar}$ , since the beam energy per nucleon  $E/A$  was the same for all three isotopes. This, with the assumption that the electronics problem depended solely on the proton energy, justifies the use of the scaling function for all isotopes and all nuclear states.

caused such a discrepancy. For each detector (strip, PIN 1, PIN 2) the time between the zero degree detector hit and the detector response (TOF) was measured. By inspecting the Energy-TOF matrix it was confirmed that the drop in cross section occurs at a proton (lab) energy away from any detector thresholds. (If, for example, the coincidence gate was not setup properly for the PINs then a problem should occur as soon as the proton energy is high enough to trigger the first PIN (6 MeV) and one should observe a drop in cross section at the corresponding angle, i.e. 25°.)

Another explanation could be that at a certain scattering angle the beam particle misses the zero degree detector and therefore no coincidence could be registered. This possibility can be ruled out, because the radius of the zero degree detector is much

larger than the maximum scattering angle. In addition, the spread in beam spot size and the angular spread of the incoming beam are larger than the deflection caused by the scattering and no sharp transition should be observed.

Could it be that an object obstructs the flight path of the protons? This not possible, for several reasons. Firstly, one expects a smoothly vanishing cross section and not a step function with a non-zero cross section after the step. Secondly, any edge such as the target frame would degrade the resolution, since some protons will go through just a small part of that object. However the resolutions above and below that critical angle are the same. Lastly, the object should cover half the telescope, which is very unlikely to be missed during the setup or take down of the experiment.

What could cause about every second event to be lost if  $E_{lab}(^1\text{H}) \geq 8 \text{ MeV}$ ? The most likely explanation is that no coincidence gate was formed. The threshold energy (8 MeV) and the rate (about every second event) remain unclear.

In conclusion, several possibilities have been investigated, but none can explain the observed behavior. Regardless of this, an experimental problem can not be ruled out and the evidence of the previous measurements and systematic trends can not be neglected. Therefore we decided to use the previous data on  $^{36}\text{Ar}$  as a calibration for the detection efficiency. The resulting scaling curve is shown in figure 5.23. The curve was obtained by using the optical model parameters given by Kozub [46] to obtain the cross section for elastic scattering for the same angles as were used in this experiment. The calculation was used instead of the experimental values, because there are not corresponding experimental data points in Kozub's work for all points in this work. The rather surprising result is shown in figure 5.23. Shown there is the ratio of the current measurement to Kozub's data. The fitted curve is of the form

$$f(\theta) = w_0 + w_1 \cdot \text{erf} \left( \frac{\theta - w_2}{\sqrt{2}w_3} \right) + w_4\theta + w_5\theta^2, \quad (5.3)$$

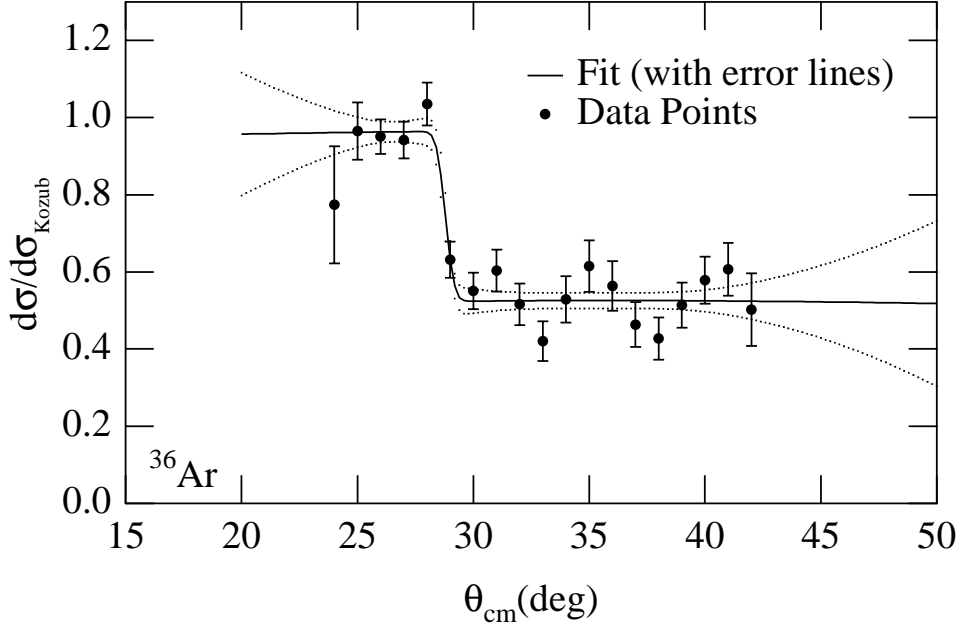


Figure 5.23: Ratio of the present data to the ones by Kozub. The fit and the corresponding error lines are explained in the text.

where the  $w_i$  are fit parameters and  $\text{erf}()$  is the error function

$$\text{erf}(x) = \int_{-\infty}^x e^{-x^2} dx \quad (5.4)$$

that allows for the smooth step in the fitted function. The error lines (dotted in the figure) were obtained via

$$\sigma^2(f(\theta)) = \sum_{ik} \left( \frac{df}{dw_i} \right) \left( \frac{df}{dw_k} \right) \sigma_{ik}^2, \quad (5.5)$$

where  $\sigma_{ik}^2$  is the covariance matrix obtained through the fitting procedure. Only data points above  $28^\circ$  are affected by the scaling procedure. Data points below that angle are not scaled. The previously described scaling function has been applied to all isotopes ( $^{36,42,44}\text{Ar}$ ) and the resulting differential cross sections are shown in figures 5.24 ( $^{36}\text{Ar}$ ) and 5.25 ( $^{42,44}\text{Ar}$ ).

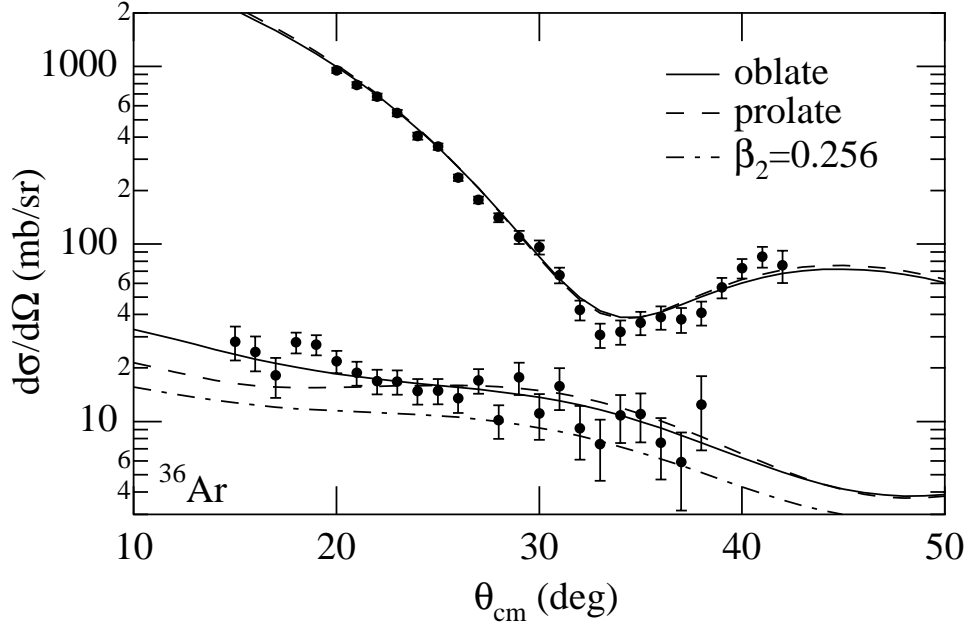


Figure 5.24: Different fits are obtained depending on the chosen shape of the nucleus. However, the measured data do not allow to distinguish between the two cases, even though it seems the oblate shape fits the inelastic data points better. Almost no difference is observed for the elastic channel.

### 5.3.3 Deformation Parameters and $M_n/M_p$

The computer code ECIS [39] was used to extract deformation parameters from the data by fitting the elastic and inelastic cross sections, where  $V$ ,  $W$ , and  $W_D$  (refer to equation 4.2), in addition to the quadrupole deformation parameter  $\beta_2$ , have been allowed to vary during the fit. Other combinations of parameters have also been tried with essentially the same results. In each case the deformations of all potentials have been set to the same value and have also been kept fixed to one another during the fitting procedure. The starting point for all fits was the Becchetti-Greenlees prediction [40]. The results of the fit are displayed in the figures as solid lines. In the rotational model prolate and oblate shapes fit the data equally well, as shown in figure 5.24. In the vibrational model the quadrupole deformation parameter  $\beta_2$  corresponds to the phonon amplitude and as in the rotational model positive and negative values were tried and they also fit the data well. The obtained deformation

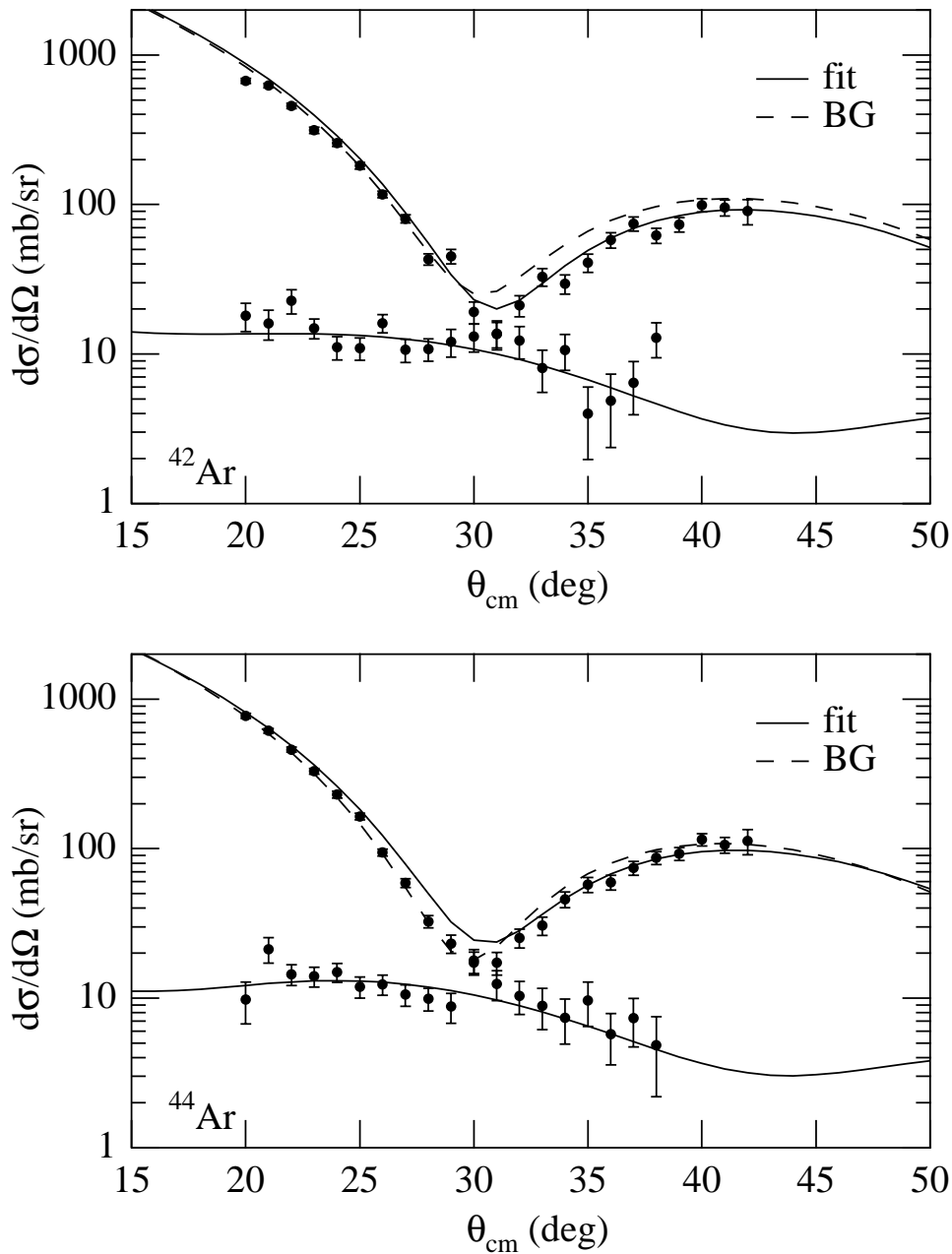


Figure 5.25: Measured cross sections and ECIS fits. Also shown are the optical model calculations for the elastic channel using the Becchetti-Greenlees optical potential parameters. The fit of the elastic data points for  $^{44}\text{Ar}$  is not as good as for the other two isotopes, but it has been verified that the extracted deformation  $\beta_2$  is quite independent of the actual optical model parameters.

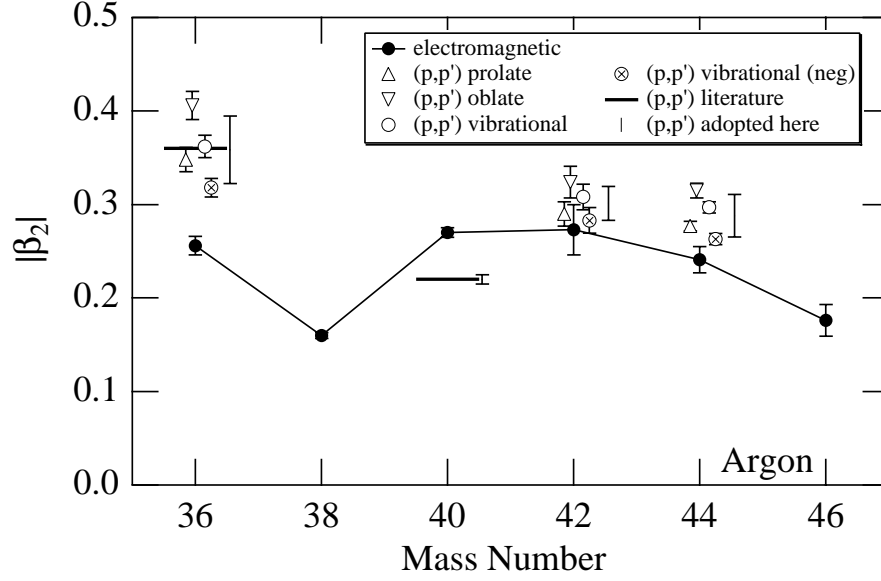


Figure 5.26: Deformation parameters obtained with the various fits: The value that was adopted in this work is the average of all four values. The assigned error bar is the sample variance of the data points about the average ( $\sigma = s := \sqrt{\frac{1}{N-1} \sum (x_i - \bar{x})^2}$ ). One is not allowed to divide this value by 2 ( $=\sqrt{4}$ ), since the four methods use the *same* data and are therefore not independent.

parameters are listed in table 5.3 and shown in figure 5.26. One can see that the deformations obtained using the various methods are grouped close together, even though their ( $1\sigma$ ) error bars do not overlap. The value that was adopted by us is the mean of all four methods and is shown as a vertical bar. Previous measurements are shown as horizontal bars. One can see that the previous measurement for  $^{36}\text{Ar}$  [47] agrees with the present result. ECIS fits have also been done, where only data points below  $\theta_{cm} \leq 28^\circ$  have been used with very similar results. The Becchetti-Greenlees calculations are also shown in figure 5.25 as dashed lines and they follow the data points well, especially for center of mass angles below the first minimum in the cross section. For larger angles, however, some deviation is apparent.

With the help of equation 4.18 and the measured deformations, the  $M_n/M_p$  values were obtained and are listed together with other properties of the Argon isotopes in table 5.4. The interaction strengths of protons with protons ( $b_p$ ) and neutrons ( $b_n$ )

Isotope	rotational		vibrational		value adopted
	pos	neg	pos	neg	here
<sup>36</sup> Ar	0.348(13)	0.406(15)	0.362(12)	0.318(10)	0.359(36)
<sup>42</sup> Ar	0.290(13)	0.324(17)	0.308(14)	0.283(14)	0.301(18)
<sup>44</sup> Ar	0.277(13)	0.315(8)	0.297(6)	0.263(6)	0.288(23)

Table 5.3: Deformation parameters  $\beta_2$  obtained with the various ECIS fits for each model (rotational and vibrational) positive and negative  $\beta_2$ s have been used. The last column gives the adopted value.

have been chosen to be 0.3 and 0.7 respectively [43, 52]. The quoted uncertainty includes a 1- $\sigma$  error in  $b_p/b_n$  of 0.3.

Figure 5.27 shows the obtained  $M_n/M_p$  values. One notices the very large value for <sup>36</sup>Ar, indicating a large isovector contribution to the excitation. This is not understood, since the excitation of an  $N = Z$  nucleus should be isoscalar by isospin symmetry. Possibly, the prescription of Bernstein (equation 4.18) to obtain  $M_n/M_p$  is not applicable and, as in the <sup>38</sup>S case (section 4.1.3), microscopic calculations might be necessary for a correct interpretation of the data. Such calculations are being performed now in collaboration with E. Bauge in France.

In future experiments, measurements of the proton scattering cross section on the single-closed-shell nuclei <sup>38</sup>Ar (N=20) and <sup>46</sup>Ar (N=28) would complete the set of  $M_n/M_p$  values for the neutron-rich argon isotopes.

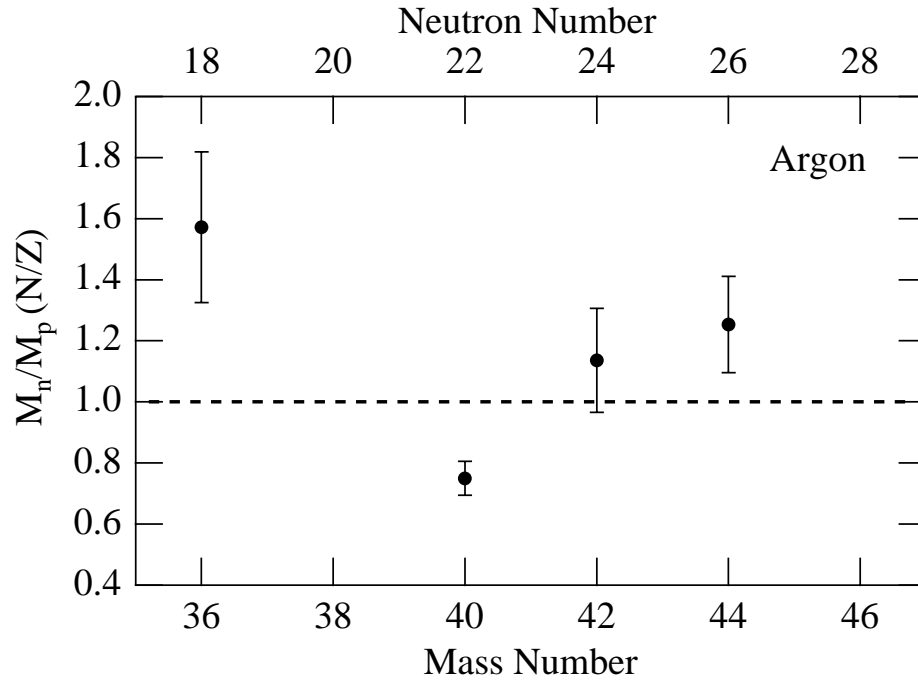


Figure 5.27: A comparison of the extracted  $M_n/M_p$  values. The value for  $^{36}\text{Ar}$  is incompatible with an isoscalar excitation that is expected for an  $N = Z$  nucleus. Measurements of  $^{38}\text{Ar}$  and  $^{46}\text{Ar}$ , which are to single-closed-shell nuclei, have not yet been performed.

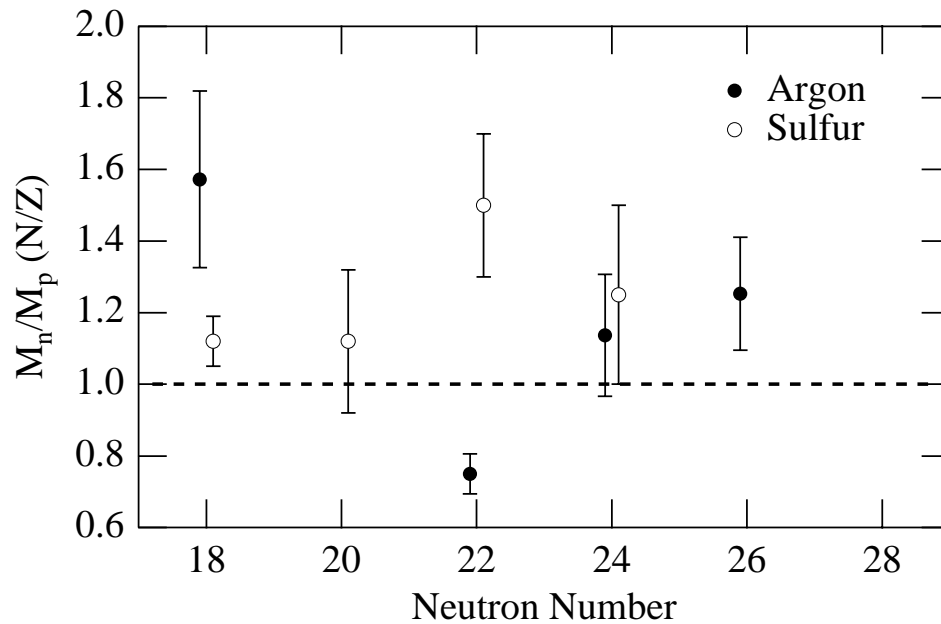


Figure 5.28: Same as figure 5.27, but here the data points for the sulfur isotopes are also included for comparison.

Isotope	$E(2_1^+)$ (MeV)	$\tau$ (ps)	$B(E2 \uparrow)$ ( $e^2 \text{fm}^4$ )	$\beta_2^{\text{em}}$	$\beta_2^{(\text{p,p}')} )$	$M_n/M_p$	$N/Z$
$^{34}\text{Ar}$	2.0909(3)	0.46(6)	222(33)	0.239(17)	—	—	0.89
$^{36}\text{Ar}$	1.97039(5)	0.46(4)	299(25)	0.256(10)	0.36 [47]	—	1.00
$^{38}\text{Ar}$	2.167472(9)	0.68(3)	125.4 (53)	0.160(3)	0.359(36) <sup>†</sup>	1.57(25) <sup>†</sup>	1.11
$^{40}\text{Ar}$	1.460859(5)	1.61(6)	380(13)	0.270(5)	0.21 [47]	—	1.22
$^{42}\text{Ar}$	1.2082(3)	3.8(9)	417(80)	0.273(27)	0.220(5) [50]	0.917(68)	1.33
$^{44}\text{Ar}$	1.144(17) <sup>†</sup>	6.0(6) <sup>†</sup>	349(41) <sup>†</sup>	0.241(14) <sup>†</sup>	0.301(18) <sup>†</sup>	1.52(23) <sup>†</sup>	1.44
$^{46}\text{Ar}$	1.554(26) <sup>†</sup>	2.3(4) <sup>†</sup>	196(39) <sup>†</sup>	0.176(17) <sup>†</sup>	—	1.81(23) <sup>†</sup>	1.56

Table 5.4: Summary of properties of Argon isotopes. All entries followed by <sup>†</sup> are results of this thesis work. Reference [47] did not report errors on the extracted deformation parameters.

# Chapter 6

## Summary

Two experiments have been performed to investigate the quadrupole collectivity of the neutron-rich argon and sulfur isotopes.

In the first experiment the nuclei  $^{38,40,42}\text{S}$  and  $^{44,46}\text{Ar}$  were studied by Coulomb excitation on a  $^{197}\text{Au}$  target. A position-sensitive, high-efficiency NaI(Tl) array was constructed and was used to detect the de-excitation photons. The experiment allowed us to determine the energy of the first excited  $J^\pi = 2^+$  states in three nuclei ( $^{40,42}\text{S}$ ,  $^{44}\text{Ar}$ ), while a previously observed state in  $^{46}\text{Ar}$  was assigned definite spin. The excitation energy of the first excited state in  $^{38}\text{S}$  was reproduced. In addition, the Coulomb excitation cross sections for all 5 isotopes ( $^{38,40,42}\text{S}$ ,  $^{44,46}\text{Ar}$ ) were measured and the reduced transition probabilities  $B(E2)$  were determined. The measurements revealed a new region of deformation around  $^{40,42}\text{S}$ . The reduced transition probability for  $^{46}\text{Ar}$  demonstrates that the  $N=28$  shell closure persists at  $Z=18$ . The power of Coulomb excitation in the investigation of heavy sd-shell nuclei can be seen in figure 6.1. Shown there is the inverse quadrupole deformation parameter  $1/|\beta_2|$  (the inverse is shown solely for illustrative purposes, since otherwise the large values in the foreground would block the view). The left-hand panel shows the available data before this Coulomb excitation experiment, while the right-hand panel shows all data

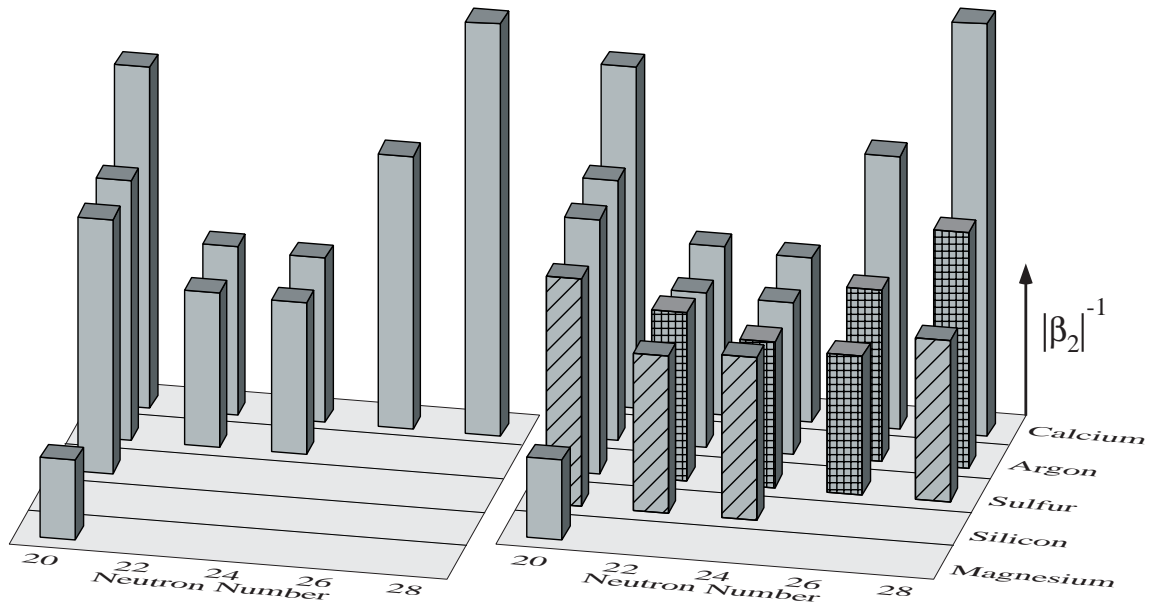


Figure 6.1: Inverse quadrupole deformation parameter. (The inverse was taken solely for illustrative purposes.) The left-hand panel shows the data that was available before this thesis work. The result from this work (cross-hatched columns) and subsequent work (hatched columns) are shown on the right.

available at the time of this writing. The cross hatched columns were measured in this Coulomb excitation experiment, and the hatched columns were measured subsequently at the NSCL.

In the second experiment the proton scattering cross sections on the unstable nuclei  $^{42,44}\text{Ar}$  were measured. The results are not completely understood and a group in France is working on microscopic nuclear matter calculations, which will help to correctly interpret the measured cross sections.

# Appendix A

## Coulomb Excitation

### A.1 Semi-Classical Approach and Perturbation Theory

As shown in section 2.3 Coulomb excitation can be treated semi-classically. One assumes a classical Rutherford trajectory but treats the excitation process quantum-mechanically. The excitation cross section from an initial state  $|i\rangle$  to a final state  $|f\rangle$  is given by

$$\frac{d\sigma}{d\Omega} = \left( \frac{d\sigma}{d\Omega} \right)_{\text{Ruth}} P_{i \rightarrow f}. \quad (\text{A.1})$$

The Rutherford cross section is given by

$$\left( \frac{d\sigma}{d\Omega} \right)_{\text{Ruth}} = \left( \frac{a_0}{2} \right)^2 \sin^{-4} \left( \frac{\theta}{2} \right), \quad (\text{A.2})$$

with  $a_0$  given by equation A.15. Treating the electromagnetic interaction potential  $V(\mathbf{r}(t))$  as a time-dependent perturbation,  $P_{i \rightarrow f}$  can be expressed to first order as

$$P_{i \rightarrow f} = |a_{i \rightarrow f}|^2 \quad \text{with} \quad a_{i \rightarrow f} = \frac{1}{i\hbar} \int_{-\infty}^{\infty} e^{i\omega_{fi}t} \langle f | V(\mathbf{r}(t)) | i \rangle dt, \quad (\text{A.3})$$

where  $\omega_{fi} = (E_f - E_i)/\hbar$ . For sufficiently high energies or large impact parameters the Rutherford trajectory can be approximated as a straight line and the electromagnetic

potentials can be obtained through a Lorentz transformation of the field of a point charge at rest

$$A(x) = \Lambda(\beta)A'(\Lambda^{-1}(\beta)x'), \quad (\text{A.4})$$

with  $A'(x')$  being the 4-vector potential of a electric point charge at the origin

$$A'(x') = (\mathbf{A}', i\phi') = (0, 0, 0, i\frac{eZ}{r}). \quad (\text{A.5})$$

$\Lambda(\beta)$  is the Lorentz transformation matrix that takes the stationary charge into a charge moving with velocity  $\beta$  (see appendix C)

$$\Lambda(\beta) = \begin{pmatrix} 1 & 0 & 0 & 0 \\ 0 & 1 & 0 & 0 \\ 0 & 0 & \gamma & -i\gamma\beta \\ 0 & 0 & i\gamma\beta & \gamma \end{pmatrix}. \quad (\text{A.6})$$

The resulting fields are the following Lienard-Wiechert expressions:

$$\phi^{(p)}(\mathbf{r}, t) = \frac{Z_p e \gamma}{\sqrt{(b-x)^2 + y^2 + \gamma^2(x-vt)^2}} \quad (\text{A.7})$$

and

$$\mathbf{A}^{(p)}(\mathbf{r}, t) = \frac{\mathbf{v}}{c}\phi^{(p)}(\mathbf{r}, t). \quad (\text{A.8})$$

The superscript  $(p)$  indicates that this is the field generated by the projectile nucleus 'measured' at position  $\mathbf{r}$  and time  $t$ . The coordinate system that is used is oriented with the  $z$ -axis in the direction of motion of the projectile. The target nucleus is located at the origin and the projectile passes with impact parameter  $b$  (displaced in the  $\mathbf{x}$  direction; i.e.  $x_p = b$ ,  $y_p = 0$ ,  $z_p = vt$ ). The electric and magnetic fields are given by

$$\begin{aligned} \mathbf{E} &= -\frac{1}{c}\frac{\partial \mathbf{A}}{\partial t} - \nabla\phi \\ \mathbf{B} &= \nabla \times \mathbf{A} \end{aligned} \quad (\text{A.9})$$

More explicitly:

$$(E_{\perp} =)E_x = \frac{eZ_p\gamma b}{(b^2 + \gamma^2v^2t^2)^{\frac{3}{2}}} = \frac{\gamma E_0}{(1 + (\frac{t}{\tau})^2)^{\frac{3}{2}}}$$

$$\begin{aligned}
E_z &= -\frac{eZ_p\gamma vt}{(b^2 + \gamma^2 v^2 t^2)^{\frac{3}{2}}} = -\frac{\gamma E_0}{(1 + (\frac{t}{\tau})^2)^{\frac{3}{2}}} \frac{t}{\tau} \\
(B_{\perp} =) B_y &= \beta E_x = \beta \frac{eZ_p\gamma b}{(b^2 + \gamma^2 v^2 t^2)^{\frac{3}{2}}} = -\frac{\beta\gamma E_0}{(1 + (\frac{t}{\tau})^2)^{\frac{3}{2}}} \\
B_z &= 0
\end{aligned}$$

with  $\tau = \frac{b}{\gamma v}$  and  $E_0 = \frac{eZ_p}{b^2}$ .  $\tau$  defines the collision time.

After expanding  $\phi$  and  $\mathbf{A}$  in multipole moments Winther and Alder [5] obtain the following excitation amplitudes

$$a_{i \rightarrow f} = -i \frac{Z_t e^2}{\hbar \gamma v} \sum_{\pi \lambda \mu} G_{\pi \lambda \mu} \left( \frac{c}{v} \right) (-)^{\mu} K_{\mu}(\xi(b)) \sqrt{2\lambda + 1} k^{\lambda} \frac{\langle I_f M_f | \mathcal{M}(\pi \lambda - \mu | I_i M_i) \rangle}{e}, \quad (\text{A.10})$$

with (for  $\mu \geq 0$ )

$$\begin{aligned}
G_{E\lambda\mu} \left( \frac{c}{v} \right) &= i^{\lambda+\mu} \frac{\sqrt{16\pi}}{\lambda(2\lambda+1)!!} \left( \frac{(\lambda-\mu)!}{(\lambda+\mu)!} \right)^{\frac{1}{2}} \left( \left( \frac{c}{v} \right) - 1 \right)^{-\frac{1}{2}} \\
&\times \left( \frac{(\lambda+1)(\lambda+\mu)}{2\lambda+1} P_{\lambda-1}^{\mu} \left( \frac{c}{v} \right) - \frac{\lambda(\lambda-\mu+1)}{2\lambda+1} P_{\lambda+1}^{\mu} \left( \frac{c}{v} \right) \right)
\end{aligned}$$

for electric excitations ( $\pi = E$ ) and

$$G_{M\lambda\mu} \left( \frac{c}{v} \right) = i^{\lambda+\mu+1} \frac{\sqrt{16\pi}}{\lambda(2\lambda+1)!!} \left( \frac{(\lambda-\mu)!}{(\lambda+\mu)!} \right)^{\frac{1}{2}} \left( \left( \frac{c}{v} \right) - 1 \right)^{-\frac{1}{2}} \mu P_{\lambda}^{\mu} \left( \frac{c}{v} \right) \quad (\text{A.11})$$

for magnetic excitations ( $\pi = M$ ).  $P_{\lambda}^{\mu}(x)$  are associated Legendre functions evaluated for  $x > 1$ . For  $\mu < 0$  the following relations can be used

$$G_{E\lambda-\mu} = (-)^{\mu} G_{E\lambda\mu} \quad \text{and} \quad G_{M\lambda-\mu} = -(-)^{\mu} G_{M\lambda\mu}. \quad (\text{A.12})$$

Even though  $\mu$  is listed as a summation index it is actually fixed by the nuclear matrix element to be

$$\mu = M_f - M_i \quad (\text{A.13})$$

and can be identified with the angular momentum transfer along the beam direction.

The quantity  $\xi(b)$  is the adiabaticity parameter given by

$$\xi(b) = \frac{\omega_{fi}}{v\gamma} \left( b + \frac{\pi a_0}{2\gamma} \right) \quad (\text{A.14})$$

where  $a_0$  is the half-distance of closest approach in head-on collisions, assuming the nuclei are point-like and if *non-relativistic* kinematics is used

$$a_0 = \frac{Z_t Z_p e^2}{m_0 v^2}. \quad (\text{A.15})$$

$m_0$  is the reduced mass of the two nuclei. The second term in the parentheses in equation (A.14) is a correction term that takes the recoil of the target nucleus into account. This expression is obtained by comparing the relativistic result with the low-energy Coulomb excitation result when large impact parameters are considered, therefore justifying the use of straight line trajectories [5].

### A.1.1 Cross Sections

The excitation cross section is obtained by integrating the product of the Rutherford cross section and the excitation probability. A sum over final and an average over initial magnetic substates must be performed, since they are not observed in the experiment.

$$\begin{aligned} \sigma_{i \rightarrow f} &= 2\pi \int_{b_{min}}^{\infty} \rho d\rho \frac{1}{2I_i + 1} \sum_{M_i, M_f} |a_{i \rightarrow f}|^2 \\ &= \left( \frac{Z_p e^2}{\hbar c} \right)^2 \sum_{\pi \lambda \mu} k^{2(\lambda-1)} \frac{B_t(\pi \lambda, I_i \rightarrow I_f)}{e^2} \left| G_{\pi \lambda \mu} \left( \frac{c}{v} \right) \right|^2 g_\mu(\xi(b_{min})). \end{aligned}$$

The function  $g_\mu$  is defined as

$$\begin{aligned} g_\mu(\xi(b)) &= 2\pi \left( \frac{\omega}{v\gamma} \right)^2 \int_b^{\infty} \rho d\rho |K_\mu(\xi(\rho))|^2 \\ &= 2\pi \int_\xi^{\infty} |K_\mu(x)|^2 x dx \\ &= \pi \xi^2 \left[ |K_{\mu+1}(\xi)|^2 - |K_\mu(\xi)|^2 - \frac{2\mu}{\xi} K_{\mu+1}(\xi) K_\mu(\xi) \right]. \end{aligned}$$

The  $K_\mu$  are modified Bessel functions.

The above expressions have been programmed using MATHEMATICA [53]. Given below is the MATHEMATICA code for the symbolic definitions (one can use them

for symbolic calculations as well as for numerical ones) of the functions  $G_{E\lambda\mu}\left(\frac{c}{v}\right)$  and  $g_\mu(\xi)$ . The code is very compact, illustrating the power of MATHEMATICA.

```

GE[lam_,mu_,invtbeta_]:= (-1)^mu * GE[lam,-mu,invtbeta] /; (mu<0)
GE[lam_,mu_,invtbeta_]:=
  I^(lam+mu) *
  Sqrt[16 Pi]/(lam*(2 lam +1)!!) *
  Sqrt[(lam-mu)!/(lam+mu)!] *
  Sqrt[invtbeta^2 - 1]^(-1) *
  (
  (lam+1)(lam+mu)/(2 lam + 1) * LegendreP[lam-1,mu,invtbeta, LegendreType -> Complex ] -
  lam * (lam-mu+1)/(2 lam + 1) * LegendreP[lam+1,mu,invtbeta, LegendreType->Complex ]
  )
  /; ( (invtbeta > 1)&& (mu<=lam) && (mu>=0) ) )
gAl[mu_,xi_]:= Module[{mupos},
  mupos=Abs[mu];
  Pi xi^2 ( Abs[BesselK[mupos+1,xi]]^2 - Abs[BesselK[mupos,xi]]^2 -
  2 mupos/xi BesselK[mupos+1,xi] BesselK[mupos,xi] ) ]

```

## A.1.2 Relation Between Impact Parameter and Deflection Angle

The impact parameter can be related to the scattering angle by calculating the momentum transfer. In lowest order the momentum transfer to the target nucleus is

$$p_x^{(t)}(t) = \int_{-\infty}^t - \left( \frac{\partial \phi_p(t)}{\partial x} \right)_{\mathbf{r}=0} Z_t e dt. \quad (\text{A.16})$$

The subscript  $\mathbf{r} = 0$  means that we evaluate the field (generated by the projectile) at the original position of the target nucleus, which is the origin of the coordinate system. Evaluation of the integral results in

$$p_x^{(t)}(\infty) = -\frac{2Z_t Z_p e^2}{bv}, \quad (\text{A.17})$$

where  $Z_{t,p}$  are the proton numbers of target and projectile,  $b$  is the impact parameter, and  $v$  is the projectile velocity. Since the total momentum is conserved the momentum transfer to the projectile is the same (but opposite in sign)

$$p_x^{(p)}(\infty) = -p_x^{(t)}(\infty) = \frac{2Z_t Z_p e^2}{bv}. \quad (\text{A.18})$$

The momentum in the  $\mathbf{z}$ -direction is almost unchanged and given by the product of the relativistic factor  $\gamma$ , the (initial) velocity of the projectile  $v$ , and the projectile mass  $m_p$ ,

$$p_z = \gamma m_p v . \quad (\text{A.19})$$

Hence, the deflection angle in the laboratory is given by

$$\theta_{lab} = \frac{p_x}{p_z} = \frac{2Z_t Z_p e^2}{\gamma m_p v^2} b^{-1} , \quad (\text{A.20})$$

where small angles have been assumed. Alternatively one can use the equation of motion in the center of mass system and calculate the scattering angle as a function of impact parameter assuming a relativistic Coulomb trajectory [54]

$$b = \frac{a_0}{\gamma} \cot\left(\frac{1}{2}\theta_{cm}\right) \quad \text{with} \quad a_0 = \frac{Z_p Z_t e^2}{m_0 v^2} . \quad (\text{A.21})$$

The relation between the laboratory and the center of mass angle is given by equation C.46. Both methods give identical results (within the approximations).

## A.2 Some Formulas

In the following a list of useful equations is given. The relations will not be derived.

### A.2.1 Relations between $\beta_2$ , $Q_0$ , $\mathbf{B}(\mathbf{E}2)$ . . .

The nuclear radius for an axially symmetric nucleus is given by

$$R(\theta) = R_0(1 + \beta_2 Y_{20}(\theta, \phi)) . \quad (\text{A.22})$$

Multipole moments are defined as

$$Q_{LM} = \frac{1}{e} \int \rho(\mathbf{r}) r^L Y_{LM}(\theta, \phi) d\mathbf{r} , \quad (\text{A.23})$$

$$Q_{ij} = \int \rho(\mathbf{r})(3x_i x_j - r^2 \delta_{ij}) d\mathbf{r} , \text{ and for } L=0 \text{ and } M=2 \quad (\text{A.24})$$

$$Q_{20} = \sqrt{\frac{16\pi}{5}} \frac{3}{4\pi} Z e R_0 \beta_2, \quad (\text{A.25})$$

where  $\beta_2$  is the quadrupole deformation parameter,  $R_0$  is the nuclear radius (e.g.  $R_0 = 1.2 \text{ fm} A^{\frac{1}{3}}$ ), and  $Z$  is the nuclear proton number. In first order approximation, the deformation  $\beta_2$  is related to the B(E2) through

$$\beta_2 = \frac{4\pi}{3} \sqrt{B(E2; 0^+ \rightarrow 2^+)} \frac{1}{Z e R_0^2}. \quad (\text{A.26})$$

Electromagnetic transition probabilities are given by

$$\mathcal{W}(\pi\lambda, J_i \rightarrow J_f) = \frac{8\pi(\lambda+1)}{\lambda((2\lambda+1)!!)^2} \frac{k^{2\lambda+1}}{\hbar} B(\pi\lambda; J_i \rightarrow J_f) \quad \text{with} \quad k = \frac{p}{\hbar} = \frac{E_\gamma}{\hbar c}. \quad (\text{A.27})$$

The transition probability is related to the lifetime  $T$  and half-lifetime  $T_{\frac{1}{2}}$

$$T = \mathcal{W}^{-1} = \frac{T_{\frac{1}{2}}}{\ln 2}. \quad (\text{A.28})$$

The  $B(\pi\lambda)$  values are defined as

$$\begin{aligned} B(\pi\lambda, 0 \rightarrow \lambda) &= \sum_{\mu M_f} |\langle J_f M_f | \mathcal{M}(\pi\lambda\mu) | J_i M_i \rangle|^2 \\ &= \frac{1}{2J_i + 1} |\langle J_f || \mathcal{M}(\pi\lambda) || J_i \rangle|^2. \end{aligned}$$

Energy-weighted electromagnetic sum-rules from [5]

$$\sum_f B(\pi\lambda, i \rightarrow f) \cdot (E_f - E_i) = \begin{cases} 14.8 \frac{NZ}{A} e^2 \text{fm}^2 \cdot \text{MeV} & \text{for } \lambda = 1 \\ 5.0 \lambda(2\lambda + 1) Z R^{2\lambda-2} e^2 \text{fm}^2 \cdot \text{MeV} & \text{for } \lambda \geq 2, \end{cases} \quad (\text{A.29})$$

with  $R \approx 1.2 A^{\frac{1}{3}} \text{fm}$ .

Single particle estimates (Weisskopf units) are defined as [9]

$$B_w(E\lambda) = \frac{1}{4\pi} \left( \frac{2}{\lambda + 3} \right)^2 R^{2\lambda} e^2, \quad (\text{A.30})$$

and

$$B_w(M\lambda) = \frac{10}{\pi} \left( \frac{2}{\lambda + 3} \right)^2 R^{2(\lambda-1)} \mu_N^2. \quad (\text{A.31})$$

## A.2.2 Constants

$$\hbar c = 197 \text{ MeV fm} \quad (\text{A.32})$$

$$\alpha = \frac{1}{137} \quad (\text{A.33})$$

$$e^2 = \alpha \hbar c = 1.44 \text{ MeV fm} \quad (\text{A.34})$$

$$\mu_N = \frac{e \hbar c}{2M_p c^2} \quad (\text{A.35})$$

# Appendix B

## $\gamma$ -Ray Angular Distribution

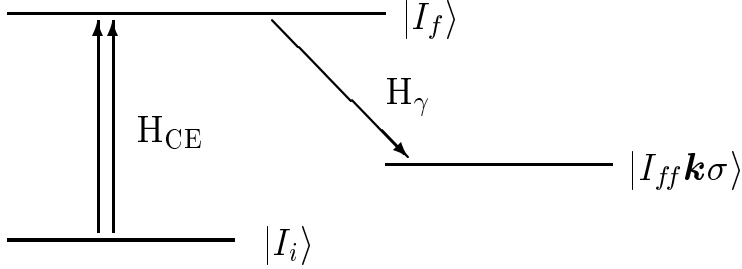
### Following Relativistic Coulomb

### Excitation

The excitation process does not populate the magnetic substates of the excited state evenly and hence the angular distribution of emitted photons will be anisotropic. In order to determine the detection efficiency the angular distribution of photons must be calculated and included in equation (2.33). In the following the  $\gamma$ -ray angular distribution for intermediate energy Coulomb excitation is derived.

## B.1 General Structure

Perturbation theory is applied to the process



Here  $H_{\text{CE}}$  and  $H_\gamma$  represent the interaction Hamiltonians for Coulomb excitation and radiative  $\gamma$ -decay, respectively. The amplitudes for the two processes are given by

$$a_{i \rightarrow f} = \langle I_f M_f | H_{\text{CE}} | I_i M_i \rangle \quad (\text{B.1})$$

and

$$a_{f \rightarrow ff} = \langle I_{ff} M_{ff} \mathbf{k} \sigma | H_\gamma | I_f M_f \rangle, \quad (\text{B.2})$$

where the final state consists not only of a nuclear state but also of a photon state with wave-vector  $\mathbf{k}$  and polarization  $\sigma$ . The amplitude for the whole process is then given by

$$\begin{aligned} a_{i \rightarrow ff} &:= a_{i \rightarrow f \rightarrow ff} = \sum_{M_f} a_{i \rightarrow f} a_{f \rightarrow ff} \\ &= \sum_{M_f} a_{i \rightarrow f} \langle I_{ff} M_{ff} \mathbf{k} \sigma | H_\gamma | I_f M_f \rangle \end{aligned}$$

where the sum goes over all possible magnetic quantum numbers of the intermediate state.<sup>1</sup>

---

<sup>1</sup>One could view this process also as one where the state  $|f\rangle = \sum_{M_f} a_{i \rightarrow f} |I_f M_f\rangle$  decays to state  $|ff\rangle = |I_{ff} M_{ff} \mathbf{k} \sigma\rangle$ , from which follows that

$$a_{i \rightarrow ff} = \langle ff | H_\gamma | f \rangle = \sum_{M_f} a_{i \rightarrow f} \langle I_{ff} M_{ff} \mathbf{k} \sigma | H_\gamma | I_f M_f \rangle \quad (\text{B.3})$$

From the transition amplitude one gets the transition probability by taking the absolute square, summing over final magnetic substates and polarizations and averaging over the initial magnetic substates. Since the final result is an angular distribution which will be normalized to unity at the end, constant factors in the equations will be dropped without special notice; e.g. the factor  $\frac{1}{2I_i+1}$  from the averaging over the initial magnetic quantum number ( $M_i$ ) is not shown in B.4. The angular dependence of the transition probability is due to the presence of the vector  $\mathbf{k}$  in the amplitude  $a_{i \rightarrow ff}$ .  $\theta$  and  $\varphi$  are the spherical coordinates of the vector  $\mathbf{k}$ .

$$\begin{aligned}
W(\theta, \varphi) &= \sum_{M_i, M_{ff}, \sigma} |a_{i \rightarrow ff}|^2 \\
&= \sum_{M_i, M_{ff}, \sigma} \left| \sum_{M_f} a_{i \rightarrow f} \langle I_{ff} M_{ff} \mathbf{k} \sigma | H_\gamma | I_f M_f \rangle \right|^2 \\
&= \sum_{\substack{M_i, M_{ff}, \sigma \\ M_f, M'_f}} a_{i \rightarrow f} a_{i \rightarrow f'}^* \langle I_{ff} M_{ff} \mathbf{k} \sigma | H_\gamma | I_f M_f \rangle \\
&\quad \times \langle I_{ff} M_{ff} \mathbf{k} \sigma | H_\gamma | I_f M'_f \rangle^*
\end{aligned} \tag{B.4}$$

## B.2 Detailed Derivation

### B.2.1 What is $\langle I_{ff} M_{ff} \mathbf{k} \sigma | H_\gamma | I_f M_f \rangle$ ?

$H_\gamma$  is a scalar operator, a spherical tensor operator of rank zero. This is clear from rotational symmetry.

Usually  $H_\gamma$  is expanded into a nuclear part and a (external) field part

$$H_\gamma = \sum_{\lambda, \mu} \mathbf{O}_{\lambda\mu}^{(nuc)} \mathbf{O}_{\lambda\mu}^{(field)}, \tag{B.5}$$

where the operator  $\mathbf{O}_{\lambda\mu}^{(nuc)}$  is a spherical tensor of rank  $\lambda$ , which usually appears in textbooks to derive transition probabilities. The difference is that  $\mathbf{O}^{(nuc)}$  operates between two nuclear states and  $\mathbf{O}^{(field)}$  operates between a one photon and a vacuum

state. The product of the two amplitudes can be related to the transition probability for one particular multipolarity  $\lambda$ . This expansion of  $H_\gamma$  is not needed for this derivation. The only information needed is that  $H_\gamma$  is a *scalar* operator.

In order to use this property  $H_\gamma$  needs to be sandwiched between angular momentum eigenstates. The nuclear part is already fine, but the photon part is given in plane wave eigenstates. Therefore we insert a complete set of photon angular momentum states:

$$\begin{aligned}
& \langle I_{ff} M_{ff} \mathbf{k} \sigma | H_\gamma | I_f M_f \rangle \\
&= \sum_{L,M} \langle I_{ff} M_{ff} \mathbf{k} \sigma | I_{ff} M_{ff} LM \rangle \langle I_{ff} M_{ff} LM | H_\gamma | I_f M_f \rangle \\
&= \sum_{L,M} \langle \mathbf{k} \sigma | LM \rangle \langle I_{ff} M_{ff} LM | H_\gamma | I_f M_f \rangle \\
&= \sum_{\substack{L,M \\ L',M'}} \langle \mathbf{k} \sigma | LM \rangle \langle I_{ff} M_{ff} LM | L' M' \rangle \langle L' M' | H_\gamma | I_f M_f \rangle \\
&= \sum_{L,M} \langle \mathbf{k} \sigma | LM \rangle \langle I_{ff} M_{ff} LM | I_f M_f \rangle \frac{1}{\sqrt{2I_f + 1}} \langle I_f || H_\gamma || I_f \rangle .
\end{aligned}$$

From the second to the third line the nuclear part in the first bracket was dropped. In the fourth line another complete set of states was inserted to express  $|ff\rangle$  in terms of the total angular momentum. To get to the last line the Wigner-Eckart-theorem was used.

$\langle \mathbf{k} \sigma | LM \rangle$  is the overlap between a photon-state with wavevector  $\mathbf{k}$  and polarization  $\sigma$  with another photon state with sharp angular momentum  $L$  and projection  $M$ . We can rewrite  $|\mathbf{k} \sigma\rangle$  in terms of  $|\mathbf{z} \sigma\rangle$  by using the rotation operator

$$|\mathbf{k} \sigma\rangle = R(\mathbf{z} \rightarrow \mathbf{k}) |\mathbf{z} \sigma\rangle . \quad (\text{B.6})$$

Inserting a complete set of states and multiplying by  $\langle LM|$  from the left gives

$$\langle LM | \mathbf{k} \sigma \rangle = \sum_{L'M'} \langle LM | R(\mathbf{z} \rightarrow \mathbf{k}) | L' M' \rangle \langle L' M' | \mathbf{z} \sigma \rangle . \quad (\text{B.7})$$

The rotation operator  $R(\mathbf{z} \rightarrow \mathbf{k})$  connects only states of the same angular momentum

and the sum reduces to a sum over  $M'$  only.

$$\langle LM|\mathbf{k}\sigma\rangle = \sum_{M'} \langle LM|R(\mathbf{z} \rightarrow \mathbf{k})|LM'\rangle \langle LM'|\mathbf{z}\sigma\rangle \quad (\text{B.8})$$

$$= \sum_{M'} (D_{MM'}^L(\mathbf{z} \rightarrow \mathbf{k}))^* \langle LM'|\mathbf{z}\sigma\rangle, \quad (\text{B.9})$$

where the  $D_{MM'}^L$  are the matrix elements of the rotation operator in the angular momentum basis (see equation B.20). To find an expression for  $\langle LM|\mathbf{z}\sigma\rangle$ , which is the angular momentum representation of a photon traveling in the  $\mathbf{z}$  direction, one has to expand the photon field in terms of angular momentum eigenfunctions which was done e.g. in [55]. The result is<sup>2</sup>

$$\langle \mathbf{z}\sigma|LM\pi\rangle = \begin{cases} \sqrt{\frac{2L+1}{2}} \delta_{\sigma M} & : \quad \pi = (-)^L \\ \sqrt{\frac{2L+1}{2}} \sigma \delta_{\sigma M} & : \quad \pi = (-)^{(L+1)} \end{cases} \quad (\text{B.10})$$

Here  $\delta_{\alpha\beta}$  is the usual Kronecker Delta. The  $\sigma$  in the second line is very important. Combining equations B.8 and B.10 it follows that

$$\langle \mathbf{k}\sigma|LM\rangle = \sqrt{\frac{2L+1}{2}} D_{M\sigma}^L(\mathbf{z} \rightarrow \mathbf{k}) [\delta_{\mathbf{E}L} + \sigma \delta_{\mathbf{M}L}]. \quad (\text{B.11})$$

Hence the following expression for the matrix-elements<sup>3</sup> of  $H_\gamma$  are obtained

$$\begin{aligned} \langle I_{ff} M_{ff} \mathbf{k}\sigma | H_\gamma | I_f M_f \rangle &= \sum_{L,M} \sqrt{2L+1} \langle I_{ff} M_{ff} LM | I_f M_f \rangle \\ &\quad \times D_{M\sigma}^L(\mathbf{z} \rightarrow \mathbf{k}) [\delta_{\mathbf{E}L} + \sigma \delta_{\mathbf{M}L}], \end{aligned}$$

where the  $\delta_{\pi L}$  are factors which are given explicitly in e.g. [56], but this information is not needed in this derivation. The  $\delta_{\pi L}$ 's can be related to the mixing ratio for mixed multipole transitions.

---

<sup>2</sup>At this point we also have to introduce parity, which was not needed so far; in the previous formulas parity was implicitly contained in the summation over  $L$  since for gamma decay  $\pi$  and  $L$  are not independent as soon as the nuclear spins are given.

<sup>3</sup>See also [56] page 329

## B.2.2 The Angular Distribution

Putting the matrix elements of  $H_\gamma$  into the expression for the angular distribution

B.4 one gets

$$\begin{aligned}
 W(\theta, \varphi) = & \sum_{\substack{M_i, M_{ff}, \sigma \\ M_f, M'_f \\ L, M, L', M'}} a_{i \rightarrow f} a_{i \rightarrow f'}^* \sqrt{(2L+1)(2L'+1)} \\
 & \times \begin{pmatrix} I_{ff} & L & I_f \\ M_{ff} & M & -M_f \end{pmatrix} \begin{pmatrix} I_{ff} & L' & I_f \\ M_{ff} & M' & -M'_f \end{pmatrix} (-)^{(-L+M_f)+(-L'+M'_f)} \\
 & \times D_{M\sigma}^L D_{M'\sigma'}^{L'} [\delta_{E_L} + \sigma \delta_{M_L}] [\delta_{E_{L'}} + \sigma \delta_{M_{L'}}]^*,
 \end{aligned} \tag{B.12}$$

where the Clebsch-Gordan Coefficients have been replaced by expressions involving  $3j$ -symbols (B.28).  $D_{M\sigma}^L D_{M'\sigma'}^{L'}$  can be evaluated as follows<sup>4</sup>:

$$\begin{aligned}
 D_{M\sigma}^L D_{M'\sigma'}^{L'} & = (-)^{M'-\sigma} D_{M\sigma}^L D_{-M'-\sigma}^{L'} \\
 & = (-)^{M'-\sigma} \sum_{j, m, m'} (2j+1) \begin{pmatrix} L & j & L' \\ M & m & -M' \end{pmatrix} \begin{pmatrix} L & j & L' \\ \sigma & m' & -\sigma \end{pmatrix} D_{mm'}^j \\
 & = (-)^{M'-\sigma} \sum_{j, m} (2j+1) \begin{pmatrix} L & j & L' \\ M & m & -M' \end{pmatrix} \begin{pmatrix} L & j & L' \\ \sigma & 0 & -\sigma \end{pmatrix} D_{m0}^j(\alpha, \beta, \gamma) \\
 & = (-)^{M'-\sigma} \sum_{j, m} \sqrt{2j+1} \begin{pmatrix} L & j & L' \\ M & m & -M' \end{pmatrix} \begin{pmatrix} L & j & L' \\ \sigma & 0 & -\sigma \end{pmatrix} Y_{jm}(\beta, \alpha)
 \end{aligned}$$

Here, use has been made of the relations B.23, B.25, and B.27.

Using B.35 one can evaluate the sum over  $M_{ff}$  which only occurs in the first two  $3j$ -symbols in B.12

$$\begin{aligned}
 & \sum_{M_{ff}} \begin{pmatrix} I_{ff} & L' & I_f \\ M_{ff} & M' & -M'_f \end{pmatrix} \begin{pmatrix} I_{ff} & L & I_f \\ M_{ff} & M & -M_f \end{pmatrix} \\
 & = (-)^{2L+I_{ff}+M'-M_f} \sum_{k, \kappa} (-)^k (2k+1) \begin{pmatrix} L' & L & k \\ M' & -M & \kappa \end{pmatrix} \\
 & \quad \times \begin{pmatrix} I_f & I_f & k \\ M'_f & -M_f & \kappa \end{pmatrix} \left\{ \begin{matrix} L' & L & k \\ I_f & I_f & I_{ff} \end{matrix} \right\},
 \end{aligned}$$

---

<sup>4</sup>if no arguments are given we always assume the same Euler angles

with the following result:

$$\begin{aligned}
W(\theta, \varphi) &= \sum_{\substack{M_i, \sigma, k, \kappa \\ M_f, M'_f \\ L, M, L', M'}} a_{i \rightarrow f} a_{i \rightarrow f'}^* \sqrt{(2L+1)(2L'+1)} (2k+1) \\
&\quad \times \begin{pmatrix} L & L' & k \\ M & -M' & \kappa \end{pmatrix} \begin{pmatrix} I_f & I_f & k \\ M_f & -M'_f & \kappa \end{pmatrix} \begin{Bmatrix} L & L' & k \\ I_f & I_f & J \end{Bmatrix} \\
&\quad \times (-)^{(M_f-L)+(M'_f-L')+(2L+M'-M_f)+k} \\
&\quad \times (-)^{M'-\sigma} \sum_{j,m} (2j+1) \begin{pmatrix} L & j & L' \\ M & m & -M' \end{pmatrix} \begin{pmatrix} L & j & L' \\ \sigma & 0 & -\sigma \end{pmatrix} Y_{jm}^* \delta_L \delta_{L'} .
\end{aligned}$$

Here,  $\delta_\lambda$  stands for  $[\delta_{E\lambda} + \sigma\delta_{M\lambda}]$ . The sum over  $M$  and  $M'$  can now be performed:

$$\begin{aligned}
&\sum_{M, M'} (-)^{2M'} \begin{pmatrix} L & L' & k \\ M & -M' & \kappa \end{pmatrix} \begin{pmatrix} L & j & L' \\ M & m & -M' \end{pmatrix} \\
&= \sum_{M, M'} \begin{pmatrix} L & L' & k \\ M & -M' & \kappa \end{pmatrix} \begin{pmatrix} L & j & L' \\ M & m & -M' \end{pmatrix} \\
&= \sum_{M, M'} \begin{pmatrix} L & L' & k \\ M & -M' & \kappa \end{pmatrix} \begin{pmatrix} L & L' & j \\ M & -M' & m \end{pmatrix} (-)^{L+L'+j} \\
&= \frac{(-)^{L+L'+k}}{2k+1} \delta_{kj} \delta_{m\kappa} .
\end{aligned}$$

Summing over  $\sigma$  yields:

$$\sum_{\sigma=\{1,-1\}} \begin{pmatrix} L & j & L' \\ \sigma & 0 & -\sigma \end{pmatrix} \delta_L \delta_{L'} = \begin{cases} 2 \begin{pmatrix} L & j & L' \\ 1 & 0 & -1 \end{pmatrix} \delta_L \delta_{L'} & : j \text{ even} \\ 0 & : j \text{ odd} \end{cases}$$

To get this result the symmetry properties of the  $3j$ -symbol (B.30) and the *parity selection rules* for  $E\lambda$  and  $M\lambda$  transitions were used.<sup>5</sup>

$$\pi_1 \pi_2 = \begin{cases} (-)^L & : \text{ for } E\lambda \text{ transitions} \\ (-)^{L+1} & : \text{ for } M\lambda \text{ transitions} \end{cases} \quad (\text{B.13})$$

Therefore

$$W(\theta, \varphi) = \sum_{\substack{k \text{ even}, \kappa, M_i \\ M_f, M'_f, L, L'}} a_{i \rightarrow f} a_{i \rightarrow f'}^* \sqrt{(2L+1)(2L'+1)} (2k+1)$$

---


$${}^5 \text{e.g.: for } \pi_1 \pi_2 = + \text{ and } \begin{Bmatrix} L = \text{even} \\ L = \text{odd} \end{Bmatrix} \Rightarrow \begin{Bmatrix} \delta_L = \delta_{E L} \\ \delta_L = \underline{\sigma} \delta_{M L} \end{Bmatrix}$$

$$\begin{aligned}
& \times \begin{pmatrix} I_f & I_f & k \\ M_f & -M'_f & \kappa \end{pmatrix} \begin{pmatrix} L & k & L' \\ 1 & 0 & -1 \end{pmatrix} \begin{Bmatrix} L & L' & k \\ I_f & I_f & I_{ff} \end{Bmatrix} \\
& \times (-)^{(M_f-L)+(M'_f-L')+(2L-M_f)+(L+L'+k)+k} \\
& \times Y_{k\kappa}^* \delta_L \delta_{L'} \\
= & \sum_{\substack{k \text{ even}, \kappa, M_i \\ M_f, M'_f, L, L'}} a_{i \rightarrow f} a_{i \rightarrow f'}^* \sqrt{(2L+1)(2L'+1)(2k+1)} \\
& \times \begin{pmatrix} I_f & I_f & k \\ M_f & -M'_f & \kappa \end{pmatrix} \begin{pmatrix} L & k & L' \\ 1 & 0 & -1 \end{pmatrix} \begin{Bmatrix} L & L' & k \\ I_f & I_f & I_{ff} \end{Bmatrix} \\
& \times (-)^{M'_f} Y_{k\kappa}^* \delta_L \delta_{L'} \\
= & \sum_{\substack{k \text{ even}, \kappa, M_i \\ M_f, M'_f, L, L'}} a_{i \rightarrow f} a_{i \rightarrow f'}^* \begin{pmatrix} I_f & I_f & k \\ M_f & -M'_f & \kappa \end{pmatrix} \\
& \times (-)^{M'_f} F_k(L, L', I_{ff}, I_f) Y_{k\kappa}^* \delta_L \delta_{L'}
\end{aligned}$$

If particles are detected symmetrically around the z-axis one can integrate over  $\varphi_{\text{particle}}$  which is equivalent to integrating, or averaging, over  $\varphi_\gamma$ . Using B.36 yields the final result:

$$\begin{aligned}
W(\theta) &= \sum_{\substack{k \text{ even}, M_i \\ M_f, M'_f, L, L'}} a_{i \rightarrow f} a_{i \rightarrow f'}^* \begin{pmatrix} I_f & I_f & k \\ M_f & -M'_f & 0 \end{pmatrix} (-)^{M'_f} \\
& \times F_k(L, L', I_{ff}, I_f) \sqrt{2k+1} P_k(\cos(\theta)) \delta_L \delta_{L'} \\
= & \sum_{\substack{k \text{ even}, M_i \\ M_f, L, L'}} a_{i \rightarrow f} a_{i \rightarrow f}^* \begin{pmatrix} I_f & I_f & k \\ M_f & -M_f & 0 \end{pmatrix} (-)^{M_f} \\
& \times F_k(L, L', I_{ff}, I_f) \sqrt{2k+1} P_k(\cos(\theta)) \delta_L \delta_{L'} \\
= & \sum_{\substack{k \text{ even}, M_i \\ M_f, L, L'}} |a_{i \rightarrow f}|^2 \begin{pmatrix} I_f & I_f & k \\ M_f & -M_f & 0 \end{pmatrix} (-)^{M_f} \\
& \times F_k(L, L', I_{ff}, I_f) \sqrt{2k+1} P_k(\cos(\theta)) \delta_L \delta_{L'}
\end{aligned}$$

$$\begin{aligned}
W(\theta) &= \sum_{\substack{k \text{ even}, M_i \\ M_f, L, L'}} |a_{i \rightarrow f}|^2 \begin{pmatrix} I_f & I_f & k \\ M_f & -M_f & 0 \end{pmatrix} (-)^{M_f} \\
& \times F_k(L, L', I_{ff}, I_f) \sqrt{2k+1} P_k(\cos(\theta)) \delta_L \delta_{L'}
\end{aligned} \tag{B.14}$$

## B.3 Angular Distribution Using the Winther and Alder Excitation Amplitudes

Putting the excitation amplitudes from [5] into the expression for the angular distribution B.14 yields<sup>6</sup>

$$\begin{aligned}
 W(\theta) = & \sum_{\substack{k \text{ even}, M_i, \\ M_f, L, L'}} \left| \sum_{\mu} G_{\lambda\mu} \left( \frac{c}{v} \right) K_{\mu}(\xi) (-)^{\mu} (-)^{M_f} \begin{pmatrix} I_f & \lambda & I_i \\ -M_f & -\mu & M_i \end{pmatrix} \right|^2 \\
 & \times \begin{pmatrix} I_f & I_f & k \\ M_f & -M_f & 0 \end{pmatrix} (-)^{M_f} F_k(L, L', I_{ff}, I_f) \sqrt{2k+1} P_k(\cos(\theta)) \delta_L \delta_{L'} .
 \end{aligned}$$

The absolute square of the excitation amplitude can be written as follows

$$\begin{aligned}
 & \left| \sum_{\mu} G_{\lambda\mu} \left( \frac{c}{v} \right) K_{\mu}(\xi) (-)^{\mu} (-)^{M_f} \begin{pmatrix} I_f & \lambda & I_i \\ -M_f & -\mu & M_i \end{pmatrix} \right|^2 \\
 & = \sum_{\mu, \mu'} G_{\lambda\mu} \left( \frac{c}{v} \right) K_{\mu}(\xi) (-)^{\mu} \begin{pmatrix} I_f & \lambda & I_i \\ -M_f & -\mu & M_i \end{pmatrix} \\
 & \quad \times G_{\lambda\mu'} \left( \frac{c}{v} \right)^* K_{\mu'}(\xi)^* (-)^{\mu'} \begin{pmatrix} I_f & \lambda & I_i \\ -M_f & -\mu' & M_i \end{pmatrix} \\
 & = \sum_{\mu} |G_{\lambda\mu} \left( \frac{c}{v} \right)|^2 |K_{\mu}(\xi)|^2 \begin{pmatrix} I_f & \lambda & I_i \\ -M_f & -\mu & M_i \end{pmatrix} \begin{pmatrix} I_f & \lambda & I_i \\ -M_f & -\mu & M_i \end{pmatrix}
 \end{aligned}$$

The last step could be performed since  $\mu$  and  $\mu'$  are fixed by the  $3j$ -symbols. Hence

$$\begin{aligned}
 W(\theta) = & \sum_{\substack{k \text{ even}, M_i, \\ M_f, L, L'}} \sum_{\mu} |G_{\lambda\mu} \left( \frac{c}{v} \right)|^2 |K_{\mu}(\xi)|^2 \begin{pmatrix} I_f & \lambda & I_i \\ -M_f & -\mu & M_i \end{pmatrix} \begin{pmatrix} I_f & \lambda & I_i \\ -M_f & -\mu & M_i \end{pmatrix} \\
 & \times \begin{pmatrix} I_f & I_f & k \\ M_f & -M_f & 0 \end{pmatrix} (-)^{M_f} F_k(L, L', I_{ff}, I_f) \sqrt{2k+1} P_k(\cos(\theta)) \delta_L \delta_{L'} .
 \end{aligned}$$

Using B.35 one can evaluate the sum over  $M_i$  which only occurs in the first two  $3j$ -symbols

$$\begin{aligned}
 & \sum_{M_i} \begin{pmatrix} I_f & \lambda & I_i \\ -M_f & -\mu & M_i \end{pmatrix} \begin{pmatrix} I_f & \lambda & I_i \\ -M_f & -\mu & M_i \end{pmatrix} \\
 & = (-)^{2I_f + I_i - M_f - \mu} \sum_{k', \kappa} (-)^{k'} (2k' + 1) \begin{pmatrix} I_f & I_f & k' \\ -M_f & M_f & \kappa \end{pmatrix} \\
 & \quad \times \begin{pmatrix} \lambda & \lambda & k' \\ \mu & -\mu & \kappa \end{pmatrix} \left\{ \begin{matrix} I_f & I_f & k' \\ \lambda & \lambda & I_i \end{matrix} \right\}
 \end{aligned}$$

---

<sup>6</sup>See [5] or appendix A for a definition of  $G_{\lambda\mu}(\frac{c}{v})$ ,  $K_{\mu}(\xi)$  and  $\xi$ .

$$\begin{aligned}
W(\theta) = & \sum_{\substack{k \text{ even}, \mu \\ M_f, L, L'}} |G_{\lambda\mu}(\frac{c}{v})|^2 |K_\mu(\xi)|^2 (-)^{-M_f-\mu} \sum_{k', \kappa} (-)^{k'} (2k' + 1) \\
& \times \begin{pmatrix} I_f & I_f & k' \\ -M_f & M_f & \kappa \end{pmatrix} \begin{pmatrix} \lambda & \lambda & k' \\ \mu - \mu & \kappa \end{pmatrix} \left\{ \begin{matrix} I_f & I_f & k' \\ \lambda & \lambda & I_i \end{matrix} \right\} \begin{pmatrix} I_f & I_f & k \\ M_f & -M_f & 0 \end{pmatrix} \\
& \times (-)^{M_f} F_k(L, L', I_{ff}, I_f) \sqrt{2k+1} P_k(\cos(\theta)) \delta_L \delta_{L'}
\end{aligned}$$

Summing over the  $M_f$  in the first and the last  $3j$ -symbol (B.29) gives a  $\delta_{k k'} \delta_{0 \kappa}$ .

Therefore

$$\begin{aligned}
W_b(\theta) = & \sum_{\substack{k \text{ even}, \mu \\ L, L'}} |G_{\lambda\mu}(\frac{c}{v})|^2 |K_\mu(\xi)|^2 (-)^\mu \begin{pmatrix} \lambda & \lambda & k \\ \mu - \mu & 0 \end{pmatrix} \\
& \times \left\{ \begin{matrix} I_f & I_f & k \\ \lambda & \lambda & I_i \end{matrix} \right\} F_k(L, L', I_{ff}, I_f) \sqrt{2k+1} P_k(\cos(\theta)) \delta_L \delta_{L'} .
\end{aligned}$$

Here, we also indicated the impact parameter  $b$  in the formula, which was implicitly assumed before. The remaining step is to integrate this formula over impact parameters with a minimum of  $b_{min}$ , which is e.g. determined by  $\theta_{max}$  from the experiment

$$W(\theta) = \int_{b_{min}}^{\infty} W_b(\theta) b db . \quad (\text{B.15})$$

As in appendix A the integral over the square of the modified Bessel function

$$\int_{b_{min}}^{\infty} |K_\mu(\xi)|^2 b db \quad (\text{B.16})$$

can be expressed using the Winther and Alder function  $g_\mu(\xi)$

$$\begin{aligned}
g_\mu(\xi(b)) &= 2\pi \left( \frac{\omega}{v\gamma} \right)^2 \int_b^{\infty} \rho d\rho |K_\mu(\xi(\rho))|^2 \\
&= 2\pi \int_\xi^{\infty} |K_\mu(x)|^2 x dx \\
&= \pi \xi^2 \left[ |K_{\mu+1}(\xi)|^2 - |K_\mu(\xi)|^2 - \frac{2\mu}{\xi} K_{\mu+1}(\xi) K_\mu(\xi) \right] .
\end{aligned}$$

Thus

$$W(\theta) = \sum_{\substack{k \text{ even}, \mu \\ L, L'}} |G_{\lambda\mu}(\frac{c}{v})|^2 g_{\mu}(\xi) (-)^{\mu} \begin{pmatrix} \lambda & \lambda & k \\ \mu & -\mu & 0 \end{pmatrix} \quad (\text{B.17})$$

$$\times \left\{ \begin{matrix} I_f & I_f & k \\ \lambda & \lambda & I_i \end{matrix} \right\} F_k(L, L', I_{ff}, I_f) \sqrt{2k+1} P_k(\cos(\theta)) \delta_L \delta_{L'} . \quad (\text{B.18})$$

Usually the angular distribution is expressed as

$$W(\theta) = \sum_{k \text{ even}} a_k P_k(\cos(\theta)) \quad (\text{B.19})$$

The following the MATHEMATICA code calculates the coefficients  $a_k$  in front of the Legendre polynomials:

```

(* i gets excited to f and decays to ff
StatesI = {{Ji,Pi},{Jf,Pf},{Jff,Pff},delta}
*)
SRules = {
  JiS[x_]  => x[[1,1]], (* initial spin *)
  PiS[x_]  => x[[1,2]], (* initial parity *)
  JfS[x_]  => x[[2,1]], (* excited spin *)
  PfS[x_]  => x[[2,2]], (* excited parity *)
  JffS[x_] => x[[3,1]], (* final spin *)
  PffS[x_] => x[[3,2]], (* final parity *)
  DeltaMixS[x_] => x[[4]] (* mixing for simultaneous E2 and M1 decay *)
}

AngDis[K_,P_,T_,S_]:=
Module[{LamMin,LamMax,ParityChange,kMax,tab,PureElamTransition},
  CalcKin[K,P,T]; (* first do the kinematic calculation *)
  (* check for the involved transitions *)
  LamMin = Abs[JfS[S]-JffS[S]];
  LamMin = Rationalize[LamMin]; (* make sure we have an integer *)
  If[(LamMin==0)&&(JfS[S]+JffS[S]>0),LamMin=1,Print["siw" ]];
  (* there is no M0 or E0 transition *)
  (* find out what multipolarities for deexcitation are possible *)
  If[PfS[S]!=PffS[S],ParityChange=True,ParityChange=False,Print["siw,ParityChange"]];
  If[!IntegerQ[LamMin],Print["LamMin is no integer; LamMin = ",LamMin];Return[]];
  (* we need to consider Elam and M(lam-1) transitions if the following is FALSE *)
  PureElamTransition = (!ParityChange && EvenQ[LamMin]) || (ParityChange && OddQ[LamMin]);
  If[ PureElamTransition,
    LamMax=LamMin, (* Pure ELamMin transition *)
    LamMax=Min[LamMin+1,JfS[S]+JffS[S]], (* for Mlam transition consider next
    higher E transition if at all possible *)
    Print["siw AngularDistrib"];
    Print["LamMax ",LamMax];
    Print["LamMin ",LamMin];
  (* now we can determine the coeff. in front of the P_lm *)
  (* first we determine kMax *)
  kMax=Min[2JfS[S],2LamMax];
  tab=Table[Sum[
  (*
    Print["l1 ",l1];
    Print["l2 ",l2];
    Print["mu ",mu]; *)
    If[l1==LamMin,1,DeltaMixS[S],Print["siw AngularDistrib 2"]] *
    If[l2==LamMin,1,DeltaMixS[S],Print["siw AngularDistrib 3"]] *
    Abs[GE[LamN[P],mu,1/BetaK[K]]]^2 gA1[mu,XiHoK[K]] (-1)^mu *
    ThreeJSymbol[{LamN[P],mu},{LamN[P],-mu},{k,0}] *
    SixJSymbol[{JfS[S],JfS[S],k},{LamN[P],LamN[P],JiS[S]}]
    F[k,JffS[S],l1,l2,JfS[S]] Sqrt[2k+1],
    {l1,LamMin,LamMax},{l2,LamMin,LamMax},
    (* sum over the possible deexcitation multipolarities *)
    {mu,-LamN[P],LamN[P]} (* sum over magnetic QN of excitation *)
  ] (* close Sum *)
  ,{k,0,kMax,2}]; (* close Table-loop *)
  Do[
    Print["a",k," = ", N[ tab[[k/2+1]] / tab[[1]] ] ],{k,0,kMax,2}];
  tab/tab[[1]] // Together
]//.SRules//.NKRules

(* set the necessary attributes for AngDis *)
SetAttributes[AngDis,HoldFirst]

W[theta_,dis_List,K_:1]:=
Module[{Wcm,Wcontracted,Wboost},
  Wcm[t]:= 1/(4Pi) Plus@@ (Table[LegendreP[2k,Cos[t]],{k,0,Length[dis]-1}]^Times^dis);
  If[!ListQ[K], Return[Wcm[theta]] ];
  Wcontracted[t]:= Wcm[t] * DomCmDomLab[t,BetaK[K]] // .KRules;
  Wboost[t]:= Wcontracted[ThetaCm[t,BetaK[K]] ] // .KRules;
  Wboost[theta]
]

```

## B.4 Angular Momentum Re-coupling Coefficients, Rotation Matrices and Related Formulas

The phase convention used for the Clebsch-Gordan coefficients is that of Condon and Shortly [57].

### B.4.1 Angular Momentum Representation of the Rotation Matrix

**Definition**

$$\begin{aligned}
 D_{mm'}^j(\alpha, \beta, \gamma) &:= \langle jm' | \mathcal{R}^{-1}(\alpha, \beta, \gamma) | jm \rangle = \langle jm | \mathcal{R} | jm' \rangle \\
 &= \langle jm' | e^{iJ_z \gamma} e^{iJ_y \beta} e^{iJ_z \alpha} | jm \rangle \\
 &= \langle jm' | e^{im' \gamma} e^{iJ_y \beta} e^{im \alpha} | jm \rangle \\
 &= e^{im' \gamma} d_{mm'}^j(\beta) e^{im \alpha}
 \end{aligned} \tag{B.20}$$

$$d_{mm'}^j(\beta) := \langle jm' | e^{iJ_y \beta} | jm \rangle \tag{B.21}$$

**Symmetry Properties**

$$(D_{M\sigma}^L(\alpha, \beta, \gamma))^* = D_{\sigma M}^L(-\gamma, -\beta, -\alpha) \tag{B.22}$$

$$= (-)^{M-\sigma} D_{-M-\sigma}^L(\alpha, \beta, \gamma) \tag{B.23}$$

$$D_{M\sigma}^L(\alpha, \beta, \gamma) = (-)^{M-\sigma} D_{\sigma M}^L(\gamma, \beta, \alpha) \tag{B.24}$$

**Special Values of Indices**

$$D_{m0}^l(\alpha, \beta, \gamma) = \sqrt{\frac{4\pi}{2l+1}} Y_{lm}(\beta, \alpha) \tag{B.25}$$

$$D_{0\sigma}^l(\alpha, \beta, \gamma) = (-)^\sigma \sqrt{\frac{4\pi}{2l+1}} Y_{l\sigma}(\beta, \gamma) \quad (\text{B.26})$$

**Product of two rotation matrices of the same Eulerian angles  $\theta_i$**

$$\begin{aligned} & D_{m_1\sigma_1}^{j_1}(\theta_i) D_{m_2\sigma_2}^{j_2}(\theta_i) \\ &= \sum_{j,m,\sigma} (2j+1) \begin{pmatrix} j_1 & j & j_2 \\ m_1 & m & m_2 \end{pmatrix} \begin{pmatrix} j_1 & j & j_2 \\ \sigma_1 & \sigma & \sigma_2 \end{pmatrix} D_{m\sigma}^{j*}(\theta_i) \end{aligned} \quad (\text{B.27})$$

## B.4.2 Some Properties of the Clebsch - Gordan - Coefficients and 3j-Symbols

Relation between Clebsch-Gordan-Coefficients and 3j-symbols

$$\langle j_1 j_2 m_1 m_2 | JM \rangle = (-)^{j_1 - j_2 + M} \sqrt{2J+1} \begin{pmatrix} j_1 & j_2 & J \\ m_1 & m_2 & -M \end{pmatrix} \quad (\text{B.28})$$

Orthogonality of the 3j-symbols

$$\sum_{M, M'} \begin{pmatrix} J & J' & j_1 \\ M & M' & m_1 \end{pmatrix} \begin{pmatrix} J & J' & j_2 \\ M & M' & m_2 \end{pmatrix} = \frac{1}{2j_1+1} \delta_{j_1 j_2} \delta_{m_1 m_2} \quad (\text{B.29})$$

$$\begin{pmatrix} J_1 & J_2 & J_3 \\ m_1 & m_2 & m_3 \end{pmatrix} = (-)^{J_1 + J_2 + J_3} \begin{pmatrix} J_1 & J_2 & J_3 \\ -m_1 & -m_2 & -m_3 \end{pmatrix} \quad (\text{B.30})$$

$$= \begin{pmatrix} J_2 & J_3 & J_1 \\ m_2 & m_3 & m_1 \end{pmatrix} \quad (\text{B.31})$$

$$= (-)^{J_1 + J_2 + J_3} \begin{pmatrix} J_2 & J_1 & J_3 \\ m_2 & m_1 & m_3 \end{pmatrix} \quad (\text{B.32})$$

## B.4.3 Some Properties of the 6j-symbols

Symmetries of the 6j-symbols

$$\left\{ \begin{matrix} j_1 & j_2 & j_3 \\ J_1 & J_2 & J_3 \end{matrix} \right\} = \left\{ \begin{matrix} j_2 & j_1 & j_3 \\ J_2 & J_1 & J_3 \end{matrix} \right\} \quad (\text{B.33})$$

$$= \left\{ \begin{matrix} J_1 & J_2 & j_3 \\ j_1 & j_2 & J_3 \end{matrix} \right\} \quad (\text{B.34})$$

Relation between  $3j$ - and  $6j$ -symbols

$$\begin{aligned}
& \sum_l \begin{pmatrix} I & j_1 & j_2 \\ l & m_1 & m_2 \end{pmatrix} \begin{pmatrix} I & J_1 & J_2 \\ l & M_1 & M_2 \end{pmatrix} \\
&= (-)^{2J_1+I+m_1+M_2} \sum_{k,\kappa} (-)^k (2k+1) \begin{pmatrix} j_1 & J_1 & k \\ m_1 & -M_1 & \kappa \end{pmatrix} \\
&\quad \times \begin{pmatrix} j_2 & J_2 & k \\ -m_2 & M_2 & \kappa \end{pmatrix} \left\{ \begin{matrix} j_1 & J_1 & k \\ J_2 & j_2 & I \end{matrix} \right\}
\end{aligned} \tag{B.35}$$

#### B.4.4 $Y_{lm}$

Relation between  $Y_{lm}$  and  $P_l^m$

$$Y_{lm}(\theta, \phi) = \sqrt{\frac{2l+1}{4\pi} \frac{(l-m)!}{(l+m)!}} P_l^m(\cos(\theta)) e^{im\phi} \tag{B.36}$$

#### B.4.5 $\gamma - \gamma$ Correlation Function

Definition

$$\begin{aligned}
F_k(L, L', I_1, I_2) &= (-)^{I_1+I_2-1} \sqrt{(2k+1)(2I_2+1)(2L+1)(2L'+1)} \\
&\quad \times \begin{pmatrix} L & L' & k \\ 1 & -1 & 0 \end{pmatrix} \left\{ \begin{matrix} L & L' & k \\ I_2 & I_2 & I_1 \end{matrix} \right\}
\end{aligned} \tag{B.37}$$



# Appendix C

## Relativistic Kinematics

This chapter develops some formulas that are needed for computer calculations, which are used in chapter 5 to obtain the excitation energy and center of mass scattering angle from the measured particle energy and laboratory scattering angle. We will not have a single formula as a final result, but rather instructions on how to combine certain formulas to obtain what is desired.

The formulas are derived and in the last section a summary is presented.

### C.1 Notation and Preliminaries

We will use the Minkowski notation with  $x_4 = ix_0$  and  $c = 1$ . To obtain the equations with the correct power of  $c$  at the right place, just follow these replacement rules:

$$p \longrightarrow cp \quad , \quad m \longrightarrow mc^2 \quad , \quad \text{and} \quad \beta \longrightarrow \frac{v}{c} \quad (\text{C.1})$$

Repeated indices are summed implicitly.

If one knows a certain 4-vector in one system, one applies a Lorentz transformation to obtain this quantity in a different system. For practical purposes consider only transformations in the  $\mathbf{z}$ -direction since one can obtain others by simply combining

Lorentz transformations and rotations. Assuming:

$$p = \begin{pmatrix} \mathbf{p} \\ i E \end{pmatrix} \quad (\text{C.2})$$

then  $p'$  is obtained through

$$p'_i = \Lambda_{ij} p_j, \quad (\text{summing over } j \text{ is implicit}) \quad (\text{C.3})$$

with  $\Lambda$  given by:

$$\Lambda = \begin{pmatrix} 1 & 0 & 0 & 0 \\ 0 & 1 & 0 & 0 \\ 0 & 0 & \gamma & -i\gamma\beta \\ 0 & 0 & i\gamma\beta & \gamma \end{pmatrix} \quad (\text{C.4})$$

with  $\beta = \frac{v}{c}$  and

$$\gamma = \frac{1}{\sqrt{(1 - \beta^2)}}. \quad (\text{C.5})$$

Consider the 4-momentum of a particle initially at rest

$$p = \begin{pmatrix} 0 \\ i m \end{pmatrix} = \begin{pmatrix} 0 \\ i E_{cm} \end{pmatrix}. \quad (\text{C.6})$$

The momentum after a boost in z-direction with velocity  $\beta$  is given by

$$p' = \Lambda_{ij} p_j = \begin{pmatrix} 0 \\ 0 \\ \gamma\beta m \\ i \gamma m \end{pmatrix}. \quad (\text{C.7})$$

$p'$  can also be written as<sup>1</sup>

$$p' = \begin{pmatrix} 0 \\ 0 \\ p' \\ i E' \end{pmatrix} \quad (\text{C.8})$$

Comparison of the two results yields the following very useful formulas:

$$E = \gamma m \quad \text{and} \quad p = \gamma\beta m = \beta E. \quad (\text{C.9})$$

---

<sup>1</sup>We will use  $p'$  to label both the 4-vector and the magnitude of the total momentum. It should be clear what is meant from the context.

Taking the scalar product of  $p$  with itself yields  $p \cdot p = -m^2$ . Since  $p \cdot p$  is a Lorentz scalar it has to be equal to  $p' \cdot p' = \mathbf{p}^2 - E^2$ . One obtains the well known result

$$E^2 = p^2 + m^2 \tag{C.10}$$

which can alternatively be obtained through the following

$$\begin{aligned} E^2 &= \gamma^2 m^2 = m^2 + (\gamma^2 - 1)m^2 \\ &= m^2 + \gamma^2 \beta^2 m^2 \\ &= m^2 + p^2 . \end{aligned}$$

The first line is an identity and going to the second line the definition of  $\gamma$  (equation C.5) has been used.

We see that  $\Lambda$  operates on the particle states and not on the frame of reference. A boost by  $\beta$  is equivalent to choosing a new frame which moves with velocity  $-\beta$ .

## C.2 Collision of Two Particles

Consider a collision  $B(A, A')B'$ , which means that B is the stationary target and A is the projectile. After the reaction we have the ejectile  $A'$  and the recoil  $B'$ . Figure C.1 and table C.1 show the quantities involved:  $E$  denotes the total energy,  $m$  the rest mass,  $T$  is the kinetic energy defined as  $E - m$ , and  $p$  is the momentum. The subscripts  $_{cm}$  and  $_{lab}$  refer to the center of mass and laboratory coordinate systems, respectively.

To obtain an expression for the total energy in the center of mass system, consider the contraction of the total 4-momentum. This is a Lorentz scalar, meaning that this quantity does not change when going from one frame to another ( $p_{cm} \cdot p_{cm} = p_{lab} \cdot p_{lab}$ )

$$\begin{aligned} p_{cm} \cdot p_{cm} &= -E_{cm}^2 \\ &= p_{lab} \cdot p_{lab} = p_{lab}^2 - E_{lab}^2 \end{aligned}$$

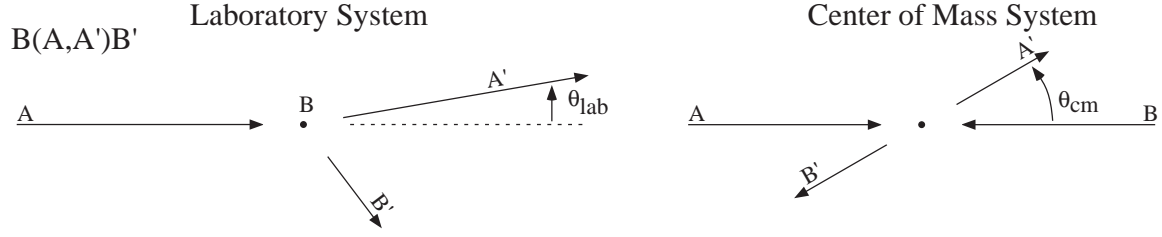


Figure C.1: Schematic drawing of a collision of two particles in the laboratory system and center of mass system. The arrows symbolize the momenta of the particles.

Quantity	Coordinate system	
	laboratory	center of mass
$p_A$	$\begin{pmatrix} 0 \\ 0 \\ p_{A_{lab}} \\ iE_{A_{lab}} \end{pmatrix}$	$\begin{pmatrix} 0 \\ 0 \\ p_{A_{cm}} \\ iE_{A_{cm}} \end{pmatrix}$
$p_B$	$\begin{pmatrix} 0 \\ 0 \\ 0 \\ im_B \end{pmatrix}$	$\begin{pmatrix} 0 \\ 0 \\ p_{B_{cm}} \\ iE_{B_{cm}} \end{pmatrix} = \begin{pmatrix} 0 \\ 0 \\ -p_{A_{cm}} \\ iE_{B_{cm}} \end{pmatrix}$
$p_{A'}$	$\begin{pmatrix} \mathbf{p}_{A'_{lab}} \\ iE_{A'_{lab}} \end{pmatrix} = \begin{pmatrix} p_{A'_{lab}} \sin(\theta_{A'_{lab}}) \\ 0 \\ p_{A'_{lab}} \cos(\theta_{A'_{lab}}) \\ iE_{A'_{lab}} \end{pmatrix}$	$\begin{pmatrix} \mathbf{p}_{A'_{cm}} \\ iE_{A'_{cm}} \end{pmatrix} = \begin{pmatrix} p_{A'_{cm}} \sin(\theta_{A'_{cm}}) \\ 0 \\ p_{A'_{cm}} \cos(\theta_{A'_{cm}}) \\ iE_{A'_{cm}} \end{pmatrix}$
$p_{B'}$	$\begin{pmatrix} \mathbf{p}_{B'_{lab}} \\ iE_{B'_{lab}} \end{pmatrix} = \begin{pmatrix} p_{B'_{lab}} \sin(\theta_{B'_{lab}}) \\ 0 \\ p_{B'_{lab}} \cos(\theta_{B'_{lab}}) \\ iE_{B'_{lab}} \end{pmatrix}$	$\begin{pmatrix} -\mathbf{p}_{A'_{cm}} \\ iE_{B'_{cm}} \end{pmatrix}$
$p = p'$	$\begin{pmatrix} 0 \\ 0 \\ p_{A_{lab}} \\ i(E_{A_{lab}} + m_B) \end{pmatrix} = \begin{pmatrix} 0 \\ 0 \\ p_{A_{lab}} \\ i(E_{lab}) \end{pmatrix}$	$\begin{pmatrix} 0 \\ iE_{cm} \end{pmatrix}$

Table C.1: Momenta of particles before and after scattering in the center of mass frame and the laboratory frame (see also figure C.1).  $p$  is the total momentum of particles A and B combined.

$$\begin{aligned}
&= p_{lab}^2 - (E_{A_{lab}}^2 + 2E_{A_{lab}}m_B + m_B^2) \\
&= -(m_A^2 + 2E_{A_{lab}}m_B + m_B^2),
\end{aligned}$$

where in the last step  $E^2 = p^2 + m^2$  was used. Therefore

$$E_{cm}^2 = 2E_{A_{lab}}m_B + m_A^2 + m_B^2. \quad (\text{C.11})$$

In order to obtain an expression for the energies of the individual particles in the center of mass frame, we use the fact that in the center of mass frame the linear momenta of the two particles add up to zero ( $\mathbf{p}_{A_{cm}} + \mathbf{p}_{B_{cm}} = 0$ ), therefore:

$$\begin{aligned}
\mathbf{p}_{A_{cm}}^2 &= \mathbf{p}_{B_{cm}}^2 \\
E_{A_{cm}}^2 - m_A^2 &= E_{B_{cm}}^2 - m_B^2.
\end{aligned}$$

Using  $E_{cm} = E_{A_{cm}} + E_{B_{cm}}$  to replace e.g.  $E_{A_{cm}}^2$  yields

$$E_{cm}^2 = 2E_{B_{cm}}E_{cm} - m_B^2 + m_A^2 \quad (\text{C.12})$$

or

$$E_{B_{cm}} = \frac{E_{cm}^2 + m_B^2 - m_A^2}{2E_{cm}}. \quad (\text{C.13})$$

From  $E_{B_{cm}}$  one can obtain  $\beta_{B_{cm}}$  through:

$$\begin{aligned}
\gamma_{B_{cm}} &= \frac{E_{B_{cm}}}{m_B} \\
\beta_{B_{cm}} &= \sqrt{1 - \gamma_{B_{cm}}^{-2}}
\end{aligned}$$

Since particle  $B$  is at rest in the laboratory system, the velocity of  $B$  in the center of mass  $\beta_{B_{cm}}$  is equal to the velocity of the center of mass in the laboratory  $\beta_{cm}$ :

$$\beta_{cm} = \beta_{B_{cm}}. \quad (\text{C.14})$$

Other ways to obtain  $\beta_{cm}$  are

$$\beta_{cm} = \frac{p_{lab}}{E_{lab}} = \frac{p_{A_{lab}}}{E_{A_{lab}} + m_B} = \frac{\beta_{A_{lab}}E_{A_{lab}}}{E_{A_{lab}} + m_B} \quad (\text{C.15})$$

or

$$\gamma_{cm} = \frac{E_{lab}}{E_{cm}} = \frac{E_{A_{lab}} + m_B}{E_{cm}} \longrightarrow \beta_{cm} \quad (\text{C.16})$$

$$\beta_{cm} = \sqrt{1 - \gamma_{cm}^{-2}}. \quad (\text{C.17})$$

### C.2.1 Relation Between $\theta_{cm}$ and $\theta_{lab}$

From table C.1

$$p_{A'_{lab}} = \begin{pmatrix} p_{A'_{lab}} \sin(\theta_{A'_{lab}}) \\ 0 \\ p_{A'_{lab}} \cos(\theta_{A'_{lab}}) \\ iE_{A'_{lab}} \end{pmatrix} \quad \text{and} \quad p_{A'_{cm}} = \begin{pmatrix} p_{A'_{cm}} \sin(\theta_{A'_{cm}}) \\ 0 \\ p_{A'_{cm}} \cos(\theta_{A'_{cm}}) \\ iE_{A'_{cm}} \end{pmatrix} \quad (\text{C.18})$$

$p_{A'_{lab}}$  is also given by

$$\begin{aligned} p_{A'_{lab}} &= \Lambda_{cm \rightarrow lab} p_{A'_{cm}} \\ &= \begin{pmatrix} 1 & 0 & 0 & 0 \\ 0 & 1 & 0 & 0 \\ 0 & 0 & \gamma & -i\gamma\beta \\ 0 & 0 & i\gamma\beta & \gamma \end{pmatrix} \begin{pmatrix} p_{A'_{cm}} \sin(\theta_{A'_{cm}}) \\ 0 \\ p_{A'_{cm}} \cos(\theta_{A'_{cm}}) \\ iE_{A'_{cm}} \end{pmatrix} \\ &= \begin{pmatrix} p \sin(\theta) \\ 0 \\ \gamma(p \cos(\theta) + \beta E) \\ i\gamma(\beta p \cos(\theta) + E) \end{pmatrix}_{A'_{lab}} \end{aligned}$$

Three equations result:

$$\begin{aligned} p_{A'_{lab}} \sin(\theta_{A'_{lab}}) &= p_{A'_{cm}} \sin(\theta_{A'_{cm}}) \\ p_{A'_{lab}} \cos(\theta_{A'_{lab}}) &= \gamma(p_{A'_{cm}} \cos(\theta_{A'_{cm}}) + \beta E_{A'_{cm}}) \\ E_{A'_{lab}} &= \gamma(\beta p_{A'_{cm}} \cos(\theta_{A'_{cm}}) + E_{A'_{cm}}) \end{aligned}$$

Dividing the first by the second equation yields

$$\begin{aligned} \tan(\theta_{A'_{lab}}) &= \frac{\sin(\theta_{A'_{cm}})}{\gamma(\cos(\theta_{A'_{cm}}) + \frac{\beta E_{A'_{cm}}}{p_{A'_{cm}}})} \\ &= \frac{\sin(\theta_{A'_{cm}})}{\gamma \left( \cos(\theta_{A'_{cm}}) + \frac{\beta}{\beta_{A'_{cm}}} \right)}. \end{aligned} \quad (\text{C.19})$$

If  $\beta > \beta_{A'_{cm}}$  then there is a maximum scattering angle, which can be found by setting the derivative  $\partial\theta_{A'_{lab}}/\partial\theta_{A'_{cm}}$  equal to zero. The result is

$$\tan(\theta_{A'_{lab}}^{\max}) = \frac{\beta_{A'_{cm}}}{\gamma(\sqrt{\beta^2 - \beta_{A'_{cm}}^2})}. \quad (\text{C.20})$$

Unfortunately there is no closed expression for  $\theta_{A'_{cm}}$ , because there is no closed expression for  $E_{A'_{lab}}$  as a function of  $\theta_{A'_{lab}}$ . To solve numerically one uses the previous formula iteratively until agreement is reached. But the formulas are useful for the special case where one particle is a photon.

$$\begin{aligned} \tan(\theta_{A'_{cm}}) &= \frac{\sin(\theta_{A'_{lab}})}{\gamma\left(\cos(\theta_{A'_{lab}}) - \frac{\beta}{\beta_{A'_{lab}}}\right)} \\ E_{A'_{cm}} &= \gamma(-\beta p_{A'_{lab}} \cos(\theta_{A'_{lab}}) + E_{A'_{lab}}). \end{aligned}$$

## Photons

For photons the previous formulas can be simplified, since the photon (rest) mass is zero and it follows that

$$E = p \quad \text{and} \quad \beta = 1. \quad (\text{C.21})$$

Therefore:

$$\begin{aligned} \tan(\theta_{cm}) &= \frac{\sin(\theta_{lab})}{\gamma(\cos(\theta_{lab}) - \beta)} \\ \tan(\theta_{lab}) &= \frac{\sin(\theta_{cm})}{\gamma(\cos(\theta_{cm}) + \beta)} \\ E_{cm} &= \gamma E_{lab}(1 - \beta \cos(\theta_{lab})) \\ E_{lab} &= \gamma E_{cm}(1 + \beta \cos(\theta_{cm})) \end{aligned}$$

## C.2.2 Solid Angle Relation

To find the relation between the solid angle subtended in the laboratory and the center of mass system use

$$\frac{d\Omega_{lab}}{d\Omega_{cm}} = \frac{d(\cos(\theta_{lab}))}{d(\cos(\theta_{cm}))}. \quad (\text{C.22})$$

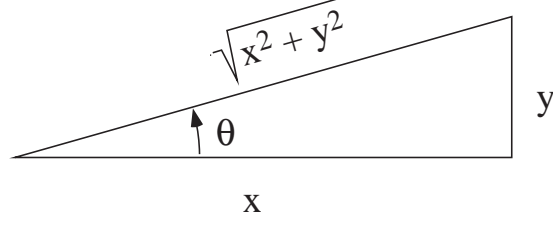


Figure C.2: Relation between  $x, y$ , and  $\theta$ .

From figure C.2 it follows that

$$\tan(\theta) = \frac{y}{x} \quad (\text{C.23})$$

and comparison to equation C.19 shows that  $x$  and  $y$  are given as

$$\begin{aligned} x &= \gamma \left( \cos(\theta_{A'_{cm}}) + \frac{\beta}{\beta_{A'_{cm}}} \right) \\ y &= \sin(\theta_{A'_{cm}}). \end{aligned}$$

In order to find  $\cos(\theta_{lab})$  we use

$$\cos(\theta) = \frac{x}{\sqrt{x^2 + y^2}}. \quad (\text{C.24})$$

Therefore

$$\cos(\theta_{lab}) = \frac{\gamma \left( \cos(\theta_{A'_{cm}}) + \frac{\beta}{\beta_{A'_{cm}}} \right)}{\sqrt{\sin^2(\theta_{A'_{cm}}) + \gamma^2 \left( \cos(\theta_{A'_{cm}}) + \frac{\beta}{\beta_{A'_{cm}}} \right)^2}}. \quad (\text{C.25})$$

With the abbreviations of  $(\sin(\theta_{A'_{cm}}) \rightarrow s)$ ,  $(\cos(\theta_{A'_{cm}}) \rightarrow c)$ , and  $(\frac{\beta}{\beta_{A'_{cm}}} \rightarrow \beta)$  it follows that

$$\begin{aligned} \frac{d(\cos(\theta_{lab}))}{d(\cos(\theta_{cm}))} &= \gamma(\gamma^2(c + \beta)^2 + s^2)^{-\frac{1}{2}} - \gamma(c + \beta)(\gamma^2(c + \beta)^2 + s^2)^{-\frac{3}{2}}(\gamma^2(c + \beta) - c) \\ &= \frac{\gamma(\gamma^2(c + \beta)^2 + s^2) - \gamma(\gamma^2(c + \beta)^2 - c^2 - c\beta)}{(\gamma^2(c + \beta)^2 + s^2)^{\frac{3}{2}}} \\ &= \frac{\gamma(1 + c\beta)}{(\gamma^2(c + \beta)^2 + s^2)^{\frac{3}{2}}}. \end{aligned}$$

After reversing the substitutions

$$\frac{d\Omega_{lab}}{d\Omega_{cm}} = \frac{\gamma \left( 1 + \cos(\theta_{A'_{cm}}) \frac{\beta}{\beta_{A'_{cm}}} \right)}{\left( \gamma^2 \left( \cos(\theta_{A'_{cm}}) + \frac{\beta}{\beta_{A'_{cm}}} \right)^2 + \sin^2(\theta_{A'_{cm}}) \right)^{\frac{3}{2}}}. \quad (\text{C.26})$$

## Photons

For photons the last formula simplifies to

$$\frac{d\Omega_{lab}}{d\Omega_{cm}} = \frac{\gamma(1 - \cos(\theta_{cm})\beta)}{(\gamma^2(\cos(\theta_{cm}) + \beta)^2 + \sin(\theta_{cm})^2)^{\frac{3}{2}}} \quad (\text{C.27})$$

The denominator can further be simplified to (using the same notation as before)

$$\begin{aligned} s^2 + \gamma^2(c + \beta)^2 &= s^2 + \gamma^2c^2 + 2\gamma^2c\beta + \gamma^2\beta^2 \\ &= 1 - c^2 + \gamma^2c^2 + 2\gamma^2c\beta + \gamma^2 - 1 \\ &= (\gamma^2 - 1)c^2 + 2\gamma^2c\beta + \gamma^2 \\ &= \gamma^2(\beta^2c^2 + 2c\beta + 1) \\ &= \gamma^2(1 + \beta c)^2, \end{aligned}$$

where  $\gamma^2\beta^2 = \gamma^2 - 1$  and  $\cos^2 + \sin^2 = 1$  was used. Hence

$$\frac{d\Omega_{lab}}{d\Omega_{cm}} = \frac{1}{\gamma^2(1 + \beta \cos(\theta_{cm}))^2} = \left(\frac{E_{cm}}{E_{lab}}\right)^2. \quad (\text{C.28})$$

## C.3 Decay of $A$ into $B_i \{i=1,2,\dots,N\}$

The 4-vector of particle  $A$  in the center of momentum is given by

$$p_{A_{cm}} = \begin{pmatrix} 0 \\ iE_{cm} \end{pmatrix} = \begin{pmatrix} 0 \\ im_A \end{pmatrix} = p_B = \sum_i p_{B_{cm}^{(i)}} = \begin{pmatrix} 0 \\ i \sum_i E_{B_{lab}^{(i)}} \end{pmatrix}, \quad (\text{C.29})$$

and in the lab

$$p_{A_{lab}} = p_{B_{lab}} = \sum_i \begin{pmatrix} \mathbf{p}_{B_{lab}^{(i)}} \\ iE_{B_{lab}^{(i)}} \end{pmatrix}. \quad (\text{C.30})$$

$p_{A_{cm}}^2$  has to be equal to  $p_{A_{lab}}^2$  and it follows that

$$\begin{aligned} m_A^2 &= - \left( \sum_i p_{B_{lab}^{(i)}} \right)^2 \\ &= \left( \sum_i E_{B_{lab}^{(i)}} \right)^2 - \left( \sum_i \mathbf{p}_{B_{lab}^{(i)}} \right)^2. \end{aligned}$$

$m_A$  calculated in this way is known as the invariant mass. The excitation energy of particle  $A$  is obtained as

$$E_A^* = m_A - m_A^{(0)} , \quad (\text{C.31})$$

and the breakup energy is

$$E_A^{br} = m_A - \sum_i m_{B_i} . \quad (\text{C.32})$$

$m_A^{(0)}$  is the mass of particle  $A$  in its ground state.

## C.4 Summary of Formulas

### C.4.1 General

$$\gamma = \frac{1}{\sqrt{1-\beta^2}} \quad ; \quad \beta = \sqrt{1-\gamma^{-2}} \quad ; \quad \gamma^2\beta^2 = \gamma^2 - 1 \quad (\text{C.33})$$

$$E = \gamma m \quad (\text{C.34})$$

$$p = \beta E \quad (\text{C.35})$$

$$E^2 = p^2 + m^2 \quad (\text{C.36})$$

$$\frac{\partial \gamma}{\partial \beta} = \gamma^3 \beta \quad (\text{C.37})$$

### C.4.2 Total Energy in the Center of Mass System $E_{cm}$

$$E_{cm}^2 = 2E_{A_{lab}}m_B + m_A^2 + m_B^2 \quad \text{with} \quad E_{A_{lab}} = T_{A_{lab}} + m_A \quad (\text{C.38})$$

### C.4.3 Individual Energies in the Center of Mass System

$$E_{A_{cm}} = \frac{E_{cm}^2 + m_A^2 - m_B^2}{2E_{cm}} \quad (\text{C.39})$$

$$E_{B_{cm}} = \frac{E_{cm}^2 + m_B^2 - m_A^2}{2E_{cm}} \quad (\text{C.40})$$

$$E_{A'_{cm}} = \frac{E_{cm}^2 + m_{A'}^2 - m_{B'}^2}{2E_{cm}} \quad (\text{C.41})$$

$$E_{B'_{cm}} = \frac{E_{cm}^2 + m_{B'}^2 - m_{A'}^2}{2E_{cm}} \quad (\text{C.42})$$

#### C.4.4 Velocity of the Center of Mass in the Laboratory $\beta_{cm}$

Equation numbers are given above the arrows.

$$E_{A_{lab}} \xrightarrow{C.38} E_{cm} \xrightarrow{C.34} \gamma_{cm} = \frac{E_{lab}}{E_{cm}} \xrightarrow{C.33} \beta_{cm} \quad (C.43)$$

or

$$E_{A_{lab}} \xrightarrow{C.38} E_{cm} \xrightarrow{C.40} E_{B_{cm}} \xrightarrow{C.34} \gamma_{B_{cm}} \xrightarrow{C.33} \beta_{B_{cm}} = \beta_{cm} \quad (C.44)$$

or

$$E_{A_{lab}} \xrightarrow{C.38} \gamma_{A_{cm}} \longrightarrow \beta_{A_{cm}} \xrightarrow{C.35} p_{A_{lab}} = p_{lab} \xrightarrow{C.35} \beta_{cm} = \frac{p_{lab}}{E_{lab}} \quad (C.45)$$

The first possibility is the easiest, but one might choose a different one depending on what other quantities are needed later on.

#### C.4.5 Relation Between $\theta_{cm}$ and $\theta_{lab}$

$$\tan(\theta_{A'_{lab}}) = \frac{\sin(\theta_{A'_{cm}})}{\gamma \left( \cos(\theta_{A'_{cm}}) + \frac{\beta}{\beta_{A'_{cm}}} \right)}, \quad (C.46)$$

where  $\beta$  is the velocity of the center of mass system in the laboratory system.

#### Photons

$$\tan(\theta_{cm}) = \frac{\sin(\theta_{lab})}{\gamma(\cos(\theta_{lab}) - \beta)}$$

$$\tan(\theta_{lab}) = \frac{\sin(\theta_{cm})}{\gamma(\cos(\theta_{cm}) + \beta)}$$

$$E_{cm} = \gamma E_{lab}(1 - \beta \cos(\theta_{lab}))$$

$$E_{lab} = \gamma E_{cm}(1 + \beta \cos(\theta_{cm}))$$

#### C.4.6 Solid Angle Relation

$$\frac{d\Omega_{lab}}{d\Omega_{cm}} = \frac{\gamma \left( 1 - \cos(\theta_{A'_{cm}}) \frac{\beta}{\beta_{A'_{cm}}} \right)}{\left( \gamma^2 \left( \cos(\theta_{A'_{cm}}) + \frac{\beta}{\beta_{A'_{cm}}} \right)^2 + \sin(\theta_{A'_{cm}})^2 \right)^{\frac{3}{2}}} \quad (C.47)$$

## Photons

$$\begin{aligned}\frac{d\Omega_{lab}}{d\Omega_{cm}} &= \frac{1}{\gamma^2(1 + \beta \cos(\theta_{cm}))^2} \\ &= \left(\frac{E_{cm}}{E_{lab}}\right)^2 \\ &= \gamma^2(1 - \beta \cos(\theta_{lab}))^2\end{aligned}$$

### C.4.7 Invariant Mass

$$m_A^2 = \left(\sum_i E_{B_{lab}^{(i)}}\right)^2 - \left(\sum_i \mathbf{p}_{B_{lab}^{(i)}}\right)^2. \quad (\text{C.48})$$

The excitation energy of particle  $A$  is obtained as

$$E_A^* = m_A - m_A^{(0)}, \quad (\text{C.49})$$

and the breakup energy is

$$E_A^{br} = m_A - \sum_i m_{B_i}. \quad (\text{C.50})$$

# Appendix D

## Simulation of the Proton Scattering Experiment

A simulation program was written in FORTRAN that simulates the full detector response, the geometry of the setup, the beam emittance, as well as energy loss and angular straggling of the recoil protons in the target.

The code uses the NSCL histogrammer SMAUG for the generation of the spectra and since it is also linked to the standard analysis routines, actual data can be used as a starting point for the simulation. In this case actual tracking data are used in order to study the effect of the beam emittance on the resolution.

### D.1 Structure of Computer Code

- Event Generation
  - scatter two particles in center of mass system; option to use cross section data or flat cross section
  - transformation to the lab system
  - depending on settings rotate coordinate system and/or move origin to match the incoming particle; the incoming particle is defined by actual measured PPAC data

- calculate and subtract the energy loss [48] in the target from the proton energy; the scattering occurs at a random depth in the target; add straggling [58] to the proton direction; see figure 5.15;
- Measurement
  - check which detectors are hit (that includes the particle and proton detectors)
  - add detector response (energy resolution, position resolution...) to “measured” signals
- Analysis
  - same (or similar) as analysis of real data

## D.2 Description of Input File

The following is a sample input file. It was used to create the spectra in figure 5.16.

```
m_a           : 33533.7840
m_b           : 938.2723
m_ap0        : 33533.7840
m_bp0        : 938.2723
beam_energy   : 1211.0400
de           : 0.0200
use_cs       : F
ex_en_ap     : 0.0000
target_thickness : 2.7000
axis_rotate  : T
target_intercept_calc : T
do_angl_stragl : T
stragl_max_iter : 10
e_noise      : 0.1000
pos_res_10mev : 1.0000
strip_x_randomize : T
ppac1_resolution : 8.0000
ppac2_resolution : 3.0000
tof_distance  : 40.0000
tof_resolution : 0.0000
hit_check_zero : T
hit_check_tel : T
zero_radius   : 38.1000
t_wethinkitis : 1211.0400
tracking_pos  : T
tracking_angle : T
corr_for_target_th : T
tof_correction : F
file_cs_gs_data : SYS$GAMMA3:[96035.SIMUL.36AR]cs_gs.data
file_cs_ex_data : SYS$GAMMA3:[96035.SIMUL.36AR]cs_ex.data
tot_cs_max    : 300.000
```

All parameters are described in table D.1. If `use_cs=T` then two states are included, one with excitation energy (=Q-value) of zero and the other with excitation energy `ex_en_ap`. The cross section data files `file_cs_gs_data` and `file_cd_ex_data` are used for both states, respectively. If `use_cs=F` then only one state is used with a flat cross section and excitation energy of `ex_en_ap`.

Item	Description
m_a	projectile mass (MeV)
m_b	target mass (MeV)
m_ap0	ejectile mass (MeV)
m_bp0	recoil mass (MeV)
beam_energy	beam energy (MeV)
de	beam energy spread
use_cs	if T then use cross section given in the files <code>file_cs_gs_data</code> for the elastic scattering and <code>file_cs_ex_data</code> for the excited state
ex_en_ap	excitation energy of excited state; see text
target_thickness	target thickness (mg/cm <sup>2</sup> )
axis_rotate	if F then use z-axis as incoming direction; if T use direction supplied by PPAC data
target_intercept_calc	if F projectile hits target in the center ( $x = 0, y = 0$ ), if T see <code>axis_rotate</code>
do_angl_stragl	if T include angular straggling in target
stragl_max_iter	take a maximum of <code>stragl_max_iter</code> steps for the proton to travel out of the target
e_noise	noise in energy detectors (Silicon) (MeV) (FWHM)
pos_res_10mev	position resolution of strip detectors (mm) (FWHM)
strip_x_randomize	if T randomize position perpendicular to strip
ppac1_resolution	resolution of first PPAC (mm) (FWHM)
ppac2_resolution	resolution of second PPAC (mm) (FWHM)
tof_distance	distance between time of flight detectors (m)
tof_resolution	resolution of time of flight detectors (ns)
hit_check_zero	if T check if ejectile hits zero degree detector
hit_check_tel	if T check if proton hit telescopes
zero_radius	radius of zero degree detector (mm)
t_wethinkitis	beam energy used for analysis; can be different from <code>beam_energy</code> in order to include systematic errors
tracking_pos	if T use tracking to calculate position on target
tracking_angle	if T use tracking to calculate incoming beam direction; if F use z-axis
corr_for_target_th	if T correct measured proton energy for half of the target thickness
tof_correction	if T use time of flight information to correct for beam energy spread; not implemented yet
file_cs_gs_data	path to file containing the elastic cross section; use if <code>use_cs</code> is T
file_cs_ex_data	same as previous for inelastic scattering
tot_cs_max	maximum possible cross section for correct calculation; if the cross section (from the previous two entries) is larger than <code>tot_cs_max</code> then <code>tot_cs_max</code> will be used

Table D.1: Explanation of input file for simulation.

# Appendix E

## Differential Cross Section

The number of reactions  $N_r$  observed in a detector is proportional to the number of incoming beam particles  $N_b$  and the number of target nuclei per unit area  $N_t$ . For a particle detector that has a perfect intrinsic detection efficiency (like the silicon detectors used in the proton scattering experiment, but unlike the photon detectors used in the Coulomb excitation experiment) the factor of proportionality  $\sigma := \frac{N_r}{N_t N_b}$  is given by pure geometrical considerations as

$$\sigma = \int_{\Omega} \frac{d\sigma}{d\Omega} \sin(\theta) d\phi d\theta, \quad (\text{E.1})$$

where  $\frac{d\sigma}{d\Omega}$  is the differential cross section of the reaction to be observed. The integral goes over  $\Omega$ , which corresponds to the solid angle covered by the detector. Assuming a constant differential cross section within  $\Omega$

$$\frac{d\sigma}{d\Omega} = \sigma \left( \int_{\Omega} \sin(\theta) d\phi d\theta \right)^{-1}. \quad (\text{E.2})$$

The integral over  $\phi$  can be replaced in the following way

$$\begin{aligned} \int_{\Omega} \sin(\theta) d\phi d\theta &= \int_{\theta} \sin(\theta) \int_0^{2\pi} \epsilon(\theta) d\phi d\theta \\ &= 2\pi \int_{\theta} \sin(\theta) \epsilon(\theta) d\theta. \end{aligned}$$

$\epsilon(\theta)$  is the detection efficiency as a function of angle  $\theta$ , defined as the fraction of particles (all with scattering angle  $\theta$ ) that are actually detected. This efficiency can be obtained from geometrical considerations of the angular coverage or from a Monte Carlo simulation of the experimental setup.

The differential cross section is obtained from the number of observed reactions  $N_r$  in the following way: For a sufficiently small  $\theta$  integration range one can assume  $\epsilon(\theta)$  (and also  $\sin(\theta)$ ) to be constant and obtains

$$\begin{aligned} \frac{d\sigma}{d\Omega} &= \frac{\sigma}{2\pi \epsilon(\theta) (\cos(\theta_{low}) - \cos(\theta_{high}))} \\ &= \sigma \frac{1}{2\pi \epsilon(\theta)} \frac{1}{\sin(\theta) \Delta\theta} \\ &= \frac{N_r}{N_t N_b} \frac{1}{2\pi \epsilon(\theta)} \frac{1}{\sin(\theta) \Delta\theta} , \end{aligned}$$

with

$$\begin{aligned} N_r &: && \text{Number of reactions observed} \\ N_b &: && \text{Total number of beam particles} \\ N_t &: && \text{Total number of target particles (}^1\text{H per cm}^2\text{)} \\ \epsilon(\theta) &: && \text{efficiency for particle detection at angle } \theta \\ \theta_{low}, \theta_{high}, \theta &: && \text{lower, higher limit and centroid of } \theta \text{ bin} \end{aligned} \quad (\text{E.3})$$

In the proton scattering experiment  $N_t$  is given by:

$$N_t = N_{1\text{H}} \frac{N_A}{M} d_t , \quad (\text{E.4})$$

where  $N_{1\text{H}}$  is the number of  $^1\text{H}$  atoms per molecule,  $d_t$  is the target thickness in units of mass per area,  $N_A$  is the Avogadro number, and  $M$  is the molar mass (mass of  $N_A$  molecules). For the polypropylene target ( $\text{CH}_2$ ) used in the  $(p, p')$  experiments

$$\begin{aligned} N_{1\text{H}} &= 2 \\ N_A &= 6.022 \cdot 10^{23} \text{ mol}^{-1} \\ M &= 14 \frac{\text{g}}{\text{mol}} \\ N_{1\text{H}} \frac{N_A}{M} &= 2 \cdot 6.022 \cdot 10^{23} \frac{1}{\text{mol}} \frac{1}{14 \frac{\text{g}}{\text{mol}}} \end{aligned}$$

$$= 8.603 \cdot 10^{22} \text{ g}^{-1}$$

Therefore

$$\frac{d\sigma}{d\Omega} = \frac{1.850 \cdot 10^6}{d_t / (\text{mg cm}^{-2})} \frac{N_r}{N_b} \frac{1}{\epsilon(\theta)} \frac{1}{\sin(\theta) \Delta\theta} \cdot \text{mb} . \quad (\text{E.5})$$

Equation E.5 gives the differential cross section in  $\frac{\text{mb}}{\text{sr}}$  given the target thickness in  $\text{mg cm}^{-2}$ .  $1 \text{ mb} = 10^{-27} \text{ cm}^2$  was used.



# Appendix F

## A New Method for Particle Tracking

### F.1 Traditional Tracking

From the geometry of the setup (see figure F.1) it follows that the position on the target  $x_t$  (the target is located at  $z_t = 0$ ) is given by

$$x_t = \frac{x_1 z_2 - x_2 z_1}{z_2 - z_1}, \quad (\text{F.1})$$

and the slope  $\frac{dx}{dz}$  is given by

$$\frac{dx}{dz} = \frac{x_2 - x_1}{z_2 - z_1}, \quad (\text{F.2})$$

where  $x_{1(2)}$  is the (measured) x-coordinate of the particle at  $z = z_{1(2)}$ , which is the z-coordinate of detector 1(2). The error of the target position  $\sigma(x_t)$  is

$$\sigma^2(x_t) = \left( \frac{z_2}{z_2 - z_1} \sigma(x_1) \right)^2 + \left( \frac{z_1}{z_2 - z_1} \sigma(x_2) \right)^2, \quad (\text{F.3})$$

where  $\sigma(x_{1(2)})$  is the uncertainty in the measurement of the position  $x_{1(2)}$ . The error in the slope of the particle trajectory  $\sigma\left(\frac{dx}{dz}\right)$  is

$$\sigma^2\left(\frac{dx}{dz}\right) = \left(\frac{1}{z_1 - z_2}\right)^2 (\sigma^2(x_1) + \sigma^2(x_2)). \quad (\text{F.4})$$

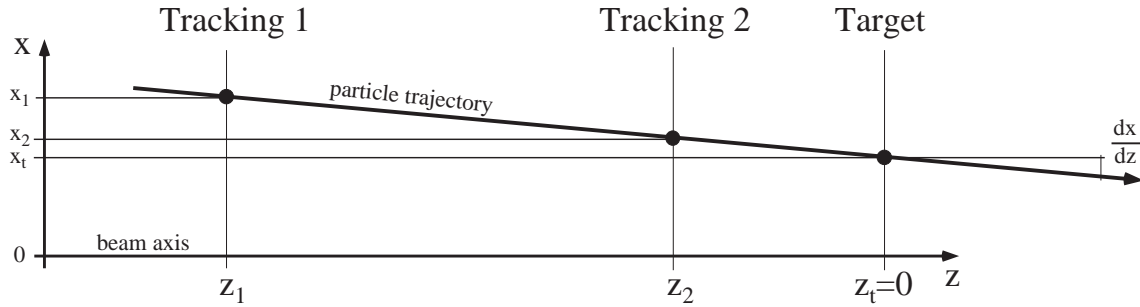


Figure F.1: Setup for particle tracking. Two tracking detectors determine the position of the beam particle  $x_{1,2}$  at two points along the beam line, from which the position on the target and the slope of the trajectory can be determined. The coordinates of the tracking detectors are  $z_1$  (detector 1) and  $z_2$  (detector 2). The target is located at  $z_t = 0$

## F.2 New Method

In the following a new algorithm for the determination of the target intercept and the slope of the trajectory is presented. The new method is superior to the traditional method, especially if the resolution of the tracking detectors is poor.

### F.2.1 Some Beam Physics

The slope of a particle trajectory is not independent of the (transverse) position of the particle. This is illustrated in figure F.2. Shown is the phase-space-ellipse (PSE), i.e. the slope of the beam trajectory is plotted as a function of transverse position. In an ideal case the width ( $= 2 \cdot W$ ) is zero and the slope of the trajectory is a linear function of the particle position. Hence we can infer from *one* position measurement alone the trajectory of the particle. A prerequisite is, of course, a knowledge of the orientation of the PSE (i.e. the slope  $S$ ). The width of the PSE introduces a large uncertainty, however.

Assuming that the main beam direction is along the  $z$ -axis of the coordinate system, it follows that the slope of the trajectory  $\frac{dx}{dz}$  as a function of position  $x$  is

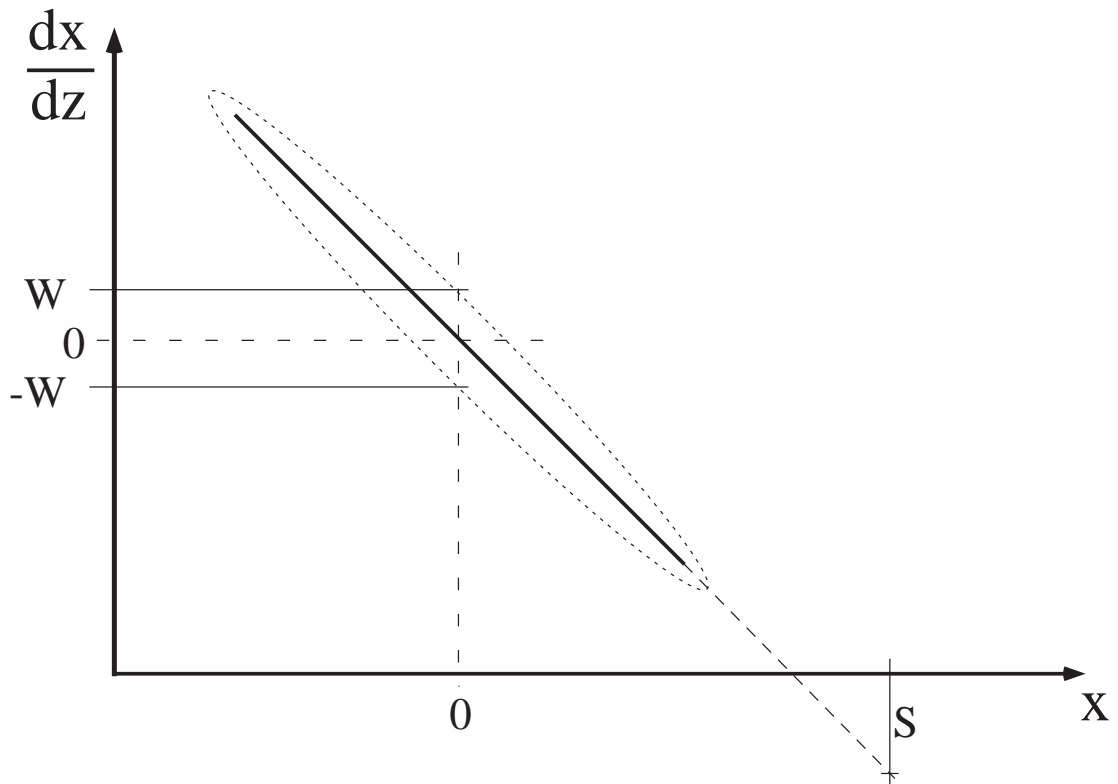


Figure F.2: Phase-space-ellipse (PSE) of the beam can be approximated by a straight line. The error that is introduced is  $W$ , the half-width of the PSE. The slope  $S$  is defined as  $S = \frac{d(dx/dz)}{dx}$ .

obtained through

$$\frac{dx}{dz} = Sx . \quad (\text{F.5})$$

It is important to not confuse the slope of the trajectory  $\frac{dx}{dz}$  with the slope of the PSE  $S$ . The latter changes as one goes along the beam-direction ( $S$  is negative before the focus, infinity at the focus, and positive after the focus of the beam). It is the same for all particles and a property of the beam as a whole. In contrast  $\frac{dx}{dz}$  is different for each particle. For the same particle, however, it is independent of the position along the beam-line  $z$ .

The position on the target is given by

$$x_t = x_1 + (z_t - z_1) \frac{dx}{dz} = x_1 - z_1 \frac{dx}{dz} . \quad (\text{F.6})$$

The uncertainty of the particle slope is

$$\sigma^2 \left( \frac{dx}{dz} \right) = S^2 \sigma^2(x_1) + W^2 , \quad (\text{F.7})$$

where the first term is due to the resolution of the detector and the second term is the half-width of the PSE (see figure F.2). The two contributions are independent and are therefore added in quadrature. The uncertainty in the position on the target is

$$\begin{aligned} \sigma^2(x_t) &= \sigma^2(x_1) + z_1^2 S^2 \sigma^2(x_1) + z_1^2 W^2 \\ &= (1 + z_1^2 S^2) \sigma^2(x_1) + z_1^2 W^2 . \end{aligned}$$

If the beam is focused at the target position the term  $1 + z_1^2 S^2 = 0$  and the position resolution is equal to  $z_1^2 W^2$ , which yields essentially the beam spot size. The approximation of the PSE as a straight line results in a constant calculated position at the focus, and hence, the position resolution is equal to the half-width of the beam-spot. If the resolution of the tracking detectors results in a resolution at the target (using standard tracking), that is larger than the beam-spot size, then it is of course better

to assume a constant position on the target. But what happens if the beam-spot is on the order of the resolution? Then one should combine the *three* different methods (the usual one and the new method applied to *both* tracking detectors) to determine the target point  $x_t$  and the slope  $\frac{dx}{dz}$ . The new method relies on the independence of all three procedures, which is only almost true. For instance the error due to the width of the PSE is the same for both tracking detectors and should therefore be added linearly.

Another advantage of the new method is that it can be applied, if the beam is not focused at the target, but instead slightly before or behind. The assumption of a constant target point would result in a much worse resolution.

## F.2.2 Determination of Position and Slope

Assuming independence of the three measurements one finds the target position as the weighted average:

$$x_t = \left( \sum_i \frac{1}{\sigma^2(x_t^{(i)})} \right)^{-1} \sum_i \frac{x_t^{(i)}}{\sigma^2(x_t^{(i)})}, \quad (\text{F.8})$$

and the slope of the trajectory as

$$\frac{dx}{dz} = \left( \sum_i \frac{1}{\sigma^2\left(\frac{dx}{dz}^{(i)}\right)} \right)^{-1} \sum_i \frac{\frac{dx}{dz}^{(i)}}{\sigma^2\left(\frac{dx}{dz}^{(i)}\right)}, \quad (\text{F.9})$$

with uncertainties given by

$$\sigma^2(x_t) = \left( \sum_i \frac{1}{\sigma^2(x_t^{(i)})} \right)^{-1} \quad (\text{F.10})$$

and

$$\sigma^2\left(\frac{dx}{dz}\right) = \left( \sum_i \frac{1}{\sigma^2\left(\frac{dx}{dz}^{(i)}\right)} \right)^{-1}. \quad (\text{F.11})$$

The slope  $S$  and the half-width  $W$  of the PSE in terms of the beam emittance  $\epsilon$ , the beam-spot size at the focus  $D$ , the position of the focal point  $f$  at any position  $z$

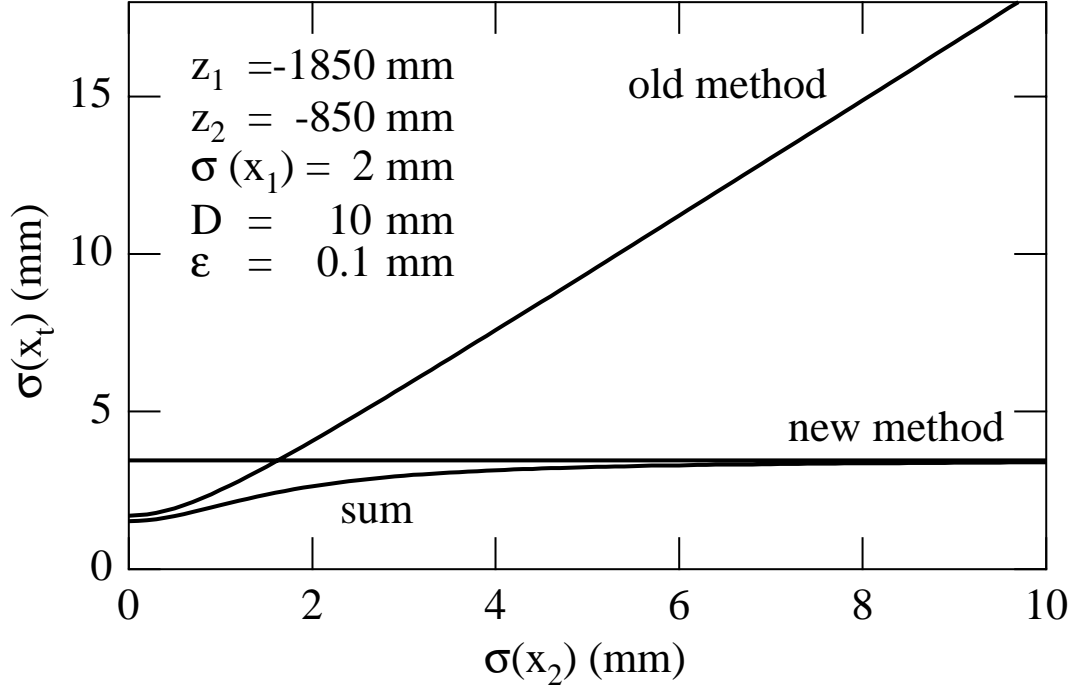


Figure F.3: Comparison of old and new method. Shown is the resolution of the target position  $\sigma(x_i)$  as a function of the resolution of the second tracking detector  $\sigma(x_2)$ . The positions of the tracking detector with respect to the target  $z_{1,2}$  are roughly 1 m and 2 m. The beam-spot size  $D$  is 10 mm and the emittance  $\epsilon$  is 0.1 mm. One can see that if the resolution of the second detector is larger than 2 mm the new method is better, and even for a resolution of 1 mm the weighted average of both methods results in an improvement.

along the beam-line are [59]:

$$S = -\frac{1}{z - f} \quad (\text{F.12})$$

and

$$W = \left( \left( \frac{D}{2\epsilon} \right)^2 + \left( \frac{2(z - f)}{D} \right)^2 \right)^{-\frac{1}{2}}. \quad (\text{F.13})$$

Figure F.3 shows an example. The new resolution is considerably better as soon as the resolution of the tracking detector is larger than 2 mm. In experiments where tracking is crucial not only the target position but also the slope of the trajectory is of importance and the effect of the different tracking methods can not easily be estimated.

### F.2.3 Practical Method

For practical purposes it is hard to determine the slope of the PSE  $S$  for a given detector position and beam profile. A better procedure is to consider it a parameter and optimize it until the best resolution is reached. This procedure has been applied here, and figure F.4 shows the effect on the energy resolution for the reaction  $^{36}\text{Ar}(p, p')^{36}\text{Ar}^*$ . The resolutions of the tracking detectors are 8 mm and 3 mm (FWHM) and the new method results in a better resolution by almost a factor of 2. The position resolution of one detector was so poor because of a strong rate dependence. See section 5.1.2.

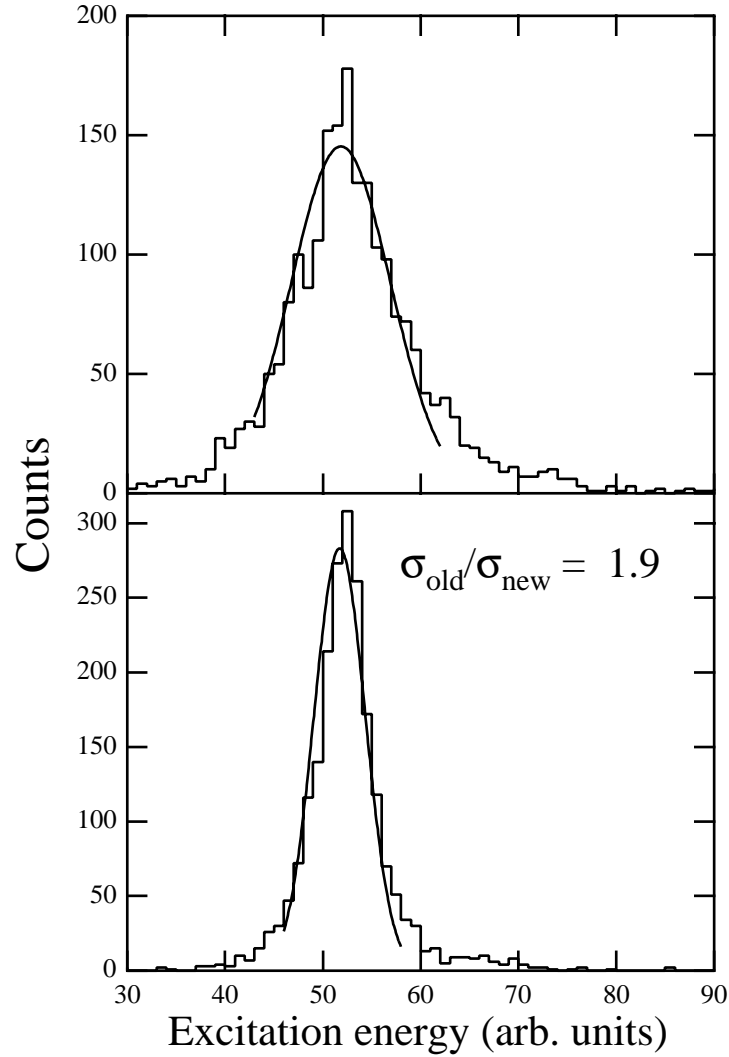


Figure F.4: Measured excitation energy with angular cut in  $\theta_{cm} = 25^\circ - 30^\circ$ . The top panel shows the spectrum obtained if normal tracking is used, whereas the bottom panel shows the same spectrum but the new tracking method is applied. The resolution improves by almost a factor of 2.

# Appendix G

## Fitting of Spectra

In order to fit a spectrum one needs to assign proper errors  $\sigma_i$  to each point  $x_i$  ( $i = 0, 1 \dots$ ). Since in each channel the number of points is “counted”, Poisson statistics applies and an estimate is to assign

$$\sigma_i = \sqrt{x_i} . \tag{G.1}$$

This is only an estimate, since the real error has to be taken from the parent distribution, which is not known. The estimate from equation G.1 is especially bad if the statistics is low. As a general rule, the number of counts per channel should be more than 10 [22].

For lower statistics it is necessary to take the error from the fitted curve (i.e.  $\sigma_i^2 = f(x_i)$ , where  $f(x)$  was fitted to the data points  $y_i$  as  $f(x_i) = y_i$ ), which should follow the parent distribution much closer. However, there is another reason to use the errors obtained from the fitted curve, which is explained in the following.

Consider a set of data points  $\{x_i, y_i\}$  and a function  $f(x)$  is fitted to these points. The  $\chi^2$  of the fit is given through

$$\chi^2 = \sum_i \left[ \frac{1}{\sigma_i^2} (y_i - f(x_i))^2 \right] . \tag{G.2}$$

Writing  $f(x)$  as  $b \cdot f(x)$  with parameter  $b$  yields

$$\chi^2 = \sum_i \left[ \frac{1}{\sigma_i^2} (y_i - b \cdot f(x_i))^2 \right]. \quad (\text{G.3})$$

Since  $\chi^2$  has a minimum for the best fit it follows that

$$\frac{\partial \chi^2}{\partial b} = -2 \sum_i \left[ \frac{1}{\sigma_i^2} (y_i - b f(x_i)) \cdot f(x_i) \right] = 0. \quad (\text{G.4})$$

$\chi^2$  can be written as

$$\chi^2 = \sum_i \left[ \frac{y_i}{\sigma_i^2} (y_i - b f(x_i)) - b \frac{f(x_i)}{\sigma_i^2} (y_i - b f(x_i)) \right].$$

The last term is proportional to  $\frac{\partial \chi^2}{\partial b}$  and is thus equal to zero. It follows that

$$\chi^2 = \sum_i \frac{y_i}{\sigma_i^2} (y_i - b f(x_i)). \quad (\text{G.5})$$

Setting  $\sigma_i^2 = y_i$  yields

$$\chi^2 = \sum_i y_i - \sum_i b f(x_i) = \text{Area}(\text{DATA}) - \text{Area}(\text{FIT}) \quad (\text{G.6})$$

Thus the fit underestimates the area of the data by  $\chi^2$ , which can be quite considerable.

However if one sets  $\sigma_i^2 = f(x_i)$ , i.e. the error is deduced from the fitted curve, then it follows from equation G.4 that

$$0 = \frac{\partial \chi^2}{\partial b} = -2 \sum_i (y_i - b f(x_i)), \quad (\text{G.7})$$

and thus

$$\sum_i (y_i - b f(x_i)) = \text{Area}(\text{DATA}) - \text{Area}(\text{FIT}) = 0. \quad (\text{G.8})$$

Therefore the fitted function has the same area as the data.

In practice, one starts out with errors derived from the data ( $\sigma_i^2 = y_i$ ) and when the fit looks good one uses the errors derived from the fitted function ( $\sigma_i^2 = f(x_i)$ ) and fits again.

# LIST OF REFERENCES

- [1] G.R. Satchler, *Introduction to Nuclear Reactions* (Oxford University Press, 1990).
- [2] A. Bohr and B.R. Mottelson, *Nuclear Structure, Vol. 1 and 2*, (World Scientific, 1998).
- [3] A.M. Bernstein *et al.*, *Comments Nucl. Part. Phys.* **11**, 203 (1983).
- [4] K. Alder *et al.*, *Rev. Mod. Phys.* **28**, 432 (1956).
- [5] A. Winther and K. Alder, *Nucl. Phys.* **A319**, 518 (1979).
- [6] C.A. Bertulani and G. Baur, *Physics Reports* **163**, 299 (1988).
- [7] B. Davids *et al.*, *Phys. Rev. Lett.* **81**, 2209 (1998).
- [8] C.J. Benesh *et al.*, *Phys. Rev.* **C40**, 1198 (1989).
- [9] S.S.M. Wong, *Introductory Nuclear Physics* (Prentice Hall, 1990).
- [10] S. Wan *et al.*, *Z. Phys.* **A358**, 213 (1997).
- [11] J.D. Jackson, *Classical Electrodynamics* (John Wiley & Sons, 1975).
- [12] H. Scheit *et al.*, *Phys. Rev. Lett.* **77**, 3967 (1996).
- [13] H. Geissel *et al.*, *Annu. Rev. Nucl. Part. Sci.* **45**, 163 (1995).

- [14] B. M. Sherrill *et al.*, *Nucl. Instrum. Methods* **B56**, 1106 (1991).
- [15] M.J. Chromik *et al.*, *Phys. Rev.* **C55**, 1676 (1997).
- [16] O. Sorlin *et al.*, *Phys. Rev.* **C47**, 2941 (1993).
- [17] T.R. Werner *et al.*, *Phys. Lett.* **B335**, 259 (1994); *Nucl. Phys.* **A597**, 327 (1996).
- [18] R. Harkewicz, *Rev. Sci. Instrum.* **67**, 2176 (1996).
- [19] D. Swan, *et al.*, *Nucl. Instrum. Methods* **A348**, 314 (1994).
- [20] J.N. Carter *et al.*, *Nucl. Instrum. Methods* **196**, 477 (1982).
- [21] N. I. Kaloskamis *et al.*, *Nucl. Instrum. Methods* **A330**, 447 (1993).
- [22] P.R. Bevington, D.K. Robinson, *Data Reduction and Error Analysis for the Physical Sciences* (WCB/McGraw-Hill, 1992).
- [23] H. Scheit *et al.*, *Nucl. Instrum. Methods* **A422**, 124 (1998).
- [24] J.W. Olness *et al.*, *Phys. Rev.* **C34**, 2049 (1986).
- [25] P.M. Endt, *Nucl. Phys.* **A521**, 1 (1990).
- [26] P.M. Endt, *Nucl. Phys.* **A633**, 1 (1998).
- [27] G.M. Crawley *et al.*, *Phys. Lett.* **B64**, 143 (1976).
- [28] W. Mayer *et al.*, *Phys. Rev.* **C22**, 2449 (1980).
- [29] S. Raman *et al.*, *At. Data Nucl. Data Tables* **36**, 1 (1987).
- [30] B.A. Brown and B.H. Wildenthal, *Ann. Rev. Nucl. Sci.* **38**, 29 (1988).
- [31] W.A. Richter *et al.*, *Nucl. Phys.* **A523**, 325 (1991).
- [32] E.K. Warburton, J.A. Becker and B.A. Brown, *Phys. Rev.* **C41**, 1147 (1990).

- [33] G. Kraus *et al.*, *Phys. Rev. Lett.* **73**, 1773 (1994).
- [34] S. Raman *et al.*, *Phys. Rev.* **C43**, 556 (1991).
- [35] G.R. Satchler, *Direct Nuclear Reactions* (Oxford University Press, 1983).
- [36] E. Gadioli and P.E. Hodgson, *Pre-Equilibrium Nuclear Reactions* (Oxford University Press, 1992).
- [37] D. Larson *et al.*, *Phys. Lett.* **B42**, 153 (1972).
- [38] S.M. Austin, *An Empirical Effective Interaction; in The (p,n) Reaction and the Nucleon-Nucleon Force* (Plenum Publishing Corporation, 1980).
- [39] J. Raynal, Computer code ECIS88, unpublished.
- [40] F.D. Becchetti, Jr. and G.W. Greenlees, *Phys. Rev.* **182**, 1190 (1969).
- [41] J.-P. Jeukenne *et al.*, *Phys. Rev.* **C16**, 80 (1977).
- [42] M.D. Cortina-Gil *et al.*, *Phys. Lett.* **B401**, 9 (1997).
- [43] J.H. Kelley *et al.*, *Phys. Rev.* **C56**, R1206 (1997).
- [44] N. Alamanos *et al.*, Preprint, (1998).
- [45] V.A. Madsen *et al.*, *Phys. Rev.* **C12**, 1205 (1975).
- [46] R.L. Kozub, *Phys. Rev.* **172**, 1078 (1968).
- [47] R.R. Johnson and R.J. Griffiths, *Nucl. Phys.* **A117**, 273 (1968).
- [48] J.F. Janni, *At. Data Nucl. Data Tables* **27**, 150 (1982).
- [49] *DEC Fortran: Language Reference Manual* (Digital Equipment Corporation, 1995).

- [50] R. De Leo *et al.*, *Phys. Rev.* **C31**, 362 (1985).
- [51] Private communication with Francois Marechal. Data is not yet published.
- [52] M.A. Kennedy *et al.*, *Phys. Rev.* **C46**, 1811 (1992).
- [53] S. Wolfram *The Mathematica Book*, (Cambridge University Press, 1996).
- [54] A.N.F. Aleixo and C.A. Bertulani, *Nucl. Phys.* **A505**, 448 (1989).
- [55] Frauenfelder, H. and R.M. Steffen, 1965, *Alpha-, Beta- and Gamma-ray Spectroscopie*, Vol 2, ed. K. Siegbahn .
- [56] K. Alder and A. Winther, *Electromagnetic Excitation* (North-Holland, Amsterdam, 1975).
- [57] E.U. Condon, G.H. Shortly, *The Theory of Atomic Spectra* (Cambridge University Press, 1935).
- [58] G.R. Lynch and O.I. Dahl *Nucl. Instrum. Methods* **B58**, 6 (1991).
- [59] H. Wollnik, *Optics of Charged Particles* (Academic Press, 1987).
- [60] R. Anne *et al.*, *Z. Phys.* **A352**, 397 (1995).
- [61] R.F. Casten, *Nuclear Structure from a Simple Perspective* (Oxford University Press, 1990).
- [62] *International School of Heavy Ion Physics; 4th Course: Exotic Nuclei* Ed. R.A. Broglia and P.G. Hansen (World Scientific, 1998).
- [63] M. Fauerbach *et al.*, *Phys. Rev.* **C56**, R1 (1997).
- [64] R.D. Gill, *Gamma-Ray Angular Correlations* (Academic Press, 1975).
- [65] T. Glasmacher *et al.*, *Phys. Lett.* **B 395**, 163 (1997).

- [66] K.L.G. Heyde, *The Nuclear Shell Model* (Springer-Verlag, 1994).
- [67] R. W. Ibbotson *et al.*, *Phys. Rev. Lett.* **80**, 2081 (1998).
- [68] *IGOR Pro User's Guide, IGOR Pro Programming and Reference Manual*, (WaveMetrics Inc., 1996).
- [69] W.R. Leo, *Techniques for Nuclear and Particle Physics Experiments* (Springer-Verlag, 1994).
- [70] T. Motobayashi *et al.*, *Phys. Lett.* **B346**, 9 (1995).
- [71] C.M. Perey and F.G. Perey, *At. Data Nucl. Data Tables* **17**, 1 (1976).
- [72] F. Petrovich *et al.*, *Ann. Rev. Nucl. Part. Sci.* **36**, 29 (1986).
- [73] P. Ring, P. Schuck, *The Nuclear Many-Body Problem* (Springer-Verlag, 1980).
- [74] T. Suomijärvi *et al.* *Nucl. Phys.* **A509**, 369 (1990).

